Dissertation zur Erlangung des Doktorgrades

der Fakultät für Chemie und Pharmazie

der Ludwig-Maximilians-Universität München

Engineering of Bioinspired Nanoparticles for Drug Delivery and Targeting

Bernard Manuel Haryadi

aus

Bandung, Indonesien

2022

Erklärung

Diese Dissertation wurde im Sinne von § 7 der Promotionsordnung vom 28. November 2011 von Herrn Prof. Dr. Gerhard Winter von der Fakultät Chemie und Pharmazie betreut.

Eidesstattliche Versicherung

Diese Dissertation wurde eigenständig und ohne unerlaubte Hilfe erarbeitet.

München, den 20.06.2022

_____
Bernard Manuel Haryadi

Dissertation eingereicht am	:	30.06.2022
1. Gutachter	:	Prof. Dr. Gerhard Winter
2. Gutachter	:	Prof. Dr. Wolfgang Frieß
Mündliche Prüfung am	:	26.07.2022

For My Beloved Family

“Look deep into nature, and then you will understand everything better.”

Albert Einstein (1879 - 1955)

ACKNOWLEDGEMENTS

The recent dissertation was prepared between 2015 and 2022 at the Department of Pharmacy, Pharmaceutical Technology and Biopharmaceutics at the Ludwig-Maximilians-University (LMU) Munich, Germany under the supervision of Prof. Dr. Gerhard Winter. This doctoral study would not have been possible without the main financial support of the Deutscher Akademischer Austauschdienst (DAAD) and other support from many people, to whom I am indebted.

First and foremost, I would like to express my deepest thankfulness to my doctoral father Prof. Dr. Gerhard Winter, for his dedicated and inspiring guidance throughout the entire dissertation. Moreover, I would like to thank him for the given trust and freedoms to develop, enliven, and be responsible for all the consequences of my own scientific ideas. These remarkably add a new depth and perspective to this dissertation, besides the motivating discussions with him and his outstanding scientific expertise. I am also really thankful for the great opportunities and support to present my works at numerous international conferences and to arrange my research stay at the University of Kansas, not to mention the financial support at the end of my study period. Thank you for the interests in my works, especially the tremendous patience as well as understanding for the unpredictable, hard time during the dissertation writing. It was very tough and difficult, but in the end, we are happy to get through it and let the “tough cookie out the mud”. Thank you also for all the social activities and the good working atmosphere within the group, making the institute an enjoyable place and an unforgettable lifetime experience. Additionally, I do appreciate and will always remember all personal advice and guidance, particularly regarding the importance of giving other people the indispensable chances to experience personal development and prove themselves, as he epitomized by himself and with Jack Welch’s case. Under his supervision, I did not only improve as a scientist, but also gained a lot in my personal development.

I would like to thank PD Dr. habil. Julia Engert for her scientific enthusiasm and caring character. Her scientific advice and support in preparing publications were a very critical part of this dissertation.

Prof. Dr. Wolfgang Friess and Prof. Dr. Olivia Merkel, are thanked for the continuing support and guidance. I appreciate the constructive nature of their criticism, especially during the weekly seminar. I also thank Dr. Gerhard Simon, Sabine Kohler, Alice Hirschmann, Ayla Tekbudak, Regine Bahr, Susanne Petzel, and Imke Leitner for their constant support in all lab-keeping and administrative processes during my study.

This multidisciplinary dissertation would not have been possible without the support of many enthusiastic cooperation partners. I would like to express my thankfulness, starting with Prof. Dr. Rainer Jordan for supporting my work and the opportunity to visit his lab at the Technical University of Dresden. In this context, I also want to thank Dr. Ihsan Amin, Rene Schubel, Daniel Hafner, and all other members of this group to share their knowledge about Atomic Force Microscope (AFM), mechanical properties measurement, and Ellipsometer with me.

I would like to express my gratitude to Prof. Dr. Teruna J. Siahaan to give me the opportunity to stay in his lab at the University of Kansas. He kindly shared his scientific expertise, motivating life insight, and loaned his bike during my research stay. I deeply enjoyed our regular scientific meetings, common talks, and farewell lunch. Brian M. Kopec is thanked for the interesting and fruitful cooperation. Kavisha Ulapane, Rucha Mahadik, Kelly Schwinghammer, Isaac Alejandro Nevarez-Saenz, Subhradweep Patra, and Jinyan He are also thanked a lot for the many help during my stay in Lawrence, Kansas. Evan Schmidt is also acknowledged to let me experience the “real” States’ life, openness, and friendship.

I would like to thank Dr. Roman Mathaes for sharing his non-spherical particle expertise and academic-nonacademic experiences, especially during my first months at the LMU. Dr. Anna Salvati for the introduction to the biomolecular corona science-related area. Barbara Kneidl and PD Dr. med. Lars Lindner (Arbeitsgruppe Liposomen, Medizinische Klinik und Poliklinik III, Klinikum der Universität München, München, Germany) are thanked for the use of Liposofast-Basic™ in the initial stage of cell membrane development. Christian Minke is kindly acknowledged for helping me with Scanning Electron Microscope-Energy Dispersive X-Ray (SEM-EDX) measurements. Dr. Aditi Mehta, Lorenz Isert, and Natascha Hartl are highly thanked for the kind gift of human monocytes cell line THP-1–introduction to work with cell lines, the help with the confocal laser scanning microscopy, and the use of flow cytometry in the uptake study, respectively. Philipp Nickels and Rafal Krzyszton, and Prof. Dr. Joachim Radler are thanked for the initial trial with Atomic Force Microscope. Xiaohan Zhang and Prof. Dr. Christina Papadakis are thanked for the opportunity to work with Small Angle X-Ray Scattering (SAXS). Tom Podewin (group of Prof. Dr. Anja Hoffmann-Röder, LMU Munich) and Mirko Wagner (group of Prof. Thomas Carell, LMU Munich) for the introduction of Circular Dichroism (CD) spectrometer. Prof. Dr. Thomas Carell is kindly acknowledged for the access to the CD

spectrometer. Dr. Andreas Tosstorff is thanked for the introduction to the molecular modeling. Leibniz Rechenzentrum (LRZ) is thanked for continuous and direct support for computational work, in particular, Dr. Momme Allalen and Dr. Martin Ohlerich LRZ, and the rest of the LRZ team members that are not mentioned here. Dr. Jacob Gavartin, Dr. Kai Welke, Dr. Katalin Phimister, Dr. Felix Wolfheimer, and Rita Podzuna from Schrödinger, Inc. are also acknowledged for their prime and prompt support concerning Schrödinger Software.

Thanks are extended to Prof. Dr. Wolfgang Frieß, Prof. Dr. Olivia Merkel, Prof. Dr. Franz Bracher, Prof. Dr. Stefan Zahler, and Prof. Dr. Hristo Svilenov, for kindly serving as my dissertation examination board members.

I also want to thank all my colleagues and friends, especially from the groups of Prof. Dr. Winter, Prof. Dr. Friess, and Prof. Dr. Merkel. The numerous social activities, such as skiing or hiking trips, the “Doktoranden Stammtisch”, the Thursday sports with ”LMU Shakers”, or even just hanging out together, such as playing football, billiards, and video games. These made the doctoral journey an unforgettable time. Specifically, my former labmates Ute, Teresa, Andy, and Sebastian are thanked for their encouragement and the humorous hours at work. Also, to my long-standing friends from school, Fajar, Reiner, and Ian, thank you for your support, may our friendship be timeless. For any people who are unintentionally, unspecifically mentioned herein, it does not mean that I have forgotten your help. I sincerely thank you as well.

Finally, I would like to thank and dedicate this dissertation to my father Hendrikus, mother Laurensia, and siblings: Amelia and Johan for their endless support and prayers. Without their love and companions, I would not be who I am today. They have sacrificed a lot and ensuring that I can pursue my dreams. You are still and forever my anchors. Especially for my mother, after this dissertation I believe it is my turn to be more available for and take care of you. I know you are stronger than you think. We will meet in person again soon, after being more than 11,000 km and nearly 6 years apart. This dissertation is also dedicated to my grandmother, Tresnawati, who sadly passed away in June 2021. She was one of the most important supporters in my life. I wish she could still be with us.

Last but not least, Raisa. I am really grateful for your continuous care and unconditional love through thick and thin. To have you by my side for more than 15 years (and counting) is really beyond my wildest fantasy. I am sorry if I could not find better words to express my gratitude from the bottom of my heart! Simply, I believe no words can express it enough. If it is not because of you, this dissertation, including the eye-catching schematics herein, would never come true.

TABLE OF CONTENTS

TABLE OF FIGURES (INCLUDING THE SUPPLEMENTARY ONES)

Supplementary Figures

TABLE OF TABLES (INCLUDING THE SUPPLEMENTARY ONES)

Supplementary Tables

TABLE OF EQUATIONS (INCLUDING THE SUPPLEMENTARY ONES)

Supplementary Equations

I. AIM OF DISSERTATION

Since its conception in the initial 1960s, particulate carriers (especially at the nanoscale) are vastly investigated for biomedical applications, such as drug delivery and vaccination. Most of the studies utilize spherical particles yielding different particle properties. Common design parameters are core materials, size, surface charge, and attached target ligands. In contrast, particle shape and mechanical properties (e.g. elasticity) are traditionally ignored. The current dissertation aims to comprehensively integrate and optimize these attributes into a novel and promising system.

The motivation to delve into non-spherical and naturally-derived particles for different drug delivery applications was inspired by several instances from Mother Nature. The idea was to bestow the unique properties of the natural examples to particulate drug delivery systems possessing tailored shapes. For example, the erythrocytes, which circulate 100 - 120 days in the body before they are eliminated by macrophages, reportedly contain various “markers of self” and are virtually oblate. Meanwhile, the non-spherical geometry and the flexibility of the erythrocytes are necessary to pass through thin microcapillaries. Besides erythrocytes, particular bacterial strains, such as *Pseudomonas aeruginosa, Escherichia coli, Bacillus subtilis,* and *Vibrio cholerae* own a non-spherical geometry with a very distinctive in vivo fate. For example, *Pseudomonas aeruginosa* evades phagocytosis by the immune system and can circulate extraordinarily long in the human body. It is still speculative whether the immune system becomes insensitive to such non-spherical organisms or the bacteria have adapted and elicited adequate responses to combat the immune system.

The combined innovative approach between non-spherical and naturally-derived particles is expected to be an auspicious alternative to established synthetic materials used for decorating therapeutic and delivery systems, i.e. polyethylene glycol (PEG). PEG is a well-known standard for evading non-specific clearance by the mononuclear phagocyte system (MPS) or also called the reticuloendothelial system (RES) via biomolecular opsonin adsorption minimization mechanism. Ultimately, PEG confers long-circulating characters to the conjugated drug and/or delivery systems inside an organism’s body. However, it can reportedly induce the formation of anti-PEG antibodies after multiple administrations. Consequently, clearance of linked constituents gradually increases. Therefore, the non-spherical bioinspired red blood cell membrane-coated nanoparticle (non-spherical BCCN) appears hypothetically propitious as a possible solution for PEG-related issues and is elaborated therein.

This dissertation is divided into two parts:

1. Experimental

The experimental part (covering optimization and physicochemical characterization, in vitro as well as in vivo studies of particles) is the core of this dissertation. In this part, non-spherical particle shape stability upon storage and in physiological conditions is scrutinized and unraveled. Later, optimized BCCN formulations were evaluated using in vitro macrophages uptake as well as in vivo pharmacokinetics and biodistribution to prove their ability to evade phagocytosis and prolong the circulation time, respectively.

2. Computational

In the computational part, alleged biomolecular corona components (that originate from the cell membrane and blood plasma) and inevitable residual synthetic stabilizers were the subjects of all-atom molecular dynamics simulations studying the adsorption affinity and rates of such substances to core particles. The computational results confirmed all experimental findings and assisted further understanding of biomolecular (especially protein) adsorption behavior. Ultimately, the interfacial and biophysicochemical properties of compiled (physiological-therapeutic protein) bioinformatic data were generated.

In this dissertation, the essential guideline for assessing and tackling unexpected shape evolution of non-spherical nanoparticles (produced using various materials and fabrication methods with the focus still on the film-stretching method under dry heat condition) were first established (Chapter II). In the second stage, an innovative method using extracted red blood cell membranes (later called as NErys / Nanoerythrosomes) was applied to non-spherical nanoparticles resulting in non-spherical BCCNs. BCCNs' effectiveness in avoiding immune cells and prolonging core particle circulation time was assessed using in vitro cell lines and in vivo experiments, consecutively. The rationales thereof are deeply and comprehensively investigated using auxiliary biophysicochemical characterizations and in silico studies (Chapter III).

II. NON-SPHERICAL NANOPARTICLE SHAPE STABILITY IS AFFECTED BY COMPLEX MANUFACTURING ASPECTS: ITS IMPLICATIONS FOR DRUG DELIVERY AND TARGETING

Bernard Manuel Haryadi[1]; Daniel Hafner[2]; Ihsan Amin[2a]; Rene Schubel[2]; Rainer Jordan[2]; Gerhard Winter[1]; Julia Engert[1b] (2019)*

[1]Pharmaceutical Technology and Biopharmaceutics, Department of Pharmacy, Ludwig-Maximilians-Universität München, Butenandtstraße 5, 81377 Munich, Germany

[2]Professur für Makromolekulare Chemie, Department Chemie, Technische Universität Dresden, Mommsenstraße 4, 01069 Dresden, Germany

*Corresponding author: bernard-manuel.haryadi@cup.uni-muenchen.de; bmharyadi@gmail.com

[a]Current Address: Leibniz-Institute for Plasma Science and Technology (INP) Greifswald, Felix-Hausdorff-Straße 2, 17489 Greifswald, Germany

[b]Current Address: Regional Office for Health and Social Affairs Berlin (LAGeSo), Turmstraße 21, 10559 Berlin, Germany

This chapter has been published in the Advanced Healthcare Materials, 8 (18), 1900352 and **highlighted** as **"Hot Topic: Drug Delivery"** by Wiley-VCH in August-September 2019.

All experiments were designed and carried out by myself, except Atomic Force Microscope (AFM) which was conducted in close collaboration with Technische Universität Dresden. A detailed list of other contributions is listed in Section "Acknowledgements". This article was written by myself.

1. Abstract

Shape of nanoparticles is known recently as an important design parameter influencing considerably the fate of nanoparticles with and in biological systems. Several manufacturing techniques to generate non-spherical nanoparticles as well as studies on in vitro and in vivo effects thereof have been described. However, non-spherical nanoparticle shape stability in physiological-related condition and the impact of formulation parameters on non-spherical nanoparticle resistance still need to be investigated. To address these issues, we explored different nanoparticle fabrication methods using biodegradable polymers to produce non-spherical nanoparticles via the prevailing film-stretching method. In addition, systematic comparison to other nanoparticle systems prepared by different manufacturing techniques and less biodegradable materials (but still commonly utilized for drug delivery and targeting) was conducted. The study evinced that the strong interplay from multiple nanoparticle properties (i.e. internal structure, Young's modulus, surface roughness, liquefaction temperature [glass transition (Tg) or melting (Tm)], porosity, and surface hydrophobicity) was present. It is not possible to predict the non-sphericity longevity by merely one or two factor(s). The most influential features in preserving the non-sphericity of nanoparticles were existence of internal structure and low surface hydrophobicity (i.e. surface free energy (SFE) > ~55 mN/m, material-water interfacial tension < 6 mN/m), especially if the nanoparticles were soft (< 1 GPa), rough (R_{rms} > 10 nm), porous (> 1 m^2/g), and in possession of low bulk liquefaction temperature (< 100^oC). Interestingly, low surface hydrophobicity of nanoparticles could be obtained indirectly by the significant presence of residual stabilizers. Therefore, it is strongly suggested that non-sphericity of particle system is highly dependent on surface chemistry but cannot be appraised separately from other factors. Our results and reviews will allot valuable guideline for the design and manufacturing of non-spherical nanoparticles having adequate shape stability, thereby appropriate with their usage purposes. Furthermore, they can assist in understanding and explaining the possible mechanism of non-spherical nanoparticle effectivity loss and distinctive material behavior at the nanoscale.

Keywords: drug delivery and targeting, geometries, morph transformation, non-spherical particles, particle shape stability

Graphical Abstract

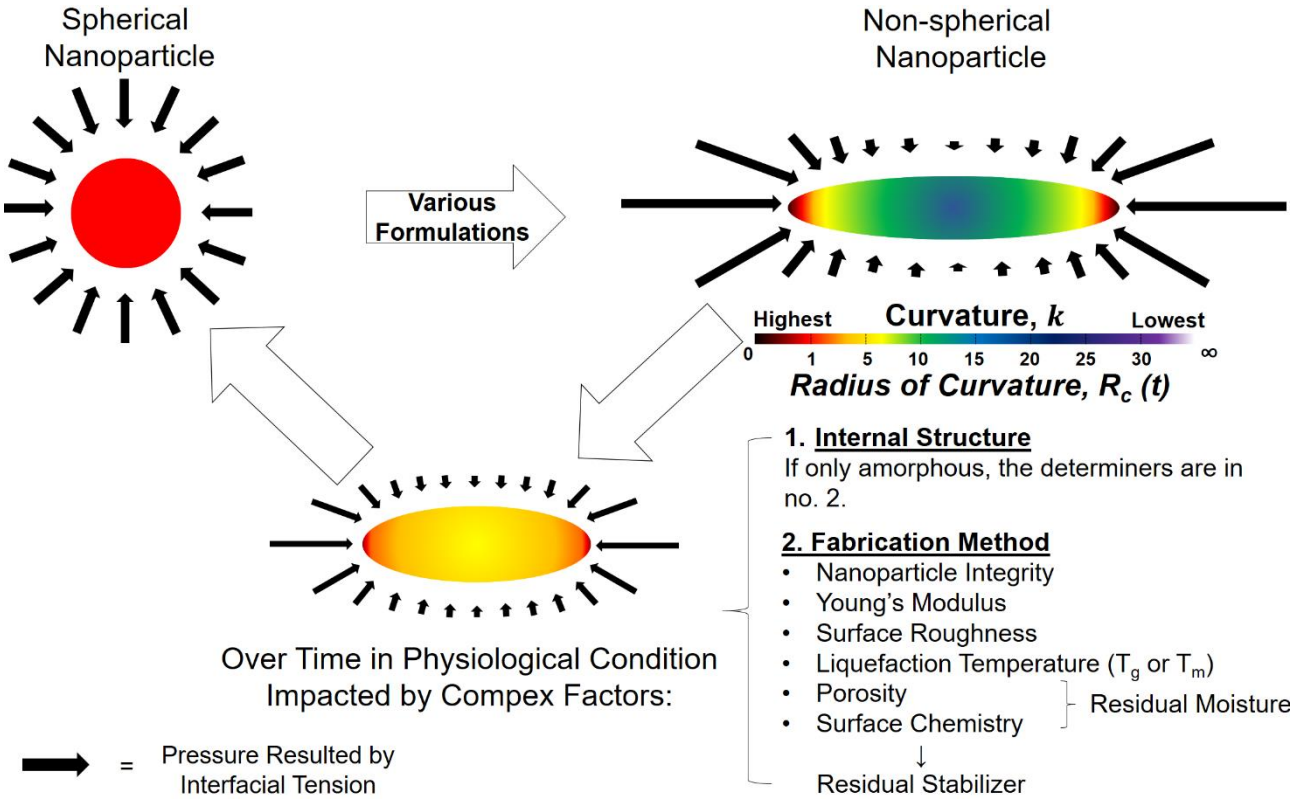

2. Introduction

For a long time biodegradable nanoparticle drug delivery systems have been investigated for numerous applications such as cancer treatment, vaccination, and iron replacement[1, 2]. Nanoparticles may extend the half-life of delivered drug[3, 4], avoid drug degradation[5], and modulate uptake into antigen-presenting[6, 7] or other target cells[8-10]. The bio-physicochemical characteristics of drug delivery systems, viz. size, charge, surface behavior and composition of the polymer are conventionally considered, as these key factors impact on particle biodistribution. Although all aforementioned characteristics have been optimized to circumvent the rapid clearance by the mononuclear phagocyte system (MPS) in the spleen and liver[3], in vivo results frequently fail to meet the expectation[3]. Thus, there is a need to refine this flaw, for instance by means of the geometry aspect.

Classically, particle shape has been disregarded as a feature which may switch the biodistribution and circulation half-life. Sundry manufacturing methods, such as mechanical stretching[6, 11-13], lithography[14-16], non-wetting templates[17], and microfluidics[18], enable the preparation of non-spherical nanoparticles and entitle the further investigation of particle geometry's influence on biological half-life and fate. It has been demonstrated that (prolate) ellipsoid particles display a lower internalization by macrophages[8, 19, 20]. In contrast, other geometries like discs (oblate ellipsoid) induce phagocytosis[21]. Ellipsoid particles also permit better antigen delivery to T-cells[9, 22]. These findings indicate that particle shape can be an eminent element affecting the fate of particulate drug delivery systems. However, the stability of nanoparticle shapes is still not much studied for biodegradable-biocompatible particles.

Therefore, it was the aim of our study to comprehensively examine the correlation between non-spherical biodegradable nanoparticle shape stability and the physicochemical properties factors behind it, in physiological-related condition (37°C, phosphate buffer saline [PBS] pH 7.4 310 mOsm). The film-stretching method was employed under dry heat to produce non-spherical nanoparticles from the spherical ones. The spherical nanoparticles were prepared by diverse fabrication methods (a. cross-linking: physical & chemical; b. molecular entanglement: emulsion solvent extraction & nanoprecipitation) and biodegradable materials (O-carboxymethyl chitosan [O-CMCHS], gelatin, carboxyl-ended poly(D,L-lactic acid) [PLA-COOH], and poly(D,L-lactic-co-glycolic acid) [PLGA-COOH]). In addition, we benchmarked the results to the common model, but less biodegradable nanoparticles (carboxylated poly(styrene) [PS-COOH] and silica [SiO_2] nanoparticles). In principle, several determining factors related to the nanoparticle shape stability have been elucidated and suggest that they strongly affect each other. In fact, the significant extent of residual

stabilizers, which existed on nanoparticles, exhibited the best stability in terms of non-sphericity. We also discuss thoroughly this underlying issue and its potential implications for drug delivery and targeting.

3. Results

All spherical nanoparticles as a base of non-spherical nanoparticles were prepared in the similar hydrodynamic size (Table II-1). Subsequently, the stretching in one direction with a stretching factor of 3 was performed towards spherical samples embedded in a PVA (Mowiol® 40-88; bulk Tg~85°C[23]) film using a custom built device (Figure II-1a) at certain stretching condition for different materials (Table S II-1; see also Methods in Supporting Information for further details of particles embedment in the PVA film). The characteristics of resulted non-spherical (quasi prolate / elongated) nanoparticles after the standardized washing steps (see Methods in Supporting Information) are depicted in Table II-1 & Figure II-1b-c. The increase of hydrodynamic size & polydispersity index (PDI) was clearly observed on non-spherical nanoparticles, whereas zeta potential exhibited practically no change.

Table II-1. Characteristics of Spherical and Non-Spherical Nanoparticles Used in the Study

No.	Polymer	Preparation Method	Involvement of Stabilizer	Hydrodynamic Size, S_h (nm)		Polydispersity Index, *PDI*		Zeta Potential (mV)		Yield (%)
				Spherical	Non-Spherical	Spherical	Non-Spherical	Spherical	Non-Spherical	
1	**PLA-COOH**	Nanoprecipitation	No	179.3 ± 4.1	404.5 ± 17.8	0.055 ± 0.043	0.215 ± 0.096	-14.2 ± 0.6	-15.5 ± 1.7	96.2 ± 3.2
		Emulsion Solvent Extraction	Yes (PVA)	175.1 ± 3.3	413.7 ± 20.4	0.043 ± 0.033	0.213 ± 0.028	-7.6 ± 1.4	-8.2 ± 2.3	80.6 ± 2.1
			Yes (P407)	180.8 ± 0.6	419.3 ± 9.9	0.055 ± 0.023	0.254 ± 0.027	-9.6 ± 2.3	-8.4 ± 1.5	75.5 ± 2.3
			Yes (TPGS)	153.5 ± 2.6	410.0 ± 14.1	0.134 ± 0.029	0.194 ± 0.019	-11.5 ± 0.9	-10.9 ± 1.2	72.1 ± 2.0
2	**PLGA 75/25-COOH**	Nanoprecipitation	No	172.3 ± 3.8	390.6 ± 6.9	0.081 ± 0.010	0.273 ± 0.023	-13.4 ± 2.3	-14.1 ± 0.5	95.7 ± 3.9
		Emulsion Solvent Extraction	Yes (PVA)	168.1 ± 0.8	430.3 ± 13.4	0.029 ± 0.028	0.223 ± 0.025	-8.5 ± 1.7	-7.6 ± 0.6	81.1 ± 0.8
3	**PLGA 50/50-COOH**	Nanoprecipitation	No	176.6 ± 0.9	346.8 ± 6.6	0.022 ± 0.015	0.157 ± 0.063	-12.6 ± 1.2	-11.5 ± 1.0	63.8 ± 1.5
4	**O-CMCHS**	Ionic Gelation	No	167.6 ± 0.8	382.6 ± 7.3	0.168 ± 0.007	0.145 ± 0.047	-11.4 ± 0.6	-3.7 ± -0.3	35.2 ± 0.2
5	**Gelatin**	One-Step Desolvation	No	188.1 ± 1.5	1007.0 ± 173.9	0.053 ± 0.009	0.632 ± 0.234	-16.6 ± 1.0	-2.0 ± 0.3	81.4 ± 0.3
6	**PS-COOH**	Emulsion Polymerization	Yes (sulfate ester derivative)	178.8 ± 3.0	341.4 ± 9.7	0.032 ± 0.022	0.191 ± 0.031	-30.3 ± 0.8	-17.2 ± 0.3	N/A#
7	**SiO_2 (AR3)**	Polymerization	Yes (CTAB)	N/A#	255.5 ± 5.3	N/A#	0.228 ± 0.023	N/A#	-26.3 ± 1.5	88.3 ± 0.4*
8	**SiO_2 (AR8)**	Polymerization	Yes (CTAB)	N/A#	929.0 ± 16.2	N/A#	0.478 ± 0.023	N/A#	-22.9 ± 1.7	89.7 ± 0.2*

Data is expressed as mean ± standard deviation (n=3).
#N/A: Not Applicable.
*Only these yields represent the direct (without film-stretching) processes in fabricating non-spherical nanoparticles. Other yields are based on the production of the spherical nanoparticles.

3.1. Effect of Fabrication Method

First, the comparison between two fabrication methods (cross-linking vs molecular entanglement) was performed. Because of the stabilizer/surfactant absence in the cross-linking method, nanoprecipitation (no stabilizer/surfactant; also called solvent displacement[24, 25] elsewhere) is the main focus in molecular entanglement development instead of methods involving stabilizer (e.g. emulsion solvent extraction; also called [emulsion] solvent diffusion[24, 26] or [emulsion] solvent evaporation[2, 24]) (Table II-1).

The size of cross-linked hydrogel nanoparticles demonstrated by SEM micrographs (Figure II-1b) was measured in dry milieu (leading to significant particle shrinking), thus may be considerably different as reported by dynamic light scattering (DLS) in Table II-1[27]. No significant shrinking of nanoparticles occurred on more solid nanoparticles composed from aliphatic polyesters via nanoprecipitation and commercial standard PS-COOH (Figure II-1c). After 3-times stretching from its initial length, both cross-linked hydrogel nanoparticles appeared to be slightly elongated with initial aspect ratio (defined as the proportion of length to width ellipsoid particle) of 1.62 ± 0.18 and 1.11 ± 0.09 for gelatin and O-CMCHS, consecutively. These aspect ratios were much lower compared to the theoretical calculation (Figure II-1d & Supplemental Calculation). In addition, considerable swelling was exhibited by both, mainly gelatin nanoparticles (Figure II-1b).

Over time, an obvious discrepancy was noted between the shape stability of the non-spherical nanoparticles. These discrepancies were not equal for all particles, but were strongly affected by many factors, including the fabrication method. To allow better shape stability prediction and comparison between the tested samples, the typical shifting time ($t_{1/2}$) (expressed as the time needed for a half decrease of initial aspect ratio) was calculated. In hours, both non-spherical cross-linked hydrogel particles became virtually spherical at 37°C (aspect ratio = 1; figures not shown), with gelatin demonstrated slightly better shape stability (Figure II-1e). Due to swelling and poor shape stability, gelatin and O-CMCHs are only used as references in elucidating the factors affecting shape transformation of non-spherical nanoparticles.

Meanwhile, non-spherical nanoparticles formulated by aliphatic polyesters (Table S II-2) and nanoprecipitation method exhibited much higher $t_{1/2}$ at 37°C (Figure II-1e, Figure II-2 and Figure II-3a[left], b & c), with PLGA 50/50-COOH (~44 kDa) being the inferior one with almost 6 days. Because of this, our further study with emulsion solvent extraction method (involving stabilizer) for aliphatic polyesters is only focused on PLA-COOH and PLGA 75/25-COOH. Besides, the recent indication to use low molecular weight of aliphatic polyesters (~15 kDa) for drug delivery[28] due to the success in clinical study, reinforces our polymer choices. As expected, the $t_{1/2}$ of PLGA 75/25-COOH & PLA-COOH nanoparticles by nanoprecipitation were much greater at 5°C (Figure II-1e, Figure II-2b, and Figure II-3b).

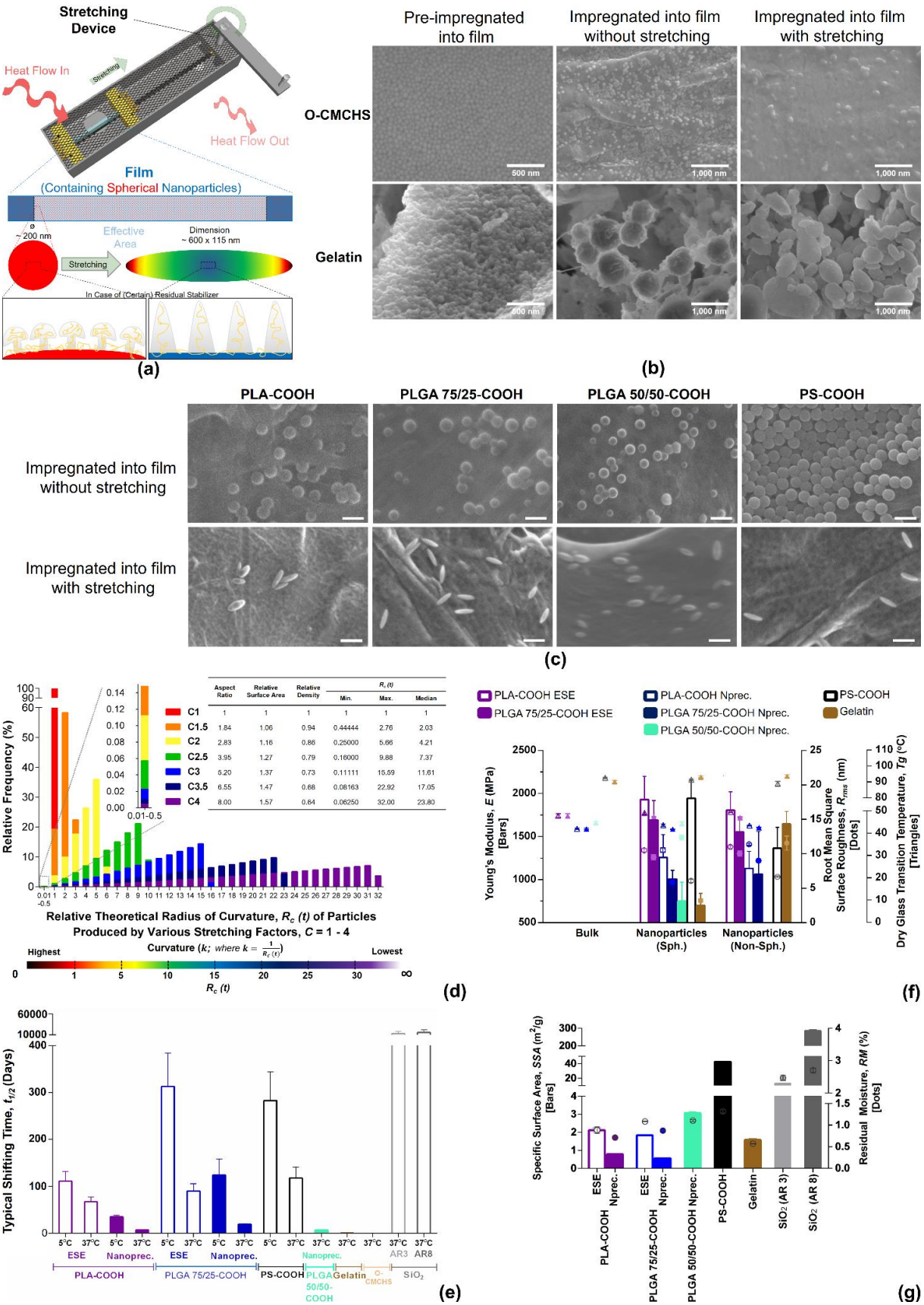

Figure II-1. (a) Schematic of film-streching device utilized in this study for fabrication of non-spherical nanoparticles from spherical ones. It is also displayed the common and plausible architecture alteration of polymers at the nanoparticle interface after stretching[187], involving the transition from "mushroom" to "brush" configuration. Scanning electron micrographs of spherical and non-spherical (b) cross-linked hydrogel nanoparticles, encompassing O-CMCHS & gelatin, as well as (c) aliphatic polyesters (prepared by nanoprecipitation) & PS-COOH nanoparticles (scale bars = 500 nm). For clarity, spherical nanoparticles of aliphatic polyesters and PS-COOH before their incorporation into film are not shown. (d) Critical physical factors on prolate ellipsoid particle influenced by uniaxial stretching process. (e) Calculation of typical shifting time ($t_{1/2}$) from aspect ratio (AR) of particles. (f) Mechanical properties of tested nanoparticles. (g) Physiosorption-based surface characteristics of various evaluated nanoparticles. Unless otherwise specified in Methods in Supporting Information, data represent mean ± standard deviation (n=3).

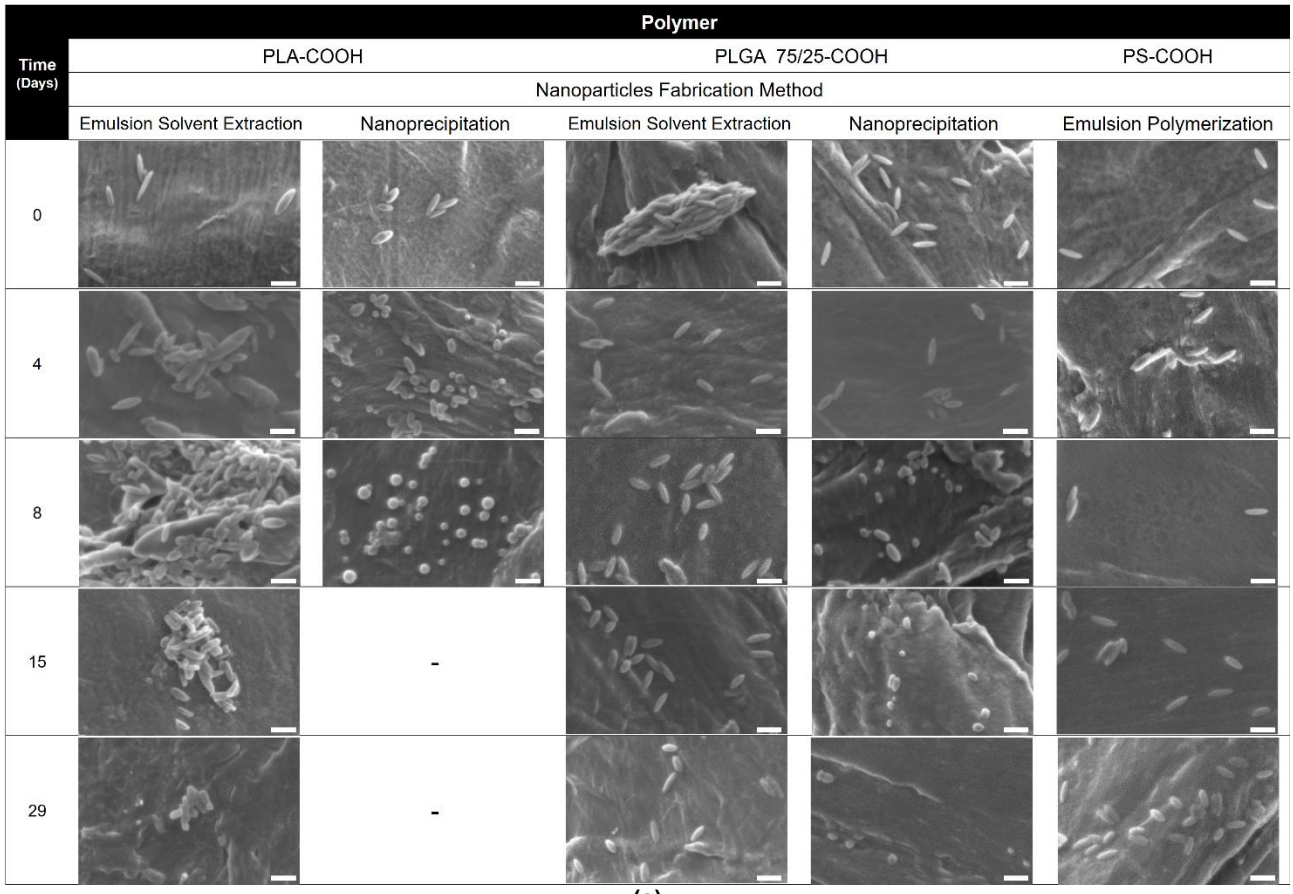

(a)

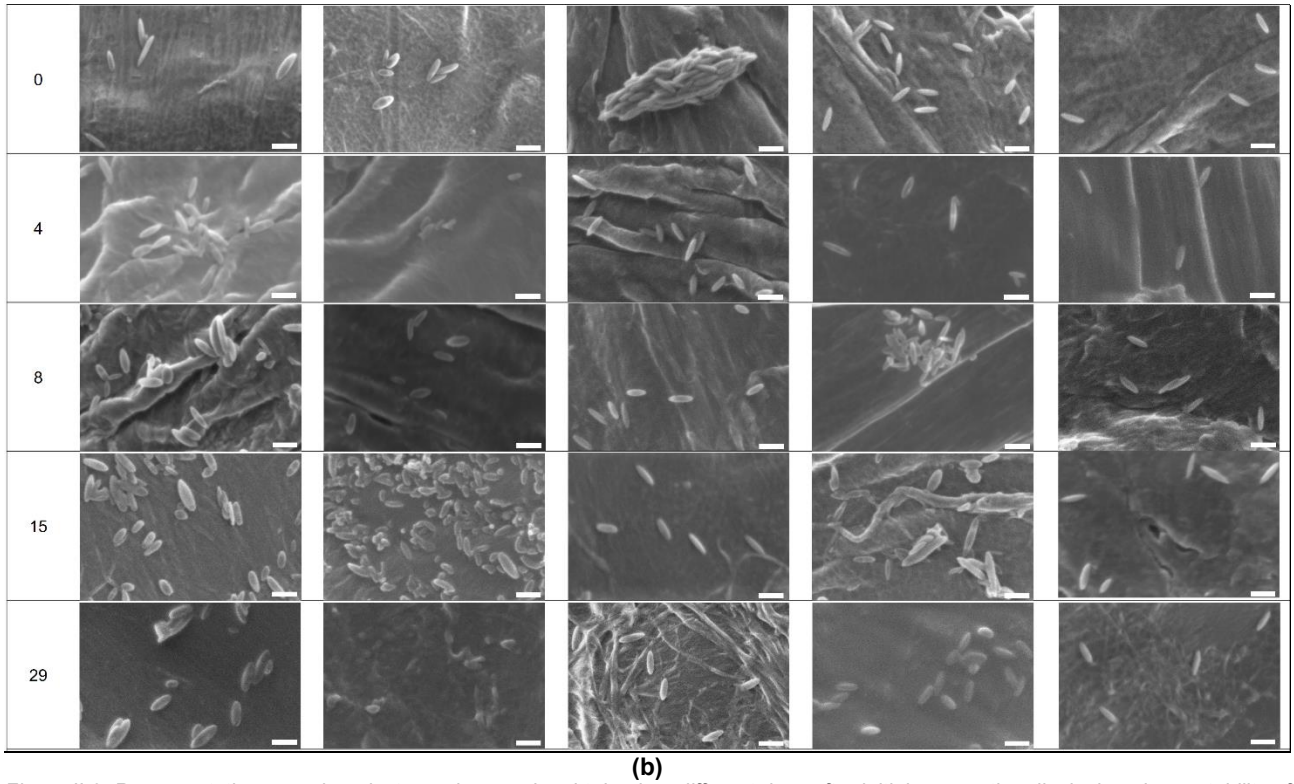

(b)

Figure II-2. Representative scanning electron micrographs obtained on different days after initial preparation displaying shape stability of non-spherical aliphatic polyesters (PLA-COOH & PLGA 75/25-COOH) and PS-COOH nanoparticles. Nanoparticles were dispersed in phosphate buffer saline (PBS) pH 7.4 310 mOsm for a maximum of 29 days at (a) 37°C and (b) 5°C. Scale bars = 500 nm.

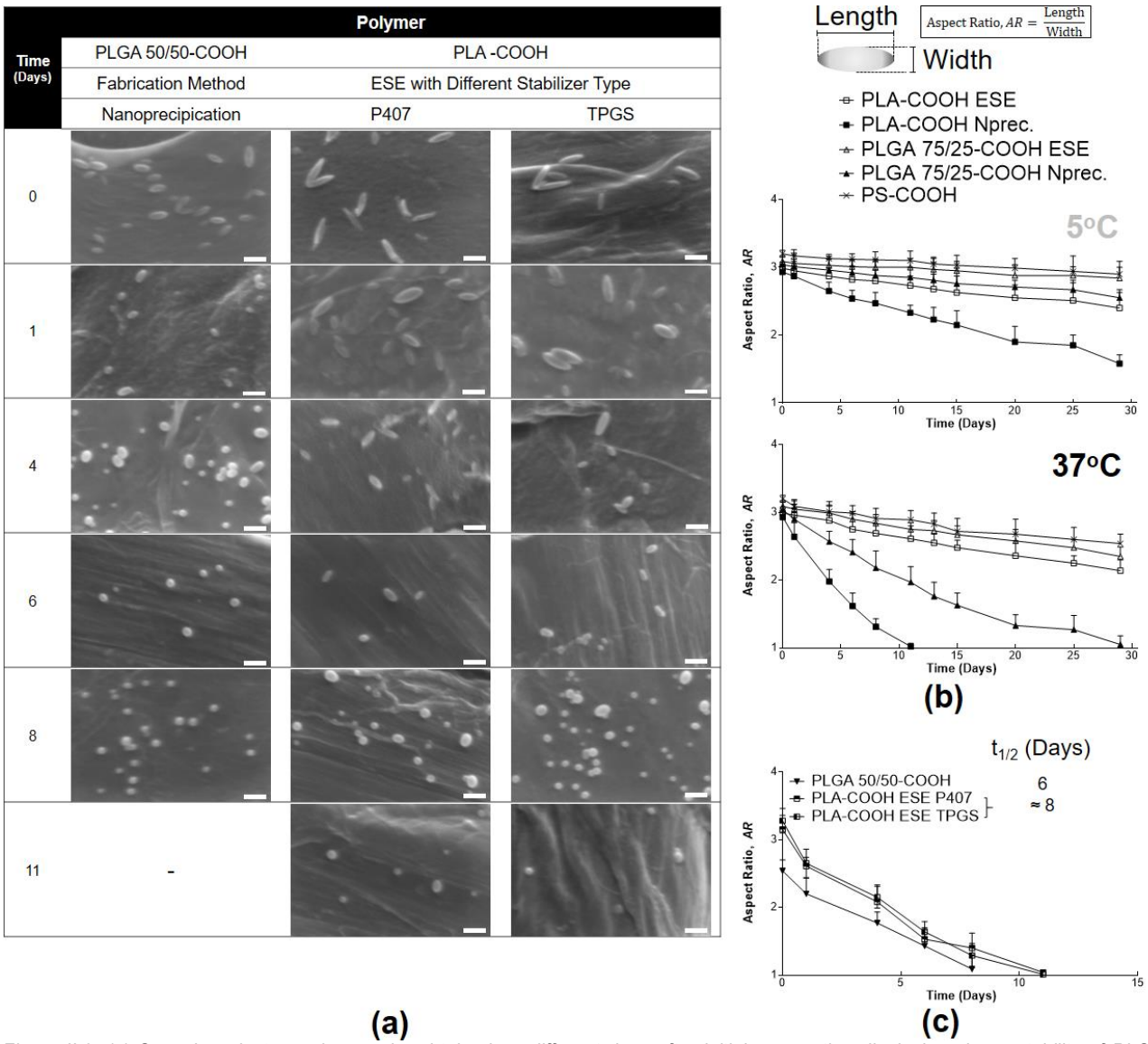

Figure II-3. (a) Scanning electron micrographs obtained on different days after initial preparation displaying shape stability of PLGA 50/50-COOH nanoparticles (formulated by nanoprecipitation) and PLA-COOH nanoparticles (manufactured by emulsion solvent extraction (ESE) technique with the variation of utilized stabilizers; in this figure, Poloxamer 407 denoted "P407" and TPGS are evaluated instead of PVA used in Figure II-2). Scale bars = 500 nm. (b) & (c) Plots of aspect ratio (AR) over time of aliphatic polyester prepared by different fabrication methods and PS-COOH nanoparticles at 5°C and 37°C. Figure II-3b corresponds to the micrograph results from Figure II-2a & b, meanwhile Figure II-3c was derived from the measurement results of Figure II-3a. Aspect ratio (AR) is calculated as described in the top of Figure II-3b.

Nonetheless, the shape stabilities of non-spherical PLGA 75/25-COOH and PLA-COOH nanoparticles formulated by nanoprecipitation were still much poorer than the commercial standard PS-COOH prepared by emulsion polymerization (Figure II-1e, Figure II-2, and Figure II-3b), i.e. approximately less than one-sixth at 37°C and less than half at 5°C. By applying emulsion polymerization in commercial standard PS-COOH, stabilizer was used during the preparation process and residual stabilizer may present in nanoparticles (Polysciences' Product Information)[29]. To also permit stabilizer contribution in aliphatic polyester nanoparticles, an emulsion solvent extraction method with different stabilizers was employed. PVA (Mowiol® 4-88), a semi-crystalline polymer, elicited dramatic improvement of non-spherical shape stability for PLA-COOH and PLGA 75/25-COOH, both at 37 and 5°C (Figure II-1e, Figure II-2, and Figure II-3b). At 37°C, the

$t_{1/2}$ was enhanced up to about 11 times for PLA-COOH and 5 folds for PLGA 75/25-COOH. Other stabilizers (a) Poloxamer 407 (P407) and (b) D-α-Tocopherol Polyethylene Glycol 1000 Succinate (TPGS) were also evaluated in the fabrication of non-spherical PLA-COOH by emulsion solvent extraction. However, they failed to increase the non-spherical shape stability of PLA-COOH (Figure II-3a & c). No considerable $t_{1/2}$ alteration was observed between nanoparticles manufactured by emulsion solvent extraction using these stabilizers compared to the nanoprecipitation at 37°C, i.e. between 6 - 8 days (Figure II-3a & c). In this part, it can be summarized that for biodegradable polymers, PLGA 75/25-COOH prepared by emulsion solvent extraction using PVA is the longest-lasting aliphatic polyester in terms of non-sphericity. It is characterized by $t_{1/2}$ at 5°C for almost 1 year and at 37°C for roughly 3 months (Figure II-1e). For this reason, PVA is chosen as the main discussion and stabilizer evaluated further in this report.

Beside aspect ratio reduction, the inclinations to be spherical ultimately at 37°C for non-spherical nanoparticles synthesized by film-stretching method were also supported by the results of hydrodynamic size measurement and PDI by DLS (Figure II-4). DLS detected a gradual decrease of both parameters. There was no significant change of zeta potential and pH for all nanoparticles stored at 5°C, but substantial alteration of zeta potential and pH towards more acidic environment was observed at 37°C on both aliphatic polyester nanoparticles (Figure II-4). Meanwhile, PS-COOH nanoparticles exhibited practically no change of zeta potential and pH during observation (Figure II-4).

To elaborate the causal factor of non-spherical shape instability on nanoparticles, the other factors (mechanical properties, porosity and hydrophobicity) are studied on selected nanoparticles and their data is displayed in the next sections.

3.2. Effect of Mechanical Properties: Young's Modulus, Surface Roughness (R_{rms}) & Tg

All nanoparticles were initially analyzed for mechanical properties in dry condition. Using atomic force microscope (AFM), it was revealed that they had relatively smooth surfaces, demonstrated by R_{rms} (Figure II-1f & Figure II-5a) about tens nm or less[30, 31], and proportional Young's modulus to their bulk and the similar particles reported elsewhere[23, 32-34]. Spherical gelatin and spherical PLGA 50/50-COOH nanoparticles (via nanoprecipitation) showed the smoothest and roughest surface (R_{rms} = 3.2 vs 12.4 nm). As expected, cross-linked system is rather smooth[35]. Regarding the Young's modulus, the softest and stiffest nanoparticles belong to gelatin (~0.7 GPa) and PS-COOH (~2 GPa) nanoparticles. Meanwhile, the Tg trends of (spherical) nanoparticles were: (a) slightly lower than the bulk for aliphatic polyesters via

nanoprecipitation and PS-COOH, and (b) slightly higher than the bulk for aliphatic polyesters via emulsion solvent extraction and gelatin (Figure II-1f).

After stretching, there were no considerable Young's modulus, surface roughness, and Tg differences of dry nanoparticles (prepared by lyophilization protocol; Figure S II-1). The exception were: (a) gelatin nanoparticles obtaining greater Young's modulus and surface roughness about 2-folds and 3-folds, respectively, as well as (b) PS-COOH and aliphatic polyesters, experiencing Tg reduction around 3°C (Figure II-1f). Nevertheless, there were clear trends that Young's moduli of stretched (non-spherical) aliphatic polyesters were: (a) slightly lower for nanoparticles prepared by nanoprecipitation (possibly due to Young's modulus confinement effect[36]) and (b) slightly higher for nanoparticles formed via emulsion solvent extraction utilizing PVA (Figure II-1f). Besides, all stretched nanoparticles roughened after stretching, as depicted by greater R_{rms} (Figure II-1f) and rougher sample surface profiles (Figure II-5b vs a). The post-stretching roughening effect is similar as commonly reported in micro-macroscale objects and various polymers[37, 38].

Surprisingly, it was revealed from the AFM results that between nanoparticles fabricated by nanoprecipitation, the spherical PLGA 50/50-COOH nanoparticles (the least-stable ones in terms of non-sphericity) have greater roughness (R_{rms} = 12.4 nm) compared to PLGA 75/25-COOH (R_{rms} = 5.9 nm) and PLA-COOH (R_{rms} = 9.5 nm). This result could be correlated with the porosity and hydrophobicity measurement, which are displayed and discussed in the subsequent sections.

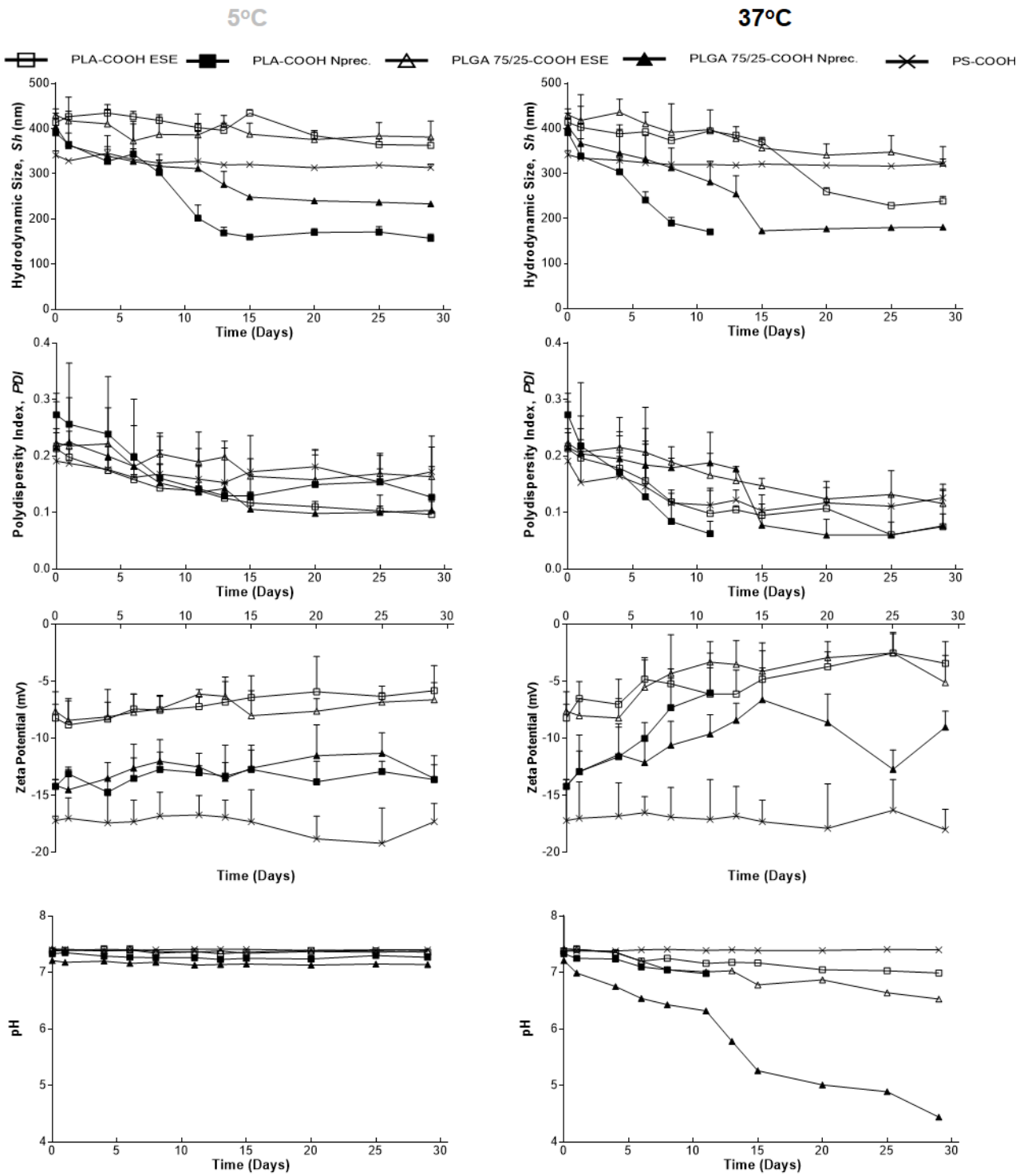

Figure II-4. Plots of hydrodynamic size, polydispersity index/PDI, zeta potential, and final preparation pH of low molecular weight aliphatic polyesters (PLA-COOH & PLGA 75/25-COOH) and PS-COOH nanoparticles over time. Aliphatic polyesters were prepared by different fabrication methods: emulsion solvent extraction (ESE) using PVA and nanoprecipitation. The data and time points in this figure correspond to Figure II-2 and Figure II-3b.

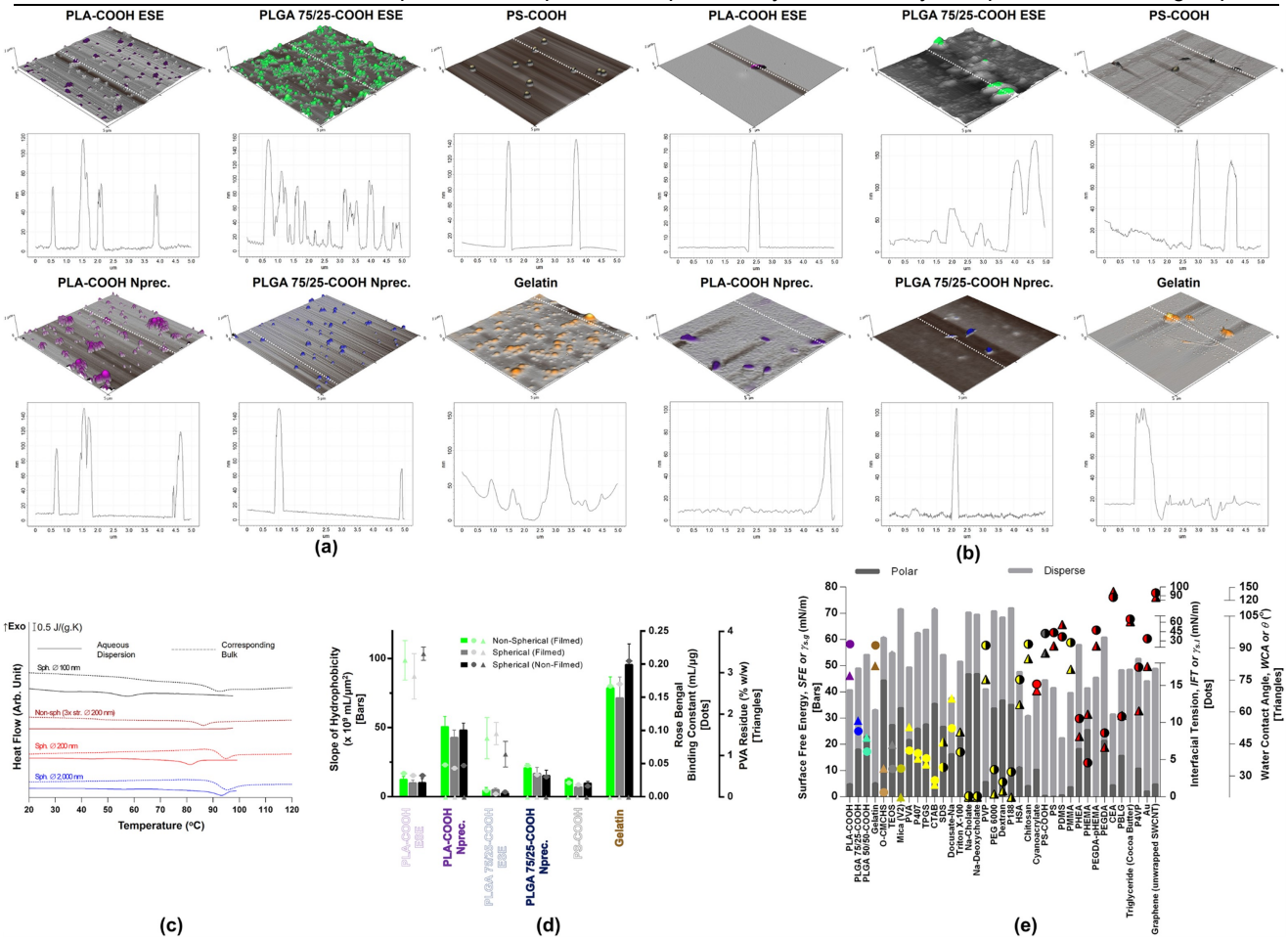

Figure II-5. Atomic force microscope (AFM)'s 3D representations and surface or height profiles of evaluated (a) spherical and (b) non-spherical nanoparticles. (c) Calorimetric thermograms of PS-COOH nanoparticles (solid lines), altogether with thermograms of their corresponding "bulk" polymer resulted from nanoparticles via annealing (dashed lines). These thermograms describe the dramatic disparity of nanoparticle Tg measured on dispersed or dry state. (d) Nanoparticle's surface hydrophobicity (displayed by the slope of hydrophobicity and binding constant; the greater values mean greater hydrophobicity) and residual stabilizer (PVA) concentration profiles of tested nanoparticles. (e) Correlation database of surface free energy (SFE), material-water interfacial tension and water contact angle (WCA) of various common materials functionalized as main component or excipient (e.g. stabilizer) in nanoparticle formulations. The used materials in our current non-spherical nanoparticle study are designated as points (either dot or triangle) without black borderline (and their corresponding bars), whereas points with black borderline (and their corresponding bars) show common materials for non-spherical nanoparticle fabrication used in other researches. The full points (and their corresponding bars) depict values generated from our measurement, while the half-filled points (and their corresponding bars) designate the recalculation values of interfacial activity parameters (using Owens and Wendt approach[223]) from references. Yellow (and their corresponding bars) represents our and commonly-used stabilizers, while red (and their corresponding bars) is denoted as commonly reported materials in synthesizing biodegradable and/or non-spherical nanoparticles for drug delivery and targeting. Abbreviations and further details of referred materials-nanoparticles: (1) SDS (sodium dodecyl sulfate)[168, 224], (2) Docusate-Na[168], (3) Triton® X-100[124, 225], (4) Na-Cholate & -Deoxycholate[129, 226], (5) PVP (poly(vinylpyrrolidone))[137, 227], (6) PEG (poly(ethylene glycol))[209] 6000[228], (7) Dextran[194, 228], (8) Poloxamer 188[127, 229], (9) HSA (human serum albumin)[134, 230], (10) Chitosan[98, 178], (11) Cyanoacrylate[98, 231], (12) PS-COOH (carboxylated poly(styrene))[4, 232], (13) PS (poly(styrene))[19, 223], (14) PDMS (poy(dimethylsiloxane))[83, 223], (15) PMMA (poly(methyl methacrylate))[83, 223], (16) PHEA (poly(hydroxyethyl acrylate))[71, 73, 233, 234], (17) PHEMA (poly(hydroxyethyl methacrylate))[233], (18) PEGDA (poly(ethylene glycol) diacrylate)[14-16, 71, 73, 79, 86, 235]-PHEMA (poly(hydroxyethyl methacrylate))[236], (19) CEA (2-carboxyethyl acrylate)[71, 73, 86], (20) PBLG (poly(γ-benzyl L-glutamate))[142, 237], (21) Triglyceride (cocoa butter)[115, 116, 160, 163, 164, 238], (22) P4VP (poly(4-vinyl pyridine))[149, 150, 239], (23) Au (gold)[220, 240], and (24) SWCNT (single-walled carbon nanotubes)[46, 241].

To further confirm the marginal trend of Tg modulation of dry nanoparticles (dry Tg) compared to their bulk, the Tg of nanoparticles dispersed in aqueous medium (wet Tg) was also evaluated. Only polymers which could be successfully and proportionally stretched into non-spherical nanoparticles were studied, namely aliphatic polyesters and PS-COOH. None of aliphatic polyester nanoparticles (initial ø ~200 nm), however, exhibited a wet Tg_s. It was very probable that their wet Tg_s were superimposed by large endothermic peak of aqueous ice melting process (data not shown). It was reported[39, 40] that even in macroscopic scale, aliphatic polyesters exhibited Tg reduction up to ~10 - 20°C, when they were contacted with high humidity (e.g.

90%RH) or water for 1 hour or more. The longer the contact time with humidity or water, the greater the Tg depreciation. On the other hand, PS-COOH nanoparticles (initial ø ~200 nm) showed more distinct Tg reduction, i.e. about 15°C, compared to the dry ones (3°C) (Figure II-5c vs Figure II-1f). To study deeper the size dependence of Tg of polymers under soft confinement (nanoparticles dispersed in aqueous medium), other diameters of PS-COOH nanoparticles (100 & 2,000 nm) were measured. The wet Tg of the PS-COOH nanoparticles lessen as the hydrodynamic size was reduced from 2,000 to 100 nm, and thus the disparity against their bulk Tg grew considerably with smaller hydrodynamic size (1 vs 39°C, respectively) (Figure II-5c vs Figure II-1f). Similar finding was reported elsewhere[41]. Moreover, heat capacity change (ΔCp) appeared to be lesser with smaller hydrodynamic size, which is consistent with the published results[42, 43]. Both phenomena (the reduction of wet Tg and ΔCp) seemed to occur remarkably on non-spherical PS-COOH, obtained by 3x stretching of spherical PS-COOH (initial ø 200 nm). This may be attributed to the smaller particle size (in width and height dimension) (Figure II-5b vs a), existence of much lower radius of curvature ($R_c(t)$), and wide variance of $R_c(t)$ on nanoparticles (Figure II-1d). Likewise, the greater Tg diminution as smaller (hereafter denoted Tg confinement effect) & more aspherical PS-COOH nanoparticles, it is also very reasonable to propose that the Tg confinement effect occurred in the case of other nanoparticle materials, including aliphatic polyesters. Not to mention, because all nanoparticles for shape stability study were dispersed in the physiological-related medium (PBS pH 7.4 310 mOsm), it was very likely that the stronger ΔCp reduction occurred. The salt presence was reported to diminish ΔCp of macromolecules significantly[44]. As a result, less energy (represented by temperature and interfacial tension) is required to increase the polymer chain mobility in non-spherical nanoparticles, thus leads to more dramatic shape changes towards spheres. The Tg confinement effect further delineates that lower temperature (i.e. 37 or 5°C) may still induce the aspect ratio decrease on tested non-spherical nanoparticles, mainly aliphatic polyesters.

3.3. Effect of Porosity of Particles

To quantify the porosity and hydrophobicity of the nanoparticles, physiosorption-based methods (specific surface area (SSA) and residual moisture analysis) were performed (Figure II-1g). The analyses were conducted on starting spherical nanoparticles to generate more reliable and directly comparable results due to no swelling and similar nanoparticle size. The SSA of biodegradable nanoparticles that were included in film-stretching process highly varied, depending on the nanoparticle integrity, molecular weight and bulkiness of the polymer chain.

For instance, with respect to nanoparticles prepared without any stabilizer or surfactant, PLGA 50/50-COOH and gelatin nanoparticles were the least compact, displayed by SSA of around 3.05 and 1.57 m^2/g, consecutively. For nanoparticles prepared by nanoprecipitation, again PLGA50/50-COOH ("high" molecular weight [MW], bulkier) was the most porous or least compact, whereas PLGA 75/25-COOH ("low" MW, less bulky) had the lowest porosity or highest compactness (0.55 m^2/g).

Furthermore, stabilizer had a strong effect on SSA, such as in emulsion solvent extraction for aliphatic polyesters, resulting about 2-fold SSA compared to the nanoprecipation (Figure II-1g). Overall, the nanoparticle material, having the highest porosity and produced to be non-spherical nanoparticles by stretching method, was PS-COOH (SSA ~42 m^2/g). We assume that the different amount of residual stabilizer may be one of the critical factors for the SSA differences between these groups. Our assumption was supported by quite diverse SSA value reported for aliphatic polyesters by emulsion solvent extraction (3 - 10 m^2/g)[45] and PS-COOH by emulsion polymerization (29 m^2/g)[46] nanoparticles. These reports used similar nanoparticle properties as reported here, namely diameter ~200 nm, PDI < 0.1, and negative zeta potential of tens mV (for aliphatic polyesters).

Meanwhile, the residual moisture results appeared as a function of porosity (Figure II-1g) and bulk-nanoparticle hydrophobicity (Figure II-5d & e). In general, the higher the residual moisture, the greater the SSA, and the lesser hydrophobic the materials or nanoparticles. In other words, the presence of residual stabilizer may increase the SSA and residual moisture. Nonetheless, a large SSA did not negatively correlate to non-spherical nanoparticle shape stability, if the sufficient mechanical properties and appropriate hydrophobicity (indirectly encompassing residual stabilizer) were present.

3.4. Effect of Hydrophobicity of Materials & Particles

All nanoparticles (Figure II-5d) were evaluated using the hydrophobic (log P 1.5[47]) anionic Rose Bengal dye method. Overall, the sequence of hydrophobicity between different nanoparticles (regardless of their shape) was as following (from the highest to the lowest): gelatin, PLA-COOH by nanoprecipitation, PLGA 75/25-COOH by nanoprecipitation, PLA-COOH by emulsion solvent extraction, PS-COOH and PLGA 75/25-COOH by emulsion solvent extraction. This strong trend was inversely proportional with the non-spherical nanoparticle shape stability at 37°C (Figure II-1e), but poorly correlated to the bulk hydrophobicity (Figure II-1e). Hence, the particle hydrophobicity study showed its importance.

No significant difference was found between initial spherical and film-embedded (without stretching) spherical nanoparticles in terms of nanoparticle hydrophobicity parameters, except for gelatin (Figure II-5d). Unexpectedly, gelatin exhibited considerable lower hydrophobicity, ascribed presumably by strong adsorption of PVA (Mowiol® 40-88 as the film matrix) onto gelatin nanoparticles. This adsorption may be responsible for the tangled thread-like structure around filmed and film-stretched gelatin nanoparticles in SEM and AFM (Figure II-1b & Figure II-5b). As the further proof of PVA (semi-crystalline polymer) presence, the hydrophilicity (Figure II-5d), Young's modulus, and surface roughness (Figure II-1f) of the non-spherical gelatin nanoparticles were greater compared to the initial spherical gelatin nanoparticles. This may be attributed to the typical properties of semi-crystalline polymer after stretching[48], namely demonstration of higher crystallinity. However, we could not measure the exact concentration of adsorbed PVA onto gelatin nanoparticles like to the aliphatic polyesters, due to the interference of adjacent hydroxyl (Figure S II-2) in gelatin against colorimetric reagents in the reaction[49].

As expected, the significant hydrophobicity reduction of PLA-COOH and PLGA 75/25-COOH nanoparticles fabricated by emulsion solvent extraction using PVA was strongly associated to its residue in nanoparticles, with the larger amount of PVA resided to PLA-COOH (the more hydrophobic polymer) compared to PLGA 75/25-COOH, namely about 3% vs 1.5%, respectively (Figure II-5d). Stronger PVA adsorption to the more hydrophobic materials aligns with established report[50]. Nonetheless, our results demonstrated that the intrinsic material hydrophobicity still played a dominant role in determining the nanoparticle hydrophobicity and non-spherical shape stability.

With regard to PS-COOH, we presumed that the superiority of non-spherical shape stability may also be aided by the presence of residual stabilizer utilized in the nanoparticle formation, beside by the relative high dry bulk Tg of PS-COOH (i.e. ~93°C, which is still slightly higher than gelatin, ~91°C) (Figure II-1f) and bulk[32]-nanoparticle Young's Modulus PS(-COOH) ~2 GPa. This proposition is highly reinforced with the slightly poorer hydrophobicity data of bulk PS-COOH compared to gelatin (Figure II-5e). The unsupportive situation (Figure II-5e) encompassed the much lower polar component of surface free energy (SFE) (or so-called surface polarity, *Xp*), water contact angle (WCA) and most important one: high material-water interfacial tension. We propose that the high material-water interfacial tension is the main, external, and rigorous driven force generating the biggest pressure on the tip of non-spherical nanoparticles (in other words, on the smallest $R_c(t)$ of non-spherical nanoparticles [Figure II-1d]) (Equation II-1, adapted from Defay

et al.[51]). Consequently, the high interfacial tension leads to thermodynamically favorable spherical shape.

$$\Delta p = \frac{\gamma_{s.l}}{R_c(t)} \qquad \textit{Equation II-1}$$

where Δp is the induced pressure, $\gamma_{s.l}$ is the solid-liquid interfacial tension (i.e. material-water) and $R_c(t)$ is the radius of curvature.

Hence, it is momentous to evaluate the suspected residual stabilizer in the starting PS-COOH nanoparticles (dispersed in HPW), like PVA in the case of aliphatic polyesters by emulsion solvent extraction. First, using fast-acceptable sensitivity (i.e. Energy Dispersive X-Ray [EDX]) and routine (i.e. CHNS elemental or so-called oxygen combustion) analysis, it seemed that the PS-COOH nanoparticles were totally clean from the suspected sulfate ester derivatives (e.g. sodium dodecyl sulfate [SDS], docusate sodium, etc.). Using CHNS analysis, only C & H elements were detected with the ratio of 89.37% vs 7.62%, attributed likely to C & H from PS-COOH molecules. However, when the starting PS-COOH nanoparticles were measured in the instrument with a lower limit of detection, i.e. inductively coupled plasma atomic emission spectroscopy (ICP-AES), it evidenced 520 ± 70 ppm sulfur (S) and 100 ± 50 ppm sodium (Na), likely associated to the existence of residual stabilizers which may bestow remarkable non-spherical PS-COOH nanoparticles shape stability.

3.5. Comparison to Non-Spherical Silica (SiO2) Nanoparticles

Because (mesoporous) non-spherical SiO2 nanoparticles are subject of many publications ranging from the manufacture until in vivo study[52, 53-56], non-spherical SiO_2 nanoparticles were benchmarked to our non-spherical polymeric nanoparticles fabricated by film-stretching method. We synthesized two different aspect ratios (AR) of plain mesoporous non-spherical SiO_2 nanoparticles, namely ~3 (simulating the similar aspect ratio and dimension with the stretched nanoparticles) and ~8 (Figure II-6). From the shape stability aspect, both non-spherical SiO_2 nanoparticles were excellent and superior against the most stable non-spherical PLGA 75/25-COOH manufactured by emulsion solvent extraction using PVA. The evidences were demonstrated by only slight diminution of aspect ratio, hydrodynamic size, and PDI after the storage in physiological-related condition for 29 days. The $t_{1/2}$ values are more than 10,000 and 13,000 days for aspect ratio 3 and 8, respectively (Figure II-1e). The exceptional non-sphericity was in the same fashion as reported previously[57]. Simultaneously, zeta potential and pH of non-spherical SiO_2 nanoparticle preparation remained relatively stable (Figure II-6).

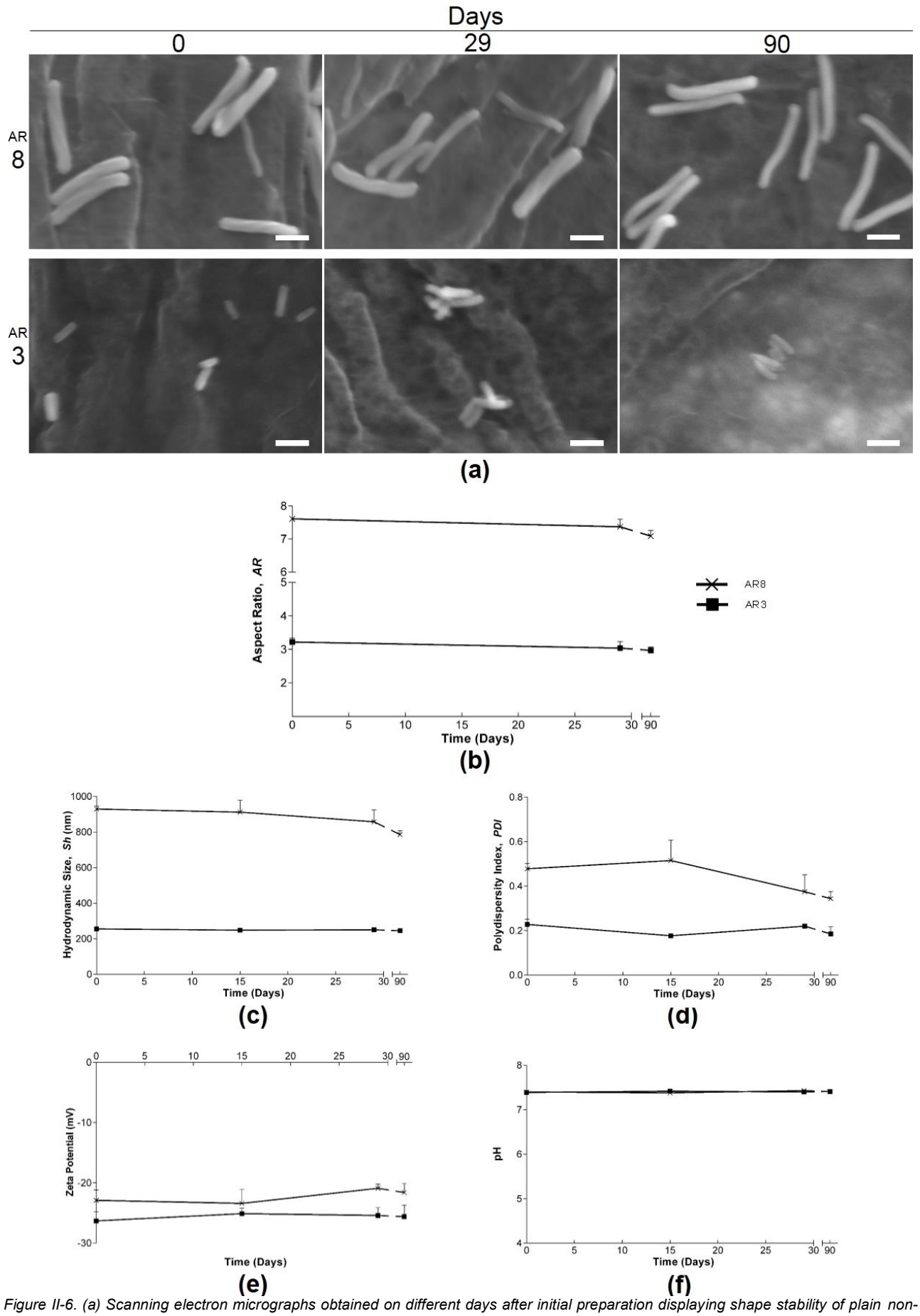

Figure II-6. (a) Scanning electron micrographs obtained on different days after initial preparation displaying shape stability of plain non-spherical mesoporous SiO_2 nanoparticles with the aspect ratio of ~8 & ~3. Nanoparticles were dispersed in phosphate buffer saline (PBS) pH 7.4 310 mOsm for a maximum of 90 days at 37°C. Scale bars = 500 nm. Plots of (b) aspect ratio (AR), (c) hydrodynamic size, (d) polydispersity index/PDI, (e) zeta potential and (f) final preparation pH of corresponding non-spherical mesoporous SiO_2 nanoparticles.

Using the available instruments (i.e. differential scanning calorimeter [DSC] & thermogravimetric analysis [TGA]) and their working temperature range, neither liquefaction temperature (i.e. melting temperature [Tm]) nor other thermal events of non-spherical SiO_2 nanoparticles could be detected. It was reported, nonetheless, the T_m of bulk SiO_2 was 1,600°C[58]. Meanwhile, the Young's modulus (bulk) and surface roughness of bulk-mesoporous nanoparticle of SiO_2 were reported 73 GPa[59] and R_{rms} or R_a (average roughness) ~2.5 - 10 nm[60], respectively. The porosity and residual moisture of non-spherical SiO_2 nanoparticles for the aspect ratio 3 were ~12.98 m^2/g and 2.47%, whereas for the aspect ratio 8 were 285.6 m^2/g and 2.70% (Figure II-1g). These values may be interpreted that the mechanical properties (the prodigious liquefaction temperature and Young's Modulus, yet relative smooth surface) and hydrophilicity of non-spherical SiO_2 nanoparticles successfully overpowered the impressive porosity in relation to elicit the tremendous non-spherical nanoparticle shape stability.

To further elucidate the hydrophobicity degree of SiO_2, the Rose Bengal method was applied. As expected, the hydrophobicity of SiO_2 (regardless of their aspect ratios) is much lower compared to the formerly tested polymers, characterized by virtually no Rose Bengal adsorption onto SiO_2 particles. Consequently, no graphic can be plotted like aliphatic polyesters, PS-COOH, and gelatin nanoparticles in Figure II-5d. Furthermore, "SiO_2 bulk" (roughly represented by tetraethyl orthosilicate [TEOS], the monomer of SiO_2 nanoparticles]) also exhibited relative low hydrophobicity, displayed by high SFE about 55 mN/m, low material-water interfacial tension approximately 3.8 mN/m and WCA around 45° (Figure II-5e). We suggest that both first parameters are better to be correlated with the non-spherical shape stability compared to merely WCA due to the absence of non-polar or hydrophobic component consideration in WCA.

Likewise, residual stabilizer determination for PS-COOH nanoparticles, fast-acceptable methods (EDX and Fourier Transform Infrared [FTIR]) were employed to both non-spherical SiO_2 nanoparticles. The results demonstrated that no bromide peak from cetyltrimethylammonium bromide (CTAB) and a carbon chain band (wavenumber 3,000 - 2,800 cm^{-1}) in the washed non-spherical SiO_2 nanoparticles (data not shown), implying that both nanoparticles might be entirely clean from residual surfactant. The similar results concerning the absence of Br after several washing steps of non-spherical mesoporous SiO_2 nanoparticle were reported formerly[54]. Nevertheless, it is plausible that the residual amount of CTAB is lower than limit of detection of the used technique. Therefore, oxygen combustion method was performed and revealed that C, H, and N elements existed in both aspect ratios of SiO_2 nanoparticles with the ratio of about 1.00%, 3.12% and 1.99%

respectively, but no Br was detected. To convince the residual CTAB in both non-spherical SiO_2 nanoparticles, Br analysis was performed using an inductively coupled plasma mass spectrometry (ICP-MS) and demonstrated that more than 96.8 ppb Br were detected.

4. Discussions

Here, the study for non-spherical nanoparticles fabrication covers the bottom-up methods, encompassing cross-linking (physical and chemical), molecular entanglement (nanoprecipitation & emulsion solvent extraction), and polymerization. We focus in these methods due to the potential thereof as the controlled release matrix. It is also possible to obtain non-spherical nanoparticles by diverse top-down methods (e.g. milling[61], homogenization[62], evaporative / antisolvent precipitation / solvent-diffusion[63, 64]), but these approaches are commonly intended to enhance the dissolution of drug substances due to the greater surface area of non-spherical nanoparticles compared to the spherical ones with the same volume (or so-called: greater surface-to-volume ratio; Figure II-1d).

Through the implementation of film-stretching method to the spherical nanoparticles (produced by the first two aforementioned bottom-up methods), it is basically believed that the shape-memory programming is introduced to the nanoparticles[65, 66]. The spherical nanoparticles may be regarded as a primary shape. Subsequently, the primary shape is then mechanically deformed into a secondary shape at temperatures exceeding the bulk Tg (e.g. Table S II-1 vs Figure II-1f). In this work, it was undergone merely uniaxially (, however, it was also reported the plausibility of biaxial stretching[4, 33, 67, 68], imparting much higher aspect ratio, surface area, and variation of radius of curvature ($R_c(t)$), but very low density of particle constituents [Supplemental Calculation] compared to the uniaxial one). Consequently, the sample is cooled below the bulk Tg, while still under stretching, to induce crystallization. Next, the secondary shape is preserved through an abrupt reduction in polymer chain mobility. Generally, the recovery to the primary shape in shape-memory is then attained by simply heating the unconstrained network above dry bulk Tg. The resulting increment in polymer chain mobility permits the entropic energy lost during stretching to be converted into a restorative force that reestablishes the primary shape of the network. Nevertheless, we reported here that the recovery to the original state occurred below the bulk Tg (chiefly at physiological-related condition: 37°C, PBS pH 7.4 310 mOsm), depending on the complex physicochemical parameters of bulk & fabricated nanoparticles.

In principle, it appears that by stretching or formation of non-spherical particles, the neater alignment of polymer chain arrangement in nanoparticle is formed. The higher order is, however, not favored

thermodynamically. At higher temperature (e.g. 37°C), the larger entropy is triggered, which may lead back the polymer chain to the preferable disorientation. The degree of polymer chain mobility, indicated by the rate of shape transformation into spheres in this report, is subject of multifarious physicochemical properties of bulk

& fabricated nanoparticles (discussed in the following sections). On the contrary, as expected, nanoparticle storage at lower temperature (e.g. 5°C) can aid to lessen the entropy level, thereby reduce dramatically the higher disorientation inclination of polymer chain arrangement. In other words, low storage temperature maintains longer the non-sphericity of nanoparticles.

4.1. Effect of Fabrication Method

4.1.1. Cross-Linking

In principle, the swelling of hydrogels (e.g. O-CMCHS and gelatin) at physiological pH (7.4) was very favorable, even for the highly (chemically) cross-linked hydrogel system as demonstrated elsewhere[69]. It is due to the existence of charge from the isoelectric point of the polymers (i.e. isoelectric point [IEP] of O-CMCHS: 2.0 - 4.0[69]; gelatin type B: 4.7 - 5.4[58]) at physiological pH. We have tried to harvest both non-spherical cross-linked hydrogel nanoparticles from PVA (Mowiol® 40-88) film using only highly purified water (HPW; pH 5.5 - 5.8) as well, however, the exaggerate swelling still occurred (similar appearances like in Figure II-1b). The considerable swelling in the non-spherical cross-linked hydrogel nanoparticles by the film-stretching method may be explained by the facts that swelling is more pronounced in the cases of smaller submicron (i.e. size $\leq$ 200 nm), less cross-linked (for O-CMCHS), and heated particles[16, 70]. From these findings, it can also be inferred that swelling is actually displayed by hydrogel particles prepared by any materials (e.g. poly(hydroxyethyl acrylate) / PHEA, poly(ethylene glycol) diacrylate / PEGDA[70], derivatives of hydroxyl PEG acrylate groups[71, 72], etc.) and methods (i.e. imprint lithography, irrespective from its subtypes[16, 70], particle replication in nonwetting templates [PRINT®][71-76], etc.), but they are in the much lesser degree.

In our study, although the employed gelatin nanoparticles as prepared by Geh et al.[77] had been highly cross-linked (~85%) using the standard chemical (covalent) cross-linker (i.e. glutaraldehyde), dramatic swelling thereof after embedment in PVA film matrix still took place (Figure II-1b). This might be more associated to the heating history of gelatin nanoparticles in PVA film matrix (including its strong interaction with PVA as presented in the section “Results”) as well as its small submicron size. Moreover, the strong interaction between hydrophobic part of gelatin and PVA was utilized to develop gelatin nanoparticles

without crosslink[78]. The remarkable interaction may also occur between PVA and other hydrogel systems, such as lithography (e.g. S-FIL[14], J-FIL[15, 79], and D-FIL[16]) or PRINT®[71-73, 75] method.

Nonetheless, the stretched gelatin nanoparticles had a slightly (far from ideal; Figure II-1d) non-spherical (prolate) shape, favorably associated to the immediate shape transformation during harvesting and storage in physiological-related condition. This might be explained merely due to the greater hydrophobicity of gelatin bulk materials (higher than other protein, such as human serum albumin [HSA]; Figure II-5e) and nanoparticles (as exhibited in section "Results"). It is because in principle, the covalently cross-linked networks (like in gelatin nanoparticles) should show affine deformation towards stretching[80]; meaning it should behave likewise the thermoplastic polymers (e.g. aliphatic polyesters, polystyrene, etc.)[65]. In the case of O-CMCHS owning the poorest nanoparticle non-sphericity, it may rather be ascribed to the lack of nanoparticle integrity, due to the consideration of its high bulk hydrophilicity (Figure II-5e) and Tg (140 - 150°C)[81].

Regardless of the poor results of non-spherical cross-linked hydrogel nanoparticle shape stability, we also suggest that because of the exaggerate swelling, film-stretching method seemed inappropriate for the production of non-spherical cross-linked hydrogel nanoparticles. Hence, this paper remonstrates the prior suggestion by Champion et al. (2010)[82] that the film-stretching method would be rather versatile for the non-spherical nanoparticles fabrication using various bulk materials and nanoparticles. Nevertheless, film-stretching method may be still appropriate for other (more solid) cross-linked particles (e.g. poly(methyl methacrylate) [PMMA][83]).

For the manufacturing of milder swollen non-spherical hydrogel micro- and nanoparticles (which usually have low [but tunable] Young's modulus[71-73]), imprint lithography or PRINT® technology (a top-down method[84]) may provide more promising possibilities. However, certain component material(s) on both technologies are not biodegradable, e.g. PEGDA[14, 85]. Furthermore, and importantly, we should be aware and critical to the potential instability of their non-spherical shape in relation to the comprehensive manufacturing aspects, mainly the hydrophobic degree of particle component materials (Figure II-5e). Some of examples of these system are discussed below.

For the first instance, the synthesis of moderately hydrophobic non-spherical (biconcave or complex oblate ellipsoid) hydrogel microparticles has been demonstrated (with the details: particle Young's modulus 7.8-

63.9 x 10^{-6} GPa[73]; consisting of PHEA [~up to 80% as main polymer], 2-carboxyethyl acrylate / CEA [10% as negative charge bearing agent], and PEGDA [1 - 10% as cross-linker; bulk Young's modulus: 0.01 - 3 GPa[86]). By virtue of deliberation of their comprehensive manufacturing aspects (i.e. low Young's modulus, poor bulk Tg [likely < 22°C[87], depending on the water content], and moderate hydrophobicity of their components and final preparation [which may be comparable to aliphatic polyesters; Figure II-5e]), we believe that this system is favorably to encounter shape transformation into spheres in physiological-related condition, even the transformation rate is possibly slower than at the nanoscale[26]. But, there was no report regarding its non-spherical shape instability because they used 0.1% PVA (2 kDa) as dispersant that definitely stabilizes the shape of non-spherical microparticles (recall the case of our residual PVA results).

Second, PEGDA cross-linked by synthetic peptide (acrylated Gly-Phe-Leu-Gly-Lys / GFLGK) was employed to produce non-spherical hydrogel nanoparticles[14]. By using similar extensive approach as above, it is known that PEGDA nanoparticles have low, but tunable nanoparticle Young's modulus 0.255x10^{-6} - 3 GPa[86] (depending on cross-link density), poor bulk Tg (~-34°C, regardless of its cross-link density[88]), Tg confinement effect, small $R_c(t)$, and mild-moderate hydrophobicity of their components. Based on these data, we propose that the nanoparticles may experience considerable non-spherical shape instability in physiological-related condition. Our proposal is strongly evinced by the very rapid transformation of similar non-spherical nanoparticles into spheres after the contact of (unconstrained) particles with highly purified water (HPW)[89]. Therefore, the omission of supposedly high amount of stabilizer (PVA 31 kDa) post synthesis process was performed[14]. From these two examples, it is noteworthy to point out that the presence of proper stabilizer exhibits the superior non-spherical particle shape stability.

Lately, instead of optimizing the commercially available stabilizer and materials for supporting the excellent non-spherical particle shape stability, it is not surprising that the trend in finding and utilizing less hydrophobic novel polymers as particle core grows significantly. The eminent examples thereof encompass the members of hydroxyl PEG acrylate (HPA) group[71], such as triethylene glycol monoacrylate (TEGA)[72, 75], and tetraethylene glycol monoacrylate (HP_4A)[74, 76, 90]. Nevertheless, these new polymers have bulk Tg much lower than their parent polymer PEGDA[91], where the hydrophobicity is inversely proportional to the length of hydrophilic side groups[91] (e.g , i.e. Tg TEGA -48°C[91] vs Tg PEGDA -34°C[88]). Therefore, it will be very fascinating to investigate the best compromise between the hydrophobicity aspects and the other physicochemical properties (e.g. Tg, Young's modulus, etc.).

4.1.2. Molecular Entanglement

To hinder excessive aggregation (principally during nanoprecipitation), the entanglement of polymer chain should be optimized by an appropriate polymer molecular weight. Relative low molecular weight polymer is highly recommended[92], such as ~17 kDa (as used here). The larger molecular weight (~44kDa) of PLGA 50/50-COOH is still proper for nanoprecipitation process (; which is in agreement as reported up to ~61 kDa or 0.67 dL/g intrinsic viscosity[93]). However, the higher the polymer molecular weight by nanoprecipitation, the lower the nanoparticle yield due to the more aggregates formation (Table II-1). The low molecular weight aliphatic polyester (17 kDa) might have surface active properties[94], thereby permits better nanoparticle yield and integrity as well as compactness (low porosity). Therefore, it is not surprising that the higher porosity of aliphatic polyester nanoparticles (i.e. PLGA 50/50-COOH 0.67 dL/g) prepared by nanoprecipitation has been developed as “sponge” core for toxin entrapment[95].

It is notorious that aliphatic polyesters[26, 65] and PS(-COOH)[96] have shape-memory properties. For aliphatic polyesters, the shape-memory properties are more pronounced in the case of ester-ended variant, very low molecular weight (4.1 kDa) and very low bulk T_g (27°C)[26]. Whereas, carboxyl-ended modification has better solubility in water and physiological pH, thus enables lower interfacial tension to the nanoparticles during their dispersion on these media. It is also known that the smaller the particle size (in submicron or nanoscale), the higher possibility and rate of shape change[26, 96]. This finding is associated to the larger impact of interfacial tension at the nanoscale[26, 96] and lower $R_c(t)$ (Figure II-1d). Even the shape shifting of pure macroscopic poly(styrene) / PS sheet ($R_c(t) \infty$) was reported at a temperature below its bulk Tg, viz. 60°C[97] vs 100°C[23], consecutively.

From the “Results” section, it is very clear that the involvement of particular stabilizer (only PVA [Mowiol® 4-88] in the emulsion solvent extraction for PLA-COOH and PLGA 75/25-COOH; sulfate ester in the emulsion polymerization for PS-COOH; and CTAB in the condensation for SiO_2) might result the meaningful residual stabilizer albeit thorough and strictly standardized washing process, leading to much superior non-spherical nanoparticle shape stability in physiological-related condition. We believe and hypothesize that pure PS-COOH or PS nanoparticles (produced by surfactant-free process and in the same size range as tested here) may impart poorer non-spherical shape stability in physiological-related condition due to their higher bulk hydrophobicity than the carboxyl-ended aliphatic polyesters (Figure II-5e). Likewise, we suggest that the non-spherical shape stability may also occur in the case of non-spherical core-(hydrophobic)shell systems having comparable or more inferior (e.g. Tg) physicochemical properties than materials tested here, such as

cyanoacrylate-chitosan[98], PLGA 15/85-chitosan[8, 99], and PMMA-(PS-PDMS)[83] (poly(methyl methacrylate); poly(styrene); poly(dimethylsiloxane)) (Table II-2 & Figure II-5e). However, there was no implicit report regarding the particle shape stability thereof inasmuch as the dispersion unavailability in physiological-related condition (e.g. 5°C[98], high stabilizer content[83, 100], constrained in [unreleased from] rigid matrix[89], or in organic liquid[83]), too short observation time (e.g. 1 hour[8]), and particle storage only at dry and room temperature. According to our confirmative study, it is true that by storage of non-spherical aliphatic polyester nanoparticles at 25°C (at ambient relative humidity) for 12 months in the constrained (unharvested) state in the PVA film, there was practically no aspect ratio decrease thereof (data not shown). To date, only few publications emphasize the plausibility of non-spherical particle shape transformation in physiological-related condition[26, 85].

4.1.3. Uncompromisable Requisite of Hydrophilic & Strongly Attached Stabilizer for Hydrophobic Bulk-Nanoparticles

To preserve the non-sphericity of nanoparticles, it was known that in the PRINT® system, 0.1 - 0.5% PVA (with very high interfacial activity due to the low degree of hydrolysis [75%] with 2 kDa, 20 kDa or 22 kDa) is utilized intentionally as nanoparticle dispersant, including for in vivo study[71-73, 75, 76, 101]. Instead of thorough washing, others also preferred to keep the high amount of PVA (2% 31 kDa[14]) or give extra Poloxamer (such as 0.75%[102] or 1%[103]) as dispersant in final preparation to endow better nanoparticle stability and circulation time. Importantly, some extra dispersant actually might not help much to stabilize the nanoparticles in the real physiological environment due to the rigorous dilution of the dispersant and if the stabilizer easily detaches from the nanoparticle surfaces[104]. Hence, the additional stabilizer post nanoparticle formation is mandatory for stabilizers that are weakly bound onto nanoparticles, such as Poloxamer 407[103] on aliphatic polyester nanoparticles[105]; otherwise the stabilizers were too inadequate to protect the nanoparticles from opsonization. In the case of our study, it is very reasonable that the P407 stabilizer is extracted by PVA used as the film matrix due to its strong retention to PVA[106]. Meanwhile, in case of TPGS, TPGS may have too low affinity (due to too hydrophilic) onto PLA-COOH nanoparticles, as reported elsewhere[106, 107]. In-depth discussion of residual stabilizers is presented in the section “Discussion: Effect of Hydrophobicity of Materials & Particles”.

Table II-2. Physicochemical Contrast of Non-Spherical Polymeric Core-Shell Nanoparticles Prepared by Film-Stretching Method

Parameters	Example					
	1		2		3	
Component	**Core**	**Shell**	**Core**	**Shell**	**Core**	**Shell**
Material	Cyanoacrylate (PIBCA)	Chitosan (Low Viscosity)	PLGA 15/85 (Degradex® from Phosphorex, Inc., Hopkinton, USA)	Chitosan	PMMA	PS-PDMS (Block Copolymer)
Reported in Reference(s)	[98]		[8, 99]		[83]	
Young's Modulus (GPa)	~0.002[242]	0.002 - 0.003[243]	N/A#	~0.002[243]	~3[23]	PS 3.2 - 3.4[23] PDMS 0.36 - 0.87[244]
Tg (°C)	Bulk 130[245]	Bulk ~100 - 150[81]	Nanoparticle 40 - 41[8, 99] Bulk N/A#	Bulk ~100 - 150[81]	Bulk 106 - 113[23]	PS Bulk 100[23] PDMS Bulk ~123 - 150[23]
Bulk Hydrophobicity	Refer to Figure II-5e	Refer to Figure II-5e	-	Refer to Figure II-5e	Refer to Figure II-5e	Refer to Figure II-5e
Positive Remarks	• High bulk Tg (PIBCA & Chitosan) • Dry heat stretching procedure • Further information availability of chitosan properties		• High bulk Tg (Chitosan)		• Intermediate (PS) & high (PMMA < PDMS) bulk Tg • Intermediate (PDMS) & relative high Young's Modulus (PS & PMMA) • Dry heat stretching procedure • A little information availability of washing process & used polymer molecular weight	
Negative Remarks	• High hydrophobicity (PIBCA slightly < chitosan slightly < gelatin) • Very low Young's modulus (PIBCA ≈ Chitosan)		• Very low bulk Tg & relative lower Young's modulus of PLGA 15/85 (due to high glycolide percentage)[58] • Very low Young's modulus (Chitosan) • Low wet Tg (nanoparticles) • Oil bath during stretching (thus, involvement of additional potential contaminants & organic solvent)		• Great hydrophobicity (PMMA ≈< PS slightly < PDMS)	
Unknown Information	• Residual stabilizer amount • Details of washing process (including washing & redispersion factor) • Details of PIBCA (e.g. molecular weight) • Nanoparticle integrity (~porosity ~residual moisture) • Surface roughness • Nanoparticle hydrophobicity		• Residual stabilizer amount • Details of washing process (including washing & redispersion factor) • Details of core-shell materials (e.g. molecular weight) • Nanoparticle integrity (~porosity ~residual moisture) • Surface roughness • Nanoparticle hydrophobicity		• Residual stabilizer amount • More about washing & redispersion factor • Nanoparticle Integrity (~porosity ~residual moisture) • Surface roughness • Nanoparticle hydrophobicity	

#N/A: Not Available.
Abbreviations: PIBCA: poly(isobutylcyanoacrylate); PLGA: poly(D,L-lactic-co-glycolic acid); PMMA: poly(methyl methacrylate); PS: poly(styrene); PDMS: poly(dimethylsiloxane).

4.2. Effect of Mechanical Properties: Young's Modulus, Surface Roughness (R_{rms}) & Tg

In principle, roughness (surface topography) correlates with the hydrophobicity (surface energy / surface chemistry) and wettability (WCA)[37]. The impact of surface roughness may seem trivial, but our results showed its significance (recall the shape instability of rough non-spherical PLGA 50/50 by nanoprecipitation). Due to the necessity of sophisticated instrument for particle's roughness measurement (e.g. AFM), only a small number of papers have reported the influence of surface roughness to physiological-related phenomenon, e.g. protein adsorption[108] or so-called corona. This phenomenon get more and more spotlights[109] because of its high correlation into clinical effect[110, 111].

Confinement effect was proved to be affected by the interfacial activities (in decreasing phase transition [including liquefaction] temperature of confined materials, irrespective of object geometry), existence of residual stabilizer, and kind of dispersion media[41, 112, 113]. Atoms at a free surface (such as in nanoparticles) encounter a diverse local milieu than do atoms in the bulk material. As a consequence, the energy related to these atoms will commonly be different from the atoms in the bulk. The additional energy linked with surface atoms is called surface free energy (SFE). In bulk materials, such SFE is characteristically ignored because it is attributed with merely a few layers of atoms near the surface and the ratio of the volume occupied by the surface atoms and the total volume of material of interest is low. Conversely, for smaller objects, the surface-to-volume ratio becomes very significant, and so does the effect of SFE[36].

In general, macroscale objects have virtually no tendency to experience confinement effect compared to microscale[85, 114] and nanoscale[36, 42] objects. This trend may be ascribed to the higher surface-to-volume

ratio of the nanoscale objects. Strong confinement effect on phase transition (e.g. liquefaction [Tg or Tm]) temperatures in nanoscale objects or radius of curvature does not only occur on polymeric systems (as reported here and elsewhere[41, 42]), but also on any materials, both non-metallic (e.g. water[51], lipid[115, 116], etc.) and metallic ones (e.g. gold [Au][117, 118], lead [Pb][119], tin [Sn][119], bismuth [Bi][119], etc.). Interestingly, it was reported that even in macroscale, certain polymer cases, such as bulk aliphatic polyesters, were also prone to the reduction of Tg due to absorption of non-freezable water[39, 40]. However, to our best knowledge, there is still no report discussing the relation between Tg confinement effect and non-spherical particle shape stability. Therefore, this report is the first one which proposes to correlate thereof. Nevertheless, it has been actually reported the shape evolution from the non-spherical to spherical nanoparticles on aliphatic polyester derivative (i.e. PEG block copolymer)-microparticles (initial Feret's diameter ~50 µm)[85] and aliphatic polyester micro-nanoparticles (initial & final sphere ø 0.15 - 4 µm)[26]. The PEG-aliphatic polyester block copolymer (having a lower bulk Tg than its native aliphatic polyester) was also described to encounter the Tg confinement effect[120]. Both reports used stabilizers during the nanoparticle formation, i.e. polysorbate (Tween®) 20 (0.5%) during the washing step for the former and PVA (2%; molecular weight 10 - 30 kDa) during the solvent diffusion (also known as emulsion solvent extraction) process. The plausible rationale of residual stabilizer will be discussed deeper in the section "Results: Effect of Hydrophobicity of Materials & Particles".

For nanoprecipitation system (containing only aliphatic polyesters), the smaller Young's modulus and Tg are ascribed to merely confinement effect due to the smaller size (width & height) of nanoparticles and presence of very low $R_c(t)$ (Figure II-1d). Meanwhile, in the emulsion solvent extraction containing significant residual PVA, the slightly higher of mechanical properties are designated to the PVA, which is semi-crystalline[121, 122] and gains higher crystallinity after stretching[123]. It was also obviously observed the slightly growth of formulation's Tg of nanoparticles containing residual PVA due to antiplasticization effect, as reported elsewhere[124]. As comparison, in case of the presence of amorphous and crystalline variants in a polymer (e.g. polyethylene terephtalate [PET][125] or polypropylene [PP][126]), polymer stretching generally increases Tg and Young's modulus several folds inasmuch as crystallinity enhancement.

In many cases, residual stabilizers can also be problematic due to the decline of particle's Tg in final preparation. Although some other common stabilizers (Poloxamer[105, 127], TPGS[128], cholic acid in sodium salt form[129] and polysorbate [Tween®] 80[130]) are practically easy to be cleaned from particles, but in an adequate amount in the final preparation, they are reported to lessen the system Tg. The Tg reduction is well

known as the presumable main reason of burst release in drug delivery[131]. In our formulation, the insignificant amount of resided Poloxamer 407 and TPGS is well represented as the insignificant changes of formulation Tg (data not shown). It was reported when acting as stabilizer, TPGS would distribute only on the particle surface and by washing up more than 2 times, the remaining TPGS on the surface could not be detected anymore by X-ray photoelectron spectroscopy (XPS)[132, 133]. This may be the proper explanation for the poor protection of TPGS for non-spherical PLA-COOH nanoparticles fabricated by emulsion solvent extraction. In contrary, the particular amount and type of PVA (possessing high interfacial activity) could adhere irreversibly on particles surface prepared by emulsion solvent extraction via molecular interpenetration and multilayer adsorption mechanism[134], thus affects particle's physical properties (including drug release from nanoparticles) and cellular uptake[135, 136]. Interestingly, with regard to the residual stabilizer, the affinity and extent of residual PVA, Poloxamer, and TPGS on aliphatic polyester nanoparticles prepared by emulsion solvent extraction can also be differentiated from the freeze-drying results in highly purified water (HPW) and without additional cryoprotectant (our unpublished data; in preparation). Only PVA could elicit spontaneous redispersion and practically no aggregation, which can be assigned as the sufficient amount and strong adsorption of PVA on nanoparticles. The aggregation degree of nanoparticles synthesized by the aid of Poloxamer 407 & TPGS is as inferior as the nanoparticles prepared by nanoprecipitation (no stabilizer). These results are in agreement to previous publications with other materials and shapes of nanoparticles[127, 132, 137]. Based on the experimental results, we propose a systematic approach to better explain and predict the non-washability of particular stabilizers, as depicted in-depth in the section "Discussion: Effect of Hydrophobicity of Materials & Particles".

4.2.1. Reverse Proof of Complex Physicochemical Properties Interplays

4.2.1.1. First instance: Successful Stretching at the Temperature Below Bulk Tg using Nanoparticles Composed of Low Young's Modulus, but High Tg Material

Palazzo et al.[98] interestingly reported that the manufacture of non-spherical nanoparticles using film-stretching method uniaxially could be undergone far (~50 - 100°C) below the bulk Tg of the polymer (Table II-2). To our best knowledge, only this paper reports the success of film-stretching method below the Tg. Others[4, 13, 68, 138, 139] (including this report) always employ the temperature higher (normally ~20 - 30°C) than the bulk Tg, regardless of the used stretching medium [dry heating or oil bath] & nanoparticle materials. Moreover, Lu et al.[138] should perform the stretching ~100°C higher than the Tg due to their device limitation. Palazzo et al. works might be feasible inasmuch as the low Young's Modulus of the used materials (cyanoacrylate: i.e. poly(isobutylcyanoacrylate) [PIBCA] & chitosan; both ~0.002 GPa; Table II-2). We do not

believe the reason that Tg confinement effect could be applied to explain it, because our works convincingly showed the inability to stretch PS-COOH nanoparticles (the highest nanoparticle Young's modulus that can be stretched in our study: ~2 GPa; Figure II-1f), even at its bulk Tg (Figure S II-3). Conversely, ours confirmed that Tg should vary in diverse medium, as reported elsewhere[113].

Nevertheless, we still can infer that the obvious interplay presence between Young's modulus and Tg yielded the certain resistance for stretching process (Figure S II-3). In this case, although bulk Tg of PS-COOH (~93°C; Figure II-1g) is much lower than both bulk Tg in Palazzo's work (in-between ~100 - 150°C; Table II-2), PS-COOH nanoparticles cannot be proportionally stretched as our standard stretching process at 120°C (Figure II-2). Moreover, stretching PS-COOH nanoparticles at its bulk Tg only generate lemon-like nanoparticles partially from total nanoparticle population (Figure S II-3). Our generated shape resembles the nanoparticle shape produced by them. This shape might be attributed to the weak elastic deformation because of the high resistance from polymer chain mobility in nanoparticles. In addition, because of high bulk (cyanoacrylate & chitosan) hydrophobicity, high material-water interfacial tension may also induce the nanoparticle shape switch during harvesting in aqueous medium (Figure II-5e).

4.2.1.2. Second Instance: Unsuccessful Stretching at the Temperature Far Above Bulk Tg using Nanoparticles composed of High Young's Modulus, but Low Tg Materials

Cauchois[140] reported his failure to stretch spherical poly(γ-benzyl-L-glutamate) (PBLG) nanoparticles using film-stretching method. PBLG, a rigid[141] liquid crystalline material, has an unique (helical) internal structure, thus may exhibit either spherical or elongated particles, depending on its variants[142]. It has rather high hydrophobicity (in-between PLA-COOH & PLGA 75/25-COOH; Figure II-5e), bulk Young's modulus 34 GPa[143], and Tg ~19°C[144]. He found out that even the stretching process was performed at the temperature (i.e. 150°) far above the bulk Tg, spherical PBLG nanoparticles were unsuccessful to be deformed into the elongated ones[142]. The hydrogen bond, which should take an account as the main driving force in transforming stretched particles[12], seems work limitedly for "soft" material (< 10 GPa[145]), such as PS and PMMA[83]. To sum up, the Young's modulus of particles appears also to be one of a critical factor (besides Tg) determining the success of film-stretching method.

Based on both instances, we can conclude that the unavoidable interplay between multiple factors (Young's modulus, Tg, and surface chemistry) determines the deformability degree of nanoparticles (in this section, it is characterized by the success degree of non-spherical nanoparticle formation by film-stretching method).

We estimate that the deformability degree in the film-stretching method may favorably represent (but of course, still less a couple order of magnitude) the geometry sensitiveness of non-spherical nanoparticles in the real aqueous dispersion towards the interfacial tension. Therefore, these evidences reinforce our hypothesis that the complex interplay of manufacturing aspects may affect the non-spherical nanoparticle stability. We cannot only concern in one-two aspect(s) and neglect the others.

4.2.2. Correlation of Interfacial Phenomena towards Geometry and Internal Structure

Because of the interfacial tension, spherical particles (having no specific internal structure [like all experimented here using Wide Angle X-Ray Diffractometry, data not shown] or merely amorphous state in nature) are formed thermodynamically from non-spherical particles in order to minimize the contact area to water (recall the relative surface area comparison of the same volume objects, but different shape in Figure II-1d & Supplemental Calculation). This phenomenon arises from the energetic cost of forming a surface. Therefore, the SFE of the system is minimized when the particle shape is spherical. Besides, spherical state may permit polymer chain inside nanoparticles to have larger cohesive energy[146, 147]. Meanwhile, the greater surface area of non-spherical state (and the contribution of very low $R_c(t)$) will introduce more pronounced interfacial tension eliciting higher pressure. Consequently, the pressure would play a dominant role in the enhancement of polymer chain mobility on the surface, leading to the particle shape shifting into spheres[148]. To summarize, here is the condensed hypothesized correlation: the higher the hydrophobicity of materials/nanoparticles, the higher the interfacial tension, the higher the pressure working on nanoparticle surface, the faster the shape transformation into spheres. In brief, there is a sturdy relation between surface chemistry (hydrophobicity) and non-spherical shape stability/existence, as long as no robust or rigid internal structure. Our hypothesis is described on the next following examples.

First, beside well-defined amorphous aliphatic polyesters and PS-COOH studied here, another best example for the aforementioned hypothesis is poly(4-vinyl pyridine) (P4VP), an amorphous and a weakly hydrophilic polymer (Figure II-5e). Likewise the aliphatic polyesters, P4VP (grafted by PS) exhibits shape-memory properties depending on media pH[149-151]. In contrast to aliphatic polyesters, the P4VP hydrophobicity becomes lesser at pH lower than its pKa (5.5) and reaches maximum at higher pH[149, 151]. Therefore, these findings are recently employed to produce a pH sensitive block copolymer with polystyrene (PS-b-P4VP)[149, 150]. In accordance to our interfacial activity database (Figure II-5e) and other aspects of P4VP (bulk Young's Modulus 4.05 GPa[152] & Tg 142°C[23]) and PS, it may be plausible that the non-spherical / elongated (so-called pupa-like) particles made from PS-b-P4VP may demonstrate relaxation into the spherical ones in

physiological-related condition[149]. Our suggestion relies on the report by Deng et al.[150] revealing three key points that also fully support our hypothesis: (a) addition of higher amount PVA (0.1%; 13 - 23 kDa & 88% hydrolyzed) during the manufacturing is indispensable for the greater nanoparticle hydrophilicity and thus, abundance of non-spherical nanoparticles; (b) weakly elongated internal structure exhibited by PS-b-P4VP (each material component Young's modulus ~ < 4 GPa) can only be demonstrated with the considerable amount of PVA; and (c) higher hydrophobicity caused by the incorporation of hydrophobic gold (Au) ~40% (Figure II-5e; bulk Young's modulus ~65 GPa[153] & Tm 1,064°C[154]) results the plumper nanoparticles (decrease of aspect ratio).

Second, to give a diverse / contrary approach, the tunably amphiphilic (SFE ~22 - 45 mN/m)[155] poly(2-oxazoline) family was demonstrated. The increase of nanoparticle hydrophobicity by the incorporation of hydrophobic drug (i.e. Docetaxel (logP 2.4[156]) or Paclitaxel (logP 3.24[156]) into the amphiphilic worm-like poly(2-oxazoline) micelles (or so-called "filomicelles"; bulk Young's modulus ~2-20s x 10^{-6} GPa[157] & bulk Tg ~80°C[155])) is proven to trigger an immediate transformation of non-spherical nanoparticles into spherical nanoparticles[158]. The higher the hydrophobicity induced by the particular drug (i.e. Paclitaxel) and higher drug loading (leading to larger particle-water interfacial tension), the more spontaneous and entire the spherical shape switch. In contrary to our current results displaying the preferable transformation from non-spherical into spherical particles during storage, Schulz et al. (2014)[158, 159] reported that their drug-loaded nanoparticles turned gradually from spherical into worm-like particles due to the release of hydrophobic drug from nanoparticles (up to ~60% for 25 days). Their observation was conducted at room temperature (~25°C) & 37°C[159] (far below the drug loaded-nanoparticle Tg 73 - 76°C) and in physiological-related medium (phosphate buffer saline [PBS] pH 7.4 310 mOsm).

Third, for nanoparticles having its own definite internal structure, large interfacial tension because of high hydrophobicity or very low Young's modulus could be simply overcome. As a consequence, they may generate superior shape stability[142] or even, non-spherical nanoparticles spontaneously from the spheres over time[115, 160, 161, 162, 163].

The former example is represented by PBLG[142]. Inasmuch as its superior Young's modulus and comparable hydrophobicity to PLA-COOH & PLGA 75/25-COOH (details are referred to the previous subsection "Reverse Proof of Complex Physicochemical Properties Interplays"), it is very plausible that the non-sphericity of PBLG nanoparticles may stay longer in an aqueous dispersion in physiological-related

condition. The lower bulk Tg of PBLG does not appear to significantly induce the non-spherical shape instability.

Whereas, the latter instance is exhibited by the crystalline lipids (e.g. triglycerides) in spherical solid lipid nanoparticles, which is stored in aqueous medium at room temperature[163, 164]. Triglyceride has high degree of hydrophobicity (Figure II-5e; represented as cocoa butter[58]), bulk Young's modulus ~0.25-0.47 x 10^{-6} GPa[165] and average Tm 31 - 34°C[58] (actual Tm ranging 11 - 73°C[116] due to the variation of trilaurin-tristearin as well as α- & β-polymorph). Considering these unsupportive properties for non-sphericity, it is really astonishing to know that triglyceride nanoparticles can arrange themselves into non-spherical nanoparticles during storage. It is likely because of the necessity to have as high as possible cohesiveness[146] and density of crystal lattice[164]. In fact, the internal non-spherical (e.g. rod) crystal habit in nanoparticles can accommodate these needs through the formation of certain internal structure, i.e. stable β-polymorph[115, 160, 161].

However, because both non-spherical PBLG and triglyceride nanoparticles already have the highest thermodynamic stability and molecular compactness, they may impart very poor drug loading[164, 166] and final preparation quality. These situations are absolutely unexpected for drug delivery. In the future, we believe that the excellent compromise of shape factor and other manufacturing aspects will become the key issues to be handled. Additionally, in accordance to the findings described in this section and our entire results, we can conclude that the internal structure is principally the most influential aspect in determining the longevity of nanoparticle shape, then followed by surface chemistry (bulk-nanoparticle hydrophobicity; which can be further divided into: residual stabilizer, core-shell structure, and not to mention surface roughness), and next by Tg-Young's modulus (-nanoparticle integrity) in the equal position.

4.3. Effect of Porosity of Particles

In many cases, porosity may correlate inversely with the Young's modulus. It can be reflected in the relation of porosity (Figure II-1g) and Young's modulus (Figure II-1f) on nanoparticles prepared without any stabilizer or surfactant. The two most porous nanoparticles in this group (i.e. PLGA 50/50-COOH and gelatin) have the smallest Young's modulus. This trend was same as reported elsewhere[167]. These two factors appeared to be the additional inducers (beside surface roughness) to explain the poor non-spherical stability of PLGA 50/50-COOH nanoparticles by nanoprecipitation.

The degree of SSA gain depends on the type and concentration of used stabilizer[168, 169] as well as sort of organic solvent[170]. These parameters are the renowned defining factors impacting the mechanical and hydrophobic properties of nanoparticles, thus also potentially affect the non-spherical nanoparticle shape stability. In addition, it has been studied the effect of diverse nanoparticle porosities[56, 171] to the physiological-related events, such as protein adsorption.

The behavior of water absorbed into nanoparticles (displayed by the residual moisture) may be associated to various reasons, e.g. the effect of capillary condensation, the confinement of water by polymer structure, the formation of clusters, or the strong interactions between the highly bipolar water molecules and the polymer polar groups[40].

4.4. Effect of Hydrophobicity of Materials & Particles

The presence of hardly removed residual stabilizer (usually surfactant) appears to be uncompromised for keeping the non-sphericity of nanoparticles in aqueous and / or physiological medium, chiefly when the bulk material is hydrophobic. Our hypothesis is totally based on our current experimental data and well supported by other references as discussed below.

4.4.1. Aliphatic Polyesters and Residual Stabilizer Thereof

For the first example, poly(vinyl alcohol) (PVA; Mowiol® 4-88), an amphiphilic stabilizer (which was added in the emulsion solvent extraction process for aliphatic polyester nanoparticles preparation) and commonly-used in the colloidal suspension, plays an important role in maintaining significantly longer the non-spherical nanoparticle shape stability. It is very interesting because the resulted non-spherical nanoparticles had been thoroughly washed. This may be explained that PVA molecules are supposed to stay at the nanoparticle-water interface after their work to decrease the interfacial tension (i.e. nanoparticle surface energy per unit area) during the initial nanoparticle formation. It has also been reported that PVA may be adsorbed or tightly associated with the surface layer and thus cannot be completely removed from the surface of nanoparticles[50, 105, 135]. In general, PVA has been preferentially chosen as emulsifier in nanoparticles fabrication due to its excellent stabilizing ability to avoid particles aggregation during post-preparative steps (e.g. freeze-drying and purifying), high yield of dry particles powder, and ease to be redispersed in solution after lyophilization[127]. But, the interest of PVA use in biodegradable nanoparticle formation was rather low because of the reported health risk caused by PVA[172]. Nevertheless, recently PVA's safety profile is vindicated and acknowledged as "acceptable"[173]. As a consequence, PVA is now already approved for several injection products by US Food and Drug Administration (FDA)[174].

In our results, residual PVA might arise dominantly from Mowiol® 4-88 (stabilizer in emulsion solvent extraction method) instead of Mowiol® 40-88 (matrix for film-stretching). This was confirmed by virtually no additional PVA adsorption onto nanoparticle surface after stretching and thorough washing of non-spherical aliphatic polyester nanoparticles fabricated by nanoprecipitation (Figure II-1d), thus no improvement of non-spherical shape stability for aliphatic polyester nanoparticles fabricated by nanoprecipitation as well (Figure II-1d). In contrary, the PVA content in aliphatic polyester nanoparticles was remarkably higher (Figure II-5d). The disparity of PVA adsorption may be delineated by the interfacial activity variance of these PVAs[121], beside the probable higher propulsion force inducing PVA entrapment during the nanoparticle formation. Mowiol® 4-88 (stabilizer), the quite low molecular weight (31 kDa) PVA with the degree of hydrolysis 88%, has surface tension ~45 mN/m at critical micelle concentration (CMC) 0.5% (our results were in accordance to the manufacturer), meaning quite high interfacial activity. This makes it as an exceptional stabilizer for dispersed system[121]. Hence, it was not surprising that Mowiol® 4-88 is chosen one the most commonly-used PVA in the production of biodegradable nanoparticles[2, 175]. Whereas, Mowiol® 40-88, the large molecular weight (205 kDa) variant of PVA with degree of hydrolysis 88%, generates surface tension ~54 mN/m at CMC 0.5%, which can be attributed to the relative smaller interfacial activity. This fact may provide reliable reasons: (a) why Mowiol® 40-88 penetration and binding to the aliphatic polyester or compact nanoparticles are low and (b) why it still can disrupt and strongly attach to the hydrophobic gelatin nanoparticles. In general, the lower molecular weight and degree of hydrolysis of PVA impart higher interfacial activity[121].

According to our results, it is highly recommended to disclose the stabilizer details (e.g. for PVA, at least the information of molecular weight and degree of hydrolysis are vital to foretell the interfacial activity). Otherwise, the residue thereof becomes more uncertain and uncontrollable. However, some publications tend to disguise the information partly[176, 177] or totally[178, 179], likely due to the confidentiality issue.

Besides, the unclear details of nanoparticle materials emanate as well. For example, some papers did not state clearly the molecular weight (/ intrinsic viscosity)[177] and/or end group[180] of used aliphatic polyesters; whereas these material properties are some of the determining factors for hydrophobicity. Our study and others[50] have shown clearly that the higher the hydrophobicity, the higher residual PVA, thus it may really modulate the non-spherical nanoparticle shape stability.

Furthermore, it is also really important to state the exact details of nanoparticle washing step (e.g. for

centrifugation, it includes: the condition [speed & temperature], exact centrifugation cycle number and dilution factor; as well as dispersing energy[181]) during their synthesis. It was reported that the residual stabilizer on the nanoparticles is very determined by the degree of washing[107, 182]. There is, however, practically no publications stating obviously all details of washing steps, and here, we propose to cope with it. The unknown washing step details makes residual stabilizer issue more challenging and unpredictable. Of course, this issue is extremely critical for non-spherical shape stability.

Based on above findings, we can infer that the detail description of employed materials (i.e. stabilizers and polymers) and washing steps in nanoparticle formation are very essential and should be declared as explicit as possible.

4.4.2. PS-COOH and Residual Stabilizer Thereof

The second residual stabilizer is based on the results of PS-COOH nanoparticles. It is very reasonable that no significant shape alteration is reported for elongated PS nanoparticles[4, 6, 13, 19, 83] because the nanoparticles may contain considerable amount of residual surfactant[43, 183]. Although some commercial nanoparticle products contain surfactants as stabilizers, sometimes the manufacturers refuse to disclose the chemical nature of the surfactant used[184]. Only few studies (including ours) successfully characterized the concealed surfactant by manufacturer, such as sulfate salt surfactant in PS nanoparticles[43].

4.4.3. Silica (SiO2) and Residual Stabilizer Thereof

Beside our results, it was also reported considerable amount of surfactant (i.e. CTAB) was left on non-spherical SiO_2 nanoparticles compared to spherical ones[53]. Li et al.[55] observed as well that besides good resistance of non-sphericity, the residual surfactant on non-spherical SiO_2 nanoparticles might help nanoparticles to be less degraded in simulated body fluids, such as gastric, intestinal and blood. Also, they observed that the larger aspect ratio the nanoparticles, the more stable the nanoparticles against degradation in simulated body fluids. Based on this result, the larger aspect ratio might be correlated to the higher residual surfactant, protecting from harsh pressure effect of water.

4.4.4. Related Issue of Residual Stabilizer

By applying film-stretching method, it is very reasonable that the configuration of residual (semi-crystalline polymeric; e.g. PVA [in our study], PEG [3000 - 20000][185], poloxamer[186], etc.) stabilizers alters significantly, such as from “mushroom” to “brush” (Figure II-1a). The configuration alteration is attributed to our results that

all stretched nanoparticles roughened after stretching [Figure II-1f, Figure II-5a & b]). The “brush” conformation is renowned for much lower hydrophobicity inasmuch as thicker polymeric layer[187]. It was reported that the stretching of the polymer chains perpendicular to the surface leads to several new physical phenomena, including higher hydrophilicity[187]. Nevertheless, it is also important to note that film-stretching method can yield lower total system density as a result of surface area growth, leading to lesser protection by stabilizer at the interface (Figure II-1d). It is prominent that lower density at the interface may cause the “mushroom” conformation[188]. Therefore, we suggest that the dynamic transition from “brush” to “mushroom” conformation does exist in the non-spherical particles manufactured by stretching method. This transition is in the contrary as usually reported in the spherical nanoparticles (from “mushroom” to “brush”)[189].

In general, it appears convincingly that the density factor is slightly more dominant than conformation aspect. The most recent evidence is that the higher degree of stretching (including biaxial than uniaxial stretching; see Figure II-1d & Supplemental Calculation), the more likely the increase of hydrophobicity, thus resulting the lower C3 complement adsorption[4]. It is well known that C3 complement has greater adsorption propensity to more hydrophilic surface[111, 190]. C3 behavior is quite anomalous, whereas the majority of opsonins exhibits faster and higher adsorption to more hydrophobic objects[191].

Residual stabilizer issue is frequently underestimated[192] and misconstrued[193]. In the former case, it has been reported that the researchers claimed to use the “uncoated” nanoparticles. However, they actually used 1% PVA (without any further specification) on their formula[192]. Therefore, the definition of “uncoated” nanoparticles should be standardized to minimize the misleading and misinterpretation of experimental results caused by the unintentional nescience. In the latter case, nevertheless the study objective is good (i.e. to see the synergistic between nanoparticle surface properties and in vitro related outcome [cytotoxicity enhancement of doxorubicin]), it is likely that the cancer cell culture study using aliphatic polyester nanoparticles produced by emulsion solvent extraction elicit bias results because of the unwary washing step (very likely just one time) and the usage of great amount of certain stabilizers above CMC (i.e. Cremophor® EL, Solutol® HS 15, and Tween® 80; in-between one-to-three orders of magnitude). Our speculation is based on another report[194] and our stabilizer physicochemical properties analysis (Table II-3; further discussed in the next section); where these two stabilizers are very plausible to not present at the interface, thus detach easily from hydrophobic aliphatic polyester nanoparticles.

Furthermore, it is also important to note that toxicity can arise from residual stabilizer on a nanoparticle synthesis. However, on many occasions complete depletion of these residues is often difficult and

sometimes impossible. The degree of stabilizer removal depends strongly to its affinity into nanoparticle matrix. For example, CTAB, which has relatively intermediate-high surface polarity (around 0.53) compared to other stabilizers (Figure II-5e), is difficult to remove from hydrophilic matrix, such as silica[195] (Figure S II-4). It was reported that thorough CTAB elimination may lead to aggregation of the nanoparticles[196]. The strongly positive charge of CTAB adsorbed onto the surface of nanoparticles can trigger cytotoxicity and rapid opsonization, succeeded by MPS clearance[197]. As a consequence, many novel manufacturing methods involving materials extracted from natural sources as a novel stabilizers (e.g. human serum albumin [HSA], bovine serum albumin [BSA], etc.) have been studied to produce various core nanoparticle materials, such as aliphatic polyester[134] and gold[198].

Additionally, the affinity of stabilizer onto nanoparticle surface may also be influenced by pH in the particular ionic stabilizers (Table II-3; logD), such as sodium cholate, sodium deoxycholate, and Solutol® HS 15. Nevertheless, some ionic stabilizers (e.g. sulfate ester group: SDS or docusate sodium) are less prone to the logD alteration, thus enable them to better protect the non-spherical nanoparticles throughout various physiological pH (e.g. non-spherical nanoparticles which are intended for oral administration route[139]).

4.4.5. Investigation, Elaboration, and Outlook of Residual Stabilizer

To extensively and systematically appraise the root causes of different residual stabilizer extent and affinity in nanoparticle system, we suggest to investigate the primary and secondary interfacial activity parameters of several commonly-used stabilizers and materials for particle formation. The former include SFE, interfacial tension, and WCA (Figure II-5e). While, the latter consist of (a). work of adhesion (also known as adhesion energy) between particle and stabilizer material in certain medium, i.e. water (WoA_3), (b). interfacial tension of core particle and stabilizer material ($IFT_{1.2}$), and (c) the difference of WoA_3 and $IFT_{1.2}$ (Figure S II-4).

In the first priority, we propose to observe the difference of WoA_3 and $IFT_{1.2}$ to which better represents the overall affinity between stabilizer and particle materials, thereby complements the WoA_3 & $IFT_{1.2}$ concepts. It was already known that WoA_3 only demonstrates the short term affinity, while $IFT_{1.2}$ describes the tension left in the formed bond (i.e. the bond's potential to break), characterizing long term affinity[199]. From the deduction of our results and others[53, 124, 127, 129, 133, 135, 136, 168, 194], the non-washability of PVA, sulfate esters, CTAB, and Triton® X-100 from various nanoparticles may strongly correlate to their primary and secondary interfacial activity parameters (Figure II-5e and Figure S II-4). Interfacial activity-based algorithms to determine the stabilizer non-washability and suitability for particle formation are suggested (Figure S II-4c).

To scrutinize the physicochemical properties that could be linked to the behavior and pattern of residual stabilizers on nanoparticle, we propose to investigate further some examples of small molecule stabilizers discussed previously here, by virtue of comparing their other, yet related experimental and computational physicochemical parameters (Table II-3). Alongside the normal reported basic physicochemical parameters for (active) substances, we consider to introduce a novel parameter, namely molecular polar surface area (PSA). PSA is the total area on molecule surface exerting merely polarized atoms (e.g. ultimately oxygen and nitrogen, also encompassing their bound hydrogens)[200]. By this way, researchers can predict the partition degree of substances (in a diverse way as the conventional one, e.g. partition coefficient [logP & logD]), thereby estimate the molecular hydrophobicity[201], conformation evolution[202], as well as behavior towards various cell membranes recently[203, 204]. PSA calculation gives results which are proportionally comparable with the accessible surface area (ASA)[205] representing area of a molecule that is accessible to solvent (i.e. water). Additionally, PSA is approximately up to 2 order magnitudes faster than ASA analysis[200]. The greater the PSA value (for instance ≥ 140 $Å^2$[203]), the more hydrophilic the substance, thus the poorer imbalance between hydrophilic and hydrophobic (or lipophilic) part of the substance, leading to its lower interaction to the more amphiphilic matters (i.e. cell membrane). Therefore, it is not surprising that higher PSA displays poor membrane or cell permeation, e.g. through intestine[203, 206] or blood-brain barrier (BBB)[206, 207]. In contrary, the lower PSA value (i.e. ≤ 60 $Å^2$) was reported to have better equilibrium between hydrophilic and hydrophobic, hence the interplay between the substance and amphiphilic substrates occurred stronger[203].

Through this inspiration and the comparison of cumulative physicochemical properties of small molecule stabilizers (Table II-3, Figure II-5e & Figure S II-4), it is getting clear that generally, non-washable stabilizers should have a certain proportion of polar (hydrophilic) and disperse (hydrophobic or non-polar) (or so-called surface polarity, Xp) depending on the nature of particles, thus it can support their resistance on particles. These non-washable characteristics (of small molecule stabilizers) are possessed by, for example sulfate esters, Triton® X-100, and CTAB, demonstrating these characteristics: low surface tension (< 40 mN/m) at CMC, high LogP (> 2), high and virtually constant LogD at various pHs (each > 2), low intrinsic solubility (< -4.0logS), and PSA < 120 $Å^2$. Interestingly, hydrophilic-lipophilic balance (HLB) parameter, which is initially and frequently used as emulsion stability descriptor[208], shows very poor correlation towards the residual stabilizer on nanoparticle system, which can be classified as suspension. Hence, HLB may be rather inappropriate to portray the stabilizer affinity on solids dispersed in liquid medium.

Table II-3. Physicochemical Properties of Small Molecule Stabilizers or Surfactants Frequently Utilized in Biomedicine-Pharmaceutical Area

Code[§]	Material	Ionic Type [+/-/0]	MW (Da)	Liquefaction Temperatures[58] (°C)	CMC (Critical Micelle Concentration) [58] (%)	Gas-Liquid aka Material (i.e. Air)-Water Interfacial Tension aka Surface Tension at CMC[57] (mN/m)	HLB		LogP [b]	LogD[b] (at pH …)				Intrinsic Solubility[c]	PSA (Polar Surface Area)[d] (Å^2)
							Experimental[57]	Calculation[a]		7.4	6.8	5.0	1.2		
a	TPGS	0	1513	Tg ~-7.5[246]; Tm ~41[247]	0.02	45	~13.2	9.15	8.81	8.81	8.81	8.81	8.81	-0.91logS	257.43
b	CTAB	+	364.5	Tg N/A[#]; Tm 232 - 247	0.033 - 0.036[248]	~33[248]	N/A[#]	7.38	2.69	2.69	2.69	2.69	2.69	-6.98logS	0
c	SDS	-	288.4	Tg N/A[#]; Tm 204 - 207	0.24	25.2	40	40.00	2.04	2.04	2.04	2.04	2.22	-5.24logS	74.81
d	Docusate Sodium	-	444.6	Tg N/A[#]; Tm 153 - 157	0.11 ~0.02 - 0.03[249]	28.7	32[168]	24.35	2.86	2.86	2.86	2.86	3.42	6.33logS	118.18
e	Triton® X-100	0	647	Tg N/A[#]; Tm 6	~0.02[250]	~30[251]	N/A[#]	3.58	4.15	4.15	4.15	4.15	4.15	-4.59logS	29.46
f	Na-Cholate	-	430.5	Tg N/A[#]; Tm 236[252]	0.63[250, 253]	~40[248]	18[254]	22.87	2.48	2.48	-0.35	1.84	2.47 6	-3.70logS	100.82
g	Na-Deoxycholate	-	414.6	Tg N/A[#]; Tm 238 - 361[252]	0.41[253]	~42[248]	16[254]	20.97	3.79	1.11	1.66	3.28	3.78	-5.02logS	80.59
h	Polysorbate 20	0	1227	N/A[#]	~0.0013[255]	~33[255]	16.7	10.60	2.39	2.39	2.39	2.39	2.39	-4.45logS	133.14
i	Polysorbate 80	0	1310	N/A[#]	~0.0013[256]	42.5	15.0	8.23	5.05	5.05	5.05	5.05	5.05	-7.10logS	133.14
j	PEG	0	350	N/A[#]		~44	N/A[#]	14.77	-1.54	-1.54	-1.54	-1.54	-1.54	0.72logS	105.07
			400	N/A[#]		~44	N/A[#]	15.05	-1.58	-1.58	-1.58	-1.58	-1.58	0.78logS	114.30
			4000	Tg -98 - <-17[185]; Tm 50 - 58	0.001 - 0.1 monomer units (mol/L)[257]	~55^ - ~65[257]	N/A[#]	32.54	-5.39	-5.39	-5.39	-5.39	-5.39	UCN*	861.93
			5000	Tg -98 - <-17[185]; Tm N/A[#]		~55^ - ~65[257]	N/A[#]	37.39	-6.47	-6.47	-6.47	-6.47	-6.47	UCN*	1074.22
			6000	Tg -17[185]; Tm 55 - 63		~55^ - ~65[257]	N/A[#]	42.22	-7.55	-7.55	-7.55	-7.55	-7.55	UCN*	1286.51
k	(m)PEG[e]	0	350	Tg -50[258]; Tm 0 - 20[258];	N/A[#]	N/A[#]	N/A[#]	14.44	-0.89	-0.89	-0.89	-0.89	-0.89	0.54logS	94.07
			4000	N/A[#]	N/A[#]	N/A[#]	N/A[#]	31.93	-4.75	-4.75	-4.75	-4.75	-4.75	UCN*	850.93
			5000	N/A[#]	N/A[#]	N/A[#]	N/A[#]	36.76	-5.83	-5.83	-5.83	-5.83	-5.83	UCN*	1063.22
			6000	N/A[#]	N/A[#]	N/A[#]	N/A[#]	41.60	-6.91	-6.91	-6.91	-6.91	-6.91	UCN*	1275.51
l	Cremophor® EL	0	2474	Tg N/A[#], Tm 19 - 20	~0.002	40.9	12 - 14	9.47	14.70	14.70	14.70	14.70	14.70	19.63logS	462.64
m	Solutol® HS 15	0	948	Tg N/A[#]; Tm ~30	0.005 - 0.02	42.3[259]	14 - 16	12.85	0.34	0.31	0.88	2.40	2.73	0.21logS	216.21

[a-d]Calculated using the Calculator Plugins in MarvinSketch software version 17.1.23.0 (2017), ChemAxon (http://www.chemaxon.com)[260]. The used method was [a]Chemaxon; [b]Consensus method. All settings were set to default. Otherwise specified, the (parent) material molecular structures for calculation were obtained either from primarily ChemSpider (http://www.chemspider.com) or secondarily PubChem (https://pubchem.ncbi.nlm.nih.gov). [§]Each molecular structure, used for imparting physicochemical properties by the computational method, is available in Supplemental Figure (Figure S II-5).

[b]LogD is analogous with logP (partition coefficient), but it provides more specific partition coefficient at different pHs. Selected pH values represent various common physiological pHs, namely circulation system[261] and tissue or both so-called extracellular[262] (~7.4)-interstitital[263] (~7.4), intestinal fluid (6.8)[264], endosomal[265] - endo-lysosomal[266] or generally so-called intracellular (5.0; 4.0 - 6.5), and gastric fluid (1.2)[264].

[c]The smaller the value, or the more negative the log value, the lower the substance solubility in water.

[d]PSA values are identic at various pHs and calculated by inclusion of all atoms.

[e](m)PEG: (mono)methoxy poly(ethylene glycol); the common hydrophilic component for formation of block copolymer with aliphatic polyesters.

[f]The relation of trade : *generic name*: Triton® X-100 : *(4-)octyl phenol (poly)ethoxylate*; Cremophor® EL : *Polyoxyl 35 Castor Oil*; Solutol® HS 15 / Kolliphor® HS 15 : *Polyoxyl 15 Hydroxystearate*.

^10% w/v substance in HPW.

*UCN: Unable to be calculated because of too complex molecular structure.

[#]N/A: Not Available.

In addition, both interfacial activity parameters (Figure II-5e) and other related physicochemical properties (Table II-3) may also be appropriate to elucidate the inability reason of several general stabilizers (e.g. polysorbate 80[194], gelatin[194], poly(vinylpyrrolidone) [PVP][194], and PEG (4000)[209]) in assisting the formation of nanoparticles. It is strongly proven that these stabilizers were deviated widely from the suggested values (Figure II-5e, Figure S II-4 & Table II-3). Our databases may complement the old report of Albertsson[210], still displaying no quantitative comparison between the macromolecular stabilizers. Nevertheless, his work is really influential to date and widely applied in pharmaceutical area[106, 211] to give insight of material (macromolecule) and nanoparticle hydrophobicity. In accordance to Albertsson's report, dextran and its derivatives are the most hydrophilic polymers, while PVA and PEG have quite similar hydrophilicity (with PVA shows higher hydrophilicity). It can explain why dextran is totally not sufficient as stabilizer for hydrophobic aliphatic polyester nanoparticles development[194], but fails to enlighten, why the more hydrophilic PVA can be a great stabilizer than PEG (4000[209]) for (aliphatic polyester) nanoparticle synthesis. In fact, to be bond with the hydrophobic aliphatic polyesters, the relative more hydrophobic PEG variant (i.e. commonly methoxyPEG [(m)PEG] 2000[212], 3400[213], till 5000[212, 214]) should be covalently linked onto the aliphatic polyester backbone forming the block copolymer; where these block copolymers may form (micelle-like) nanoparticles in aqueous solution. Logically, if the Albertsson's sequence is assumed to be fully valid, the PEG may exhibit spontaneous and higher adsorption onto hydrophobic aliphatic polyesters. The combination of interfacial activity parameters (Figure II-5e) and other related physicochemical properties of stabilizers (Table II-3) may clarify such PEG issue, i.e. PEG has too weak interfacial activity (SFE or surface tension ~55 - 65 mN/m), too high solubility in water (positive logS) and high PSA (> ~1000 $Å^2$), thus shows practically no presence at the interface due to its higher affinity to water molecules. In conclusion, the physicochemical properties generated by the computational method appear to be promising to equip our interfacial activity knowledge in comprehending its relation to the residual stabilizer.

Meanwhile, in case of big molecule (termed as macromolecule afterwards) stabilizers, hitherto it is still rather hard to connect the residual macromolecule stabilizer on nanoparticle with their physicochemical properties due to the lack of appropriate physicochemical descriptor to be linked and great complexity-plausibility of interactions. Also, even by means of computational simulation, it requires a lot of computation effort, time, and cost just for the basic physicochemical properties (e.g. Tg, WCA, etc[215]). Therefore, to date the limited experimental approach (i.e. interfacial activity parameters; Figure II-5e) is the only source to understand this phenomenon. Nevertheless, we believe that the progress of macromolecule experimental and computational research will provide tools to unveil the holy grail of residual macromolecule stabilizer on nanoparticles.

Recently, the novel trend to use computer-assisted drug formulation design commenced[216].

As an outlook, we envision that certain residual stabilizers can be vexed, both for manufacturing process and clinical translation of non-spherical nanoparticles. This is due to the fact that albeit implementation of clearly described and strictly standardized nanoparticle washing as shown in this report, in many cases we cannot neglect the existence of particular residual stabilizers. On the one hand, they can be an impressive companion for particle shape stability, yet modulate other nanoparticle physicochemical properties (e.g. Young's modulus, surface roughness, Tg, porosity, residual moisture and hydrophobicity). On the other hand they may also be a potential threat for further clinical application because almost all strongly retained stabilizers on nanoparticles are renowned for its toxicity. Careful selection of currently available stabilizers and innovative material development are demanded for the advancement of non-spherical nanoparticles. Besides, the clear divulgence of used stabilizer and washing process is very imperative. In the future, the nanoparticle research results should be more cautiously evaluated due to the inseparable influence of particle shape and surface chemistry.

4.5. Comparison to Non-Spherical Silica (SiO2) Nanoparticles and Other Systems

Learning from excellent shape stability of SiO_2 nanoparticles (still having residual stabilizer) in physiological-related condition, the further question may arise. How come if there is no residual stabilizer (or surfactant) at all during the manufacturing process? Could the non-spherical shape of nanoparticles dispersed in aqueous physiological-mimicking environment still persist? The answer is likely yes, but the Young's modulus and liquefaction temperature (either Tg or Tm) of the material should be exceptionally high. For example, very hydrophobic (single-walled) carbon nanotube (SWCNT), having Tm of 4,177°C[217] and Young modulus of 1,800 GPa making it as one of the stiffest material measured experimentally[218]), can be produced spontaneously without the presence of stabilizer using arc-discharge evaporation [219]. This technique is the same as to produce other fullerenes, such as spherical C_{60} (also, so-called Buckminsterfullerenes or buckyballs). Based on this, the member of fullerenes family may have similarity in terms of very great hydrophobicity. It has been reported that experimentally, spherical fullerenes are the most hydrophobic nanoparticles (regardless of its fabrication method) relative to gold and silver nanoparticles formulated with various stabilizers[220]. It seems that their results concerning sequence of nanoparticle hydrophobicity may have a good correlation to the bulk material hydrophobicity (Figure II-5e; case: gold vs unwrapped SWCNT). Therefore, we believe that the interfacial activity database coupled by complete bulk-nanoparticle physicochemical properties may be an initial guidance (after internal structure status) to appraise the non-

spherical particle shape stability in the dispersion medium. Since our interfacial activity database covers only the aqueous data, it is required more elaboration to provide similar database for non-spherical shape stability prediction in other dispersion medium (e.g. organic solvent, oil, etc.), which may be interested in other research areas[83, 149].

Nevertheless, nothing is perfect in this world. Albeit the high plausibility of stable non-sphericity, fullerenes family incline to flocculate in order to avoid their dispersion in solvents or viscous polymer melts[221] due to their very hydrophobic nature. Stabilizers with highly strong interfacial activity and low-intermediate surface polarity (about 44%, e.g. sulfate esters (specifically docusate sodium) and Triton® X-100[222]; recall Figure II-5e and Table II-3) are generally required to disperse the fullerenes family in aqueous dispersion medium. It can be proven with our database (Figure II-5e) and secondary interfacial activity parameter calculation, resulting the conclusion that both stabilizers are very likely non-washable from SWCNT (e.g. Triton® X-100 with WoA_3 25.51, $IFT_{1.2}$ 7.72, and the difference of WoA_3-$IFT_{1.2}$ 17.79 mN/m). However, again the inextricability of particle shape and surface chemistry (as well as other physicochemical properties) is highly accentuated.

4.6. Lesson Learned from Non-Spherical Particle Shape Stability

To make the inference of non-spherical particles shape stability, we should take into account all manufacturing aspects (including bulk and nanoparticle form) as well as their consequences to physicochemical properties. Otherwise, the fallacy is obtained. For example, if merely the hydrophobicity, molecular weight/viscosity and Tg properties in the bulk form are taken into account, it will be reasonable to put PLGA 50/50-COOH nanoparticles as the long-lasting non-spherical nanoparticles between the aliphatic polyesters produced by nanoprecipitation. In fact, it had the poorest shape stability between the aliphatic polyesters prepared by nanoprecipitation. Relative neglected properties (such as nanoparticle integrity, nanoparticle Young's modulus, nanoparticle surface roughness, nanoparticle wet Tg, nanoparticle porosity, and residual stabilizers in nanoparticles) prove clearly that they should also be carefully and simultaneously assessed. Another instance is O-CMCHS. Despite its great bulk hydrophilicity (Figure II-5e) and Tg (140 - 150°C)[81], the non-sphericity of O-CMCHS nanoparticles is the worst among other materials studied here. Lack of nanoparticle integrity is responsible for this reason.

In contrary, we cannot conclude the non-spherical shape stability based on only the (partial) nanoparticle properties. For instance, gelatin nanoparticles were the smoothest surface (R_{rms} = 3.2 nm) nanoparticles,

which usually may lead to the lesser hydrophobicity degree[37]. However, non-spherical gelatin were the one of the least stable in terms of non-sphericity. This could not be separated from the poor nanoparticle integrity (demonstrated by swelling), relative high porosity (1.57 m^2/g), soft (nanoparticle Young's modulus of 0.7 GPa) and great hydrophobicity (, both in bulk and nanoparticle forms; Figure II-5d & e). Further example, SiO_2 nanoparticles have the highest porosity (generally ranging from tens to hundreds m^2/g), that may be interpreted one of the risk of non-spherical shape instability. Nonetheless, inasmuch as very low hydrophobicity, and great mechanical properties (high Young's modulus 73 GPa, acceptable surface roughness ~2.5 - 10 nm, and Tm 1,600^oC), it turns out that SiO_2 nanoparticles is one of the most stable nanoparticles in terms of non-sphericity.

To sum up, in relation to the non-spherical particle shape stability, negative factors (high hydrophobicity, surface roughness, and porosity) of nanoparticles are counterbalanced by positive factors (existence of non-spherical structure, high stiffness, and liquefaction temperature). According to our experimental results and some available reports, the detail considerations of manufacturing aspects towards non-spherical shape stability are summarized in Table II-4.

Table II-4. Contrast and Deliberation of Manufacturing Aspects towards (Non-Spherical) Particle's Physicochemical Properties (Underlined) And Their Potential Biological Relations

Advantages	Manufacturing Aspects	Disadvantages
• ↑ aspect ratio → ↓ probability for phagocytosis by macrophages[8, 19] → ↑ circulation time[4] • ↑ surface area → ↑ "loading" of active pharmaceutical ingredients (APIs) (in case of APIs should be tethered onto surface)[9, 22, 64, 267] • ↑ polymer orientation & crystallinity* (*in case of semi-crystalline ones) → ↑ rigidity & liquefaction temperatures (Tg & Tm) → ↑ non-sphericity stability • ↑ variance of particle's radius of curvature ($R_c(t)$) → ↑ choices for other unique related phenomenas (e.g. substance adsorption-stability, liquefaction temperatures [Tg & Tm], etc.) • bestow relative same volume as the starting spherical* particles for better in vitro and in vivo study comparison (*as long as the integrity of particles is sufficient)	**Stretching (e.g. using Film-Stretching Method)**	• ↑ surface area → ↑ possibility of APIs burst release • ↓ density & amount* of stabilizer (*in certain case, e.g. P407 extracted by PVA[106]) • ↑ surface roughness As above consequences: generally ↑ contact area of pressure & hydrophobicity → ↓ non-sphericity stability • ↑ variance of particle's ($R_c(t)$) → ↑ presence, abundance & degree of highly curved surface areas → ↓ non-sphericity stability: in fact, highly curved areas / smaller ($R_c(t)$)s are already proven in vitro[268] and in vivo[118] to generally impact the following properties of adsorbed (blood) proteins: ○ ↓ total amount of adsorbed protein ○ modulate cumulative adsorbed protein's surface hydrophobicity (Φ_I) depending on particle's surface hydrophobicity[269]: ▪ ↓ ($R_c(t)$) on ↓ hydrophobic particles → ↑ Φ_I[268] ▪ ↓ ($R_c(t)$) on ↑ hydrophobic particles → ↓ Φ_I[118] → however, evidently the ↓ Φ_I and quite ↓ total amount of adsorbed protein could not avoid the strong confinement effect on ↓ liquefaction temperatures (Tg & Tm) that are caused by too ↓ $R_c(t)$ → drastically ↓ non-sphericity stability[118] ○ ↓ cumulative negative charge of adsorbed proteins, leading to the ↓ zeta potential of particles
• ↑ dissolution rate-solubility of APIs & permeability	**(Nano-)Size**	• ↑ polymer degradation • ↓ surface free energy & ↑ interfacial tension (~↑ hydrophobicity[211]) → ↑ pressure / force against particles → ↓ non-sphericity stability
	↑ surface area	
• ↑ dissolution rate-solubility and loading of APIs	**Porosity**	• ↑ polymer degradation • ↑ inclination of residual moisture → ↓ non-sphericity stability
• ↑ permeability & cellular uptake	**Hydrophobicity**	• ↓ non-sphericity stability • ↑ total amount of adsorbed (blood) protein & ↑ opsonization (, especially for ↑ Φ_I [blood] proteins[268, 269])
• ↑ viscosity, T_g & rigidity → ↑ non-sphericity stability* (*in case of non-washable stabilizer involvement during particle fabrication; e.g. emulsion solvent extraction)[26] • ↑ degradation time	**("High") Molecular Weight & Viscosity of Polymer**	• ↑ particles size & size distribution, porosity* (*in case of non-washable stabilizer involvement) & surface area • ↓ yield of fabricated nanoparticles (in case of nanoprecipitation) • ↓ elasticity & hydrophilicity • ↑ interfacial tension
• ↓ hydrophobicity (charged condition; pH is far from pKa) → ↑ non-sphericity stability	**Functional Group Modification of Polymer (viz. Carboxyl-Ended)**	• ↑ hydrolysis → ↑ degradation time (i.e. aliphatic polyesters) • ↓ permeability → ↓ cellular uptake (by healthy cells) • ↑ hydrophobicity (less-charged condition; pH is closer to pKa)[26]; example: due to relatively more acidic intracellular compartment (Table II-3) of healthy cells or extracellular compartment of cancer cells[270], -COOH (pKa 3.85) is ↑ protonated → ↓ non-sphericity stability[26]
• ↓ hydrophobicity by ↓ interfacial tension → ↓ adsorbability of (blood serum) proteins • ↑ mechanical properties (in some variants, e.g. PVA enhancing Young's modulus & Tg) • ↑ non-sphericity stability (by ↑ residual stabilizers; i.e. particular PVA, which may have biological disadvantages (as described on the right))	**Stabilizers (e.g. PVA, Poloxamer, TPGS, SDS, PEGylation, etc.)**	(if too much and highly attached residual stabilizers onto particles) • ↑ specific surface area (SSA; e.g. relatively more substantial SSA ↑ by PEG)[269, 271] &/ ↓ liquefaction temperature (e.g. Tg by PEG[272] Triton® X-100[124], Poloxamers[273], etc.) → ↑ burst release[124, 269, 271] &/ ↓ non-sphericity stability • ↓ hydrophobicity → ↓ permeability & cellular uptake • ↑ formation of specific antibodies (e.g. PEG)[274] → ↑ clearance of drug vehicles[275]
• common & safe administration media for drug delivery system • ↑ non-sphericity stability by formation of more stable polymorph[163, 276]	**Water (including humidity)**	• ↓ liquefaction temperatures (Tg[40] & Tm[277]) → ↓ non-sphericity stability by considerable interfacial tension discrepancy, specifically at less-charged condition (i.e. pH is closer to pKa [if any] of such particle material[26] in case of shape-memory polymeric particles) & ↓ particle's ($R_c(t)$) (including also metallic particles[117, 118, 119]) (Note: In agreement with compendia from several authorities[278][279][280], the pH of highly purified water [HPW] should not necessarily be 7.0, but it can be between 5.0 - 7.0, as the used HPW here, i.e. pH 5.5 - 5.8 (~endosomal pH[265]) and elsewhere[153]. Thus, water aspect should be assessed carefully and on a case-by-case basis).
• ↓ residual stabilizers until minimum depending on the nature of stabilizers (reportedly, purification efficiency of certain centrifugation ~Cross-Flow Filtration [CFF][127] aka Tangential-Flow Filtration [TFF][281] aka Ultrafiltration[282] ≥ Gel Permation Chromatography [GPC][105] aka Gel Filtration Chromatography [GFC] aka Size-Exclusion Chromatography [SEC], especially for easily washable stabilizers, e.g. Poloxamer groups[105]) → ↓ toxicity, but this may also bring disadvantages (as described on the right)	**Purification**	(if too "clean", particularly for easily washable stabilizers) • ↓ non-sphericity stability & ↑ particle aggregation[196] chiefly in case of hydrophobic, porous and/or amorphous (no specific internal structure in) particles
(only by particular compendial methods[278][280][283] [e.g. sterile filtration using membranes ≤ 0.22 µm or pre-sterilization+aseptic processing] which still virtually maintain non-sphericity stability) • ↑ sterility	**Sterilization**	(for sterile filtration) practically impossible to be applied to spherical particle Ø > 0.22 µm or non-spherical particle owning minor axes > 0.22 µm • may ↓ particle yield depending on the properties of particles (e.g. size, hydrophobicity, charge, etc.) (Many cases of compendial sterilization methods [278][279][280][283][284], e.g. (a) steam [≥ 121ºC for 15 minutes], (b) dry-heat sterilization [≥ 160ºC for ≥ 2 hours], (c) ionizing radiations (normally 25 kGy or 2.5 Mrad), either beta- or gamma-irradiation, and (d) gas (e.g. ethylene oxide with residual limit ≤ 1 ppm[285])) • generally ↑ surface roughness[31] & residual moisture aka water content[286] • ↓ Young's modulus (in case of amorphous materials)[287] • frequently ↓ molecular weights of polymers (especially for blank particles) → ↓ liquefaction temperatures (Tg & Tm[288]) & ↓ SSA → ↑ aggregation & ↑ possibility of APIs burst release[289, 290] As above consequences: ↓ non-sphericity stability Nevertheless, sterilization aspect should still be assessed carefully and on a case-by-case basis.
• ↑ stability (e.g. cryoprotectants; if lyophilization is needed)	**Other Additional Substances (e.g. APIs, Excipients, etc.)**	• ↓ non-spherical stability (i.e. counter-ion[26], substances causing preparation's pH ~pKa of [e.g. polymeric] vehicles[26], loaded[158, 291]/adsorbed hydrophobic substances[26] including proteins[291], substances ↓ liquefaction temperatures of whole particles, such as gentamicin[290], [if applicable] residual oil during particle fabrication, etc. → also ↑ burst release)
• ↑ non-sphericity stability (e.g. PBLG[142])	**(Stable, Ordered & Non-Spherical) Internal Structure / Crystal System / Crystallographic Form**	• ↓ drug loading (e.g. stable β-polymorph of crystalline lipids, such as triglycerides[115, 160, 161] • ↑ toxicity

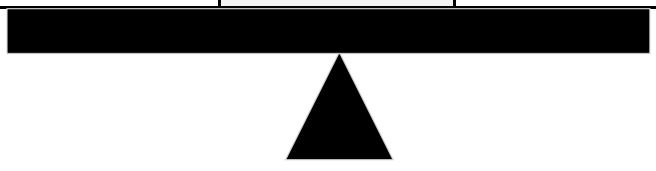

5. Conclusions

Particle shape is one of the most critical parameters in drug delivery. This momentousness should be verified further and heedfully for reliable in vitro and in vivo experiments. Our report strongly suggests that shape alteration tendencies of non-spherical particles (having no specific internal structure) to spherical particles might occur in favor of thermodynamic (due to trigger of material-water interfacial tension), and the rate at which this change occurred did not only depend on the bulk material properties and storage temperature, but also importantly on the physicochemical properties of the resulted nanoparticles. Besides, this rate of shape transformation can be simply tuned with the presence and extent of residual stabilizers. The evidence was displayed by decrease of aspect ratio (AR) and hydrodynamic size as well as polydispersity index (PDI). In case of biodegradable polymeric nanoparticles, aliphatic polyester nanoparticles prepared by emulsion solvent extraction using PVA was remarkably superior in terms of non-spherical nanoparticle shape stability compared to nanoparticles fabricated by other stabilizers, purely nanoprecipitation method, different materials and manufacturing technique. It appears that the residual stabilizers can be a great companion for nanoparticles in maintaining their non-sphericity, if they are considered as a non-toxic, biodegradable, and biocompatible material.

6. Acknowledgements

DAAD (Deutscher Akademischer Austauschdienst) is highly thanked for BMH's scholarship. The authors would like to thank Christian Minke (Department of Chemistry, Ludwig-Maximilians-Universität München, Germany) for the comprehensive and restless SEM-EDX assistance. Robert Eicher-Susanne Ebert, Jaroslava Obel (Central Analytics, Faculty of Chemistry and Pharmacy, Ludwig-Maximilians-Universität München, Germany) and Christine Sternkopf (group of Professor Christoph Haisch, Institute of Hydrochemistry, Chair of Analytical Chemistry and Water Chemistry, Technische Universität München, Germany) are kindly acknowledged for measurement of elemental analysis (oxygen combustion, ICP-AES, and ICP-MS respectively). The respectful gratitude is expressed to Aldrian Obaja Muis (Language Technologies Institute, Carnegie Mellon University, USA) for the fruitful discussion, suggestion, and validation of Supplemental Calculation. The authors are grateful to Raisa M. R. Yogiaman for the creation of the illustrations.

7. References

[1] G. Birrenbach, P. P. Speiser, *J. Pharm. Sci.* **1976**, *65*, 1763; V. Lenaerts, P. Couvreur, D. Christiaens-Leyh, E. Joiris, M. Roland, B. Rollman, P. Speiser, *Biomaterials* **1984**, *5*, 65; H. Fessi, J. P.

Devissaguet, F. Puisieux, C. Thies, *French patent* **1986**, *2*, 988; R. H. Müller, C. Lherm, J. Herbert, P. Couvreur, *Biomaterials* **1990**, *11*, 590; M. Klinger-Strobel, J. Ernst, C. Lautenschläger, M. W. Pletz, D. Fischer, O. Makarewicz, *Int. J. Nanomed.* **2016**, *11*, 575; A. C. Anselmo, S. Mitragotri, *Bioeng. Transl. Med.* **2016**, *1*, 10.

[2] D. Klose, F. Siepmann, K. Elkharraz, J. Siepmann, *Int. J. Pharm.* **2008**, *354*, 95.

[3] S. M. Moghimi, A. C. Hunter, J. C. Murray, *Pharmacol. Rev.* **2001**, *53*, 283.

[4] P. P. Wibroe, A. C. Anselmo, P. H. Nilsson, A. Sarode, V. Gupta, R. Urbanics, J. Szebeni, A. C. Hunter, S. Mitragotri, T. E. Mollnes, S. M. Moghimi, *Nat. Nanotechnol.* **2017**, *12*, 589.

[5] W. Lu, T. G. Park, *PDA J. Pharm. Sci. Technol.* **1995**, *49*, 13; W. L. Lee, Y. C. Seh, E. Widjaja, H. C. Chong, N. S. Tan, S. C. Joachim Loo, *J. Pharm. Sci.* **2012**, *101*, 2787.

[6] R. Mathaes, G. Winter, T. J. Siahaan, A. Besheer, J. Engert, *Eur. J. Pharm. Biopharm.* **2015**, *94*, 542.

[7] C. A. Fromen, T. B. Rahhal, G. R. Robbins, M. P. Kai, T. W. Shen, J. C. Luft, J. M. DeSimone, *Nanomedicine (N. Y., NY, U. S.)* **2016**, *12*, 677.

[8] R. Mathaes, G. Winter, A. Besheer, J. Engert, *Int. J. Pharm.* **2014**, *465*, 159.

[9] R. A. Meyer, J. C. Sunshine, K. Perica, A. K. Kosmides, K. Aje, J. P. Schneck, J. J. Green, *Small* **2015**, *11*, 1519.

[10] R. Agarwal, V. Singh, P. Jurney, L. Shi, S. V. Sreenivasan, K. Roy, *Proc. Natl. Acad. Sci. U. S. A.* **2013**, *110*, 17247.

[11] C. C. Ho, A. Keller, J. A. Odell, R. H. Ottewill, *Colloid. Polym. Sci.* **1993**, *271*, 469.

[12] J. A. Champion, Y. K. Katare, S. Mitragotri, *J. Controlled Release* **2007**, *121*, 3.

[13] B. Felder, *Helv. Chim. Acta* **1966**, *49*, 440.

[14] L. C. Glangchai, M. Caldorera-Moore, L. Shi, K. Roy, *J. Controlled Release* **2008**, *125*, 263.

[15] R. Agarwal, V. Singh, P. Jurney, L. Shi, S. V. Sreenivasan, K. Roy, *ACS Nano* **2012**, *6*, 2524.

[16] V. Singh, R. Agarwal, P. Jurney, K. Marshall, K. Roy, L. Shi, S. V. Sreenivasan, *J. Micro. Nanomanuf.* **2015**, *3*, 011002.

[17] J. P. Rolland, B. W. Maynor, L. E. Euliss, A. E. Exner, G. M. Denison, J. M. DeSimone, *J. Am. Chem. Soc.* **2005**, *127*, 10096; E. M. Enlow, J. C. Luft, M. E. Napier, J. M. DeSimone, *Nano Lett.* **2011**, *11*, 808; S. W. Morton, K. P. Herlihy, K. E. Shopsowitz, Z. J. Deng, K. S. Chu, C. J. Bowerman, J. M. DeSimone, P. T. Hammond, *Adv. Mater.* **2013**, *25*, 4707; J. M. DeSimone, *J. Controlled Release* **2016**, *240*, 541.

[18] S. Xu, Z. Nie, M. Seo, P. Lewis, E. Kumacheva, H. A. Stone, P. Garstecki, D. B. Weibel, I. Gitlin, G. M. Whitesides, *Angew. Chem. Int. Ed.* **2005**, *44*, 724; N. Hakimi, S. S. H. Tsai, C.-H. Cheng, D. K.

Hwang, *Adv. Mater.* **2014**, *26*, 1393; K. S. Paulsen, D. Di Carlo, A. J. Chung, *Nat. Commun.* **2015**, *6*, 6976; C. Hamon, M. Henriksen-Lacey, A. La Porta, M. Rosique, J. Langer, L. Scarabelli, A. B. S. Montes, G. González-Rubio, M. M. de Pancorbo, L. M. Liz-Marzán, L. Basabe-Desmonts, *Adv. Funct. Mater.* **2016**, *26*, 8053.

[19] J. A. Champion, S. Mitragotri, *Proc. Natl. Acad. Sci. U. S. A.* **2006**, *103*, 4930.

[20] J. A. Champion, S. Mitragotri, *Pharm. Res.* **2009**, *26*, 244; Arnida, M. M. Janát-Amsbury, A. Ray, C. M. Peterson, H. Ghandehari, *Eur. J. Pharm. Biopharm.* **2011**, *77*, 417.

[21] G. Sharma, D. T. Valenta, Y. Altman, S. Harvey, H. Xie, S. Mitragotri, J. W. Smith, *J. Controlled Release* **2010**, *147*, 408.

[22] J. C. Sunshine, K. Perica, J. P. Schneck, J. J. Green, *Biomaterials* **2014**, *35*, 269.

[23] J. E. Mark, *Polymer Data Handbook*, Oxford University Press, Oxford **1999**.

[24] B. K. Lee, Y. Yun, K. Park, *Adv. Drug Delivery Rev.* **2016**, *107*, 176.

[25] H. Fessi, F. Puisieux, J. P. Devissaguet, N. Ammoury, S. Benita, *Int. J. Pharm.* **1989**, *55*, R1.

[26] J.-W. Yoo, S. Mitragotri, *Proc. Natl. Acad. Sci. U. S. A.* **2010**, *107*, 11205.

[27] A. Bootz, V. Vogel, D. Schubert, J. Kreuter, *Eur. J. Pharm. Biopharm.* **2004**, *57*, 369.

[28] A. C. Anselmo, B. Prabhakarpandian, K. Pant, S. Mitragotri, *Transl. Mater. Res.* **2017**, *4*, 014001; J. Hrkach, D. Von Hoff, M. M. Ali, E. Andrianova, J. Auer, T. Campbell, D. De Witt, M. Figa, M. Figueiredo, A. Horhota, S. Low, K. McDonnell, E. Peeke, B. Retnarajan, A. Sabnis, E. Schnipper, J. J. Song, Y. H. Song, J. Summa, D. Tompsett, G. Troiano, T. Van Geen Hoven, J. Wright, P. LoRusso, P. W. Kantoff, N. H. Bander, C. Sweeney, O. C. Farokhzad, R. Langer, S. Zale, *Sci. Transl. Med.* **2012**, *4*, 128ra39.

[29] Polysciences; Inc, Polybead® Microspheres, Product Information (http://www.polysciences.com/skin/frontend/default/polysciences/pdf/Polybead_Microspheres.pdf), Warrington **2011**, 2 (accessed: July 2019).

[30] P. Zhang, L. Yang, Q. Li, S. Wu, S. Jia, Z. Li, Z. Zhang, L. Shi, *ACS Appl. Mater. Interfaces* **2017**, *9*, 7648.

[31] R. Dorati, M. Patrini, P. Perugini, F. Pavanetto, A. Stella, T. Modena, I. Genta, B. Conti, *J. Microencapsulation* **2006**, *23*, 123.

[32] S. Tan, R. L. Sherman, W. T. Ford, *Langmuir* **2004**, *20*, 7015.

[33] N. Doshi, A. S. Zahr, S. Bhaskar, J. Lahann, S. Mitragotri, *Proc. Natl. Acad. Sci. U. S. A.* **2009**, *106*, 21495.

[34] M. P. Neubauer, C. Blum, E. Agostini, J. Engert, T. Scheibel, A. Fery, *Biomater. Sci.* **2013**, *1*, 1160.

[35] X. Han, S. Chen, X. Hu, *Desalination* **2009**, *240*, 21.

[36] R. Dingreville, J. Qu, C. Mohammed, *J. Mech. Phys. Solids* **2005**, *53*, 1827.

[37] P.-C. Lin, S. Yang, *Soft Matter* **2009**, *5*, 1011.

[38] M. W. Lee, S. S. Latthe, A. L. Yarin, S. S. Yoon, *Langmuir* **2013**, *29*, 7758; A. Opdahl, G. A. Somorjai, *J. Polym. Sci., Part B: Polym. Phys.* **2001**, *39*, 2263.

[39] R. Steendam, M. J. van Steenbergen, W. E. Hennink, H. W. Frijlink, C. F. Lerk, *J. Controlled Release* **2001**, *70*, 71.

[40] P. Blasi, S. S. D'Souza, F. Selmin, P. P. DeLuca, *J. Controlled Release* **2005**, *108*, 1.

[41] C. Zhang, Y. Guo, R. D. Priestley, *Macromolecules* **2011**, *44*, 4001.

[42] U. Gaur, B. Wunderlich, *Macromolecules* **1980**, *13*, 1618.

[43] T. Sasaki, A. Shimizu, T. H. Mourey, C. T. Thurau, M. Ediger, *J. Chem. Phys.* **2003**, *119*, 8730.

[44] V. Le Brun, W. Friess, S. Bassarab, P. Garidel, *Pharm. Dev. Technol.* **2010**, *15*, 421.

[45] B. Semete, L. Booysen, Y. Lemmer, L. Kalombo, L. Katata, J. Verschoor, H. S. Swai, *Nanomedicine (N. Y., NY, U. S.)* **2010**, *6*, 662.

[46] T. R. Fadel, E. R. Steenblock, E. Stern, N. Li, X. Wang, G. L. Haller, L. D. Pfefferle, T. M. Fahmy, *Nano Lett.* **2008**, *8*, 2070.

[47] N. Sugita, K.-i. Kawabata, K. Sasaki, I. Sakata, S.-i. Umemura, *Bioconjugate Chem.* **2007**, *18*, 866.

[48] W. Alewelt, *Technische Thermoplaste. 4. Polyamide*, Hanser, Munich, Germany **1998**.

[49] D. P. Joshi, Y. L. Lan-Chun-Fung, J. G. Pritchard, *Anal. Chim. Acta* **1979**, *104*, 153.

[50] K. M. Shakesheff, C. Evora, I. Soriano, R. Langer, *J. Colloid Interface Sci.* **1997**, *185*, 538.

[51] R. Defay, A. Bellemans, I. Prigogine, *Surface tension and adsorption*, Longmans, London **1966**; R. J. Hunter, *Foundations of Colloid Science*, Oxford University, **2001**.

[52] Q. Cai, Z.-S. Luo, W.-Q. Pang, Y.-W. Fan, X.-H. Chen, F.-Z. Cui, *Chem. Mater.* **2001**, *13*, 258; J. G. Croissant, Y. Fatieiev, N. M. Khashab, *Adv. Mater.* **2017**, *29*, 1604634; F. Tang, L. Li, D. Chen, *Adv. Mater.* **2012**, *24*, 1504; N. Hao, L. Li, F. Tang, *Int. Mater. Rev.* **2017**, *62*, 57; X. Yang, D. He, X. He, K. Wang, J. Tang, Z. Zou, X. He, J. Xiong, L. Li, J. Shangguan, *ACS Appl. Mater. Interfaces* **2016**, *8*, 20558.

[53] S. Huh, J. W. Wiench, J.-C. Yoo, M. Pruski, V. S. Y. Lin, *Chem. Mater.* **2003**, *15*, 4247.

[54] T. Yu, A. Malugin, H. Ghandehari, *ACS Nano* **2011**, *5*, 5717.

[55] L. Li, T. Liu, C. Fu, L. Tan, X. Meng, H. Liu, *Nanomedicine (N. Y., NY, U. S.)* **2015**, *11*, 1915.

[56] J. Saikia, M. Yazdimamaghani, S. P. Hadipour Moghaddam, H. Ghandehari, *ACS Appl. Mater. Interfaces* **2016**, *8*, 34820.

[57] N. Hao, H. Liu, L. Li, D. Chen, L. Li, F. Tang, *J. Nanosci. Nanotechnol.* **2012**, *12*, 6346.

[58] R. C. Rowe, P. J. Sheskey, W. G. Cook, M. E. Fenton, *Handbook of Pharmaceutical Excipients*, Pharmaceutical Press, London, UK **2012**.

[59] C. Wong, R. S. Bollampally, *J. Appl. Polym. Sci.* **1999**, *74*, 3396.

[60] Y. Hoshikawa, H. Yabe, A. Nomura, T. Yamaki, A. Shimojima, T. Okubo, *Chem. Mater.* **2010**, *22*, 12; A. M. Lipski, C. Jaquiery, H. Choi, D. Eberli, M. Stevens, I. Martin, I. W. Chen, V. P. Shastri, *Adv. Mater.* **2007**, *19*, 553; Y. Wei, D. Jin, D. J. Brennan, D. N. Rivera, Q. Zhuang, N. J. DiNardo, K. Qiu, *Chem. Mater.* **1998**, *10*, 769; J. Moghal, J. Kobler, J. Sauer, J. Best, M. Gardener, A. A. R. Watt, G. Wakefield, *ACS Appl. Mater. Interfaces* **2012**, *4*, 854.

[61] J.-Y. Choi, C. H. Park, J. Lee, *Drug Delivery* **2008**, *15*, 347.

[62] G. Costabile, I. d'Angelo, G. Rampioni, R. Bondì, B. Pompili, F. Ascenzioni, E. Mitidieri, R. d'Emmanuele di Villa Bianca, R. Sorrentino, A. Miro, F. Quaglia, F. Imperi, L. Leoni, F. Ungaro, *Mol. Pharmaceutics* **2015**, *12*, 2604.

[63] M. Kakran, R. Shegokar, N. G. Sahoo, L. Al Shaal, L. Li, R. H. Müller, *Eur. J. Pharm. Biopharm.* **2012**, *80*, 113.

[64] S. Barua, J.-W. Yoo, P. Kolhar, A. Wakankar, Y. R. Gokarn, S. Mitragotri, *Proc. Natl. Acad. Sci. U. S. A.* **2013**, *110*, 3270.

[65] C. Wischke, M. Schossig, A. Lendlein, *Small* **2014**, *10*, 83.

[66] D. M. Le, K. Kulangara, A. F. Adler, K. W. Leong, V. S. Ashby, *Adv. Mater.* **2011**, *23*, 3278.

[67] J. A. Champion, Y. K. Katare, S. Mitragotri, *Proc. Natl. Acad. Sci. U. S. A.* **2007**, *104*, 11901.

[68] R. A. Meyer, R. S. Meyer, J. J. Green, *J. Biomed. Mater. Res., Part A* **2015**, *103*, 2747.

[69] L. Chen, Z. Tian, Y. Du, *Biomaterials* **2004**, *25*, 3725.

[70] M. Caldorera-Moore, M. K. Kang, Z. Moore, V. Singh, S. V. Sreenivasan, L. Shi, R. Huang, K. Roy, *Soft Matter* **2011**, *7*, 2879.

[71] T. J. Merkel, K. Chen, S. W. Jones, A. A. Pandya, S. Tian, M. E. Napier, W. E. Zamboni, J. M. DeSimone, *J. Controlled Release* **2012**, *162*, 37.

[72] K. Chen, T. J. Merkel, A. Pandya, M. E. Napier, J. C. Luft, W. Daniel, S. Sheiko, J. M. DeSimone, *Biomacromolecules* **2012**, *13*, 2748.

[73] T. J. Merkel, S. W. Jones, K. P. Herlihy, F. R. Kersey, A. R. Shields, M. Napier, J. C. Luft, H. Wu, W. C. Zamboni, A. Z. Wang, J. E. Bear, J. M. DeSimone, *Proc. Natl. Acad. Sci. U. S. A.* **2011**, *108*, 586.

[74] F. R. Kersey, T. J. Merkel, J. L. Perry, M. E. Napier, J. M. DeSimone, *Langmuir* **2012**, *28*, 8773.

[75] K. Chen, J. Xu, J. C. Luft, S. Tian, J. S. Raval, J. M. DeSimone, *J. Am. Chem. Soc.* **2014**, *136*, 9947.

[76] J. L. Perry, K. G. Reuter, J. C. Luft, C. V. Pecot, W. Zamboni, J. M. DeSimone, *Nano Lett.* **2017**, *17*, 2879.

[77] K. J. Geh, M. Hubert, G. Winter, *J. Microencapsulation* **2016**, *33*, 595.

[78] S. A. Khan, M. Schneider, *Macromol. Biosci.* **2014**, *14*, 1627.

[79] P. Jurney, R. Agarwal, V. Singh, D. Choi, K. Roy, S. V. Sreenivasan, L. Shi, *J. Controlled Release* **2017**, *245*, 170.

[80] J. Zidek, J. Jancar, A. Milchev, T. A. Vilgis, *Macromolecules* **2014**, *47*, 8795.

[81] Y. Dong, Y. Ruan, H. Wang, Y. Zhao, D. Bi, *J. Appl. Polym. Sci.* **2004**, *93*, 1553; F. S. Kittur, K. V. Harish Prashanth, K. Udaya Sankar, R. N. Tharanathan, *Carbohydr. Polym.* **2002**, *49*, 185.

[82] J. A. Champion, S. Mitragotri, in *Advances in Regenerative Medicine: Role of Nanotechnology, and Engineering Principles*, (Ed: V. P. Shastri, Altankov, G., Lendlein, A.), Springer, Dordrecht, Netherlands **2010**, 301.

[83] K. M. Keville, E. I. Franses, J. M. Caruthers, *J. Colloid Interface Sci.* **1991**, *144*, 103.

[84] D. A. Canelas, K. P. Herlihy, J. M. DeSimone, *Wiley Interdiscip. Rev.: Nanomed. Nanobiotechnol.* **2009**, *1*, 391.

[85] D. K. Hwang, J. Oakey, M. Toner, J. A. Arthur, K. S. Anseth, S. Lee, A. Zeiger, K. J. Van Vliet, P. S. Doyle, *J. Am. Chem. Soc.* **2009**, *131*, 4499.

[86] A. C. Anselmo, M. Zhang, S. Kumar, D. R. Vogus, S. Menegatti, M. E. Helgeson, S. Mitragotri, *ACS Nano* **2015**, *9*, 3169.

[87] A. Kyritsis, P. Pissis, J. L. Gómez Ribelles, M. Monleón Pradas, *J. Non-Cryst. Solids* **1994**, *172*, 1041.

[88] S. Kalakkunnath, D. S. Kalika, H. Lin, B. D. Freeman, *J. Polym. Sci., Part B: Polym. Phys.* **2006**, *44*, 2058.

[89] M. Caldorera-Moore, *Vol. Doctoral Dissertation*, The University of Texas at Austin, Austin, Texas, USA **2010**.

[90] C. H. Kapadia, S. Tian, J. L. Perry, J. C. Luft, J. M. DeSimone, *Mol. Pharmaceutics* **2016**, *13*, 3381.

[91] E. Riande, J. Guzmán, *Macromolecules* **1996**, *29*, 1728.

[92] S. Schubert, J. J. T. Delaney, U. S. Schubert, *Soft Matter* **2011**, *7*, 1581.

[93] C.-M. J. Hu, L. Zhang, S. Aryal, C. Cheung, R. H. Fang, L. Zhang, *Proc. Natl. Acad. Sci. U. S. A.* **2011**, *108*, 10980.

[94] P. Legrand, S. Lesieur, A. Bochot, R. Gref, W. Raatjes, G. Barratt, C. Vauthier, *Int. J. Pharm.* **2007**, *344*, 33.

[95] C.-M. J. Hu, R. H. Fang, J. Copp, B. T. Luk, L. Zhang, *Nat. Nanotechnol.* **2013**, *8*, 336; C.-M. J. Hu, R. H. Fang, B. T. Luk, L. Zhang, *Nat. Nanotechnol.* **2013**, *8*, 933.

[96] L. M. Cox, J. P. Killgore, Z. Li, R. Long, A. W. Sanders, J. Xiao, Y. Ding, *Langmuir* **2016**, *32*, 3691.

[97] B. Xu, Y. Q. Fu, M. Ahmad, J. K. Luo, W. M. Huang, A. Kraft, R. Reuben, Y. T. Pei, Z. G. Chen, J. T. M. De Hosson, *J. Mater. Chem.* **2010**, *20*, 3442.

[98] C. Palazzo, G. Ponchel, J. J. Vachon, S. Villebrun, F. Agnely, C. Vauthier, *Int. J. Polym. Mater. Polym. Biomater.* **2016**, *66*, 416.

[99] R. Mathaes, *Dissertation of Ludwig-Maximilians-Universität München, Germany* **2015**.

[100] M. Nagy, A. Keller, *Polym. Commun.* **1989**, *30*, 130.

[101] E. Enlow, *Vol. Doctoral Dissertation*, The University of North Carolina at Chapel Hill, **2010**; T. J. Merkel, *Vol. Doctoral Dissertation*, The University of North Carolina at Chapel Hill, **2011**; A. L. Galloway, A. Murphy, J. M. DeSimone, J. Di, J. P. Herrmann, M. E. Hunter, J. P. Kindig, F. J. Malinoski, M. A. Rumley, D. M. Stoltz, T. S. Templeman, B. Hubby, *Nanomedicine (N. Y., NY, U. S.)* **2013**, *9*, 523; K. Chen, *Vol. Doctoral Dissertation*, The University of North Carolina at Chapel Hill, **2013**.

[102] A. Besheer, J. Vogel, D. Glanz, J. Kressler, T. Groth, K. Mäder, *Mol. Pharmaceutics* **2009**, *6*, 407.

[103] H. M. Redhead, S. S. Davis, L. Illum, *J. Controlled Release* **2001**, *70*, 353.

[104] J. C. Neal, S. Stolnik, E. Schacht, E. R. Kenawy, M. C. Garnett, S. S. Davis, L. Illum, *J. Pharm. Sci.* **1998**, *87*, 1242.

[105] P. D. Scholes, A. G. A. Coombes, L. Illum, S. S. Davis, J. F. Watts, C. Ustariz, M. Vert, M. C. Davies, *J. Controlled Release* **1999**, *59*, 261.

[106] S. Staufenbiel, C. M. Keck, R. H. Müller, *Macromol. Symp.* **2014**, *345*, 32.

[107] L. Mu, S. S. Feng, *J. Controlled Release* **2002**, *80*, 129.

[108] K. Rechendorff, M. B. Hovgaard, M. Foss, V. P. Zhdanov, F. Besenbacher, *Langmuir* **2006**, *22*, 10885.

[109] T. Cedervall, I. Lynch, S. Lindman, T. Berggård, E. Thulin, H. Nilsson, K. A. Dawson, S. Linse, *Proc. Natl. Acad. Sci. U. S. A.* **2007**, *104*, 2050; F. Bertoli, D. Garry, M. P. Monopoli, A. Salvati, K. A. Dawson, *ACS Nano* **2016**, *10*, 10471.

[110] M. Hadjidemetriou, Z. Al-Ahmady, M. Mazza, R. F. Collins, K. Dawson, K. Kostarelos, *ACS Nano* **2015**, *9*, 8142.

[111] M. Hadjidemetriou, Z. Al-Ahmady, K. Kostarelos, *Nanoscale* **2016**, *8*, 6948.

[112] Y. Rharbi, *Phys. Rev. E* **2008**, *77*, 031806.

[113] D. Christie, C. Zhang, J. Fu, B. Koel, R. D. Priestley, *J. Polym. Sci., Part B: Polym. Phys.* **2016**, *54*, 1776.

[114] B. Bittner, M. Morlock, H. Koll, G. Winter, T. Kissel, *Eur. J. Pharm. Biopharm.* **1998**, *45*, 295.

[115] T. Unruh, H. Bunjes, K. Westesen, M. H. J. Koch, *J. Phys. Chem. B* **1999**, *103*, 10373.

[116] K. Westesen, H. Bunjes, *Int. J. Pharm.* **1995**, *115*, 129.

[117] G. Schmid, B. Corain, *Eur. J. Inorg. Chem.* **2003**, *2003*, 3081; P. Buffat, J. P. Borel, *Phys. Rev. A* **1976**, *13*, 2287.

[118] R. García-Álvarez, M. Hadjidemetriou, A. Sánchez-Iglesias, L. M. Liz-Marzán, K. Kostarelos, *Nanoscale* **2018**, *10*, 1256.

[119] M. Takagi, *J. Phys. Soc. Jpn.* **1954**, *9*, 359.

[120] Y. Yamamoto, K. Yasugi, A. Harada, Y. Nagasaki, K. Kataoka, *J. Controlled Release* **2002**, *82*, 359.

[121] Clariant; GmbH, (Ed: Clariant), Mowiol®: Polyvinyl Alcohol, Commserv, Sulzbach **1999**.

[122] R. Ricciardi, F. Auriemma, C. De Rosa, F. Lauprêtre, *Macromolecules* **2004**, *37*, 1921.

[123] Y. Bin, Y. Tanabe, C. Nakabayashi, H. Kurosu, M. Matsuo, *Polymer* **2001**, *42*, 1183.

[124] C. Bouissou, J. J. Rouse, R. Price, C. F. van der Walle, *Pharm. Res.* **2006**, *23*, 1295.

[125] M. Thielen, K. Hartwig, P. Gust, *Blasformen von Kunststoffhohlkörpern*, Hanser, Munich, Germany **2006**.

[126] W. Weißbach, M. Dahms, *Werkstoffkunde: Strukturen, Eigenschaften, Prüfung*, Vieweg+Teubner Verlag, Wiesbaden, Germany **2007**.

[127] D. Quintanar-Guerrero, A. Ganem-Quintanar, E. Allémann, H. Fessi, E. Doelker, *J. Microencapsulation* **1998**, *15*, 107.

[128] M. A. Repka, J. W. McGinity, *Int. J. Pharm.* **2000**, *202*, 63.

[129] R. Gref, A. Domb, P. Quellec, T. Blunk, R. H. Müller, J. M. Verbavatz, R. Langer, *Adv. Drug Delivery Rev.* **1995**, *16*, 215.

[130] I. M. F. Campos, T. M. Santos, G. M. F. Cunha, K. M. M. N. Silva, R. Z. Domingues, A. da Silva Cunha Júnior, K. C. de Souza Figueiredo, *J. Appl. Polym. Sci.* **2014**, *131*, 41199 (1.

[131] F. Siepmann, V. Le Brun, J. Siepmann, *J. Controlled Release* **2006**, *115*, 298; E. Piñón-Segundo, A. Ganem-Quintanar, V. Alonso-Pérez, D. Quintanar-Guerrero, *Int. J. Pharm.* **2005**, *294*, 217.

[132] L. Mu, S.-S. Feng, *Pharm. Res.* **2003**, *20*, 1864.

[133] L. Mu, S. S. Feng, *J. Controlled Release* **2003**, *86*, 33.

[134] M. F. Zambaux, F. Bonneaux, R. Gref, P. Maincent, E. Dellacherie, M. J. Alonso, P. Labrude, C. Vigneron, *J. Controlled Release* **1998**, *50*, 31.

[135] S. C. Lee, J. T. Oh, M. H. Jang, S. I. Chung, *J. Controlled Release* **1999**, *59*, 123.

[136] I. M. Adjei, B. Sharma, C. Peetla, V. Labhasetwar, *J. Controlled Release* **2016**, *232*, 83.

[137] W. Abdelwahed, G. Degobert, H. Fessi, *Int. J. Pharm.* **2006**, *309*, 178.

[138] Y. Lu, Y. Yin, Y. Xia, *Adv. Mater.* **2001**, *13*, 271.

[139] A. Banerjee, J. Qi, R. Gogoi, J. Wong, S. Mitragotri, *J. Controlled Release* **2016**, *238*, 176.

[140] O. Cauchois, *Vol. Doctoral Dissertation*, Université Paris Sud - Paris XI, **2011**.

[141] H.-A. Klok, J. F. Langenwalter, S. Lecommandoux, *Macromolecules* **2000**, *33*, 7819.

[142] O. Cauchois, F. Segura-Sanchez, G. Ponchel, *Int. J. Pharm.* **2013**, *452*, 292.

[143] T. Jaworek, D. Neher, G. Wegner, R. H. Wieringa, A. J. Schouten, *Science* **1998**, *279*, 57.

[144] P. Papadopoulos, G. Floudas, I. Schnell, T. Aliferis, H. Iatrou, N. Hadjichristidis, *Biomacromolecules* **2005**, *6*, 2352.

[145] J. Tamayo, R. García, *Langmuir* **1996**, *12*, 4430.

[146] C. Q. Sun, *Prog. Solid State Chem.* **2007**, *35*, 1.

[147] Z. Yang, W. T. S. Huck, S. M. Clarke, A. R. Tajbakhsh, E. M. Terentjev, *Nat. Mater.* **2005**, *4*, 486.

[148] W. L. Lee, H. Y. Low, *Sci. Rep.* **2016**, *6*, 23686.

[149] Y. Wu, K. Wang, H. Tan, J. Xu, J. Zhu, *Langmuir* **2017**.

[150] R. Deng, F. Liang, W. Li, Z. Yang, J. Zhu, *Macromolecules* **2013**, *46*, 7012.

[151] I. Amin, M. Steenackers, N. Zhang, A. Beyer, X. Zhang, T. Pirzer, T. Hugel, R. Jordan, A. Gölzhäuser, *Small* **2010**, *6*, 1623.

[152] T. Dequivre, E. Al Alam, J. Plathier, A. Ruediger, G. Brisard, S. Charlebois, *ECS Trans.* **2015**, *69*, 91.

[153] H. Petrova, J. Perez-Juste, Z. Zhang, J. Zhang, T. Kosel, G. V. Hartland, *J. Mater. Chem.* **2006**, *16*, 3957.

[154] P. F. Kelly, *Properties of Materials*, CRC Press, **2014**.

[155] R. Hoogenboom, *Macromol. Chem. Phys.* **2007**, *208*, 18.

[156] A. C. Moffat, Osselton, M.D. and Widdop, B., *Clarke's Analysis of Drugs and Poisons: in Pharmaceuticals, Body Fluids and Postmortem Material*, Pharmaceutical Press, London **2011**.

[157] S. Lück, R. Schubel, J. Rüb, D. Hahn, E. Mathieu, H. Zimmermann, D. Scharnweber, C. Werner, S. Pautot, R. Jordan, *Biomaterials* **2016**, *79*, 1.

[158] A. Schulz, S. Jaksch, R. Schubel, E. Wegener, Z. Di, Y. Han, A. Meister, J. Kressler, A. V. Kabanov, R. Luxenhofer, C. M. Papadakis, R. Jordan, *ACS Nano* **2014**, *8*, 2686.

[159] Y. Han, Z. He, A. Schulz, T. K. Bronich, R. Jordan, R. Luxenhofer, A. V. Kabanov, *Mol. Pharmaceutics* **2012**, *9*, 2302.

[160] H. Bunjes, F. Steiniger, W. Richter, *Langmuir* **2007**, *23*, 4005.

[161] S. Hatziantoniou, G. Deli, Y. Nikas, C. Demetzos, G. T. Papaioannou, *Micron* **2007**, *38*, 819; H. Bunjes, M. H. J. Koch, K. Westesen, *J. Pharm. Sci.* **2003**, *92*, 1509.

[162] K. Göke, E. Roese, A. Arnold, J. Kuntsche, H. Bunjes, *Mol. Pharmaceutics* **2016**, *13*, 3187.

[163] C. Freitas, R. H. Müller, *Int. J. Pharm.* **1998**, *168*, 221.

[164] H. Bunjes, K. Westesen, M. H. J. Koch, *Int. J. Pharm.* **1996**, *129*, 159.

[165] F. Maleky, A. Marangoni, *Cryst. Growth Des.* **2011**, *11*, 2429.

[166] A. Radomska-Soukharev, *Adv. Drug Delivery Rev.* **2007**, *59*, 411.

[167] V. Krstic, U. Erb, G. Palumbo, *Scr. Metall. Mater.* **1993**, *29*, 1501.

[168] Q. Xu, A. Crossley, J. Czernuszka, *J. Pharm. Sci.* **2009**, *98*, 2377.

[169] R. Ni, U. Muenster, J. Zhao, L. Zhang, E.-M. Becker-Pelster, M. Rosenbruch, S. Mao, *J. Controlled Release* **2017**, *249*, 11; E. Allémann, J.-C. Leroux, R. Gurny, E. Doelker, *Pharm. Res.* **1993**, *10*, 1732.

[170] J. Shen, K. Lee, S. Choi, W. Qu, Y. Wang, D. J. Burgess, *Int. J. Pharm.* **2016**, *498*, 274.

[171] Z. Ma, J. Bai, Y. Wang, X. Jiang, *ACS Appl. Mater. Interfaces* **2014**, *6*, 2431.

[172] C. E. Hall, O. Hall, *Lab. Invest.* **1963**, *12*, 721.

[173] T. Yamaoka, Y. Tabata, Y. Ikada, *J. Pharm. Pharmacol.* **1995**, *47*, 479; Y. Jiang, A. Schädlich, E. Amado, C. Weis, E. Odermatt, K. Mäder, J. Kressler, *J. Biomed. Mater. Res., Part B* **2010**, *93B*, 275.

[174] U.S. Food & Drug Administration, *Vol. Inactive Ingredient Search for Approved Drug Products*, FDA/Center for Drug Evaluation and Research, Silver Spring, MD, USA **2017, https://www.accessdata.fda.gov/scripts/cder/iig/index.cfm (accessed: July 2019)**.

[175] E. Allémann, R. Gurny, E. Doelker, *Int. J. Pharm.* **1992**, *87*, 247.

[176] H. Ibrahim, C. Bindschaedler, E. Doelker, P. Buri, R. Gurny, *Int. J. Pharm.* **1992**, *87*, 239.

[177] Y. Dong, S.-S. Feng, *Int. J. Pharm.* **2007**, *342*, 208.

[178] M. N. V. Ravi Kumar, U. Bakowsky, C. M. Lehr, *Biomaterials* **2004**, *25*, 1771.

[179] R. V. Diaz, I. Soriano, A. Delgado, M. Llabrés, C. Evora, *J. Controlled Release* **1997**, *43*, 59.

[180] F. Yan, C. Zhang, Y. Zheng, L. Mei, L. Tang, C. Song, H. Sun, L. Huang, *Nanomedicine (N. Y., NY, U. S.)* **2010**, *6*, 170; Y. Dong, S.-S. Feng, *Biomaterials* **2005**, *26*, 6068; R. Gurny, N. A. Peppas, D. D. Harrington, G. S. Banker, *Drug Dev. Ind. Pharm.* **1981**, *7*, 1.

[181] P. Bihari, M. Vippola, S. Schultes, M. Praetner, A. G. Khandoga, C. A. Reichel, C. Coester, T. Tuomi, M. Rehberg, F. Krombach, *Part. Fibre Toxicol.* **2008**, *5*, 14.

[182] E. Allémann, J.-C. Leroux, R. Gurny, E. Doelker, *Eur. J. Pharm. Biopharm.* **1993**, *39*, 13; Y. N. Konan, R. Gurny, E. Allémann, *Int. J. Pharm.* **2002**, *233*, 239.

[183] H. J. van den Hul, J. W. Vanderhoff, *Br. Polym. J.* **1970**, *2*, 121.

[184] R. H. Müller, D. Rühl, M. Lück, B.-R. Paulke, *Pharm. Res.* **1997**, *14*, 18.

[185] D. Q. M. Craig, *Thermochim. Acta* **1995**, *248*, 189.

[186] Z. Chen, Z. Liu, F. Qian, *Mol. Pharmaceutics* **2015**, *12*, 590.

[187] J. Rühe, in *Polymer Brushes*, Wiley-VCH Verlag GmbH & Co. KGaA, Weinheim, Germany **2005**, 1.

[188] S. M. Moghimi, J. Szebeni, *Prog. Lipid Res.* **2003**, *42*, 463.

[189] I. Hamad, O. Al-Hanbali, A. C. Hunter, K. J. Rutt, T. L. Andresen, S. M. Moghimi, *ACS Nano* **2010**, *4*, 6629.

[190] M. Malmsten, B. Lassen, J. Westin, C.-G. Gölander, R. Larsson, U. R. Nilsson, *J. Colloid Interface Sci.* **1996**, *179*, 163.

[191] D. E. Owens III, N. A. Peppas, *Int. J. Pharm.* **2006**, *307*, 93.

[192] K. Sempf, T. Arrey, S. Gelperina, T. Schorge, B. Meyer, M. Karas, J. Kreuter, *Eur. J. Pharm. Biopharm.* **2013**, *85*, 53.

[193] M. S. Singh, A. Lamprecht, *Drug Dev. Ind. Pharm.* **2016**, *42*, 325.

[194] D. Quintanar-Guerrero, H. Fessi, E. Allémann, E. Doelker, *Int. J. Pharm.* **1996**, *143*, 133.

[195] E. Tyrode, M. W. Rutland, C. D. Bain, *J. Am. Chem. Soc.* **2008**, *130*, 17434.

[196] T. Sun, Y. S. Zhang, B. Pang, D. C. Hyun, M. Yang, Y. Xia, *Angew. Chem. Int. Ed.* **2014**, *53*, 12320.

[197] A. M. Alkilany, C. J. Murphy, *J. Nanopart. Res.* **2010**, *12*, 2313.

[198] M. Tebbe, C. Kuttner, M. Männel, A. Fery, M. Chanana, *ACS Appl. Mater. Interfaces* **2015**, *7*, 5984.

[199] C. Rulison, *KRUSS Application Report AR260e* **2007**, 1.

[200] P. Ertl, B. Rohde, P. Selzer, *J. Med. Chem.* **2000**, *43*, 3714.

[201] I. Tuñón, E. Silla, J. L. Pascual-Ahuir, *Protein Eng., Des. Sel.* **1992**, *5*, 715.

[202] S. E. Feller, R. M. Venable, R. W. Pastor, *Langmuir* **1997**, *13*, 6555.

[203] K. Palm, P. Stenberg, K. Luthman, P. Artursson, *Pharm. Res.* **1997**, *14*, 568.

[204] S. V. F. Hansen, E. Christiansen, C. Urban, B. D. Hudson, C. J. Stocker, M. E. Due-Hansen, E. T. Wargent, B. Shimpukade, R. Almeida, C. S. Ejsing, M. A. Cawthorne, M. U. Kassack, G. Milligan, T. Ulven, *J. Med. Chem.* **2016**, *59*, 2841.

[205] B. Lee, F. M. Richards, *J. Mol. Biol.* **1971**, *55*, 379.

[206] J. Kelder, P. D. J. Grootenhuis, D. M. Bayada, L. P. C. Delbressine, J.-P. Ploemen, *Pharm. Res.* **1999**, *16*, 1514.

[207] D. E. Clark, *J. Pharm. Sci.* **1999**, *88*, 815.

[208] W. C. Griffin, *J. Soc. Cosmet. Chem.* **1949**, *1*, 311.

[209] L. Mu, P.-H. Seow, S.-N. Ang, S.-S. Feng, *Colloid. Polym. Sci.* **2004**, *283*, 58.

[210] P.-Å. Albertsson, in *Adv. Protein Chem.*, *Vol. 24* (Eds: C. B. Anfinsen, J. T. Edsall, F. M. Richards), Academic Press, **1970**, 309.

[211] R. H. Muller, S. S. Davis, L. Illum, E. Mak, in *Targeting of Drugs With Synthetic Systems*, (Eds: G. Gregoriadis, J. Senior, G. Poste), Springer US, Boston, MA **1986**, 239.

[212] S. Stolnik, C. R. Heald, J. Neal, M. C. Garnett, S. S. Davis, L. Illum, S. C. Purkis, R. J. Barlow, P. R. Gellert, *J. Drug Targeting* **2001**, *9*, 361; S. Stolnik, S. E. Dunn, M. C. Garnett, M. C. Davies, A. G. A. Coombes, D. C. Taylor, M. P. Irving, S. C. Purkiss, T. F. Tadros, S. S. Davis, L. Illum, *Pharm. Res.* **1994**, *11*, 1800.

[213] J. Cheng, B. A. Teply, I. Sherifi, J. Sung, G. Luther, F. X. Gu, E. Levy-Nissenbaum, A. F. Radovic-Moreno, R. Langer, O. C. Farokhzad, *Biomaterials* **2007**, *28*, 869.

[214] Y.-P. Li, Y.-Y. Pei, X.-Y. Zhang, Z.-H. Gu, Z.-H. Zhou, W.-F. Yuan, J.-J. Zhou, J.-H. Zhu, X.-J. Gao, *J. Controlled Release* **2001**, *71*, 203; Y. Choi, S. Yoon Kim, M.-H. Moon, S. Hee Kim, K.-S. Lee, Y. Byun, *Biomaterials* **2001**, *22*, 995.

[215] C. Li, E. Coons, A. Strachan, *Acta Mech. Sin.* **2014**, *225*, 1187; J. Bicerano, *Prediction of Polymer Properties*, CRC Press, **2002**.

[216] A. A. Metwally, R. M. Hathout, *Mol. Pharmaceutics* **2015**, *12*, 2800.

[217] M. S. Dresselhaus, G. Dresselhaus, P. C. Eklund, *Science of Fullerenes and Carbon Nanotubes: Their Properties and Applications*, Elsevier Science, **1996**.

[218] M. Treacy, T. Ebbesen, J. Gibson, *Nature* **1996**, *381*, 678.

[219] S. Iijima, *Nature* **1991**, *354*, 56.

[220] Y. Xiao, M. R. Wiesner, *J. Hazard. Mater.* **2012**, *215–216*, 146.

[221] J. A. Brant, J. Labille, J.-Y. Bottero, M. R. Wiesner, *Langmuir* **2006**, *22*, 3878.

[222] M. F. Islam, E. Rojas, D. M. Bergey, A. T. Johnson, A. G. Yodh, *Nano Lett.* **2003**, *3*, 269.

[223] D. K. Owens, R. C. Wendt, *J. Appl. Polym. Sci.* **1969**, *13*, 1741.

[224] B. Jańczuk, J. M. Bruque, M. L. González-Martin, E. Román-Galán, *Colloids Surf., A* **1995**, *100*, 93; D. K. Owens, *J. Appl. Polym. Sci.* **1970**, *14*, 1725.

[225] B. Jańczuk, M. L. González-Martín, J. M. Bruque, C. Dorado-Calasanz, J. M. del Pozo, *J. Colloid Interface Sci.* **1995**, *176*, 352.

[226] B. Jańczuk, M. L. Kerkeb, T. Biatrowicz, F. González-Caballero, *J. Colloid Interface Sci.* **1992**, *151*, 333.

[227] O. Planinšek, R. Pišek, A. Trojak, S. Srčič, *Int. J. Pharm.* **2000**, *207*, 77; G. E. Parsons, G. Buckton, S. M. Chatham, *Int. J. Pharm.* **1992**, *82*, 145; W. Abdelwahed, G. Degobert, H. Fessi, *Eur. J. Pharm. Biopharm.* **2006**, *63*, 87; W. Abdelwahed, G. Degobert, H. Fessi, *Int. J. Pharm.* **2006**, *324*, 74.

[228] C. J. van Oss, R. J. Good, *Journal of Macromolecular Science: Part A - Chemistry* **1989**, *26*, 1183.

[229] R. J. Chokshi, H. Zia, H. K. Sandhu, N. H. Shah, W. A. Malick, *Drug Delivery* **2007**, *14*, 33.

[230] C. Weber, C. Coester, J. Kreuter, K. Langer, *Int. J. Pharm.* **2000**, *194*, 91; K. Langer, S. Balthasar, V. Vogel, N. Dinauer, H. von Briesen, D. Schubert, *Int. J. Pharm.* **2003**, *257*, 169; C. J. Van Oss, R. J. Good, M. K. Chaudhury, *J. Chromatogr. A* **1987**, *391*, 53.

[231] E. Fattal, C. Vauthier, I. Aynie, Y. Nakada, G. Lambert, C. Malvy, P. Couvreur, *J. Controlled Release* **1998**, *53*; F. Varenne, A. Makky, M. Gaucher-Delmas, F. Violleau, C. Vauthier, *Pharm. Res.* **2016**, *33*, 1220.

[232] J. Bergendahl, D. Grasso, *AIChE J.* **1999**, *45*, 475.

[233] F. J. Holly, M. F. Refojo, in *Hydrogels for Medical and Related Applications*, *Vol. 31*, American Chemical Society, Washington, DC, USA **1976**, 252; M. Pérez Olmedilla, N. Garcia-Giralt, M. M. Pradas, P. B. Ruiz, J. L. Gómez Ribelles, E. C. Palou, J. C. M. García, *Biomaterials* **2006**, *27*, 1003.

[234] J. Guan, C. Gao, L. Feng, J. Sheng, *J. Biomater. Sci., Polym. Ed.* **2000**, *11*, 523; D. E. Rice, J. V. Ihlenfeld, Contact lens containing a fluorinated telechelic polyether, Google Patents (US4440918), **1984**.

[235] M. Ebara, J. M. Hoffman, P. S. Stayton, A. S. Hoffman, *Radiat. Phys. Chem.* **2007**, *76*, 1409.

[236] G. Tan, R. Chen, C. Ning, L. Zhang, X. Ruan, J. Liao, *J. Appl. Polym. Sci.* **2012**, *124*, 459.

[237] I.-K. Kang, Y. Ito, M. Sisido, Y. Imanishi, *Polym. J.* **1987**, *19*, 1329.

[238] S. K. H. Reinke, Katharina, J. Vieira, S. Heinrich, S. Palzer, *J. Phys. D: Appl. Phys.* **2015**, *48*, 464001.

[239] A. Voronov, A. Kohut, W. Peukert, S. Voronov, O. Gevus, V. Tokarev, *Langmuir* **2006**, *22*, 1946.

[240] P. Kim, K. Y. Suh, *Langmuir* **2007**, *23*, 4549.

[241] S. Wang, Y. Zhang, N. Abidi, L. Cabrales, *Langmuir* **2009**, *25*, 11078; X. Wang, Q. Li, J. Xie, Z. Jin, J. Wang, Y. Li, K. Jiang, S. Fan, *Nano Lett.* **2009**, *9*, 3137; J. T. Cang-Rong, G. Pastorin, *Nanotechnology* **2009**, *20*, 255102.

[242] G. Tripodo, C. Wischke, A. Lendlein, *Macromol. Symp.* **2011**, *309-310*, 49; A. B. W. Brochu, G. A. Evans, W. M. Reichert, *J. Biomed. Mater. Res., Part B* **2014**, *102*, 181.

[243] C. A. Kienzle-Sterzer, D. Rodriguez-Sanchez, C. Rha, *Die Makromolekulare Chemie* **1982**, *183*, 1353.

[244] D. Armani, C. Liu, N. Aluru, "*Re-configurable fluid circuits by PDMS elastomer micromachining*", presented at *Technical Digest. IEEE International MEMS 99 Conference. Twelfth IEEE International*

Conference on Micro Electro Mechanical Systems (Cat. No.99CH36291), Orlando, FL, USA, 21-21 Jan. 1999, **1999**.

[245] Y.-C. Tseng, S.-H. Hyon, Y. Ikada, *Biomaterials* **1990**, *11*, 73.

[246] S. Janssens, S. Nagels, H. N. d. Armas, W. D'Autry, A. Van Schepdael, G. Van den Mooter, *Eur. J. Pharm. Biopharm.* **2008**, *69*, 158.

[247] L. Mu, M.-M. Teo, H.-Z. Ning, C.-S. Tan, S.-S. Feng, *J. Controlled Release* **2005**, *103*, 565.

[248] P. K. Jana, S. P. Moulik, *J. Phys. Chem.* **1991**, *95*, 9525.

[249] W. G. Chambliss, R. W. Cleary, R. Fischer, A. B. Jones, P. Skierkowski, W. Nicholes, A. H. Kibbe, *J. Pharm. Sci.* **1981**, *70*, 1248.

[250] A. Chattopadhyay, E. London, *Anal. Biochem.* **1984**, *139*, 408.

[251] M. Ash, I. Ash, *Handbook of Industrial Surfactants*, Synapse Information Resources, Endicott, NY, USA **2010**.

[252] United States Environmental Protection Agency (EPA), Chemistry Dashboard, https://comptox.epa.gov/dashboard/, (accessed: July 2019), **2017**.

[253] A. Roda, A. F. Hofmann, K. J. Mysels, *J. Biol. Chem.* **1983**, *258*, 6362.

[254] A. M. Al-mahallawi, O. M. Khowessah, R. A. Shoukri, *Int. J. Pharm.* **2014**, *472*, 304.

[255] A. Patist, S. S. Bhagwat, K. W. Penfield, P. Aikens, D. O. Shah, *J. Surfactants Deterg.* **2000**, *3*, 53; B. A. Kerwin, *J. Pharm. Sci.* **2008**, *97*, 2924.

[256] L. S. C. Wan, P. F. S. Lee, *J. Pharm. Sci.* **1974**, *63*, 136.

[257] M. J. Schwuger, *J. Colloid Interface Sci.* **1973**, *43*, 491.

[258] B. Geetha, A. B. Mandal, T. Ramasami, *Macromolecules* **1993**, *26*, 4083.

[259] I. Matsaridou, P. Barmpalexis, A. Salis, I. Nikolakakis, *AAPS PharmSciTech* **2012**, *13*, 1319.

[260] MarvinSketch, (Version 17.1.23.0), ChemAxon (http://www.chemaxon.com), Budapest **2017**.

[261] T. B. Rosenthal, *J. Biol. Chem.* **1948**, *173*, 25.

[262] P. Allsop, M. Cheetham, S. Brooks, G. M. Hall, C. Williams, *Eur. J. Appl. Physiol. Occup. Physiol.* **1990**, *59*, 465; M. G. Dickson, D. T. Sharpe, *Br. J. Plast. Surg.* **1985**, *38*, 39.

[263] D. Street, J. Bangsbo, C. Juel, *J. Physiol. (Oxford, U. K.)* **2001**, *537*, 993.

[264] H. Rachmawati, B. M. Haryadi, K. Anggadiredja, V. Suendo, *AAPS PharmSciTech* **2015**, *16*, 692.

[265] H. Ando, A. Okamoto, M. Yokota, T. Asai, T. Dewa, N. Oku, *J. Gene Med.* **2013**, *15*, 375.

[266] K. Hu, J. Li, Y. Shen, W. Lu, X. Gao, Q. Zhang, X. Jiang, *J. Controlled Release* **2009**, *134*, 55.

[267] S. Barua, S. Mitragotri, *ACS Nano* **2013**, *7*, 9558.

[268] S. Tenzer, D. Docter, J. Kuharev, A. Musyanovych, V. Fetz, R. Hecht, F. Schlenk, D. Fischer, K. Kiouptsi, C. Reinhardt, K. Landfester, H. Schild, M. Maskos, S. K. Knauer, R. H. Stauber, *Nat. Nanotechnol.* **2013**, *8*, 772.

[269] B. M. Haryadi, G. Winter, J. Engert, *Unpublished* **2019**.

[270] B. A. Webb, M. Chimenti, M. P. Jacobson, D. L. Barber, *Nat. Rev. Cancer* **2011**, *11*, 671.

[271] J. Buske, C. König, S. Bassarab, A. Lamprecht, S. Mühlau, K. G. Wagner, *Eur. J. Pharm. Biopharm.* **2012**, *81*, 57.

[272] D. Bazile, C. Prud'homme, M.-T. Bassoullet, M. Marlard, G. Spenlehauer, M. Veillard, *J. Pharm. Sci.* **1995**, *84*, 493.

[273] T. G. Park, S. Cohen, R. Langer, *Macromolecules* **1992**, *25*, 116.

[274] T. Ishida, R. Maeda, M. Ichihara, K. Irimura, H. Kiwada, *J. Controlled Release* **2003**, *88*, 35; T. Ishida, K. Masuda, T. Ichikawa, M. Ichihara, K. Irimura, H. Kiwada, *Int. J. Pharm.* **2003**, *255*, 167.

[275] A. C. Anselmo, V. Gupta, B. J. Zern, D. Pan, M. Zakrewsky, V. Muzykantov, S. Mitragotri, *ACS Nano* **2013**, *7*, 11129.

[276] H. Yoshino, M. Kobayashi, M. Samejima, *Chem. Pharm. Bull.* **1983**, *31*, 237.

[277] J. W. Donovan, *Biopolymers* **1979**, *18*, 263; N. I. Khitarov, A. A. Kadik, *Contrib. Mineral. Petrol.* **1973**, *41*, 205.

[278] EDQM, *European Pharmacopoeia, 9th Edition, Including Subscription to Supplement 9.6-9.8*, Council of Europe, European Pharmacopoeia Commission, European Directorate for the Quality of Medicines & Healthcare, Strasbourg, France **2019**.

[279] USPC, *USP 41 - NF 36 The United States Pharmacopeia and National Formulary: Main Edition Plus Supplements 1 and 2*, United States Pharmacopeial Convention **2018**.

[280] BPC, *British Pharmacopoeia 2016 (BP 2016)*, British Pharmacopoeia Commission, **2015**.

[281] G. Dalwadi, H. A. E. Benson, Y. Chen, *Pharm. Res.* **2005**, *22*, 2152.

[282] Y. Shen, M. Y. Gee, A. B. Greytak, *Chem. Commun.* **2017**, *53*, 827.

[283] WHO, *The International Pharmacopoeia, 8th Edition*, World Health Organization, Geneva, Switzerland **2018**.

[284] Pharmaceutical and Medical Device Regulatory Science Foundation, *Japanese Pharmacopoeia, 17th Edition*, The Ministry of Health, Labour and Welfare, Tokyo, Japan **2016**.

[285] EMA, Note for guidance on limitations to the use of ethylene oxide in the manufacture of medicinal products (CPMP/QWP/159/01) (EMEA/CVMP/271/01 Rev. 1), European Medicines Agency, London, UK **2016**, 1.

[286] H. E. Williams, J. Huxley, M. Claybourn, J. Booth, M. Hobbs, E. Meehan, B. Clark, *Polym. Degrad. Stab.* **2006**, *91*, 2171.

[287] H. Shearer, M. J. Ellis, S. P. Perera, J. B. Chaudhuri, *Tissue Eng.* **2006**, *12*, 2717.

[288] M. Goldman, R. Gronsky, G. G. Long, L. Pruitt, *Polym. Degrad. Stab.* **1998**, *62*, 97; B. Burton, A. Gaspar, D. Josey, J. Tupy, M. D. Grynpas, T. L. Willett, *Bone* **2014**, *61*, 71.

[289] M. Shameem, H. Lee, K. Burton, B. C. Thanoo, P. P. Deluca, *PDA J. Pharm. Sci. Technol.* **1999**, *53*, 309; L. Montanari, M. Costantini, E. C. Signoretti, L. Valvo, M. Santucci, M. Bartolomei, P. Fattibene, S. Onori, A. Faucitano, B. Conti, I. Genta, *J. Controlled Release* **1998**, *56*, 219; A. Lendlein, M. Behl, B. Hiebl, C. Wischke, *Expert Rev. Med. Devices* **2010**, *7*, 357.

[290] W. Friess, M. Schlapp, *Eur. J. Pharm. Biopharm.* **2006**, *63*, 176.

[291] A. Castoldi, M. Empting, C. De Rossi, K. Mayr, P. Dersch, R. Hartmann, R. Müller, S. Gordon, C.-M. Lehr, *Pharm. Res.* **2018**, *36*, 22.

[292] M. K. Chun, C. S. Cho, H. K. Choi, *J. Appl. Polym. Sci.* **2001**, *79*, 1525.

[293] J. R. Lopes, W. Loh, *Langmuir* **1998**, *14*, 750.

[294] X. Shi, Y. Du, J. Yang, B. Zhang, L. Sun, *J. Appl. Polym. Sci.* **2006**, *100*, 4689; A. Anitha, V. V. Divya Rani, R. Krishna, V. Sreeja, N. Selvamurugan, S. V. Nair, H. Tamura, R. Jayakumar, *Carbohydr. Polym.* **2009**, *78*, 672.

[295] T. Govender, S. Stolnik, M. C. Garnett, L. Illum, S. S. Davis, *J. Controlled Release* **1999**, *57*, 171.

[296] Y. Lu, D. L. Slomberg, B. Sun, M. H. Schoenfisch, *Small* **2013**, *9*, 2189.

[297] V. Oberle, U. Bakowsky, I. S. Zuhorn, D. Hoekstra, *Biophys. J.* **2000**, *79*, 1447.

[298] J. G. Pritchard, D. A. Akintola, *Talanta* **1972**, *19*, 877; R. Li, X. Li, L. Liu, Z. Zhou, H. Tang, Q. Zhang, *Macromol. Rapid Commun.* **2010**, *31*, 1981.

[299] W. Schöniger, *Microchim. Acta* **1955**, *43*, 123; W. Schöniger, *Microchim. Acta* **1956**, *44*, 869.

[300] Y. Liu, X. Liu, X. Wang, *Nanoscale Res. Lett.* **2010**, *6*, 22.

8. Supporting Information

8.1. Materials and Methods

8.1.1. Materials

Carboxyl-ended poly(D,L-lactic acid) Resomer® R 202H (hereafter referred as PLA-COOH) was purchased from Evonik Röhm Industries (Darmstadt, Germany), while carboxyl-ended poly(D,L-lactic-co-glycolic acid) (PLGA) PDLG® 7502A (Lactide/Glycolide ratio 75/25; hereafter referred as PLGA 75/25-COOH) and carboxyl-ended PLGA PDLG® 5004A (Lactide/Glycolide ratio 50/50; hereafter referred as PLGA 50/50-COOH) were kindly gifted by Corbion Purac Biomaterials (Gorinchem, Netherlands). The further detail of all aforementioned polymers are presented in Table S II-2. The molecular structures thereof and other main materials used in our experiment are presented in Figure S II-2 & Figure S II-5. Carboxyl-ended poly(styrene) (PS-COOH) Polybead® particles with size of 0.1, 0.2, and 2 µm were purchased from Polysciences (Hirschberg an der Bergstrasse, Germany). Gelatin Type B, Bloom 300 from bovine skin was gifted from GELITA AG GmbH (Eberbach, Germany). O-Carboxymethyl Chitosan (O-CMCHS) with deacetylation degree 90% & degree of substitution $\geq$ 95% was purchased from Santa Cruz Biotechnology (Heidelberg, Germany). Poly(vinyl alcohol) (PVA; Tg 75 - 85°C[23]; Tm 180 - 190°C[58]) Mowiol® 40-88 (molecular weight [MW] ~205 kDa; critical micelle concentration [CMC] ~54 mN/m at ~0.5%[121]), Mowiol® 4-88 (MW ~31 kDa; ~45 mN/m at ~0.5%[121]), glutaraldehyde 25%, Poloxamer 407 (P407; MW 9.846 - 14.6 kDa[58]; Tg ~-60°C[292]; Tm 52 - 57°C[58]; ~0.98%[293]; HLB 18 - 23[58]; CMC ~26 mN/m[58] at 0.98%[293]), D-α-Tocopherol Polyethylene Glycol 1000 Succinate (TPGS), Chitosan (50 - 190 kDa & 75 - 85% deacetylated), Tetraethyl orthosilicate (TEOS) (reagent grade, 98%), Hexadecyltrimethylammonium bromide (CTAB) (BioUltra, P99%), and Dulbecco Phosphate Buffer Saline (PBS) 1x (310 mOsm) were supplied by Sigma Aldrich (Taufkirchen, Germany). Glycerol (purity 99%) was obtained from Acros Organics (Geel, Belgium). Calcium chloride was obtained from Grüssing GmbH (Filsum, Germany). Muscovite Mica V2 quality was supplied by Electron Microscopy Sciences (München, Germany). Cyanoacrylate was supplied by UHU (Bühl, Germany).

Highly purified water (HPW) was freshly prepared from ELGA PURELAB® Plus (Celle, Germany). All other materials used in this study were of at least analytical grade, utilized as received, and purchased either from Sigma-Aldrich (Taufkirchen, Germany) or VWR Prolabo (Leuven, Belgium).

8.1.2. Methods

8.1.2.1. Preparation of Spherical O-CMCHS Nanoparticles

O-CMCHS nanoparticles were synthesized by physical cross-linking, i.e. ionic gelation, with a slight modification from available report[294]. 0.5% O-CMCHS solution was prepared in distilled water. To 5 mL of

this solution, 1 mL of 1.5% calcium chloride solution was added under constant stirring (900 RPM; VARIOMAG® Electronicrührer POLY15 Thermo Fisher Scientific, München, Germany). The yielded nanoparticles were washed three times with HPW by centrifugation (10,000 xg at 5°C for each 10 min). The standardized washing factor and redispersion energy were 100^3x (thrice of each 100x) and 3.9 kJ/m^3 (Bandelin® Sonopuls GM 3200 200 W 20 kHz [Berlin, Germany] with the MS 72 probe), respectively.

8.1.2.2. Preparation of Spherical Gelatin Nanoparticles

Gelatin (type B, bloom 300) nanoparticles were prepared by chemical (covalent) cross-linking, namely one-step desolvation[77]. Briefly, 3% gelatin solution in HPW was prepared in a volume of 25 mL under constant stirring (900 RPM & 50°C; Heidolph MR 3001K, Schwabach, Germany). The pH was adjusted to a value above the isoelectric point (IEP: pH 4.5 - 5.0), i.e. pH 7.0. Acetone was then added drop-wise to the gelatin solution in order to trigger desolvation and nanoparticle formation. To ensure particle stability, 175 µL glutaraldehyde solution (25% in HPW) was added to cross-link gelatin nanoparticles. The dispersion was stirred overnight and purified by thrice ultrafiltration (Millipore S.A.S., Molsheim, France) against HPW using regenerated cellulose disc with a molecular weight cut-off (MWCO) of 100,000 Da. The standardized washing factor using ultrafiltration was made the same to the centrifugation method, namely 100^3x.

8.1.2.3. Preparation of Spherical Aliphatic Polyester Nanoparticles

Aliphatic polyester polymers (PLA-COOH, PLGA 75/25-COOH, and PLA 50/50-COOH) nanoparticles were developed using emulsion-solvent extraction[2] as well as nanoprecipitation (or so-called solvent displacement)[24, 295]. First, about 1% (w/v) aliphatic polyesters were prepared in acetone. Subsequently 5 mL of polymeric solution was added into 15 mL of the dispersant (for emulsion solvent extraction method, either 5% w/w Mowiol® 4-88 in HPW, 5% w/w P407 in HPW, or 5% w/w TPGS in HPW, meanwhile merely HPW for nanoprecipitation method) at a rate of 1 mL/min under 900 RPM (VARIOMAG® Electronicrührer POLY15 Thermo Fisher Scientific, München, Germany) and allowed to stand at least for 2 hours under fume hood for solvent evaporation until the initial dispersant volume was reached. Subsequently, nanoparticles were subject of washing thrice in HPW by centrifugation (10,000 xg at 5°C for each 10 min) and used as fresh as possible (if needed, the brief storage at 5°C until further use and characterization was performed). The standardized washing factor and redispersion energy were 100^3x (thrice of each 100x) and 3.9 kJ/m^3 (Bandelin® Sonopuls GM 3200 200 W 20 kHz [Berlin, Germany] with the MS 72 probe), consecutively. The maximum temperature during redispersion was set 8°C.

8.1.2.4. Preparation of Non-spherical (Prolate) Polymeric Nanoparticles by Film-Stretching Method

Firstly, the stretching method published by Felder et al. (1966) and Champion et al. (2007) was utilized to prepare non-spherical nanoparticles of proposed polymers. An amount of Mowiol® 40-88 intended for 5% w/w final concentration was wetted in HPW and glycerin (final concentration 2% w/w) at room temperature followed by heating the mixture at 90°C for 5 minutes. As the heated solution was cooled to room temperature, mixing was continued and afterwards the spherical particles were added to give final concentration of 0.3% w/w. The mixture was poured into molds and dried for overnight at room temperature under fume hood. The dried films (with thickness around 70 µm, residual moisture 6 - 8%, and effective stretching area 1 x 9 cm) were stretched using a custom build stretching device to 3 folds their original length in one direction under a dry heat (Figure II-1a) at a constant stretching speed of 1 mm/s and particular temperature based on the dry bulk Tg of the polymers as described in Table S II-1.

After stretching, the films were cooled down rapidly until the temperature which was lower than its bulk Tg value while the strain was still applied. To harvest the non-spherical (prolate) particles, the stretched film was dissolved in phosphate buffer saline (PBS) pH 7.4 310 mOsm 5°C with the aid of moderate agitation in continuous mode on a mini vortexer (VWR, Darmstadt, Germany) for at least 30 minutes, followed by bath sonication (Bandelin® RK510, Berlin, Germany) for 15 minutes until the PVA film was totally dissolved. Later, particles were purified three times with PBS pH 7.4 310 mOsm 5°C (10,000 xg at 5°C for each 10 min) (first by 20,000 xg for 10 min at 5°C, and the two next by 10,000 xg at the same duration and temperature). The standardized washing factor and redispersion energy were 100^3x (thrice of each 100x) and 3.9 kJ/m^3 (Bandelin® Sonopuls GM 3200 200 W 20 kHz [Berlin, Germany] with the MS 72 probe), respectively. The maximum temperature during redispersion was set 8°C. To ensure comparability, the spherical particles employed in the study were treated in the same treatment (e.g. embedment in PVA film until final washing), but stretching was not applied to the PVA film.

8.1.2.5. Preparation of Non-spherical Mesoporous SiO_2 Nanoparticles (SiO_2 Nanorod) by Polymerization

Non-spherical mesoporous SiO_2 nanoparticles with two different aspect ratios (3 & 8) were synthesized using a modified method[54, 296] through a one-step polymerization (or also so-called condensation / hydrolysis / sol-gel) under dilute SiO_2 supply and low surfactant concentration conditions with ammonium hydroxide as the base catalyst. The molar ratio of TEOS:CTAB:HPW:$NH_3.H_2O$(500 mM) in the reaction mixture (about 50 mL) was 64:16:54,760:500 and 77:22:54,760:548, for nanoparticle aspect ratio of 3 and 8, respectively. In

general, CTAB was dissolved in HPW with mild heating (900 RPM & 30°C; Heidolph MR 3001K, Schwabach, Germany). After the solution was cooled to room temperature (25°C), $NH_3.H_2O$ was added and the mixture was mixed for 1 hour. TEOS was added at the rate of 5 mL/min while the mixing continued. The mixture was further mixed for 4 h. Subsequently, the product was collected by a centrifugation at 20,000 xg (25°C) for 20 min. As-synthesized nanoparticles were suspended in ethanolic HCl (1.5 mL of HCl in 150 mL of ethanol) and heated at 60°C (900 RPM) for 6 hours to remove the excess surfactant. Later, the nanoparticles are washed in similar way as other previous nanoparticles. For the first washing sequence, the SiO_2 nanoparticles were purified three times with HPW by centrifugation (10,000 xg at 5°C for each 10 min). Later, they were washed with PBS pH 7.4 310 mOsm (10,000 xg at 5°C for each 10 min). The standardized washing factor and redispersion energy were 100^3x (thrice of each 100x) and 3.9 kJ/m^3 (Bandelin® Sonopuls GM 3200 200 W 20 kHz [Berlin, Germany] with the MS 72 probe), consecutively. The maximum temperature during redispersion was set 8°C.

8.1.2.6. Particle Concentration and Yield

The particle concentration and yield were evaluated gravimetrically using a Mettler Toledo UMX2 Ultra-microbalance (Greifensee, Switzerland). An aliquot (20 µL) of the nanoparticle samples was added in a pan made of aluminium. After drying for 2 hours at 80°C, these pans were put in a desiccator for 30 min to cool down. Subsequently, the pans were weighed with the microbalance. The content of the nanoparticles was calculated from the difference of the empty and nanoparticle-filled pan. When it was needed to concentrate the particles, Vivaspin® (MWCO of 300,000) was utilized.

8.1.2.7. Shape Stability of Non-spherical Nanoparticles

The shape stability of non-spherical nanoparticles is depicted primarily by aspect ratio (AR) values and supplementarily supported by hydrodynamic size, polydispersity index (PDI) and zeta potential via dynamic light scattering (DLS) as well as pH value (MP220, Mettler Toledo, Giessen, Germany). Aspect ratio for all figures derived from scanning electron micrographs was determined manually from at least 20 particles using ImageJ software (National Institutes of Health). Typical shifting time ($t_{1/2}$; defined as the needed time for a half decrease of the initial AR) was deduced from the fitting of obtained experimental aspect ratio data over time fitted into 0^{th}, 1^{st} and 2^{nd} order of kinetics equation. The best fit was displayed with R^2 closer to 1.

8.1.2.7.1. Scanning Electron Microscope-Energy Dispersive X-Ray (SEM-EDX)

The size, morphology and aspect ratio of different particles were investigated using scanning electron

microscopy. Each particle suspension (5 µL) with concentration of 800 µg/mL was fixed onto filter paper 589/2 (Hahnemühle FineArt GmbH, Dassel, Germany) 25 mm^2 attached to carbon self-adhesive tape on aluminium stubs. The samples were sputtered with carbon and captured at 50,000x magnification in FEI Helios G3 UC with EDX, Scanning-Transmissions-Detector and Focused Ion Beam (FIB) (FEI, Gräfelfing, Germany) at 2 kV (for all nanoparticles due to the best sample stability [no melting] under electron excitation, except 5 kV for SiO_2 nanoparticles) with a 4 mm working distance. For EDX measurement (principally to detect Br), the voltage was set up to 30 kV.

8.1.2.8. Dynamic Light Scattering (DLS)

DLS experiments were conducted using a Zetasizer Nano ZS (Malvern, Herrenberg, Germany) equipped with a 633 nm He-Ne laser. Using this instrument, the hydrodynamic size/diameter (Z-Average) of particles was measured based on light intensity fluctuations of scattered laser light detected at angle 90°, whereas zeta potential of particles was determined based on their electrophoretic mobility. An appropriate volume of each nanoparticle samples was measured in disposable poly(methyl methacrylate) (PMMA) cuvettes (Brand, Wertheim, Germany) with a path length of 12.5 mm after an appropriate equilibration time (i.e. 60 s) at 25°C. Samples were analyzed in triplicates, each triplicate with 10 sub-runs. The average hydrodynamic size and polydispersity index (PDI) were calculated by the Malvern Dispersion Technology software (version 4.20, Malvern, Herrenberg, Germany).

8.1.2.9. Atomic Force Microscope (AFM)

Determination of fine sample information details (topography), Young's modulus and surface roughness of samples were conducted with an atomic force microscope (AFM) Ntegra Solver (NT-MDT, Moscow, Russia) equipped with vibration-damped table under ambient condition (relative humidity ~50% and room temperature ~25°C) using conventional measuring head in intermittent contact mode (to prevent sample surface damages and permit repeated examination of the same sample region[297]) with a scan speed of 0.1 - 0.5 Hz. For sample preparation, 10 µL of particles dispersion was placed on a 12.5 x 12.5 mm freshly cleaved mica surface and incubated for 5 min. Later, the surface was additionally washed once with 30 µL HPW (if needed) and/or dried under a nitrogen atmosphere right away. The HA_NC polysilicon cantilever (spring constant = 3.5 N/m; resonant frequency 140 kHz) was equipped with a conical silicon tip (typical radius of curvature 10 nm and cone angle 30°). For each data point, 15 particles or more per batch were examined by measuring triplicate, with 15 s approach and 15 s retreat time. Measurements with inconsistent force-distance curves resulting from movement of the particles during the probing or unsuitable spherical

interaction were disregarded. The data were analysed with the Image Analysis 3.5 software. Meanwhile, the surface roughness parameter, i.e. the root mean square (R_{rms}), was calculated with the same data points as Young's modulus measurement. The attained pictures had at least resolution of 512 x 512 pixels.

8.1.2.10. Differential Scanning Calorimetry (DSC)

Dry glass transition temperatures (dry Tg_s) of bulk materials and nanoparticles were measured using DSC Mettler Toledo 822e (Gießen, Germany). Bulk PS-COOH samples were prepared from each different PS-COOH nanoparticle size by drying the nanoparticles via freeze drying protocol (Figure S II-1) and consequently annealing at 150°C for 20 h. Samples (~5 mg) were heated in hermetically sealed aluminium pans at a rate of 20°C/min up to 120°C under dynamic nitrogen atmosphere. The Tg_s of nanoparticles dispersed in water (2.5%) (wet Tg_s) were determined using modulated method in the same DSC instrument with a modulation rate of 0.200 K/20 s and heating rate of 5 K/min in hermetically sealed aluminium pans. Otherwise further specified, all reported Tg_s are the midpoint value between the tangents of the glass and liquid line from the total heat flow.

8.1.2.11. Physiosorption Analysis: Brunauer-Emmett-Teller (BET) Specific Surface Area (SSA) and Karl Fischer

SSA analysis was performed using an Autosorb-1 analyzer (Quantachrome, Odelzhausen, Germany) purged with Krypton. Samples were degassed under vacuum at 25°C for 2 hour prior to the measurement. The BET equation was utilized to fit data of krypton adsorption at 77 K over a relative pressure range of 0.05 - 0.3 employing 10 measurement points. Lyophilized sample (obtained using conventional protocol [Figure S II-1]) mass was around 50 - 100 mg and each formulation was analyzed at least twice with different batch. Whereas, residual moisture was undertaken coulometrically using a Karl Fischer titrator Aqua 40.00 (Analytik Jena AG, Halle (Saale), Germany) equipped with a headspace oven.

8.1.2.12. Surface Hydrophobicity

8.1.2.12.1. Contact Angle, Surface Free Energy (-Tension) and Interfacial Tension Measurement

The water contact angle (WCA) and diiodomethane contact angle measurements were performed by using a full automated Krüss DSA25E (Hamburg, Germany) contact angle goniometer in sessile drop mode (needle NE44 Ø 0.5 mm) at 20 ± 1°C. These values permit the calculation of bulk material's surface free energy (SFE) and (bulk material-water) interfacial tension(s)[223].

The thin layers were developed on clean mica surface and later, they were used as base layer of HPW or diiodomethane droplet (2 µL with a drop rate of 0.16 mL/min). Each thin layer was prepared from 100 µL sample (concentration of 1% w/w in acetone for aliphatic polyesters [PLA-COOH, PLGA 75/25-COOH & PLGA 50/50-COOH], gelatin 3% w/w in HPW, O-CMCHS 0.5% w/w in HPW, TEOS, CTAB 5.8% w/w in HPW, emulsion solvent extraction stabilizers (i.e. PVA (Mowiol® 4-88), Poloxamer 407, & TPGS) 5% w/w in HPW, docusate sodium 1% w/w in HPW[168], chitosan 1.625% w/w in 0.2 M HNO_3[98], and cyanoacrylate) spread evenly on 20 x 25 mm by drop-casting and dried under fume hood for 45 minutes. The used concentration and solvent exactly simulates the conditions of nanoparticles fabrication step. The data were acquired with the aid of the Krüss ADVANCE 1.1.02 - Drop Shape software package 20 s after drop deposition using ellipse (tangent-1). Three samples of each polymer were studied and five contact angles were measured for each sample.

Surface tension of PVAs (Mowiol® 4-88 and Mowiol® 40-88) were also analysed using the same instrument, needle and temperature in pendant drop mode and verified with a Kibron Micro Trough XL Langmuir-Blodgett film balance (Helsinki, Finland).

8.1.2.12.2. Organic Dye Adsorption Method

The hydrophobicity of the nanoparticle surfaces was determined in accordance to the Rose Bengal adsorption method[211]. Briefly, a 1,000 µg/mL of Rose Bengal dye, dissolved in 0.1 M phosphate buffer pH 7.4, was added to each nanoparticle dispersion containing varying concentrations of nanoparticles to a final volume of 1 mL. Final Rose Bengal concentration was 20 µg/mL for all dispersions, whereas final nanoparticles concentration (dispersed in 0.1 M phosphate buffer) was 500 - 2,000 µg/mL. Nanoparticles were incubated for 3 hours at 25 °C (Thermomixer Comfort, Eppendorf, Hamburg, Germany) with the dye, then centrifuged for 2 hours at 21,000 xg (Centrifuge 5418, Eppendorf, Hamburg, Germany). The amount of dye in the supernatant was quantified using UV/Vis spectroscopy (NanoDrop™ 2000c, Thermo Fisher Scientific, München, Germany) at a wavelength of 543 nm. Rose Bengal encounters partitioning between the surface of the particles and the dispersion medium.

For data evaluation, there are two common methods (and both are displayed in this paper):

I. Scatchard equation

$$\frac{r}{a} = KN - Kr$$

where r is the amount of Rose Bengal adsorbed per mg nanoparticles (µg/mg); a is the equilibrium concentration of Rose Bengal (µg/mL); K is the binding constant (mL/µg); and N is the maximum amount bound (mg/mg).

II. the partitioning quotient (PQ), where each nanoparticle concentration was calculated according to

$$PQ = \frac{\text{amount of Rose Bengal bound on surface}}{\text{amount of Rose Bengal unbound in dispersion medium}}$$

Plotting the PQ versus the total surface area of the nanoparticles generated straight lines. The slope of the resulting regression line may be considered as a degree of the hydrophobicity of the nanoparticle surfaces. The surface area of the different nanoparticle formulations was calculated from the hydrodynamic diameter of the particles. The dye solution without nanoparticles as a control was run each experiment under similar conditions to justify the dye that might adsorb to the centrifuge tubes and pipette tips.

8.1.2.13. Residual Stabilizer Concentration

8.1.2.13.1. Poly(vinyl Alcohol) (PVA)

The amount of PVA resided with the nanoparticles was determined by colorimetric method based on the formation of a colored complex between two adjacent hydroxyl groups of PVA and an iodine molecule in the presence of boric acid[298]. Briefly, 2 mg of lyophilized sample of each formulation was treated with 2mL of 0.5 M NaOH for 15 min at 60°C. Every sample was neutralized with 900 µL 1M HCl and the volume was adjusted to 5 mL with highly purified water (HPW). To each sample, it was added 3mL of boric acid (0.65 M), 0.5mL of I_2/KI (0.05 M/0.15 M) solution, and 1.5 mL of HPW. The absorbance of the samples was measured at 690 nm following incubation for 15 min at 25°C. A standard curve of PVA and control (blank nanoparticles prepared by nanoprecipitation) were prepared under identical conditions.

8.1.2.13.2. Elemental Analysis: Focus on Sulfur (S)-Sodium (Na) and Nitrogen (N)-Bromine (Br)

Trace elemental analyses with the focus on S-Na and N-Br were performed in relation to the suspected residual stabilizers of anionic sulphate ester (e.g. sodium dodecyl sulphate [SDS], docusate sodium, etc.) in PS-COOH nanoparticles and cetyltrimethylammonium bromide (CTAB) in SiO_2 nanoparticles, consecutively. After measurement by an EDX, both PS-COOH and SiO_2 nanoparticles were measured for CHNS with oxygen combustion method using a Vario Micro Cube (Elementar Analysensysteme GmbH, Langenselbold, Germany), while additional Br using a 888 Titrando (Metrohm, Herisau, Switzerland) potentiometrically according to Schöniger[299]. S & Na were reconfirmed using an inductively coupled plasma atomic emission spectroscopy (ICP-AES) Varian Vista RL (Agilent Technologies, Waldbron, Germany). All aforementioned elemental analyses were undertaken at the Central Analytics, Faculty of Chemistry and Pharmacy, Ludwig-Maximilians-Universität München, Germany. Meanwhile, Br trace in SiO_2 nanoparticles was reconfirmed using a quadrupole inductively coupled plasma mass spectrometry (ICP-MS) Elan 6100 (Perkin Elmer,

Rodgau, Germany) at Institute of Hydrochemistry, Chair of Analytical Chemistry and Water Chemistry, Technische Universität München, Großhadern, Germany.

8.1.2.14. Wide Angle X-Ray Diffractometer (WXRD)

The internal structure of different bulk and particles were investigated using the wide angle x-ray diffractometer XRD 3000 TT (GE Inspection Technologies Ahrensburg GmbH & Co. KG [formerly Rich. Seifert & Co.], Ahrensburg, Germany) equipped with a copper anode (40 kV, 30 mA, 1.54178 Å). Measurements were run with the following parameters: 0.05° (2 θ) steps and a range from 5° to 35°. Each step was performed within a time span of 2 s.

8.2. Supplemental Tables & Figures

8.2.1. Supplemental Tables

Table S II-1. Stretching Temperature for (Elongated/) Non-spherical Particles Fabrication

Polymer of Nanoparticles	Stretching Temperature (°C)
Aliphatic Polyesters (PLA-COOH, PLGA 75/25-COOH & PLGA 50/50-COOH)	80
O-CMCHS & Gelatin	160
PS-COOH	120

Table S II-2. Details of Biodegradable Aliphatic Polyester Polymers Used in This Study

Polymer	End Group	Molecular Weight (kDa)	Inherent Viscosity (dl/g)[a]	Degradation Timeframe (months)	Tg (°C; & Mid-Tg)	Manufacturer
PLA-COOH (Resomer® R 202 H)	Carboxylic acid	~17 (10 - 18)	0.20 (0.16 - 0.24)	~< 6	44 - 48 (46)	Evonik Röhm Industries
PLGA 75/25-COOH (Purasorb® PDLG 7502A)	Carboxylic acid	~17 (10 - 18)	0.20 (0.16 - 0.24)	< 6 [2 - 3][b]	40 - 45 (42.5)	Corbion Purac Biomaterials
PLGA 50/50-COOH (Purasorb® PDLG 5004A)	Carboxylic acid	~44 (38 - 54)	0.40 (0.35 - 0.60)	< 3 [0.75 - 1][b]	42 - 47 (44.5)	Corbion Purac Biomaterials

* All given data is directly from manufacturer.
[a]determined in $CHCl_3$, 25°C at 0.1% with an Ubbelhode size 0c glass capillary viscometer.
[b]from particular product information sheet of Purasorb®.

8.2.2. Supplemental Figures

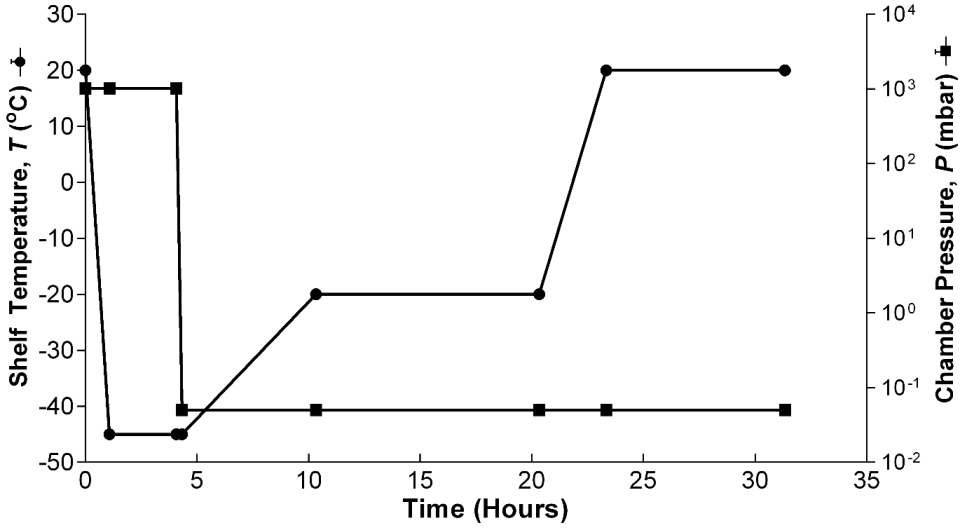

Figure S II-1. Used lyophilization protocol.

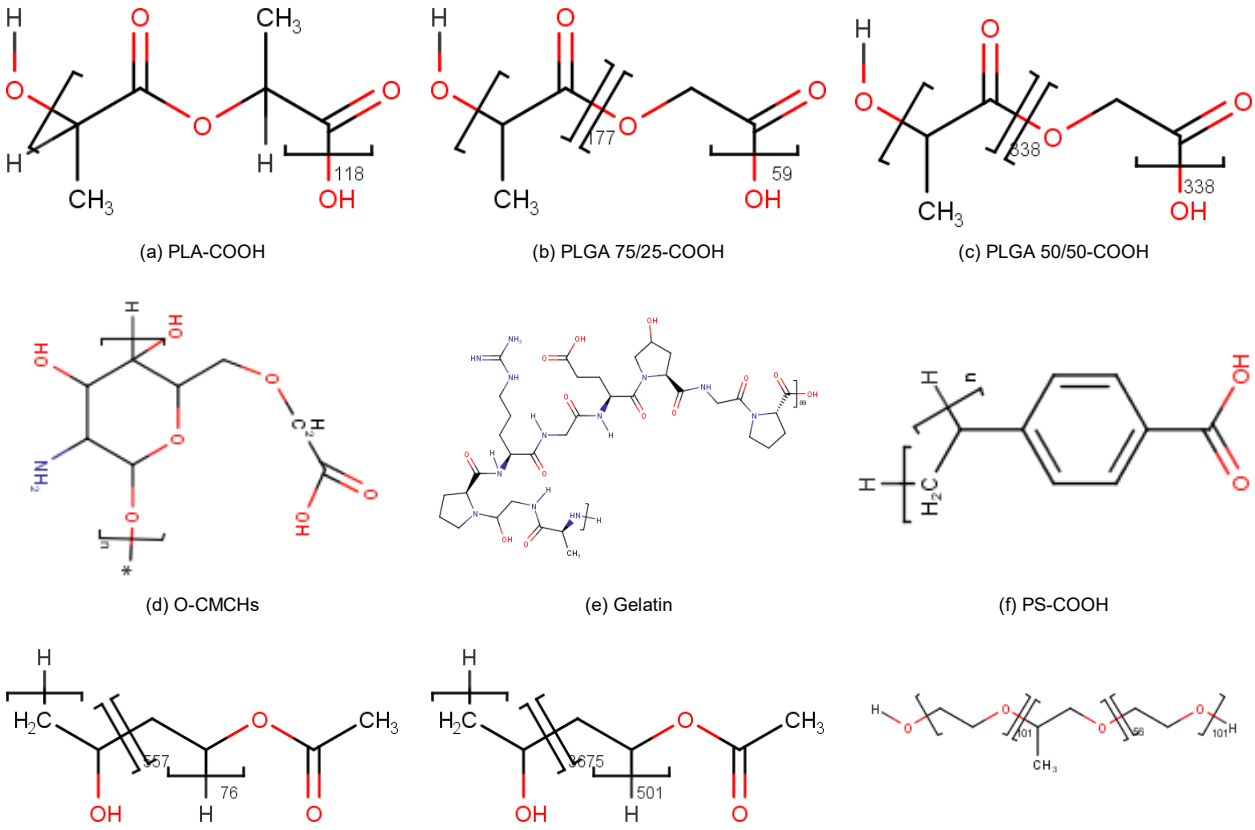

Figure S II-2. Molecular structures of involved materials in the film-stretching method in this study. For TPGS, its molecular structure is depicted in Figure S II-5a due to its participation in the physicochemical properties study using the computational method. The gelatin structure (e) is represented by the most typical segment of amino acid sequences: -Alanine-Glycine-Proline-Arginine-Glycine-Glutamic Acid-(4-Hydroxyproline)-Glycine-Proline- (-Ala-Gly-Pro-Arg-Gly-Glu-4Hyp-Gly-Pro-)[300].

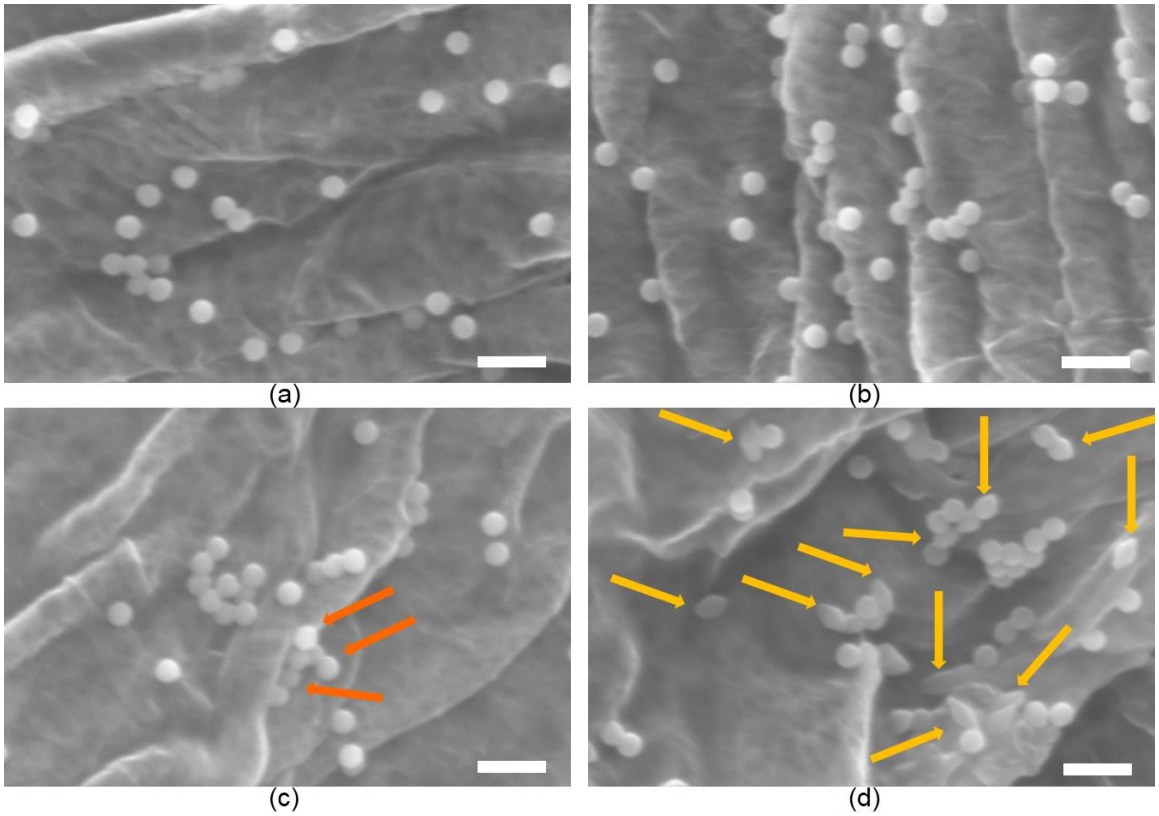

Figure S II-3. Proof of concept of glass transition temperature (Tg) variance possibility in different states (wet vs dry) using PS-COOH nanoparticles (initial ø ~200 nm). Non-spherical nanoparticles were tried to be generated from spherical ones (using the standardized film-stretching method with 3x of its initial film length, but at numerous temperatures: (a) 37, (b) 70, (c) 80 and (d) ~93°C (bulk PS-COOH Tg). Arrows depict the quasi non-spherical (lemon-like) nanoparticles. Scale bars = 500 nm.

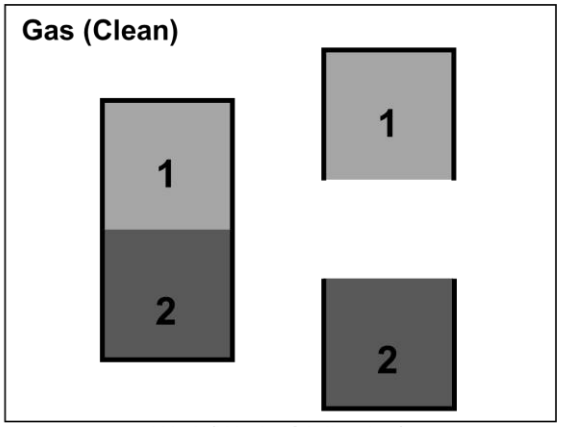

WoA (Work of Adhesion)

$$WoA = 2 \cdot \sqrt{SFE_1p \cdot SFE_2p} + 2 \cdot \sqrt{SFE_1d \cdot SFE_2d}$$

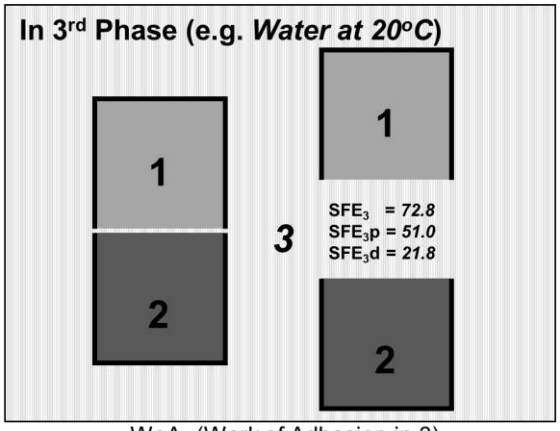

WoA_3 (Work of Adhesion in 3)

$$\mathbf{WoA_3} = IFT_{1.3} + IFT_{2.3} - IFT_{1.2}$$

where:

$$IFT_{1.3} = SFE_1 + SFE_3 - (2 \cdot (\sqrt{SFE_1p \cdot SFE_3p} + \sqrt{SFE_1d \cdot SFE_3d}))$$

$$IFT_{2.3} = SFE_2 + SFE_3 - (2 \cdot (\sqrt{SFE_2p \cdot SFE_3p} + \sqrt{SFE_2d \cdot SFE_3d}))$$

$$\mathbf{IFT_{1.2}} = SFE_1 + SFE_2 - WoA$$

(a)

Material 1 (Core Particles)	Material 2 (Stabilizer)	WoA_3 (mN/m)	$IFT_{1.2}$ (mN/m)	Difference (WoA_3-$IFT_{1.2}$; mN/m)	Proper Particle Formation Aid & Stabilizer Non-Washability?		Comparative Case(s)
					Proposed Algorithm (Fig S4c)	Experimental	
PLA-COOH	**PVA**	24.27	5.61	18.66	Yes & Yes	Yes & Yes	Quintanar-Guerrero 1996 [194]
	TPGS	20.70	8.14	12.57	Yes & No	Yes & No	-
	P407	22.30	7.24	5.06	Yes & No	Yes & No	-
	Gelatin	46.25	0.47	45.78	No & Yes	No & Yes	Quintanar-Guerrero 1996 [194]
	PVP	46.84	0.00	46.83	No & Yes	No & Yes	Quintanar-Guerrero 1996 [194]
	PS80	13.60	12.58	1.03	No & No	No & No	Quintanar-Guerrero 1996 [194]
	Dextran	12.21	13.44	-1.24	No & No	No & No	Quintanar-Guerrero 1996 [194]
	Deoxycholate-Na	2.66	21.08	-18.42	No & No	No & No	Gref 1995 [129]
PLGA 75/25-COOH	**PVA**	14.80	0.26	14.55	Yes & Yes	Yes & Yes	Scholes 1999 [105]
	PEG(6000)	9.83	2.66	7.17	No & No	No & No	Mu 2004 [209]
PLGA 50/50-COOH	**PVA**	11.84	0.02	11.81	Yes & Yes	Yes & Yes	Bouissou 2006 [124] & Lee 1999 [135]
	Triton X-100	11.59	0.06	11.52	Yes & Yes	Yes & Yes	Bouissou 2006 [124]
	SDS	9.41	0.17	9.24	Yes & Yes	Yes & Yes	Xu 2009 [168]
	Docusate-Na	14.09	0.77	13.31	Yes & Yes	Yes & Yes	Xu 2009 [168]
	TPGS	9.82	1.00	8.82	Yes & No	Yes & No	Mu 2003 [133]
	P407	10.60	0.91	9.68	Yes & No	Yes & No	Redhead 2001 [103]
	P188	6.79	2.19	4.60	Yes & No	Yes & No	Quintanar-Guerrero 1998 [127]
SiO_2 (represented as TEOS)	**CTAB**	5.34	0.65	4.68	Yes & Yes	Yes & Yes	Huh 2003 [53]
PS-COOH	**SDS**	25.77	20.22	5.55	Yes & Yes	Yes & Yes	Possible Sulfate Esters in Polybead® [29]
	Docusate-Na	37.40	13.86	23.54	Yes & Yes	Yes & Yes	Possible Sulfate Esters in Polybead® [29]

Bold: Used materials in our experimental nanoparticle study.

(b)

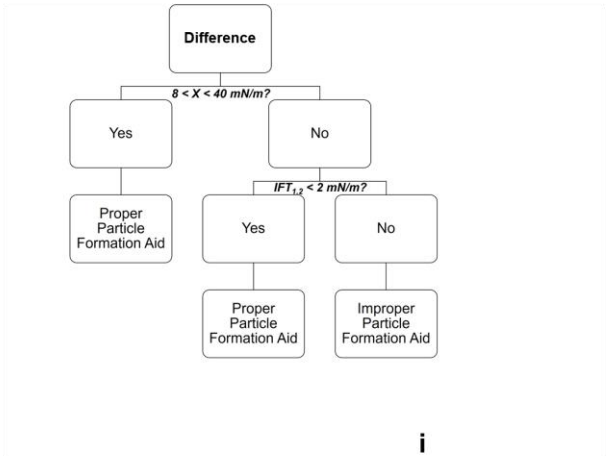

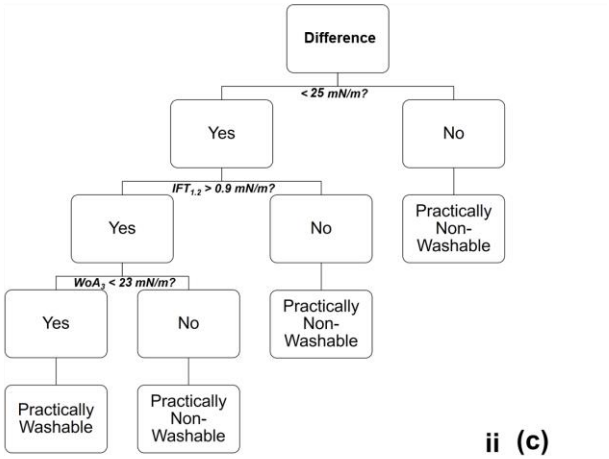

(c)

Figure S II-4. (a) Illustration and equation which are used to define secondary interfacial activity parameters: WoA_3, $IFT_{1.2}$, and difference thereof. (b) Exemplary dataset of secondary interfacial activity parameters is derived from the primary interfacial activity parameters (Figure II-5e). Using (c) our proposed algorithms (i for stabilizer properness in aiding particle formation and ii for stabilizer non-washability from particles), this dataset shows a satisfying agreement to our and other experimental results.

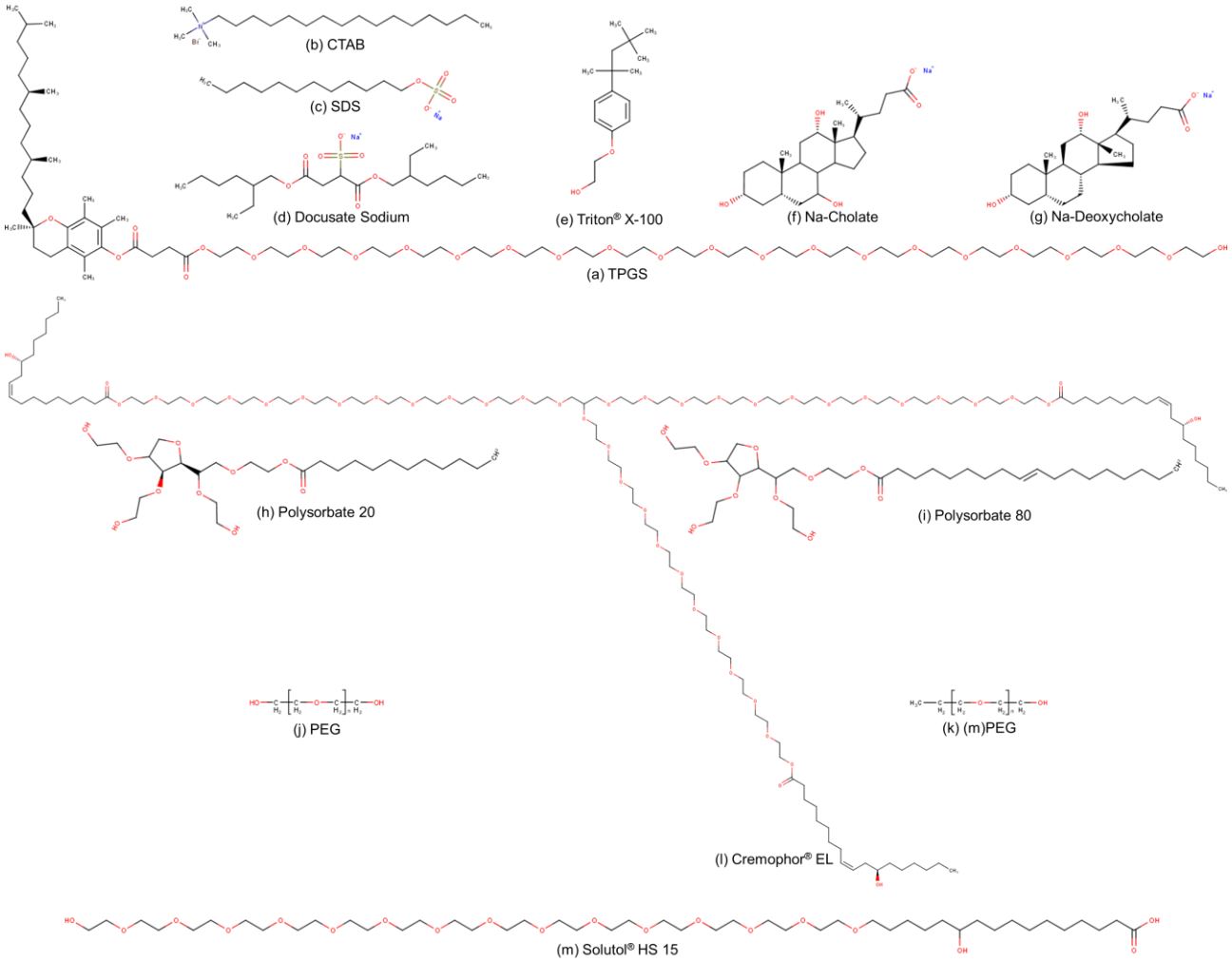

Figure S II-5. Molecular structures utilized for providing physicochemical properties (Table II-3) by computational method using the Calculator Plugins in MarvinSketch software version 17.1.23.0 (2017), ChemAxon (http://www.chemaxon.com). These structures have been validated by the software before calculation. Details of structures: (a) TPGS, (b) CTAB, (c) SDS, (d) Docusate Sodium, (e) Triton® X-100 / (4-)octyl phenol (poly)ethoxylate, (f) Na-Cholate, (g) Na-Deoxycholate, (h) Polysorbate 20, (i) Polysorbate 80, (j) PEG (n = 7 for PEG 350; n = 8 for PEG 400; n = 89 for PEG 4000; n = 112 for PEG 5000; n = 135 for PEG 6000), (k) (m)PEG (n = 7 for (m)PEG 350; and the number of n for the rest (m)PEG is the same as PEG), (l) Cremophor® EL (Polyoxyl 35 Castor Oil), and (m) Solutol® HS 15 / Kolliphor® HS 15 (Polyoxyl 15 Hydroxystearate).

8.3. Supplemental Calculation

Distribution of Normalized Radius of Curvature on Non-Spherical (Prolate Ellipsoid) Particles Obtained by Stretching Uniaxially Spherical Ones

Let S_0 be a sphere with radius R, and let S_C be a prolate ellipsoid elongated at x-axis with the same volume as S_0, with the radius of the major axis being $R \cdot C$, where C is the stretching factor. Recall that an ellipse (Figure S II-6), parameterized with the radii of the major and minor axes r_a and r_b, is defined by the following equation:

$$\frac{x^2}{r_a^2} + \frac{y^2 + z^2}{r_b^2} = 1 \qquad \textit{Equation S II-1}$$

Note that since S_C is rotationally symmetric around the x-axis, the radius of curvature at the surface of the ellipsoid is equal to the radius of curvature at the circumference of the cross section of the ellipsoid with the plane containing x-axis and the point.

The cross section with the xy-plane is an ellipse defined by the following equation:

$$\frac{x^2}{r_a^2} + \frac{y^2}{r_b^2} = 1 \quad \text{or, parameterized with t:} \begin{cases} x(t) = r_a.\cos(t) \\ y(t) = r_b.\sin(t) \end{cases} \qquad \textit{Equation S II-2}$$

And the radius of curvature $R_C(t)$ at angle t is given by:

$$R_C(t) = \frac{(r_a^2 \sin^2(t) + r_b^2 \cos^2(t))^{3/2}}{r_a r_b} \qquad \textit{Equation S II-3}$$

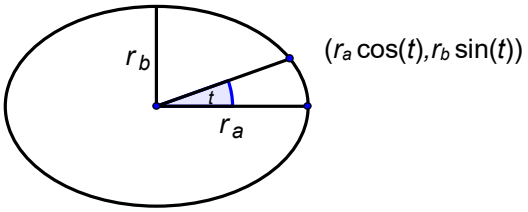

Figure S II-6. An ellipse parameterized with the angle t.

Normalizing the radius of curvature with respect to the sphere radius R and substituting $r_a = R \cdot C$ and $r_b = \frac{R}{\sqrt{C}}$ to preserve the volume of S_0, we have the following normalized radius of curvature:

$$\begin{aligned} \bar{R}_C(t) &= \frac{((R \cdot C)^2 \sin^2(t) + (\frac{R}{\sqrt{C}})^2 \cos^2(t))^{3/2}}{R \cdot (R \cdot C) \cdot (\frac{R}{\sqrt{C}})} \\ &= \frac{(C^3 \sin^2(t) + \cos^2(t))^{3/2}}{C^2} \end{aligned} \qquad \textit{Equation S II-4}$$

Now we want to calculate the distribution of normalized radius of curvature over S_C's surface.

First note that the left half and the right half of the ellipsoid is identical, and so the distribution over the whole ellipsoid is equal to the distribution over the right half of the ellipsoid.

Next, we note that the mass function of a radius of curvature $f_C(\bar{R})$ is proportional to the circumference of the corresponding circle containing the points with the specific radius of curvature.

For a given radius of curvature $\bar{R}$, the angle t defining the set of points with radius of curvature $\bar{R}$ can be found by taking the inverse of $\bar{R}_C(t)$:

$$\begin{aligned} C^4 \cdot \bar{R}_C^2(t) &= (C^3 \sin^2(t) + \cos^2(t))^3 \\ C^4 \cdot \bar{R}_C^2(t) &= (1 + (C^3 - 1)\sin^2(t))^3 \quad \text{with } \cos^2(t) = 1 - \sin^2(t) \\ C^{4/3} \cdot \bar{R}_C^{2/3}(t) - 1 &= (C^3 - 1)\sin^2(t) \\ \sin(t) &= \sqrt{\frac{C^{4/3} \cdot \bar{R}_C^{2/3}(t) - 1}{C^3 - 1}} \end{aligned}$$

, where $0 \leq t \leq \frac{\pi}{2}$, which results in $C^{-2} \leq \bar{R} \leq C^{5/2}$. For $C = 3$, this is $0.111 \leq \bar{R} \leq 15.588$.

Since the radius of the circle at angle *t* is given by Equation S II-2, we can now calculate $f_C(\bar{R})$ as follows:

$$f_C(\bar{R}) = 2 \cdot \pi \cdot \left(\frac{\bar{R}}{\sqrt{C}}\right)\left(\sqrt{\frac{C^{4/3} \cdot \bar{R}^{2/3} - 1}{C^3 - 1}}\right) = \frac{2\pi\bar{R}\sqrt{C^{4/3} \cdot \bar{R}^{2/3} - 1}}{\sqrt{C^4 - C}} \quad \textit{Equation S II-5}$$

The normalization term is:

$$\int_{\frac{1}{C^2}}^{C^{5/2}} f_C(\bar{R}) = \int_{\frac{1}{C^2}}^{C^{5/2}} \frac{2\pi\bar{R}\sqrt{C^{4/3} \cdot \bar{R}^{2/3} - 1}}{\sqrt{C^4 - C}} d\bar{R} = \frac{2\pi}{\sqrt{C(C^3 - 1)}}\left[\frac{\sqrt{C^{4/3}\bar{R}^{2/3} - 1}\ \ 15C^4\bar{R}^2 - 3C^{8/3}\bar{R}^{4/3} - 4C^{4/3}\bar{R}^{2/3} - 8)}{35C^4}\right]_{\frac{1}{C^2}}^{C^{5/2}} = \frac{2\pi}{35C^{9/2}}\ \ 15C^9 - 3C^6 - 4C^3 - 8) \quad \textit{Equation S II-6}$$

Therefore, the final distribution function $\bar{f}_C(\bar{R})$ (Equation S II-5 ÷ Equation S II-6) and its cumulative distribution function $\bar{F}_C(\bar{R})$ are:

$$\bar{f}_C(\bar{R}) = \frac{35C^4\bar{R}\sqrt{C^{4/3}\bar{R}^{2/3} - 1}}{\sqrt{C^3 - 1}(15C^9 - 3C^6 - 4C^3 - 8)} \quad \textit{Equation S II-7}$$

$$\bar{F}_C(\bar{R}) = \frac{\sqrt{C^{4/3} \cdot \bar{R}^{2/3} - 1}(15C^4\bar{R}^2 - 3C^{8/3}\bar{R}^{4/3} - 4C^{4/3}\bar{R}^{2/3} - 8)}{\sqrt{C^3 - 1}(15C^9 - 3C^6 - 4C^3 - 8)} \quad \textit{Equation S II-8}$$

Relation of Theoretical Aspect Ratio (AR_t) and Stretching Factor (C) for Prolate Ellipsoid[1]

AR_t Prolate = $C^{3/2}$ *Equation S II-9*

Relation of Theoretical Aspect Ratio (AR_t) and Stretching Factors (C_x & C_y) for Oblate Ellipsoid

AR_t Oblate = $C_x^{3/2}$. $C_y^{3/2}$ *Equation S II-10*

where C_x and C_y represent stretching factor at x and y axis, respectively. In case of C_x is identic with C_y, the Equation S II-10 can be simplified into:

AR_t Oblate = C^3 *Equation S II-11*

Table S II-3. Details of Theoretical Oblate Ellipsoid

Stretching Factor (C)	Theoretical Aspect Ratio (AR)	Relative Surface Area	Relative Density	Relative Theoretical Radius of Curvature ($R_c(t)$)	
				Minimum	Maximum
1 (Sphere)	1.000	1	1	1	1
1.5	3.375	1.32	0.75	0.13169	5.06
2	8.000	2.10	0.47	0.03125	16.00
2.5	15.625	3.19	0.31	0.01024	39.06
3	27.000	4.56	0.22	0.00412	81.00
3.5	42.875	6.18	0.16	0.00190	150.06
4	64.000	8.07	0.12	0.00098	256.00

Case study: Theoretically, by applying stretching factor of 1.5 biaxially on a sphere with a diameter of 5.519 µm, an oblate ellipsoid (~8.278 x 8.278 x 2.452 µm) owning the normal range of healthy RBC parameters[2, 3] (such as surface area and volume, ~127 μm^2 & 88 μm^3, respectively) can be generated. Through comparison with its initial sphere (that has relative surface area and radius of curvature similar to 1), this "synthetic RBC" can have 1.32-times higher surface area and extreme minimum-maximum $R_c(t)$ about 0.363 and 13.963 µm, consecutively.

Special References for This Supplemental Calculation Section

[1] Felder, B., 1966. Über die Teilchengrössenabhangigkeit der Lichtabsorption in heterogenen Systemen. II. Experimentelle Untersuchungen an Modell-Teilchen. Helvetica Chimica Acta 49, 440-453.
[2] Humphrey, J.D., O' Rourke, S. L., 2015. Stress, Motion, and Constitutive Relations, An Introduction to Biomechanics: Solids and Fluids, Analysis and Design, 2 ed. Springer-Verlag, New York, p. 384 of 692.
[3] Robertson, A.M., Sequeira, A., Kameneva, M. V., 2008. Hemorheology, in: Galdi, G.P., Rannacher, R., Robertson, A.M., Turek, S. (Eds.), Hemodynamical Flows: Modeling, Analysis and Simulation. Birkhäuser, Basel, p. 67 of 501.

III. PHAGOCYTOSIS, BIODISTRIBUTION, AND RATIONALE OF MULTIPLY BIOINSPIRED NANOPARTICLES: NON-SPHERICAL SHAPE AND CELL MEMBRANE-COATING

This chapter is in preparation for later submission as a manuscript.

All experiments and computations (i.e. bioinformatics-modelings-molecular dynamics simulations) were designed and carried out by myself, except in vivo and Atomic Force Microscope (AFM) experiments, which were conducted in close collaboration with the University of Kansas and Technische Universität Dresden, respectively. Julia Engert initiated the design of the in vivo study and collaboration with the University of Kansas and later both institutions agreed on the details thereof. A detailed list of other contributions is listed in Section “Acknowledgements”.

1. Abstract

The properties of non-spherical and cell membrane-coated nanoparticles have been proven independently to address many biophysicochemical challenges, such as higher surface area and target-specific binding for the former; immune evasion and extended blood circulation time for the latter. Nonetheless, there is still room for improvement of these systems, namely their still relatively rapid clearance, poor targeting, and absence of a system merging both aforementioned properties. Here, we developed a system merging both aspects, thereby trying to overcome these restrictions. This combined system (non-spherical bioinspired red blood cell membrane-coated nanoparticle; later abbreviated non-spherical BCCN) was substantially less phagocytized by cells of the mononuclear phagocyte system (MPS): monocytes and macrophages. Accordingly, the non-spherical BCCNs also showed a remarkably higher concentration in blood over a 72 h period and surprisingly permitted temporary accumulation in the brain for 48 h, while decreasing their uptake by liver and spleen. The non-spherical BCCNs demonstrated a ~2-fold increase of circulation time and accumulation in the brain compared to the conventional spherical BCCNs or bare non-spherical core nanoparticles (CNPs). In-depth auxiliary analyses (surface plasmon resonance, surface free energy measurements, and computational methods) rationalize the in vivo findings. The very strong and practically irreplaceable interactions of (superficially) hydrophobic proteins from the inside surface of cell membranes to the core particle materials serve as the good anchors, while also improving the right-side-out membrane orientation and integrity, regardless of protein’s alpha-helicity decrease. Additionally, this interaction also

vindicates that the better maintenance of non-spherical shape stability can only be obtained by a sufficient amount of stabilizers due to the strong affinity between particles and stabilizers. Multiply bioinspired nanoparticles, which are represented by the non-spherical BCCNs, offer a novel and promising platform for ameliorating blood pharmacokinetics and tissue delivery of nanoparticles, while concurrently evading main uptake of particles by MPS.

Keywords: particle shape stability, non-spherical particles, cell membrane-coating, monocyte-macrophage, drug delivery and targeting

Graphical Abstract

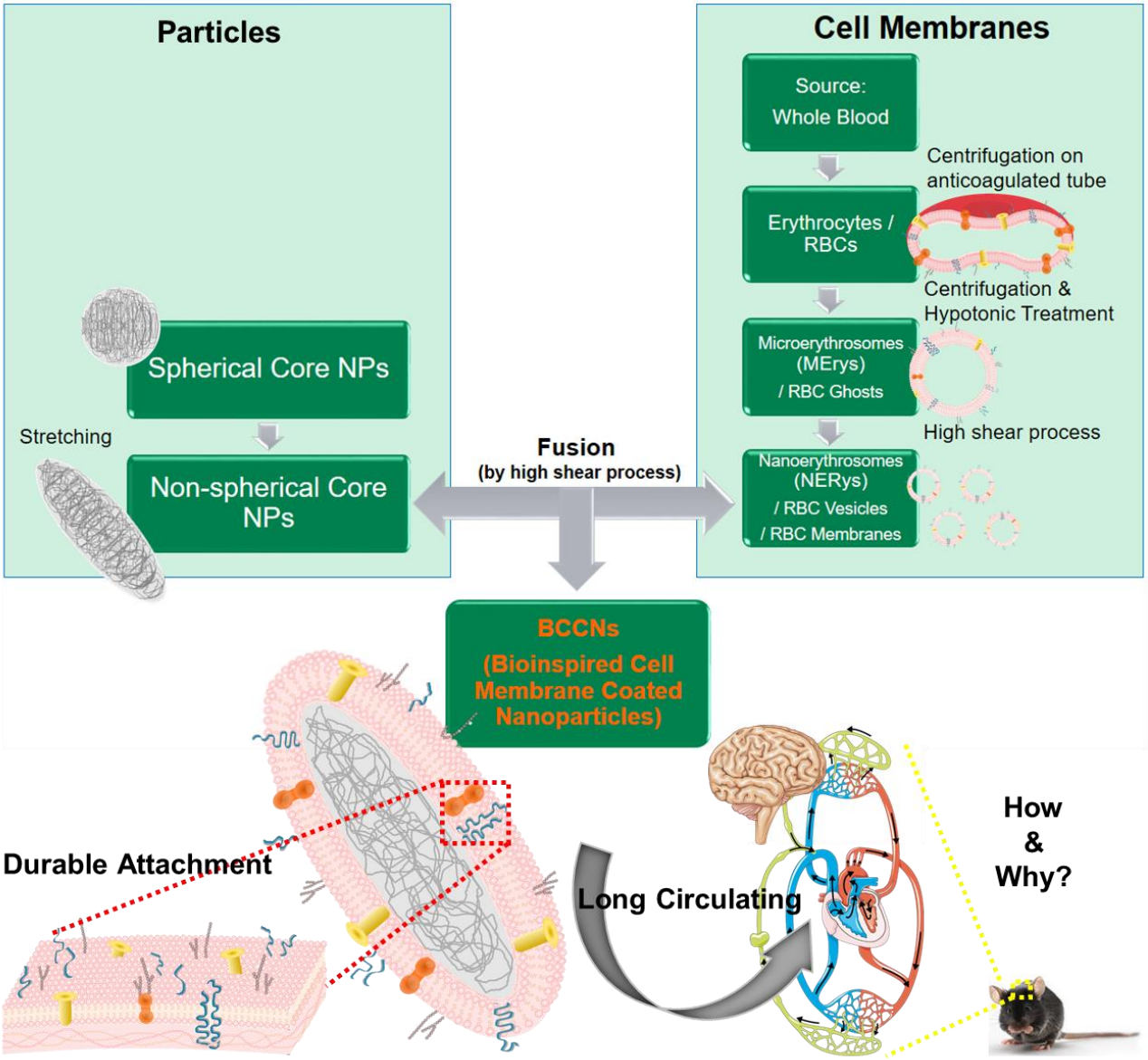

2. Introduction

Nanoparticles are widely investigated for encapsulation and targeted delivery of drugs for improving the treatment for many diseases[1]. Many preclinical studies have documented the use of nanoparticles for targeting, e.g. lung, breast, prostate, and other cancers[2]. Some of these strategies have also advanced to clinical studies and have exhibited propitious early results[3]. Encapsulation in nanoparticles provides distinct advantages over free drugs including targeting and sustained release[4]. However, nanoparticles suffer from the limitation of rapid clearance by the mononuclear phagocyte system (MPS) located primarily in the liver and spleen, thereby reducing the available dose for the disease site[5].

Numerous approaches have been proposed to address this limitation. The main classical strategy is grafting of hydrophilic polymers such as polyethylene glycol (PEG) and poloxamer molecules on the nanoparticle surface to reduce MPS uptake[6]. PEG acts to alleviate the interactions of nanoparticles with phagocytes in the MPS, thereby decreasing their immune clearance. Nevertheless, PEG-modified nanoparticles have been reported to activate the immune system and lose efficacy on repetitive administrations[7]. Conjugation of CD47 or other entities derived from this ”marker-of-self” to the surface of the nanoparticle is an alternative tactic[8-10]. Theoretically, blood elements with a favorable circulation profile may be used as “natural carriers”, bettering the nanoparticle pharmacokinetics. For instance, red blood cells (RBCs) embody an attractive carrier for optimizing nanoparticle circulation and, probably, delivery to particular tissue targets[11, 12]. Preclinical studies in various animal species revealed that the fusion of RBC membranes (also called nanoerythrosomes [NErys]; as later abbreviated here) to spherical core materials enhances core material’s delivery and therapeutic effects[9, 10, 13, 14].

On the other hand, independent in vitro studies in diverse cells of MPS demonstrated that bare non-spherical particles significantly inhibit phagocytosis[15]. This is enabled by means of higher resistance to non-specific cellular elimination compared to spherical particles, that can potentially boost the stealth properties of the membrane-coated particles. Non-spherical particles also have improved targeted interactions with cells because of a higher surface-to-volume ratio[16-18].

Therefore, attachment of NErys on non-spherical core nanoparticles (non-spherical CNPs; having the same volume as their spherical counterparts) rationally has the potential to considerably change nanoparticle fate in circulation, encompassing their phagocytosis and pharmacokinetics-biodistribution. Herein, we examine this hypothesis and show that coating of NErys on non-spherical CNPs (later called non-spherical BCCNs)

decreases nanoparticles uptake by the MPS, while prolonging their circulation time. Specifically in the section “In Vivo Biodistribution” and “Overall Rationale and Outlook”, we can see clear differences between biodistributions of the tested particles and discuss several key points in relation to biodistribution results. Additionally, further supporting analyses (e.g. surface plasmon resonance [SPR], surface free energy [SFE] measurements, computational methods, etc.) exhibit that strong and durable interactions between NErys and core material are the dominant factors for maximally protecting (especially hydrophobic) core material at least to a certain minimal radius of curvature ($R_c(t)$).

3. Materials and Methods

3.1. Materials

Spherical (⌀ 200 nm) fluorescently-loaded carboxylated poly(styrene) particles (PS-COOH) were purchased from Polysciences (Hirschberg an der Bergstrasse, Germany) and Phosphorex, Inc. (Hopkinton, MA, USA). Coumarin-6 (excitation/emission 460/500 nm[19]) from the former and Indocyanine green (ICG; excitation/emission 780/820 nm[19, 20]) from the latter were used as fluorescent loads for in vitro (uptake) and in vivo (biodistribution) studies, respectively. The average carboxylation density for both nanoparticles was 5 COOH/nm^2[21] (equivalent to a parking area of 20 Å/COOH). These starting nanoparticles were first extensively dialyzed against highly purified water using Float-A-Lyzer® G2 (molecular weight cut-off, *MWCO* 100 kDa). Thus, all produced nanoparticles for all studies herein (irrespective of functionalizations and shapes) were relatively clean from synthetic stabilizers, as exemplarily proven by Energy Dispersive X-Ray (EDX) results (Figure S III-25). Poly(vinyl alcohol) (PVA) Mowiol® 40-88 (molecular weight [MW] ~205 kDa), Coumarin-6 (Cou6), indocyanine green (ICG), fluorescamine, 1-Ethyl-3-(3-dimethylaminopropyl)carbodiimide hydrochloride (EDC), N-Hydroxysuccinimide (NHS), Hoechst 33258 solution, 4% paraformaldehyde solution, isopropanol (purity ≥ 99.5%), and Dulbecco Phosphate Buffer Saline (PBS) 1x (310 mOsm) were obtained from Sigma Aldrich (Taufkirchen, Germany). 5 kDa methoxy-PEG-amine was purchased from Nektar Therapeutics (San Francisco, CA, USA). 3-(4,5-dimethylthiazol-2-yl)-2,5-diphenyltetrazolium bromide (MTT), cathepsin S (human spleen, purity >90%, activity 183.3 mU/mg), and cathepsin B (human liver, purity >95%, activity 274 U/mg) were provided from Calbiochem (Darmstadt, Germany). Dulbecco's Modified Eagle's Medium (DMEM), Complete Gibco™ Roswell Park Memorial Institute (RPMI) 1640 Medium, and heat-inactivated fetal bovine serum (FBS) were purchased from Thermo Fisher Scientific (München, Germany). Packed human red blood cells (hRBCs) with depleted leucocyte (blood type O-) and human blood plasma (with citrate anticoagulant) were obtained from Blood Bank Klinikum Großhadern and always pre-tested for the absence of Human Immunodeficiency Virus (HIV), Hepatitis B Virus (HBV), and Hepatitis C Virus (HCV). Packed hRBCs were produced according to the "Guide to the preparation, use and quality assurance of blood components, Recommendation No. R (95) 15, 18th Edition" by the European Directorate for the Quality of Medicines & Healthcare[22], meanwhile human blood plasma was always prepared to fulfill the latest European Pharmacopoeia[23]. These blood products were only used for in vitro studies.

Endotoxin cartridges (Endosafe® -PTS™ cartridges PTS20005F; sensitivity 0.005 EU/mL) were purchased from Charles River Laboratories (Wilmington, MA, USA). Unless otherwise specified, all preparations containing proteins were stored in Eppendorf Protein LoBind® tubes (Hamburg, Germany). Highly purified water (HPW) was freshly prepared from ELGA PURELAB® Plus (Celle, Germany) and pH was adjusted to pH 7.

All other materials used in this study were of at least analytical grade, utilized as received, and purchased either from Sigma-Aldrich (Taufkirchen, Germany) or VWR Prolabo (Leuven, Belgium).

All protocols involving the use of animals (i.e. mice) were approved by the Institutional Animal Care and Use Committee (IACUC) at The University of Kansas. The animals were maintained in the Animal Care Unit with free access to food and water. Whole blood was collected from healthy female C57BL/6J mice (6 - 8 weeks; ~20 - 25 g) and was used mainly for in vivo study.

3.2. Methods

3.2.1. Experimental Laboratory Methods

3.2.1.1. Standardized Preparations of RBCs, MErys, and NErys

MErys, also known as RBCs ghosts devoid of cytoplasmic contents, were firstly prepared following previously published protocols with modifications[24]. All procedures below were undertaken aseptically under a clean bench with laminar airflow. Briefly, the obtained whole blood was immediately mixed with CPD-A solution in a volume ratio of 9:1. The whole blood was then centrifuged at 5°C 1,000 xg thrice for 5 min, then the serum and the buffy coat were carefully removed resulting in packed RBCs. These packed RBCs (with hematocrit standardized at 40% before the next processes) were washed in triplicate (1,000 xg with each 5 min at 5°C) in ice-cold PBS pH 7.4 310 mOsm prior to hypotonic medium treatment for hemolysis. The washed RBCs were suspended in 20 mOsm PBS in an ice bath for 20 min and were centrifuged again in 20 mOsm PBS at 5°C 10,000 xg thrice for each 5 min. By this step, the hemoglobin was removed, meanwhile the pink pellet MErys was collected and regularly analyzed as described in the next section: “Standardized Analyses of RBCs, MErys, NErys, and BCCNs”.

After MErys were attained, they were subjected to aseptic probe sonication utilizing a Bandelin® Sonopuls GM 3200 (200 W 20 kHz; Berlin Germany) with the MS 72 probe and maximum temperature set 8°C on the device. The set-up was for a 5 min-cycle: at 32% amplitude and pulsative mode (4 s on and 2 s off). The resulted NErys were also regularly analyzed as described in the next section: “Standardized Analyses of RBCs, MErys, NErys, and BCCNs”. Figure S III-1a shows a macroscopical appearance of these preparations.

3.2.1.2. Standardized Analyses of RBCs, MErys, NErys, and BCCNs

For method standardization, it is important to characterize the counts of RBCs, MErys, and hemoglobin concentration. By knowing these parameters, it can be assured that the processed RBCs were from healthy

cells as further characterized also by RBC indices: (a) mean corpuscular volume (MCV), (b) mean corpuscular hemoglobin (MCH), and (c) mean corpuscular hemoglobin concentration (MCHC). The equations thereof are:

$$\text{MCV (fL)} = \frac{\text{Hematocrit (\%) x 10}}{\text{Count of RBCs } (10^6 \text{ cells}/\mu\text{L})}$$

$$\text{MCH (pg)} = \frac{\text{Hemoglobin (g/dL) x 10}}{\text{Count of RBCs } (10^6 \text{ cells}/\mu\text{L})}$$

$$\text{MCHC (g/dL)} = \frac{\text{Hemoglobin (g/dL) x 100}}{\text{Hematocrit (\%)}}$$

The used RBCs were proven to be in the normal range[25] with MCV 81.1 fl, MCH 29.2 pg, and MCHC 35.9 g/dL. They should be derived from healthy cells. MErys and NErys were virtually depleted from hemoglobin because their hemoglobin level was not detectable by Drabkin's reagent (Table S III-15) and proven under a light microscope (Keyence BZ-8100 Biozero; Neu-Isenburg, Germany) in phase contrast mode (Figure S III-1b). The details of RBCs and MERys counting using a flow cytometer are depicted in Figure S III-1c.

Other methods to characterize physicochemical properties (i.e. Dynamic Light Scattering [DLS], Differential Scanning Calorimetry [DSC], Scanning Electron Microscope-Energy Dispersive X-Ray [SEM-EDX], and Atomic Force Microscopy [AFM]) were the same as previously described[16].

Protein, phospholipid, and cholesterol concentrations of samples were determined according to Bicinchoninic Assay (BCA)[26], Stewart Assay[27], and Enzymatic Cholesterol Quantification Kit[28], respectively. An equivalent amount of NErys and bare core particles was used as a positive and a negative control, respectively.

3.2.1.3. Preparation of Non-spherical Core Nanoparticles (CNPs) by Film-Stretching Method

First, the stretching method published by Felder et al. (1966) and Champion et al. (2007) was utilized to prepare non-spherical (core) nanoparticles. An amount of Mowiol® 40-88 intended for 5% w/w final concentration was wetted in HPW and glycerin (final concentration 2% w/w) at room temperature followed by heating the mixture at 90°C for 5 minutes. As the heated solution was cooled to room temperature, mixing was continued and afterward, the spherical particles were added to give a final concentration of 0.3% w/w. The mixture was poured into molds and dried for overnight at room temperature under a fume hood. The dried films (with thickness around 70 µm, residual moisture 6 - 8%, and effective stretching area of 1 x 9 cm) were stretched using a custom build stretching device (to 2- and 3-fold their original length in one direction

for prolate; 1.5-fold their original length in two directions for oblate) under a dry heat at a constant stretching speed of 1 mm/s and 120°C.

After stretching, the films were cooled down rapidly until the temperature was lower than its bulk Tg value while the strain was still applied. To harvest the non-spherical (prolate) particles, the stretched film was dissolved in phosphate buffer saline (PBS) pH 7.4 310 mOsm 5°C with the aid of moderate agitation in continuous mode on a mini vortexer (VWR, Darmstadt, Germany) for at least 30 minutes, followed by bath sonication (Bandelin® RK510, Berlin, Germany) for 15 minutes until the PVA film was totally dissolved. Later, particles were purified three times with PBS pH 7.4 310 mOsm 5°C (10,000 xg at 5°C for each 10 min) (first by 20,000 xg for 10 min at 5°C, and the two next by 10,000 xg at the same duration and temperature). The standardized washing factor and redispersion energy were 100^3x (thrice of each 100x) and 3.9 kJ/m^3 (Bandelin® Sonopuls GM 3200 200 W 20 kHz [Berlin, Germany] with the MS 72 probe), respectively. The maximum temperature during redispersion was set at 8°C. To ensure comparability, the spherical particles employed in all studies were treated in the same treatment (e.g. embedment in PVA film until final washing), but stretching was not applied to the PVA film.

3.2.1.3.1. Preparation of BCCNs

Non-spherical (or spherical) BCCNs were produced by a fusion between core nanoparticles (1 mg/mL) and NErys, which both were dispersed in a physiologically relevant medium (i.e. PBS pH 7.4 310 mOsm). The mixtures were sonicated using Bandelin® RK510 bath sonicator (Berlin, Germany) at a frequency of 35 kHz and power of 160 W for 20 min. After sonication, CNPs were incubated for 12 h at 15°C to fix or harden the NEry coating. Next, the resulting BCCNs were washed 3 times with PBS pH 7.4 310 mOsm (10,000 xg at 5°C for each 10 min). The standardized washing factor and redispersion energy were 100^3x (thrice of each 100x) and 3.9 kJ/m^3 (Bandelin® Sonopuls GM 3200 200 W 20 kHz [Berlin, Germany] with the MS 72 probe), consecutively. The maximum temperature during redispersion was set at 8°C. Similar to the previous reports[13, 29], careful centrifugation is proper to remove excess membrane-components remaining in the supernatant.

3.2.1.3.2. Preparation of PEGylated Particles as References (Used for In Vitro Study)

PEGylated particles were prepared by covalent bonding (represented by typical binding [free] energy 50 to 150 kcal/mol[30]) between 5 kDa methoxy-PEG-amine and the PS-COOH particles (which were already embedded in the PVA film [for the PEG-spherical ones] and stretched within PVA film [for PEGylated non-spherical ones] as described in the previous Section II.3.2.1.3) using carbodiimide coupling reaction. Briefly,

PS-COOH particle suspensions (1% w/w; 0.2 mL) were washed in triplicates as described in our previous report[16]. Then, they were resuspended to 2-fold dilution in HPW in a 2 mL microcentrifuge tube. PEG was added to the particle suspension in 5-fold excess particle mass. After gentle mixing, to dissolve the PEG, N-Hydroxysuccinimide (NHS) was added to the tube, followed by 600 µL of PBS pH 7.2 310 mOsm, and 1-ethyl-3-(3-dimethylaminopropyl) carbodiimide hydrochloride (EDC). Final NHS and EDC concentrations were 10 mM and 6 mM, respectively. Particle suspensions were placed on a Thermomixer Comfort (Eppendorf, Hamburg, Germany) at 900 RPM for 4 h, then centrifuged and washed thrice[16] with PBS pH 7.4 310 mOsm. Later, particles were resuspended in PBS pH 7.4 310 mOsm to the original concentration.

The PEGylation degrees of nanoparticles were quantified by the primary amine-reactive fluorescent dye (i.e. fluorescamine) using a Cary Eclipse fluorescence spectrophotometer (Agilent, Boeblingen, Germany). The excitation wavelength was set to 390 nm and emission was observed at 475 nm. The fluorescamine intensities of unreacted PEG for PEGylated and non-PEGylated particles were compared to calculate the PEGylation degree. Conversion to the average distance between two terminally attached PEG molecules and PEGylation density were performed as reported elsewhere[31].

3.2.1.4. Shape Stability of Non-spherical Nanoparticles

The shape stability of non-spherical nanoparticles is depicted primarily by aspect ratio (AR) values and supplementarily supported by hydrodynamic size, polydispersity index (PDI), and zeta potential via dynamic light scattering (DLS) as well as pH value (MP220, Mettler Toledo, Giessen, Germany). The aspect ratio for all figures derived from scanning electron micrographs was determined manually from at least 20 particles using ImageJ software (National Institutes of Health). Typical shifting time ($t_{1/2}$; defined as the needed time for a half decrease of the initial AR for prolate particles or apparent diameter for oblate particles) was deduced from the fitting of obtained experimental aspect ratio data over time fitted into 0^{th}, 1^{st}, and 2^{nd} order of kinetics equation. The best fit was displayed with R^2 closer to 1.

3.2.1.5. Scanning Electron Microscope-Energy Dispersive X-Ray (SEM-EDX)

The size, morphology, and aspect ratio of different particles were investigated using scanning electron microscopy. Each particle suspension (5 µL) at a concentration of 800 µg/mL was fixed onto filter paper 589/2 (Hahnemühle FineArt GmbH, Dassel, Germany) 25 mm^2 attached to carbon self-adhesive tape on aluminium stubs. The samples were sputtered with carbon and captured at 50,000x magnification in a FEI Helios G3 UC with EDX, Scanning-Transmissions-Detector, and Focused Ion Beam (FIB) (FEI, Gräfelfing, Germany) at 2 kV (for all nanoparticles due to the best sample stability [no melting] under electron excitation)

with a 4 mm working distance. For EDX measurement, the voltage was set up to 30 kV.

3.2.1.6. Transmission Electron Microscopy (TEM)

The morphology of samples (NErys, CNPs, and BCCNs) was investigated with TEM after fresh negative staining of samples with 1% (w/v) phosphotungstic acid (PTA) pH 7 on a FEI Titan Themis electron microscope (Hillsboro, USA) at an acceleration voltage of 120 kV. The dispersion medium of samples was freshly changed into HPW before TEM to give clear micrographs that are free from salt crystals. The amount of samples at a concentration of about 1 mg/mL (the final concentration of both non-spherical and spherical nanoparticles were made equivalent) and PTA were 10 and 5 µL, respectively. Both of them were mixed directly on the formvar/carbon films on a 400 mesh Cu grid (Agar Scientific, Wetzlar, Germany) for 1 min by pipetting the mixture up and down several times. After incubation for 1 min, the excess droplet was gently absorbed from the side of the grid by filter paper 589/2 (Hahnemühle FineArt GmbH, Dassel, Germany) until the thin film of the sample appeared.

3.2.1.7. Dynamic Light Scattering (DLS)

DLS experiments were conducted using a Zetasizer Nano ZS (Malvern, Herrenberg, Germany) equipped with a 633 nm He-Ne laser. Using this instrument, the hydrodynamic size/diameter (Z-Average) of particles was measured based on light intensity fluctuations of scattered laser light detected at angle 90°, whereas the zeta potential of particles was determined based on their electrophoretic mobility. A 200 µL of each nanoparticle sample was measured in disposable poly(methyl methacrylate) (PMMA) cuvettes (Brand, Wertheim, Germany) with a path length of 12.5 mm after an appropriate equilibration time (i.e. 60 s) at 25°C. Samples were analyzed in triplicates, each triplicate with 10 sub-runs. The average hydrodynamic size and polydispersity index (PDI) were calculated by the Malvern Dispersion Technology software (version 4.20, Malvern, Herrenberg, Germany).

3.2.1.8. Tunable Resistive Pulse Sensing (TRPS)

The additional size distribution analyses (to DLS) and concentration of NErys, CNPs, and BCCNs were measured by TRPS on a qNano Gold instrument equipped with Izon Control Suite Software 3.3 (Izon Science, Oxford, UK). Prior to the measurements, a nanopore NP 200 (with a size range of 80 - 630 nm) was fitted into the qNano Gold and a stretch of 47 mm was applied. A volume of 70 µl and 35 µl of filtered (0.22 µm) manufacturer's coating solution was loaded to the lower and upper fluid levels, respectively. Subsequently, pressure of +20 mbar was applied for 30 minutes, followed by applying a pressure of -20

mbar for 15 minutes. The coating solution was removed from the upper and lower fluid levels which were both rinsed with HPW and the upper fluid level was additionally dried with pressurized air. Calibration beads (CPC 400) were diluted twice 1 to 100 in filtered electrolyte for a final dilution of 1/10,000 in electrolyte. For the measurements, a volume of 35 µl of electrolyte was added to the upper fluid level and a pressure of +10 mbar was applied to check the cleanliness of the system (less than 10 particles/10 minutes were required). After cleaning the upper fluid level, a volume of 35 µl of the sample (calibration beads or samples of interest) was added to the upper fluid level and a pressure of 10 mbar was applied and subsequently, the measurement was started. A particle read of > 500 particles or a maximum recording time of 10 minutes were chosen as limits. For calibration beads measurements, the limit was set to a particle rate of 250-400 particles/min. The recording was paused if blockages occurred and the nanopore was unblocked according to the manufacturer's advice. All samples were run under the same stretch, baseline (by adjusting the voltage), and pressure.

3.2.1.9. Atomic Force Microscope (AFM)

Determination of fine sample information details (topography), Young's modulus, and surface roughness of samples were conducted using an atomic force microscope (AFM) Ntegra Solver (NT-MDT, Moscow, Russia) equipped with a vibration-damped table under ambient conditions (relative humidity ~50% and room temperature ~25°C) using a conventional measuring head in intermittent contact mode (to prevent sample surface damages and permit repeated examination of the same sample region[32]) with a scan speed of 0.1 - 0.5 Hz. For sample preparation, 10 µL of particle dispersions was placed on a 12.5 x 12.5 mm freshly cleaved mica surface and incubated for 5 min. Later, the surface was additionally washed once with 30 µL HPW (if needed) and/or dried under a nitrogen atmosphere right away. The HA_NC polysilicon cantilever (spring constant = 3.5 N/m; resonant frequency 140 kHz) was equipped with a conical silicon tip (typical radius of curvature 10 nm and cone angle 30°). For each data point, 15 particles or more per batch were examined by measuring triplicate, with 15 s approach and 15 s retreat time. Measurements with inconsistent force-distance curves resulting from the movement of the particles during the probing or unsuitable spherical interaction were disregarded. The data were analyzed with the Image Analysis 3.5 software. Meanwhile, the surface roughness parameter, i.e. the root mean square (R_{rms}), was calculated with the same data points as Young's modulus measurement. The attained pictures had at least a resolution of 512 x 512 pixels.

3.2.1.10. Differential Scanning Calorimetry (DSC)

Dry glass transition temperatures (dry Tg_s) of bulk materials and nanoparticles were measured using DSC

Mettler Toledo 822e (Gießen, Germany). Samples (~5 mg) were heated in hermetically sealed aluminium pans at a rate of 20°C/min up to 120°C under a dynamic nitrogen atmosphere. Unless otherwise specified, all reported Tg_s are the midpoint value between the tangents of the glass and liquid line from the total heat flow.

3.2.1.11. Particle Incubation in Blood Plasma

All particle suspensions (1 mg/mL) were incubated with different concentrations of human blood plasma in 10 mM phosphate, 0.15 M NaCl, 25 mM citrate, pH 7.4, for 1 h at 37°C (total volume, 1 mL). To ensure comparability between the results, the ratio of total particle's surface area-to-plasma concentration was kept the same for all similar particle sizes. The samples were centrifuged to sediment the particle-protein complexes. The sediment was resuspended in PBS pH 7.4 310 mOsm, transferred to a new tube, and centrifuged again to pellet the particle-protein complexes using our aforementioned standardized washing method for BCCNs. After the third washing step, the supernatant did not contain any detectable amount of proteins (detected by micro BCA assay) and the sediment was later analyzed for its composition by the following electrophoresis.

3.2.1.12. Determination and Confirmation of protein composition (MErys, NErys, and BCCNs) by SDS-PAGE, Bioanalyzer 2100, and Western Blot

To solubilize the membrane proteins from core nanoparticles, the particles were treated with SDS 0.1% beforehand SDS-PAGE and Bioanalyzer analysis. RBCs, MErys, and NErys were also run as comparisons.

i. SDS-PAGE

All samples were mixed in NuPAGE® LDS sample buffer. The samples and marker Mark12™ were then run on a NuPAGE® Novex 4 - 12% Bis-Tris 12-well minigel in 3-(N-morpholino) propanesulfonic acid running buffer using NovexSureLockXcell Electrophoresis System. The samples were run at 200 V for 40 min, and the resulted polyacrylamide gel was stained in SimplyBlue overnight for visualization.

ii. Bioanalyzer 2100

In principle, the analysis using the Bioanalyzer method is based on capillary electrophoresis on a chip system (CE-SDS), which provides sizing and quantification information of the proteins. Samples were incubated with sodium dodecyl sulfate (SDS)-containing sample buffer at 90°C (Thermomixer Comfort, Eppendorf, Hamburg, Germany) for 5 min, centrifuged, and loaded on the chip. Fluorescent dye molecules intercalated with protein-SDS micelles and the complexes were detected by laser-induced fluorescence. Data were translated into gel-like images. This data supports the results of conventional SDS-PAGE.

iii. Western Blot

All samples were analyzed by Western Blot following standard protocols and using specific antibodies (CD47; B6H12) donated by Santa Cruz Biotechnology (Heidelberg, Germany).

3.2.1.13. Surface Hydrophobicity

3.2.1.13.1. Surface Free Energy (, Surface Polarity, and Interfacial Tension) as well as Surface Pressure Measurement

Initially, the formation of the material's thin layers and other technical details were applied as described elsewhere[16, 33]. Afterward, the water contact angle (WCA) and diiodomethane contact angle of the samples were measured by using a fully automated Krüss DSA25E (Hamburg, Germany) contact angle goniometer in sessile drop mode (needle NE44 Ø 0.5 mm) at 20 ± 1°C. These values permit the determination of samples' surface free energy (SFE), surface polarity (X_p)[16], and material-water interfacial tension(IFT)[34]. Besides the contact angles, these three parameters are classified as primary interfacial activity parameters[16].

Surface pressures of samples in HPW were analyzed using a Kibron Micro Trough XL Langmuir-Blodgett film balance (Helsinki, Finland) at the same abovementioned temperature. Equilibrium surface pressure is defined as the maximum surface pressure that was stable in a range of ± 0.2 mN/m within 0.5 h. The range and the duration for this definition were the same as for the determination of (HPW/aqueous sample) surface tension in our previous work[16]. Recall that the surface pressure is the surface tension difference between HPW and each aqueous sample.

3.2.1.13.2. Organic Dye Adsorption Method

The hydrophobicity of the nanoparticle surfaces was determined in accordance with the Rose Bengal adsorption method[35]. Briefly, a 1,000 µg/mL of Rose Bengal dye, dissolved in 0.1 M phosphate buffer pH 7.4, was added to each nanoparticle dispersion containing varying concentrations of nanoparticles to a final volume of 1 mL. Final Rose Bengal concentration was 20 µg/mL for all dispersions, whereas final nanoparticles concentration (dispersed in 0.1 M phosphate buffer) was 500 - 2,000 µg/mL. Nanoparticles were incubated for 3 hours at 25°C (Thermomixer Comfort, Eppendorf, Hamburg, Germany) with the dye, then centrifuged for 2 hours at 21,000 xg (Centrifuge 5418, Eppendorf, Hamburg, Germany). The amount of dye in the supernatant was quantified using UV/Vis spectroscopy (NanoDrop™ 2000c, Thermo Fisher Scientific, München, Germany) at a wavelength of 543 nm. Rose Bengal encounters partitioning between the surface of the particles and the dispersion medium.

For data evaluation, the Scatchard equation was used as followings:

$$\frac{r}{a} = KN - Kr$$

where r is the amount of Rose Bengal adsorbed per mg nanoparticles (µg/mg); a is the equilibrium concentration of Rose Bengal (µg/mL); K is the binding constant (mL/µg); and N is the maximum amount bound (mg/mg).

3.2.1.14. Surface Plasmon Resonance (SPR)

Gold sensor chips (plain, carboxylated, or PEGylated [2 kDa]) and an OpenSPR from Nicoya Lifesciences (Kitchener, Canada) were utilized to evaluate the kinetics and binding affinities of samples to the material surfaces. The studies were performed with the 300 s on-rate, standardized 300 s off-rate, and constant flow rate of 20 µL/min measured at room temperature. After the (e.g. 300 s) dissociation of the analytes, the chip was regenerated with HCl solution (10 mM pH = 2.0 at a constant flow rate of 150 µL/min) until a stable baseline is achieved (~30 s). Different sample concentrations were diluted in the running buffer (PBS pH 7.4 310 mOsm). The data were normalized to their corresponding baseline and analyzed using the TraceDrawer® 1.8.1 Software from Ridgeview Instruments AB (Vänge, Sweden).

3.2.1.15. Protein Secondary Structure Determination (via Circular Dichroism [CD] and Fourier Transform Infrared [FTIR] Spectroscopy)

Far-UV CD spectra of all samples (particles concentration ~1 mg/mL; protein concentration 0.2 mg/mL regardless of samples [e.g. MErys and derivatives thereof, albumin, etc.]) were collected at 25°C using a Jasco J-810 spectropolarimeter (JASC, Pfungstadt, Germany). Quartz cuvettes with a 0.1 cm wavelength path were used for the measurements. 10 accumulations of each sample were taken at a speed of 20 nm/min. The spectrum of the respective buffer was subtracted for each sample. The spectra were smoothed using the Savitzky-Golay algorithm[36] with 15 smoothing points and polynomial order of 3, as well as the molar residue ellipticity (or also called Δε) was calculated as described elsewhere[37]. The secondary structure content was assigned using the K2D3 software[38] with normalization to the adsorbed proteins on particles in the separated experiments.

Meanwhile, FTIR spectra were obtained by Fourier transform infrared spectroscopy (FTIR) using a Bruker Tensor 27 spectrometer equipped with BioATR II Cell (Ettlingen, Germany). Samples (1 mg/ml particles) were analyzed by adding 35 µl thereof into the cell. The measurement temperature was controlled at 25°C using a water bath. Each spectrum comprises of an average of 120 scans at the resolution of 4 cm^{-1}. All

measurements were performed thrice in the range of 850 and 4000 cm^{-1} with the fitting procedure was focused on the amide I band (1720 - 1590 cm^{-1}) using Gaussian bands. Peak positions were assigned from the literature[39], as displayed here in Figure S III-10b.

3.2.1.16. Determination of Fluorescence Stability Incorporated into Nanoparticles

All fluorescently-loaded particles (1 mg/mL) were incubated in the same medium as for the shape stability study at 37°C and observed over 96 hours. At each predetermined time point, particles were 1x centrifuged 10,000 xg for 10 min to obtain the supernatant (, while the particles were redispersed using our standardized method[16]). The supernatants were analyzed by a Cary Eclipse fluorescence spectrophotometer (Agilent, Boeblingen, Germany) for free fluorescent dye. All measured values were on a low baseline level (Figure III-2f).

3.2.1.17. Endotoxin Determination

Endotoxin content was tested using an Endosafe® nexgen-PTS™ reader (Charles River Laboratories, Wilmington, MA, USA) after a 20 to 40-fold dilution of the particle preparations with HPW. The test was conducted according to the manufacturer's instructions. The endotoxin levels of all samples were found to be below the limit of 1 EU/mg (for 1 mg/mL particle concentration).

3.2.1.18. Phagocytic Cell Lines

Mouse macrophage (J774A.1) and human monocyte (THP-1) cell lines were attained from the German Collection of Microorganisms and Cell Cultures (Heidelberg, Germany) and kindly donated by Dr. Aditi Mehta (group of. Prof. Olivia Merkel, Ludwig-Maximilians-Universität München, Germany), consecutively.

3.2.1.19. Uptake of Particles into Phagocytes

The uptake of nanoparticles (BCCNS) in J774.A1 macrophages and THP-1 monocytes was analyzed with coumarin-6 loaded particles. J774.A1 macrophages were cultured at 4 $x10^6$ cells / 75 cm^2 in cell culture flasks (Corning®, Heidelberg, Germany) and cultivated for 3 days (37°C, 5% CO_2) in DMEM supplemented with 1% (w/v) penicillin, 1% (w/v) streptomycin, and 10% (v/v) heat-inactivated FBS. Cells were harvested at 5 x 10^7 cells / 75 cm^2 by a cell scraper and later gently tapping the culture flask against a table to optimally detach cells. The cells were centrifuged (400 xg, 5°C, 5 min) and washed with DMEM three times. 250 µl suspension of these J774.A1 macrophages was seeded at a density of 1 x 10^5 cells/well in a 24-well plate on the night before the experiment. 10 µl of a 1 mg/mL nanoparticle suspension was added in triplicate to the cells

and homogenized by gentle pipetting up and down. Negative control using 10 µl PBS pH 7.4 310 mOsm was added in parallel to the cells. The mixtures were incubated for 24 h at 37°C and 5°C.

THP-1 cells were seeded in complete Gibco™ RPMI 1640 medium supplemented with 1% (w/v) penicillin, 1% (w/v) streptomycin, and 10% (v/v) FBS. For the uptake study, 1 x 10^5 THP-1 cells were seeded to each well of a 24-well plate. The same condition and particle concentration (as described above for J774.A1 cells) were also applied to THP-1 cells.

3.2.1.20. Flow Cytometry

For flow cytometry measurements, samples were analyzed using an Attune NxT flow cytometer (Thermo Fisher Scientific, München, Germany) equipped with forward scatter, side scatter, and fluorescence detector. 488 nm excitation and 530/30 emission filter were applied for fluorescence-containing samples. Uptakes of fluorescence-containing samples into J744.A1 macrophages and THP-1 monocytes were quantified with forward scatter (FSC) sensitivity of 200 volts and green fluorescence detector sensitivity (or also called side scatter [SSC]) of 360 volts. A triplicate of 10,000 events each was collected per group. Flow cytometry data were analyzed using the Attune software using the median fluorescence per cell.

3.2.1.21. Confocal Laser Scanning Microscopy (CLSM)

The samples containing fluorescently-loaded particles (including the ones which were incubated with the cells in the uptake study) were washed three times with PBS pH 7.4 310 mOsm and fixed with 4% paraformaldehyde. A cell core staining was applied using Hoechst 33258 solution for 15 minutes. The uptake and internalization of fluorescently-loaded samples (CNPs: excitation/emission 460/500 nm; NErys & their part on BCCNs: excitation/emission 365/460 nm) into cells were examined using an inverted Leica TCS SP8 confocal laser scanning microscope (Leica Mikrosysteme Vertrieb GmbH, Wetzlar, Germany) with the identical setting for all groups. A 63x oil immersion objective was used for acquisition. Ultraviolet laser (364 nm), Argon laser (488 nm), and HeNe laser (543 nm) were used as excitation wavelengths, corresponding to the emissions of band pass (BP) 385 - 470 nm, BP 505 - 530 nm, and long pass (LP) 560 nm, respectively. All images were averaged 4 times and scan speed was set to 6. Experiments were performed in triplicate.

3.2.1.22. In Vitro Cytotoxicity Assay

Cytotoxicity of samples (NErys, CNPs, and BCCNs) was assessed as cell viability of mouse macrophages-human monocytes and was compared to the negative and positive controls (only dispersant of samples, namely PBS pH 7.4 310 mOsm, and 0.1% Triton-X in the dispersant, consecutively) using 3-(4,5-

dimethylthiazol-2-yl)-2,5-diphenyltetrazolium bromide (MTT)[40]. Briefly, cells were seeded and treated as mentioned earlier in the section “Uptake of Particles into Phagocytes”. After the same duration of treatment as described above, MTT solution in PBS (5 mg/mL; 40 µL) was added to each well under the exclusion of light. After 4 h incubation of MTT solution, the liquid medium was removed carefully and the precipitated blue formazan product was extracted in acidified isopropanol (0.04 N HCl in isopropanol; 250 µl) by shaking for 5 min at 300 RPM on a platform shaker (Heidolph Rotamax 120, Schwabach, Germany). These extracts were later centrifuged at 10,000 xg at 25ºC for 20 min to avoid light scattering effects from the particles. 150 µl of each extract’s supernatant was transferred to a 96-well plate (Greiner Bio-One International GmbH, Frickenhausen, Germany) and absorbance was measured at 570 nm using a FLUOstar Omega microplate reader (BMG Labtech, Ortenberg, Germany). The assay was performed in triplicates and pure DMSO was used as a blank.

3.2.1.23. In Vivo Biodistribution Studies

All protocols involving the use of mice were approved by the Institutional Animal Care and Use Committee (IACUC) at The University of Kansas. The experiments were performed on healthy female C57BL/6J mice (6 - 8 weeks; ~20 - 25 g) from The Jackson Laboratory (Bar Harbor, ME, USA). There were 3 time points (24-, 48-, and 72-h) and 5 treatment groups (spherical CNP, spherical BCCN, non-spherical CNP, non-spherical BCCN, and negative control: PBS pH 7.4 310 mOsm); which each treatment group contained three mice. To study the biodistribution of the nanoparticles in various tissues, all mice received an intravenous injection of 5 mg particles/kg (~100 µL) of corresponding nanoparticles (1 mg/mL NIR dye[Ex/Em 780/820 nm]-loaded nanoparticles) through the tail vein. At each of the time points following the particle injection, 3 mice were selected and sacrificed by CO_2 overdose. Later, to enable more accurate fluorescence quantification in each organ[2], mice brains, livers, spleens, lungs, kidneys, and hearts were collected after perfusion using PBS. The collected organs were carefully weighed. The total weight of blood was estimated as 6% of mouse body weight and the collected blood samples were diluted with 100 µL PBS in a 96-well plate before fluorescence measurement. The fluorescence intensity of each sample was determined using an Odyssey CLx NIRF imaging system from LI-COR Biosciences (Lincoln, NE, USA). To calculate the terminal half-lives of nanoparticle samples, these parameters were best fitted to the 1st order of kinetics equation.

3.2.1.24. Statistical Analysis

Unless otherwise stated, for all experiments (not limited to the experimental laboratory methods) describing p values, a paired Student’s t-test, unpaired Student’s t-test, or one-way ANOVA was performed, assuming

significance at $p \leq 0.05$.

3.2.2. Computational Laboratory Methods (Auxiliary Analyses)

3.2.2.1. Bioinformatic Analyses

The source for bioinformatic analyses was one of the most comprehensive protein information databases, specifically the reviewed (high quality manually annotated & non-redundant) canonical UniProt database (or specifically so-called Swiss-Prot; 2018 & 2021 release; accessed July 2018 & updated December 2021; both 20,386 entries for the human category)[41-43]. The reviewed canonical human UniProt database was further selected as the main base for biomolecular corona analysis because of these 3 considerations: (a) utilized human blood proteins and erythrocytes are mainly used in the current laboratory experiments, (b) other researchers also generally used human blood plasma / serum for protein corona analysis, and (c) still unsatisfactory annotation completeness of other species proteins (e.g. mouse[44]) in any currently existing databases (the most complete one was mouse UniProt database; accessed July 2018; 16,985 entries). For biomolecular corona analysis and later homology modeling of other species proteins, if applicable, these were BLAST-ed against the reviewed human UniProt database and their homolog human proteins were chosen based on the highest E-value and Score. It is important to do so because of the still unsatisfactory annotations of other species proteins in existing databases[45] and anticipation of any discrepancy of biological pathways in different species[46]. The used human UniProt database was also bioinformatically classified based on protein physicochemical and biological/functional properties. For comparison, the Global Substance Registration System (GSRS) of the U.S. Food and Drug Administration (FDA)/DrugBank database[47, 48, 49] (~6,000 entries in December 2021[48]) was used as a sequence source for therapeutic proteins (i.e. naturally unavailable due to their productions by genetic engineering).

For the whole sequence protein hydrophobicity indicator, the GRAVY (Grand Average of Hydropathy) score was calculated according to Kyte-Doolittle[50]. Protein's isoelectric point (IEP) and surface charge (zeta potential) at various pHs were calculated based on the specific Bjellqvist method, showing high accuracy because of the sequence length consideration[51, 52]. The aliphatic index (AI) of a protein, defined as the relative volume occupied by aliphatic side chains (alanine, valine, isoleucine, and leucine), and %hydrogen bond-forming amino acids (serine & threonine) were calculated according to Ikai[53]. In general, the greater the values thereof are, the higher the thermostability of protein is. Also, the values thereof are considered an attractive protein stability parameter (for refolding) against denaturants[53]. WEBnm@ v2.0 software was used to determine the global elasticity (/ deformation energy) of proteins using Normal Mode Analysis (NMA)[54];

the lower the values are (which are unitless), the softer / more flexible / elastic the proteins are. For multidomain proteins, the lower the values are, the higher the hinge rigidities are, corresponding to higher protein aggregation.

For the construction of protein-protein interaction (PPI) networks, STRING-DB v11.0 was used[55] and the full list of proteins arranging interactomic data is available on request. Confidence (combined) scores ≥ 0.4 were classified to be significant interactions/associations. Subsequently, they were visualized as edges (with a differential thickness corresponding linearly to their scores and) connecting protein nodes. The obtained protein-protein interaction networks (or also called protein interactomes) were also visualized and scored by the Cytoscape software[56] and the cytoHubba plugin[57]. The newly proposed and popular centrality parameters generated by the cytoHubba plugin, namely Closeness and MNC (Maximum Neighborhood Component), respectively[57], were used. These centrality parameters inform us of a proportional score and notion of which nodes have the higher impact on the network. A combination of methods for portraying the impact degree of proteins in a protein-protein interaction network is required to minimize the heterogeneous nature of the biological network. The higher the scores of the proteins (generated by these parameters) are, the higher the connectivity or interconnectedness of such proteins are[57].

3.2.2.2. Calculation Details

For synthetic molecules (including oligomers of polymers as molecular models[58]), logP values (against 1-octanol) were calculated using the highest accuracy consensus method[16, 59] in Plugins of MarvinSketch software version 17.1.23.0 (2017), ChemAxon (http://www.chemaxon.com). The used molecular structures were either downloaded as .sdf files from PubChem[60] (if available) or built using the aforementioned MarvinSketch software. Later, in the Maestro 11 interface of Schrödinger Software Release 2017-4[61], these structures were minimized using the OPLS(3) force field and the Connolly's molecular surface area (CMSA) thereof was calculated using a probe of 1.4 Å.

3.2.2.3. Correlation to Experimental Hydrophobic Interaction Chromatography (HIC) and Interfacial Activity Parameters

The protein surface hydrophobicity index (Φ), having a strong relation to the HIC results (i.e. dimensionless retention time [DRT] / apparent retention factor), was developed from the modified methodology from Lienqueo et al.[62] employing proteins' 3D-structures. Experimental HIC results were obtained under generic conditions: Phenyl-Sepharose column (e.g. MabPac HIC-10) 100 mm x 4.6 mm column, mobile phase "A": 2

M ammonium-sulfate + 0.1 M phosphate (pH = 7.0), mobile phase “B”: 0.1 M phosphate (pH = 7.0), 0 - 100% B gradient in 10 min, flow rate: 1 mL/min, temperature: 25°C.

It is assumed that each amino acid on the surface of a protein has a relative contribution to the surface properties, then:

$$\Phi_i = \Sigma(\Phi_{aan}.r_{aan}) \qquad \textit{Equation S III-1}$$

where Φ indicates the initial calculated value of the surface hydrophobicity for a given protein, n (n = 1, 2, …, 20) is the 20 different amino acids, and Φ_{aan} is the value of the hydrophobicity related to amino acid “n”. r_{aan}, the relative surface area exposed for each amino acid “n” on the surface, is defined as:

$$r_{aan} = \frac{S_{aan}}{\Sigma S_{aan}} \qquad \textit{Equation S III-2}$$

where S_{aan} is the total exposed area of the amino acid residue “n” in the protein and ΣS_{aan} is the total surface of the protein. The Parameter OPtimised Surfaces (POPS; Version 1.8.0)[63] Program was utilized to calculate the accessible surface area of each single residue in a protein using an all-atom approach and a probe radius value 1.4 Å representing a water molecule. This program takes input from 3D-structures either from the Protein Data Bank file (PDB, https://www.rcsb.org/) or the pdb file generated by the most superior homology modeling[64] using Prime™ in Maestro 11 interface of Schrodinger Software Release 2017-4[61] for unavailable/incomplete PDB (of existing proteins in reviewed UniProt database) or building intact monoclonal antibodies. The amino acid scale proposed by Cowan-Whittaker[65] was selected because of its adequateness in estimating protein surface hydrophobicity.

Although the main driving force of HIC results is the total exposed area of amino acid residues, it is also important to note that for certain proteins, such as fibrinogen, monoclonal antibodies[66], and CD47, their surface hydrophobicity and consequent HIC results are also appreciably affected by glycosylation. Furthermore, the glycosylation also substantially affects the surface activity of proteins, whereas non-/deglycosylated proteins are typically more surface active[67]. For correction thereof, here is proposed a correction factor based on glycosylation density, ρ_g:

$$\rho_g = \left(\frac{N_g^{\,2}}{c.(MW+e^2)^{-\frac{4}{MW}}}\right) \qquad \textit{Equation S III-3}$$

where N_g is the number of glycosylation sites for a given protein in the normal/healthy organism condition

(excluding in vitro or predictive [ECO:0000255] glycations), MW is the molecular weight of protein in kDa, and c values vary and are depending on glycosylation site/protein and MW as summarized in Table S III-16; all descriptors are taken from the reviewed UniProt database (2018 release; accessed July 2018; 20,386 entries)[41, 42].

Thus, the final protein surface hydrophobicity index, Φ_f is defined: *Equation S III-4*

$$\Phi_f = \Phi_i - \rho_g$$

The higher the Φ_f, the more hydrophobic the protein surface. Besides the established relations of Φ and DRT (Figure S III-23), here (Figure S III-9) are also proposed excellent correlations of Φ_f with interfacial activity parameters, such as surface free energy (*SFE*), surface polarity (*Xp*), material-water interfacial tension (*IFT*), and equilibrium surface pressure (*EqSP*). To date, specifically for studying the association between nanoparticles and corona proteins, estimations thereof are virtually limited to physicochemical properties (a) of experimental nanoparticles and (b) based on merely primary structure (i.e. sequence) of blood plasma proteins[68].

3.2.2.4. All-Atom Molecular Dynamics (AAMD)

All systems (including [membrane] proteins[69], phospholipids[70, 71], and polymers[71, 72]) were described using the state-of-the-art OPLS(3) force field[73] and the water molecules were described using the SPC model[74]. Molecular dynamics simulations were executed using the Maestro 11 interface of Schrödinger Software Release 2017-4 [61, 75]. Simulations were performed at time steps of 2 fs. Periodic boundary conditions were applied in all three directions. Cut-off radii were set at 0.9 nm for both electrostatic and van der Waals interactions. Long-range electrostatic interactions were treated using the particle-mesh Ewald (PME) method[76]. Simulations in the isothermal-isobaric (NPT) ensemble have been carried out. Temperature coupling was done with a Nose-Hoover chain thermostat[77]. Pressure coupling was regulated using the Martina-Tobias-Klein barostat[78]. Relaxation times of 1 ps and 2 ps were used for the thermostat and barostat, respectively. For cell membrane adsorption simulation, the constant lateral surface tension of membranes (40 mN/m) mimicking a real cell membrane was applied[79].

4. Results and Discussions

4.1. Non-spherical Shape Stability

Firstly, non-spherical (prolate) fluorescently-loaded carboxylated poly(styrene) (PS-COOH) nanoparticles were produced from spherical equals using 2- and 3-fold stretching factors uniaxially (Table S III-1). These bare particles acted as non-spherical and spherical core nanoparticles (CNPs) for later development of their derivatives: non-spherical and spherical bioinspired red blood cell membrane-coated nanoparticles (BCCNs), as well as non-spherical and spherical PEGylated nanoparticles (CNP-PEGs).

Coumarin-6 (Cou6) and Indocyanine green (ICG) were chosen as fluorescent loads (modelling small molecule [drugs] models) for in vitro and in vivo studies, respectively. ICG, a U.S. Food and Drug Administration (FDA)-approved near-infrared (NIR) dye, was used because it increases the specificity and sensitivity of samples in a more complex biological tissue, especially in in vivo conditions[80]. Moreover and importantly, ICG offers many potential clinical applications, specifically phototherapy (e.g. photothermal and photodynamic)[81] and angiography[49, 82]. It is, however, not possible to use NIR dye-containing samples for a part of the vitro studies due to the absence of a NIR wavelength detector in the available flow cytometry and confocal laser scanning electron microscope (CLSM). Therefore, coumarin-6 replaced ICG in such studies. Nonetheless, considering the substantial effect of additional substances affecting the shape stability of non-spherical particles[16], cellular uptake, and subsequent in vivo fate[16, 83], the rationale of the choice is maintained by the similarity of logDs at pH 7.4 (representing the circulation system) between the dyes (Table S III-2 & Figure S III-2). Additionally, a correlation-interpretation from in vitro and in vivo results could be reasonably drawn because of this similar physicochemical (and possible pharmacokinetics') properties.

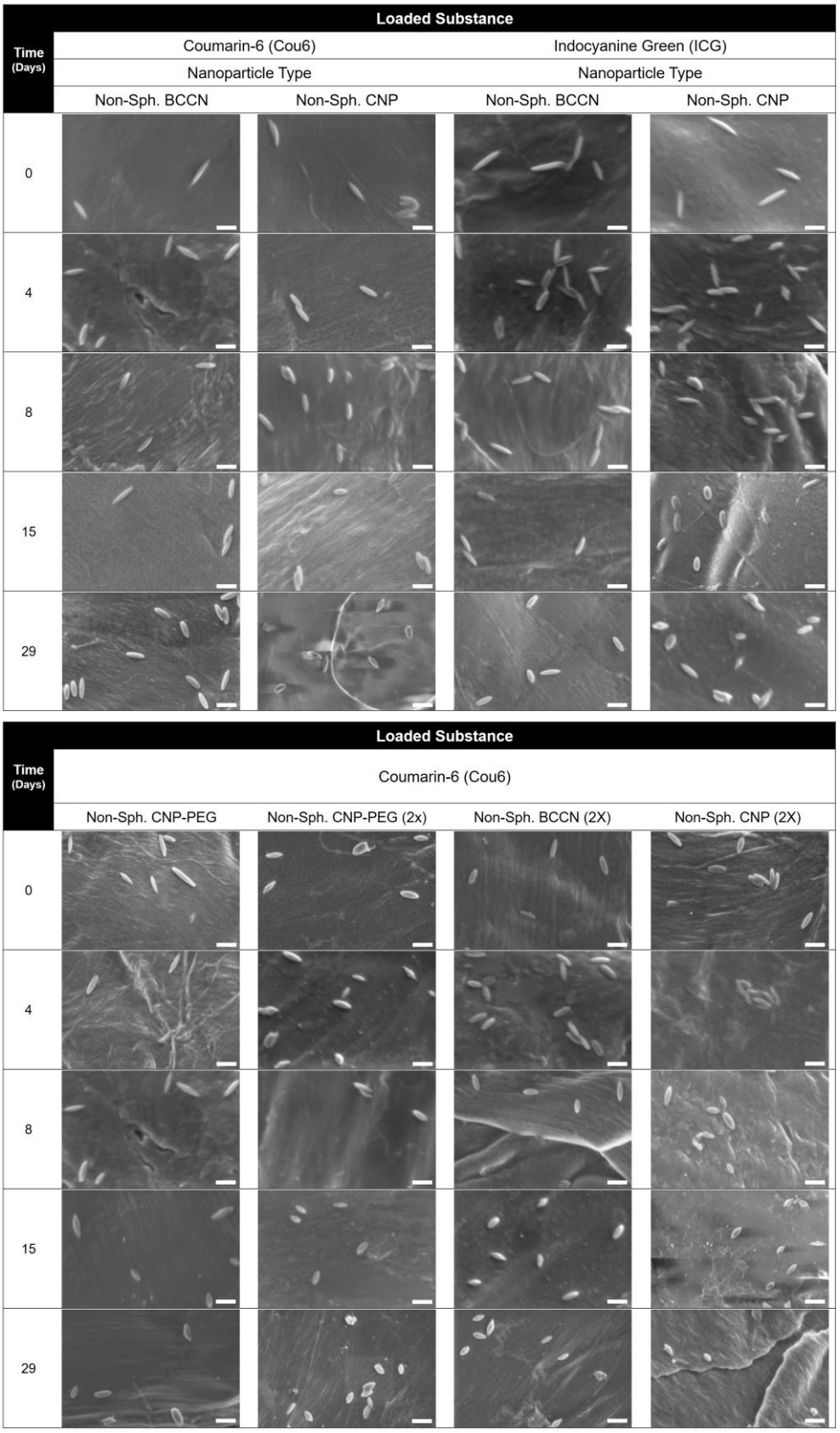

Figure III-1. Representative scanning electron micrographs, which were obtained on different days after initial preparation, display shape stability of various non-spherical PS-COOH nanoparticles involved during in vitro and in vivo studies. Nanoparticles were dispersed in 100% blood plasma for a maximum of 29 days at 37°C. Scale bars = 500 nm. Unless otherwise specified in the brackets, these non-spherical particles are 3-fold (3x) stretched and this term applies from here onwards.

Anticipatedly, both dyes were proven to always elicit similar shape stability within the same surface coating group (i.e. CNP vs BCCN; Figure III-1), demonstrated by comparable typical shifting time ($t_{1/2}$) (Figure III-2a; calculated from the data in Figure III-2b) and completeness of cell membrane-coating (Figure III-3a & Figure S III-3). Besides, both dyes within the same surface coating group particles led to comparable hydrodynamic size, polydispersity index (PDI), zeta potential, fluorescence retention of these particles, and amount of adsorbed proteins (Figure III-2c to Figure III-2g, respectively), which can serve as good bases for further in vitro and in vivo study. Importantly, compared to the unloaded polystyrene (Figure III-2a), typical shifting times of fluorescently-loaded CNPs decrease significantly, presumably due to a decrease of particles' glass transition temperature (Tg) and additional nanoparticle hydrophobicity from the dyes (Figure III-2a, Table S III-1 & Figure III-3b). These factors notoriously cause the shape transformation into spheres when there is no additional treatment (e.g. stabilizer)[16]. As also reported elsewhere, both coumarin-6[84] and ICG[85] are very reasonable to reduce systems (i.e. polymers)' Tgs where they are embedded in, presumably because of the relatively low molecular weight of the dyes, leading to a more considerable molecular difference between guest-host (dye-polymer) systems[16, 84, 86]. We envision that other more biodegradable shape-memory polymers (SMPs) are potential to be developed for non-spherical BCCNs containing ICG. ICG was already reported to be a good activator in SMPs[85], thus in the future, more biodegradable non-spherical BCCNs can rationally be triggered faster to become spheres again (if needed) and subsequently show a higher clearance rate from the circulation system.

Compared to non-spherical CNP-PEG and BCCNs (irrespective of 2- and 3-fold stretching factors), both non-spherical CNPs exhibited the fastest transformation into spheres again, indicated by the shortest typical shifting time (Figure III-1 & Figure III-2a) which enables the most rapid shifting to the lower aspect ratios (ARs; Figure III-2b). However, in the complex medium (i.e. blood plasma) it turned out that the decrease of nanoparticles' ARs could not be necessarily confirmed by fast and acceptable sizing methods, such as dynamic light scattering (DLS; as in our previous report[16]). It is because significant aggregation (specifically in the case of all CNPs) practically occurs in this medium over time, interfering with the observation of particles' reshaping into spheres. Such aggregation is clearly observable in the CNPs' DLS results: increases in hydrodynamic size and PDI over time as well as immediate shifting to more negatively charged particles until certain values, i.e. ~-20 mV) (Figure III-2c-e). These observations can be reasonably interpreted as the consequence of significant and rapid adsorption of blood plasma proteins to the particle surface until the equilibrium is reached (Figure III-2g).

Interestingly, for CNP-PEG and BCCNs, the hydrodynamic size and PDI appeared still to slightly decreasing over time, agreeing well with the minimum protein adsorption, thereby reducing the particle aggregation propensity. However, it is important to note that the amount and composition of adsorbed proteins between them differ (Figure III-2g & Figure III-4a). As expected, the least amount of adsorbed proteins was found for CNP-PEG (Figure III-2g). Surprisingly, BCCNs (both fresh and post-incubation in blood plasma; no significant difference in-between) had the highest amount of adsorbed protein compared to CNP-PEGs or even CNPs (Figure III-2g). Shape-dependent adsorption amount of blood plasma proteins to particles appeared to only be exhibited by CNPs (Figure III-2g).

Although CNP-PEG and BCCN had a similar colloidal stability in blood plasma over time (Figure III-2c & Table S III-1), their degree of shape stability and decrease of Tgs' and Young's modulus differ significantly (Figure III-2a and Figure III-3c). BCCN showed a greater typical shifting time. Cell membrane-coating on BCCNs appeared to only reduce marginally Tg and Young's Modulus (correlating also with lower consequent porosity reduction, as indicated by similar specific surface area (SSA) and residual moisture in Figure III-3d) compared to the PEG on CNP-PEG (Figure III-2a), reasonably due to antiplasticization effect and/or local gelation, which are commonly found in protein-[16, 87] & phospholipid[88]-containing formulations. This led to a better non-spherical shape stability. Expectedly, the similarly significant reduction of Tg and Young's Modulus of PEGylated formulations was also already reported elsewhere[89]. Meanwhile, the higher the surface roughness of CNP is (i.e. non-spherical > spherical CNP; Figure III-3c & e), the greater the surface roughness after the completion of the coating process is (~BCCN > PEGylated; Figure III-3c & e), indicating that higher roughness does not necessarily increase the objects'/particles' hydrophobicity[16]. Also, there was an insignificant Young's modulus decrease after loading of small molecules into particles (data not shown). These last two behaviors seemed to be similar to the macroscopic observations[90].

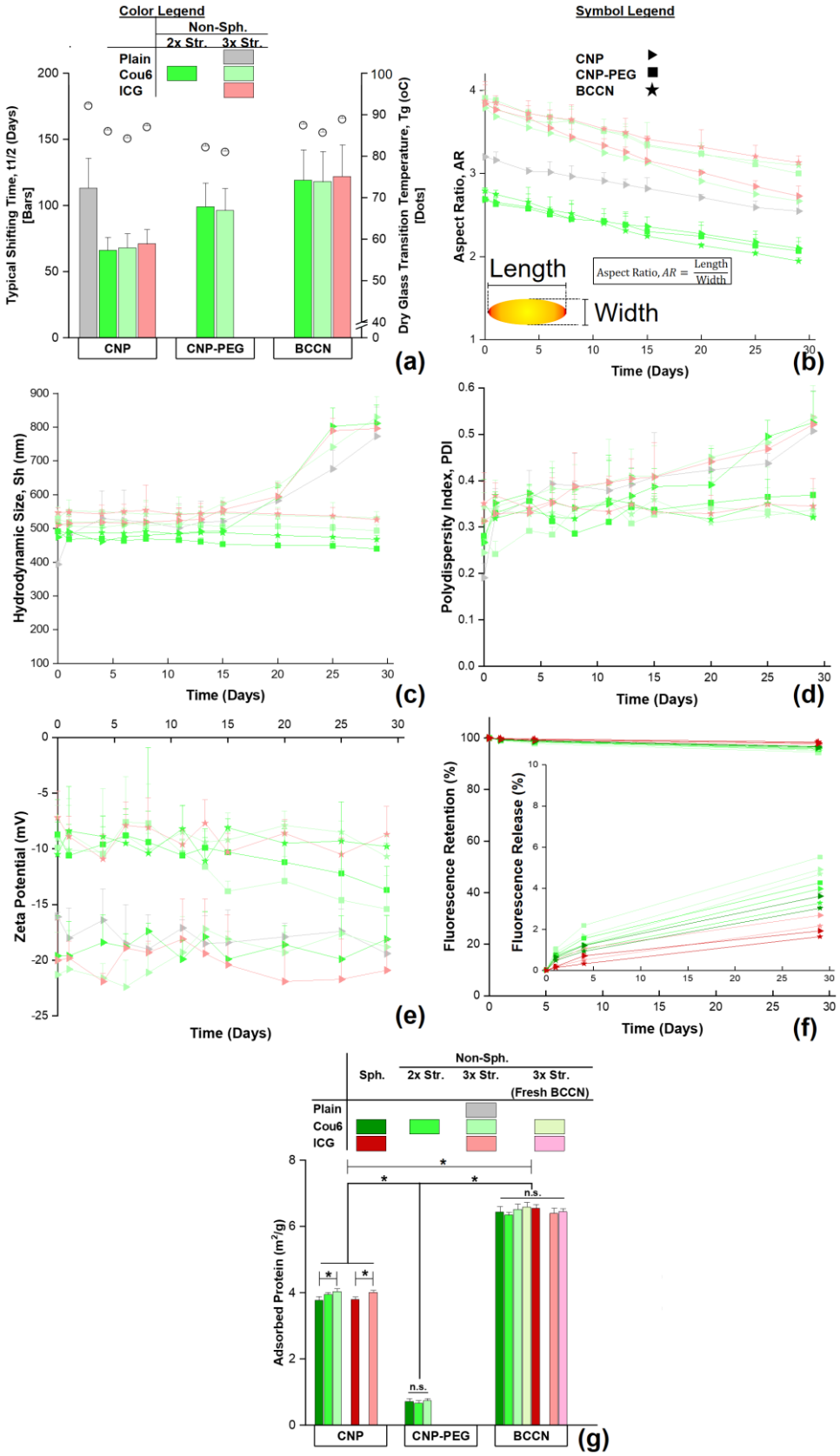

Figure III-2. (a) Calculated typical shifting time ($t_{1/2}$) from aspect ratio (AR) of particles, visually represented in Figure III-1 and numerically demonstrated over time in panel (b): AR plots of various non-spherical PS-COOH nanoparticles. Color legend in panel (a) applies until panel (g) having also an additional color legend for itself and spherical particles described in panel (f). Meanwhile, the symbol legend in panel (b) guides until panel (f). Plots of (c) hydrodynamic size, (d) polydispersity index/PDI, (e) zeta potential, and (f) fluorescence stability of the dyes in PS-COOH nanoparticles over time (which for clarity, can also be displayed as the contrary, i.e. the in vitro release thereof). (g) Quantification of total adsorbed protein to nanoparticle surfaces. Unless otherwise specified in Methods, data represents mean ± standard deviation (n = 3).

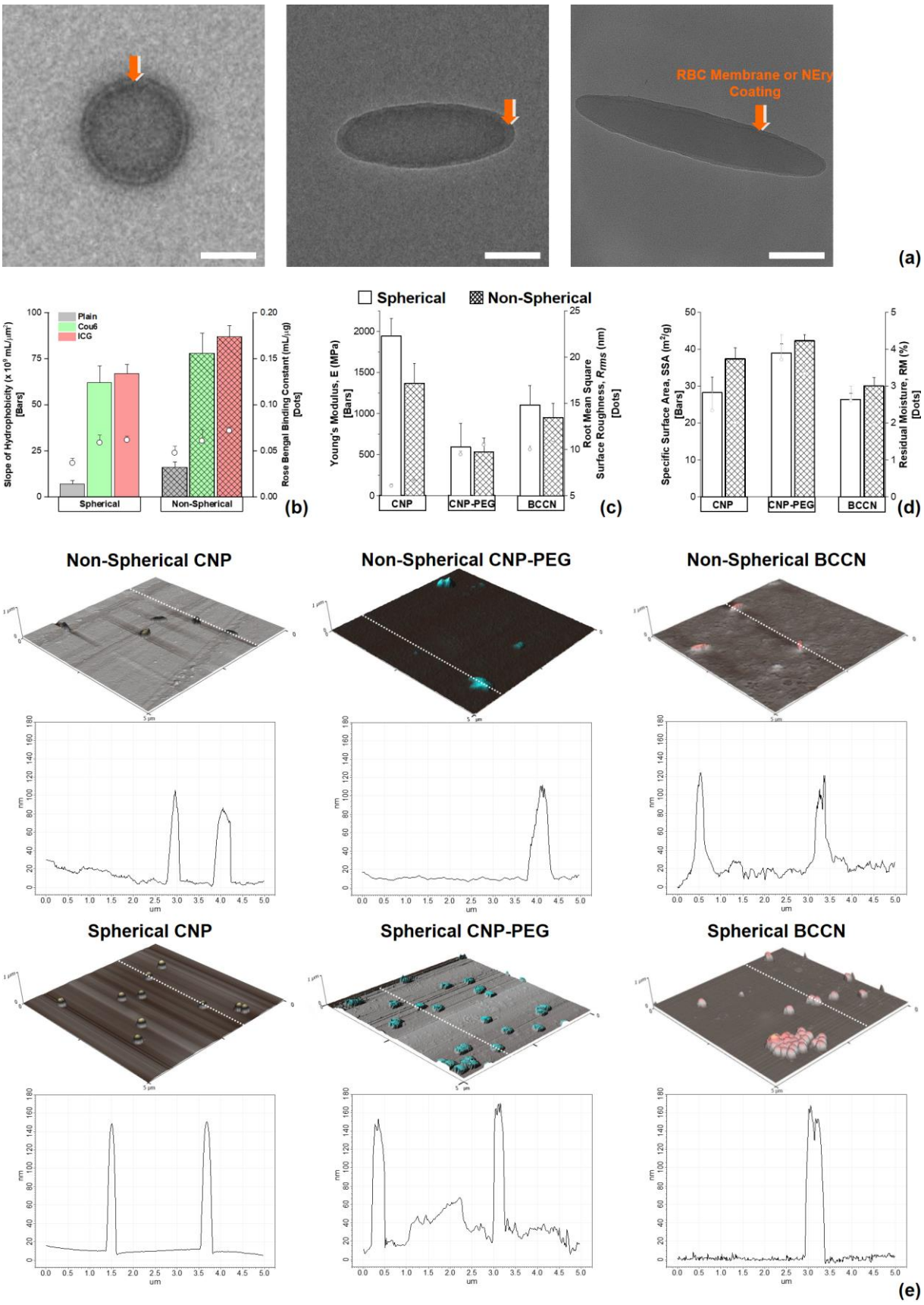

Figure III-3. (a) Representative transmission electron micrographs of different BCCN' shapes and aspect ratios (scale bars = 100 nm). Properties of evaluated nanoparticles: (b) and (c) are mechanical ones, while (d) physiosorption-based surface ones. Panel (c) and (e) were obtained using an Atomic force microscope (AFM). The latter indicates 3D representations and surface or height profiles of particles. Otherwise specified in Methods, data represents mean ± standard deviation (n = 3).

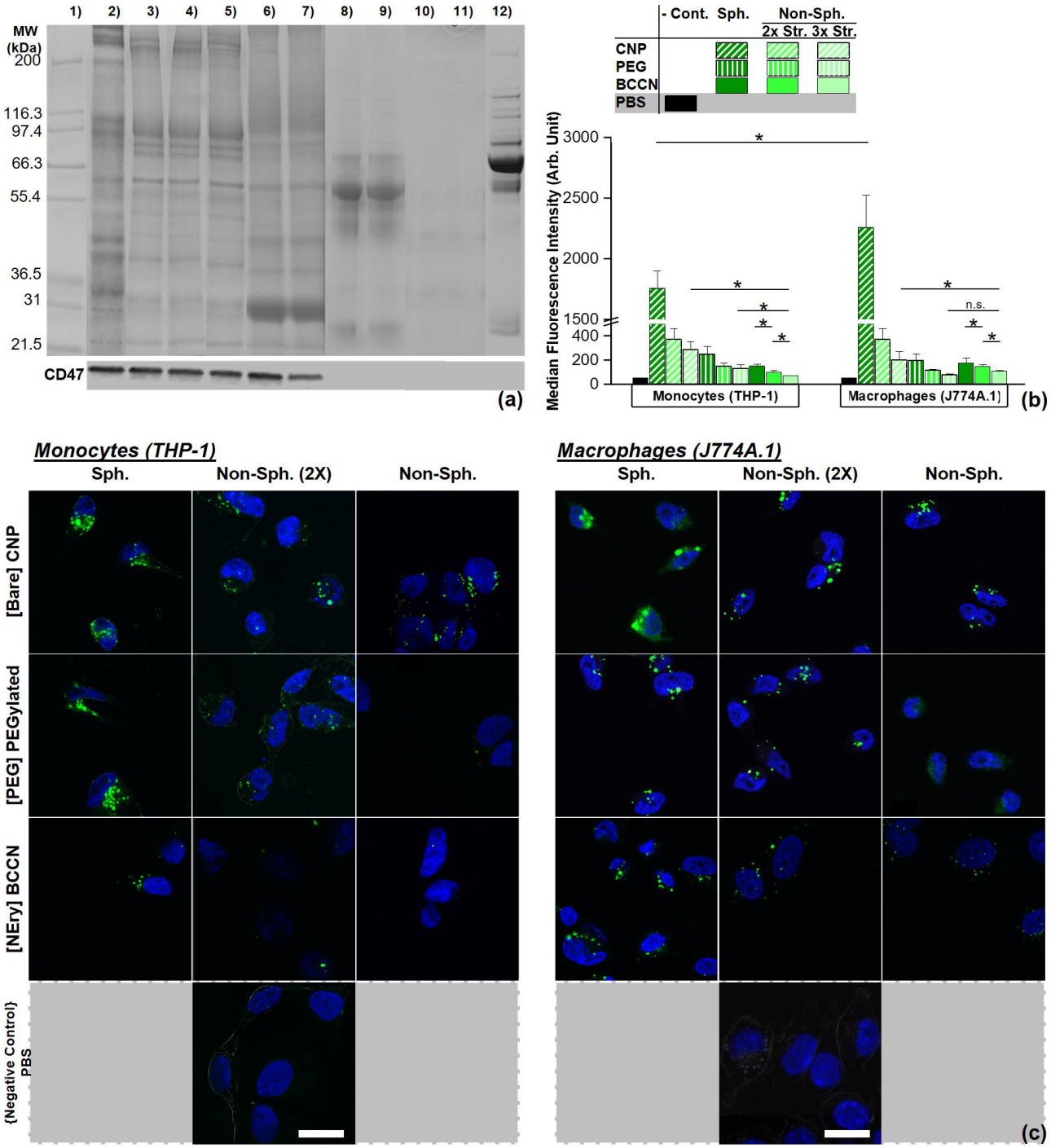

*Figure III-4. (a) Sodium dodecyl sulfate-polyacrylamide gel electrophoresis (SDS-PAGE; upper panel) and western blotting analysis of CD47 protein (lower panel) from various samples. Lane 1) markers, 2) Microerythrosomes (MErys / also called RBC Ghosts), 3) Nanoerythrosomes (NErys / also called Nanoerythrosomes), 4) Non-spherical BCCNs (freshly prepared), 5) Spherical BCCNs (freshly prepared), 6) Non-spherical BCCNs (post in blood plasma for 24 h & washed), 7) Spherical BCCNs (post in blood plasma for 24 h & washed), 8) Non-Spherical CNPs (post in blood plasma for 24 h & washed), 9) Spherical CNPs (post in blood plasma for 24 h & washed), 10) Spherical CNP-PEG (post in blood plasma for 24 h & washed), 11) Non-Spherical CNP-PEG (post in blood plasma for 24 h & washed), and 12) blood plasma. (b) Cellular uptakes of different formulations in monocytes (THP-1 cells) and macrophages (J774A.1 cells), determined by flow cytometry (n=3). *Values are significantly different ($p \leq 0.05$) and n.s.: not significant ($p > 0.05$). (c) Confocal laser scanning microscopy (CLSM) images of monocytes (left panel) and macrophages (right panel) incubated without and with various particles. Cell nuclei were stained with Hoechst 33258 (blue); particles were loaded with Coumarin-6 (Cou6) (green). The excess nanoparticles were washed out and the cells were subsequently fixed for imaging. Both exemplary flow cytometry and CLSM were experimented with using 1 mg/mL (the same concentration as used later for in vivo experiments) of particles and an incubation time of 24 h at 37°C. Scale bars = 20 µm (universal for all samples).*

4.2. In Vitro Phagocytosis

A supplementary, yet critical in vitro assessment, i.e. endotoxin content[91], was performed while transitioning from the main biophysicochemical characterization (in the previous section) to in vitro and in vivo studies. The endotoxin levels of all particles used in the in vitro and vivo study were less than 1 EU/mg (for 1 mg/mL particle concentration), assuring that the in vitro phagocytic uptake and in vivo phenomena are very less likely because of the endotoxin effect (Table S III-1).

PEGylated particles are used as the gold standard in avoiding phagocytosis through the mechanism of minimum (hydrophobic opsonin) protein adsorption. The ”brush” configurations were obtained for all PEGylated particles herein, corresponding to a PEGylation degree as high as ~33% (or average distance between two terminally attached PEG molecules ~0.77 nm or PEGylation density as dense as ~1.67 PEG/nm^2). Also, PDI values thereof were less than 0.4, indicating that the particles are relatively monodisperse and uniformly coated with PEG or NErys (Figure III-2d & Table S III-1 & Figure S III-4a).

To assess phagocytic uptake of coated and uncoated (bare) nanoparticles, in vitro models of MPS clearance were built based on phagocytes: human monocytes (THP-1 cells) and mouse macrophages (J774A.1). Nanoparticle uptake was evaluated quantitatively by flow cytometry (Figure III-4b) and qualitatively by CLSM (Figure III-4c). The median fluorescence intensity of the cells correlates proportionally with phagocytized particles. In our study, the independent modification of particles’ shape or surface chemistry (via grafting using PEG and NErys) significantly decreased phagocytosis by both monocytes and macrophages. Overall, the substantial reduction by each single factor was determined to be more than 70%, with the higher reduction degree caused by surface chemistry (NErys ~ PEG > shape; ~85% > ~70%). From the perspective of shape factor alone, groups of 3-fold stretching factor were always significantly superior to 2-fold stretched equal particles in terms of decrease of cellular uptake (average ~75% > ~65%). Altogether, surface chemistry and shape factor led up to a ~95% decrease in phagocytosis, represented by (3-fold stretching factor) non-spherical BCCN against monocytes; where this result significantly outperformed the CNP-PEG equals. This concept offers a new appealing way, because in the last decade, either non-spherical shape or membrane coating was shown to decrease phagocytosis independently[9, 15]. Also, this effect can be linked to the existence of CD47 in NErys (Figure III-4a), therefore BCCNs, specifically the 3-fold stretching factor ones (Figure III-4b). Against macrophages, however, the superiority of non-spherical BCCNs diminished and became insignificant compared to the non-spherical CNP-PEG. But, both were still significant in reducing phagocytosis compared to the CNPs and lower stretching factor BCCN formulations. This can be explained

due to little reduction of CD47 cross-reactivity between different species[8], albeit close genetic relatedness between human-mouse[92]. Because of this reason, to investigate the full potential of non-spherical BCCNs in vivo, later mouse RBCs were utilized. The phagocytic uptake studies were also conducted at 5°C to distinguish between active and passive uptake and at different doses. All samples remained to show similar trends, but they showed much lower absolute median fluorescence intensity values. This can be interpreted in a way that (1) although the phagocytic uptake is mainly driven by active transport, passive transport still, occurs to a small extent, and (2) the minimization of phagocytosis by the combination of non-spherical shape factor and NEry coating does not depend on doses (data not shown). Additionally, to anticipate possible nanoparticle toxicity effects during the further (in vivo) study, we also performed an in vitro cytotoxicity assay using 3-(4,5-dimethylthiazol-2-yl)-2,5-diphenyltetrazolium bromide (MTT; Table S III-1). Regardless of shape, all BCCNs, compared to core nanoparticles (CNPs), showed less cytotoxicity on the tested monocytes and macrophages after incubation for 24 hours (Table S III-1). Similar to our findings concerning an appreciable difference in many basic properties between nano- and macroscale objects[16], adverse effects (including cytotoxicity) of nanoparticles also cannot be predicted from the known toxicity of material of macroscopic size, which still obeys the laws of classical physics[93]. In conclusion, all particles were progressively taken up by phagocytes and showed little impact on cell viability, with the non-spherical BCCNs being the least toxic.

4.3. In Vivo Biodistribution

For the next step, we performed the in vivo experiments to explore the biodistribution of non-spherical BCCNs. Due to the comparable (or potentially more) superiority of non-spherical BCCNs compared to the non-spherical CNP-PEGs in diminishing phagocytosis by cells of MPS in previous in vitro study, we implemented the Three Rs (3Rs: Replacement Reduction Refinement[94])' principle for in vivo study. Accordingly, a head-to-head comparison of 2 factors (shape and coating) with each containing 2 variables (non-spherical vs spherical and NErys-coated [BCCNs] vs bare) was carried out to benchmark, whether the previously independent two phagocytosis avoiding techniques can synergistically be combined in real in vivo conditions.

In general, during our 72-hour observation, non-spherical BCCNs (, which were loaded with ICG) circulate for much longer and in higher percentages than both their spherical counterparts and (non-spherical as well as spherical) CNPs (Figure III-5a - c; $p \leq 0.05$). This can be reflected in the superior terminal half-life of non-spherical BCCNs, reaching ~51 hours. This value doubles than the independent formulation owning a similar

half-life (~25 h): spherical BCCN or non-spherical CNP. Furthermore, in this study, non-spherical BCCNs showed statistically significant differences in organ distribution, especially in the brain (higher) and liver (lower). Therefore, these findings may also vindicate to some extent that the long terminal half-life is usually associated with a slow redistribution from tissues, e.g. Amphotericin Liposome Injection[49, 95]. To ensure that the fluorescent load signal was because of nanoparticles and not blood remaining in organs, organs were perfused for all biodistribution studies (as detailed in Methods of In Vivo Biodistribution Studies).

For non-spherical BCCNs, significantly enhanced accumulation persisted in the brain for a period of 48 h, with the accumulation peaking at 24 h. In contrast, both non-spherical CNPs and spherical BCCNs demonstrated significantly shorter accumulation time in the brain in the same timeframe (Figure III-5a & b; $p \leq 0.05$). Considering that free ICG in vertebrates (specifically rodents, both mice and rats[96]) could not be found in the brain, nanoparticles appeared to elicit really appreciable ICG distribution to the brain, particularly non-spherical BCCNs. To put the results into perspective, the delivery/accumulation to the brain using the carrier, is orders of magnitude higher than that achieved by free substances[97]. The considerable differences in non-spherical BCCNs' brain distribution during at least 48 hours could potentially be utilized for brain targeting. In principle, nanoparticles accumulate in tissues either because of non-specific bindings (NSB) with the endothelium or because of interaction with the cells. Further and mechanistic rationale for this result is studied and discussed in the next section: "Rationale of In Vivo-In Vitro Findings, General Results".

Non-spherical BCCNs were also able to relatively avoid the liver and spleen throughout 72 h, with a higher significance occurring in the liver (Figure III-5a & b). The liver and spleen reportedly eliminate all foreign materials (with no exception for conventional synthetic nanoparticles) from the blood promptly. Developing nanoparticle formulations, that both target other organs while evading the liver and spleen, has been a challenge[98], especially for substances excreted mainly in the liver, including ICG[99]. Accordingly, non-spherical BCCNs may serve as promising carriers for such substances. Other major organs (lung, kidney, and heart) were also analyzed and displayed minor differences in particles' distribution, particularly at 72 h. This is an anticipated trend because of the gradual degradation of the particles by this time point, as indicated by the higher accumulation of the ICG in the liver. Ultimately, during the in vivo study (specifically before the determined time points), mice neither collapsed nor passed away because of the administered nanoparticles, as reinforced by in vitro cytotoxicity assay (Table S III-1). All in all, the in vivo data strongly suggest that the combination of non-spherical geometry and cell membrane-coating could enhance particles'

half-life and brain distribution, while reducing their accumulation in the liver and spleen. This fact becomes more interesting, since the minor axes of non-spherical (prolate ellipsoid) BCCNs are in a similar size range to the most commonly approved size by FDA for non-viral vectors/carriers, i.e. ~100 nm[49], opening the possibility for sterile filtration[16]. Additionally, the non-spherical BCCNs could be an efficient alternative carrier to improve the treatment of central nervous system (CNS) related diseases, such as brain cancer (i.e. glioblastoma multiforme [GBM]), Alzheimer's, Parkinson's, and multiple sclerosis (MS).

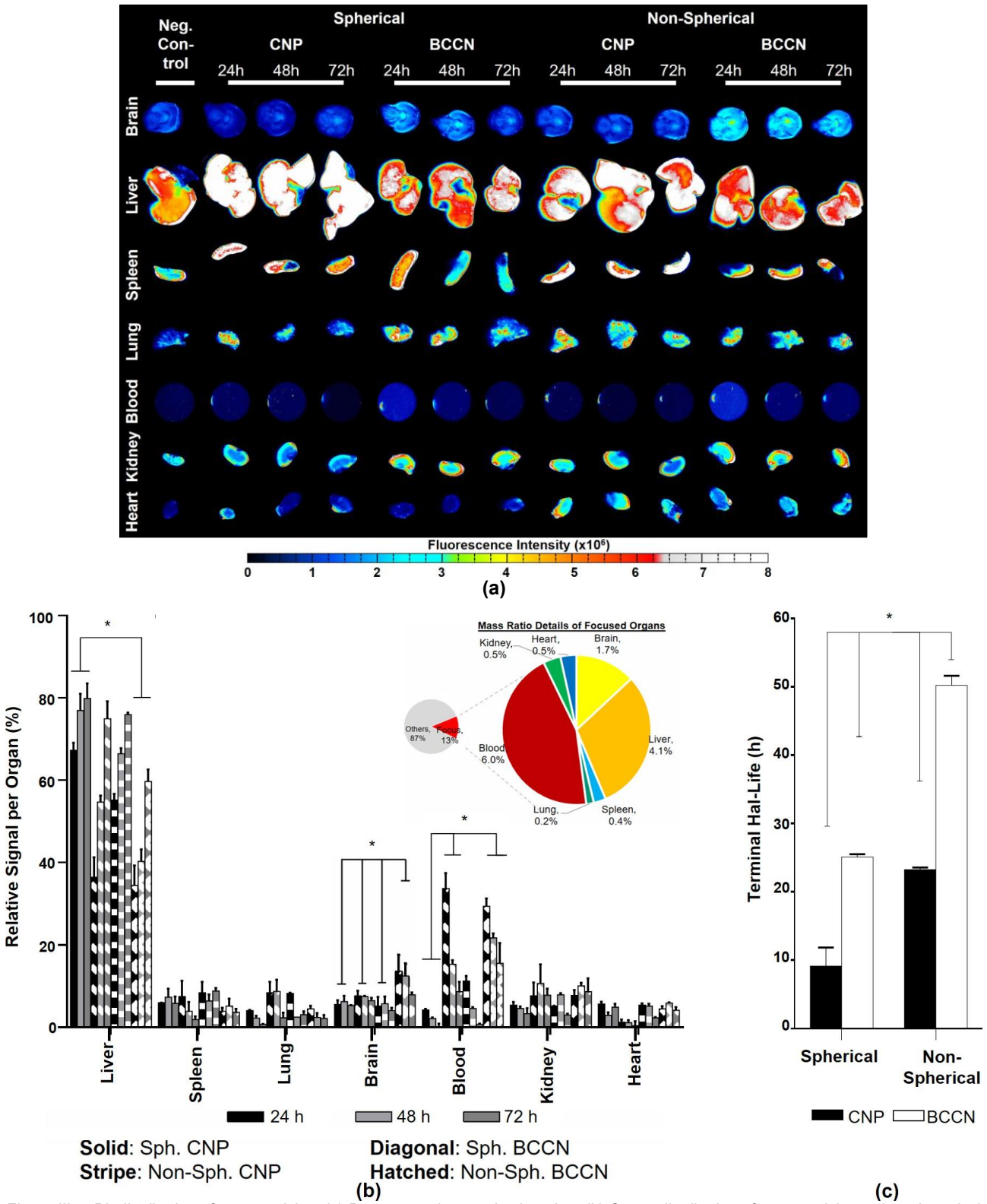

*Figure III-5. Biodistribution of nanoparticles. (a) Representative ex-vivo imaging. (b) Organ distribution of nanoparticles at 24, 48, and 72 hours. Data are expressed as mean ± standard deviation (n=3). Statistics were performed by one-way ANOVA within groups with Tukey multiple comparisons test. *Values are significantly different ($p \leq 0.05$) and n.s.: not significant ($p > 0.05$). (c) Calculated terminal half-life from the attained blood concentrations in the panel (a) and (b).*

4.4. Rationale & Outlook

4.4.1. Rationale of In Vivo-In Vitro Findings

Generally speaking, our in vivo results demonstrate that BCCNs have a prolonged half-life and accumulate in highly vascularized organs, first of all, the brain. Non-spherical BCCNs, containing several key proteins (Figure III-4a), accumulate most significantly in the brain for 48 h while CNP, without NErys coating, is limited to considerably shorter circulation times. These phenomena may be enabled by two main reasons: physiological and protein interaction factors occurring on particles.

First, for the physiological factor, all observed organs/tissues in the current study are classified as highly perfused ones (> 1 mL/100 g tissue/min)[100]. Importantly and physiologically, compared to the other observed tissues, the brain has the smallest vasculature diameters (< 25 µm)[101](Figure III-6a). This can reasonably lead to the higher deposition of particles because of relatively higher penetration, but narrower escape. Moreover, given the shape of particles, interestingly non-spherical (including prolate/elongated) particles amplify these phenomena, as indicated by the Tunable Resistive Pulse Sensing (TRPS) measurement (Figure S III-4b). Under considerable pressure (which also exists in the circulation system), most non-spherical particles (i.e. prolate, regardless of bare [CNP] or coated [BCCN]) mainly traverse the orifices with an end-on orientation as long as the particles' minor axis is smaller than the orifices. This is also similar to previous reports for non-spherical particles, involving both living cells[102] or not[103, 104]. Similar to a healthy human[105, 106], in a healthy mouse the blood pressure in and around (also called intracranial pressure) the brain[107] is proven lower, for example, (about 2-fold or more) than the lungs' counterpart[108](also called pulmonary pressure). In other words, the blood pressure in the brain (mouse ~4 mmHg [6 - 8 weeks; irrespective of gender][107]; human <10 - 15 mmHg[105]) is also strong enough to force non-spherical BCCN into the brain, but it is still weak enough to let non-spherical BCCN reside temporarily in the brain.

Secondly, to better understand protein interaction factors as well as the experimental biophysicochemical characterization, and the in vitro and in vivo findings, various bioinformatic analyses were performed involving biomolecular corona formation, particularly protein corona one(Figure III-6b-f). In Figure III-6b-f, the recommended protein names and abbreviations according to International Protein Nomenclature Guidelines[41, 42] were applied (Table S III-3 to Table S III-6), besides the colloquial/alternative protein names. The formers are used to simplify protein name translations between orthologous species (human-mouse). Unless otherwise stated in Table S III-3 to Table S III-6, only capitalization of the letters in the abbreviations differs human (all in capitals) from mouse (only the first letter in the capital).

By harnessing computer capability to understand large and complex biological data throughout experimental laboratory studies, the protein interactomes (also called protein-protein interaction network; Figure III-6b-to-c) are built from mouse (Figure S III-5—Figure S III-6) and human (Figure S III-7—Figure S III-8). Because of the highly similar interactomes from both organisms, to a current extent (i.e. proteins' biophysicochemical properties, but not their expression per organ), the abbreviations can be expected to be used interchangeably and to be represented with a single value for each protein biophysicochemical property (Table S III-3 to Table S III-6). From these in-depth bioinformatic analyses, auxiliary explanations can be developed. In general, mapping the interactomes can facilitate disentangling and further understanding of the complexity of biological pathways in organisms, particularly i.e. blood-brain axis. For a brief insight, a quadruple principle (consisting of 3 factors increasing influx into + 1 factor decreasing efflux from the brain) is herein proposed (Figure III-6d).

Intriguingly, combining our in vivo results and bioinformatic analyses results, coating of RBC on the (non-spherical) BCCNs appears to be rational using the proposed quadruple principle. In Figure III-6d, these results may be enabled by the interaction of typical erythrocytic proteins (pink-colored) and their respective receptors, either directly or indirectly via mediators (red-colored). These could be classified as "hard corona" and "soft corona", respectively. In the context of binding affinity, for example, the "soft corona" comprises proteins that are weakly attached to the surface; these proteins adsorb rapidly but are easily exchanged with proteins in the medium[109]. The "soft corona" may be more beneficial for interfacially unstable (or very slightly refoldable) proteins, utilized for targeting (discussed in the next part: "Rationale of Particle Shape Stability"). Both coronae are considered to be relevant in governing carrier interactions with cells[110].

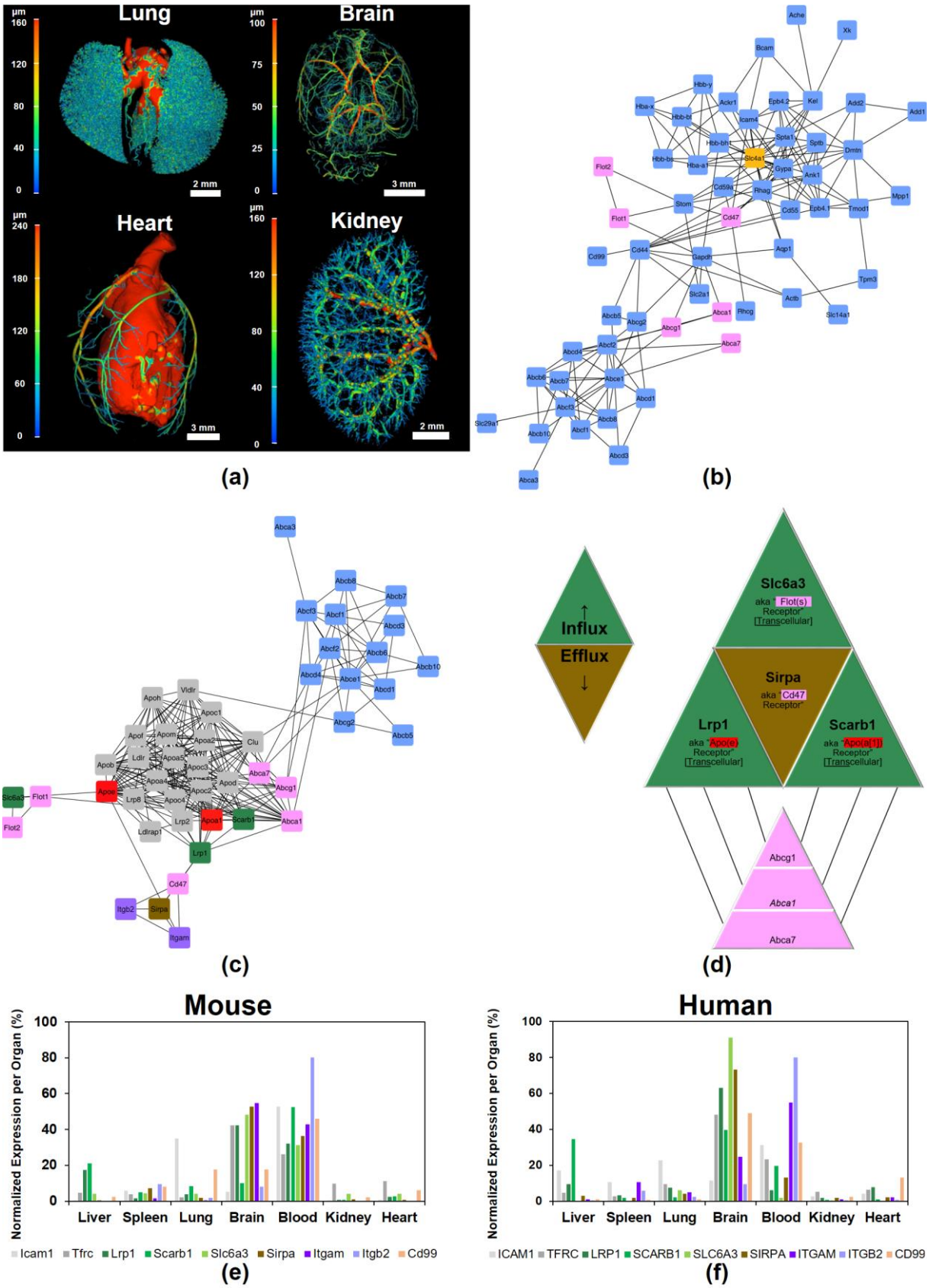

Figure III-6. (a) Mouse vessel morphometrics visualization with a color bar on each organ representing vessel diameters. Adapted from ref. [101], copyright 2011, with permission from PLoS ONE. Shortlisted interactomes of (b) erythrocytes as well as (c) currently proposed brain-targeting & -clearance principle. (d) The magnified and more detailed mechanism of the panel (c), focused on the brain-targeting principle. Distribution of normalized protein expression per organ in (e) mouse and (f) human. Data were retrieved and recalculated from BioGPS[111] and Human Protein Atlas[112], consecutively. General color references of proteins in panel (c)-(f): orange=erythrocytic focuses for cell membrane adsorption onto particle surfaces; pink=erythrocytic focuses for brain-targeting mechanism; blue=erythrocytic others; red=mediators from blood plasma; green & brown= target receptors leading to increase influx & decrease efflux of particles in

blood-brain barrier (BBB); purple=receptor(s) which may account for diminishing the "marker-of-self" effects in the organism, especially in blood-brain barrier (BBB); grey=other blood plasma and/or receptors. (The more comprehensive versions of the interactomes in this figure for panels (b) and (c) are displayed in Figure S III-5—Figure S III-6 for mouse and Figure S III-7—Figure S III-8 for human, respectively).

To go more into details of the quadruple principle, first we discuss factors increasing influx into the brain. The ATP-binding cassettes family: Abca7, Abca1, and Abcg1 (with MW ~234, ~254, and ~75 kDa, respectively) appears to be ones of the main transporters from NErys, involved in the higher accumulation of BCCNs in the brain; while a lesser extent, albeit still considerable, is shown by the interaction of flotillins (~47 kDa, especially Flotillin-1) from NErys with their receptor: Slc6a3 in the brain[113]. The ATP-binding cassettes family mediates interactions with apolipoproteins, i.e. Apolipoprotein A-I (Apoa1) and/or Apolipoprotein E (Apoe), which later introduce whole NErys to their respective receptors, i.e. Scarb1 and Lrp1, consecutively. Given the high abundance of Apoa1 in blood plasma (Table S III-5), Apoa1 alone may reasonably account for the higher nanoparticle uptake to the brain and/or permeation across the blood-brain barrier (BBB)[114]. This can be explained by the recent experimental findings, showing that Apolipoprotein A-I associates considerably (even the most one, compared to other apolipoproteins) on native and extracted RBC membranes (NErys)[115, 116]. However, in reality, these two apolipoproteins strongly appear to cooperate. This is based on the fact that besides their similar molecular weights (~30 kDa; Table S III-3), the latest findings show that the tertiary structures of this apolipoprotein family are closely related[117]. Accordingly, they rationally cross-react with their most prominent corresponding receptors. This current knowledge improves our knowledge that the cross-reaction involving Apoe may also be beyond the low-density lipoprotein receptor family (mainly Lrp1 [Prolow-density lipoprotein receptor-related protein 1][41, 42]), i.e. Scarb1 (Scavenger receptor class B member 1), or vice versa. To put apolipoproteins into perspective, it is noteworthy to consider that a Lrp1 agonist peptide, i.e. Angiopep-2 (in the conjugated form as Paclitaxel Trevatide), is the most clinically-advanced and even already approved by FDA in 2016 as an orphan drug for brain-targeting drug delivery, specifically breast cancer brain metastases (BCBM)[118]. This fact suggests that substantial indirect apolipoprotein involvement in the drug delivery and targeting still can be further explored to obtain clinical significances.

For factors decreasing efflux, to date the interaction between Cd47 and its receptor: Sirpa in the brain is practically considered the definitive factor[112, 119]. This is very rational because Sirpa is one of the proteins expressed highest in the brain compared to the other organs, both in mouse and human (Figure III-6e-to-f). Also in both organisms, Sirpa has relatively higher expression than the Mac-1 receptor(Itgam–Itgb2; Figure

III-6e-to-f), its indirect competitor through inducing Cd47 from “marker-of-self” to “marker-of senescence”[120].In the normal physiology of the brain, Cd47 can reportedly also protect endogenous matters from brain resident macrophages (i.e. microglia) by binding via their Sirpa[119, 121]. Definitely, bestowing the non-spherical (prolate) particles with ‘complete’ corona, including the all important proteins (Figure III-4a), enables higher protection from the particles’ early effluxing from the brain.

Compared to the expressions of other currently popular targets for brain targeting (such as Icam1 [Intercellular adhesion molecule 1] and Tfrc [Transferrin receptor protein 1])[122], our currently proposed set of involved receptors is expressed relatively higher in the brain compared to the other organs (Figure III-6e & f). Therefore, as also discussed above concerning the comparison of natural apolipoproteins with Angiopep-2, the currently multiple mechanisms appear to strongly account for higher brain accumulation because of not only higher influx of particles, but also lower efflux (Figure III-6d). This can act as a readily possible alternative if the conventional singly used various targeting moieties in the clinical studies fail to reproduce similar effects in the in vivo (pre-clinical) study[123]. Moreover, in the case of transferrin, a long-researched molecule for (e.g. brain or tumor) targeting, it is important to note that although its relatively high expression in the brain, transferrin turns out recently to be interfacially unstable and easily lose its targeting capabilities[124]. This is discussed further in the next section: “Structural-Interfacial Stability”.

To put our conducted bioinformatic analyses into different perspectives, they also can help to understand discrepancies of biological pathways in different species [46, 125]. For example, the different Cd99 biodistribution in different organisms (e.g. mouse vs human) is potentially causing very different kinetics and distribution of molecules interacting with Cd99[126]. Cd99, a receptor for GM1 Ganglioside’s accounting for prolonging the half-life of endogenous matters in the bloodstream of the mouse, exists with the most abundance in mouse blood(~46%;), as revealed by the bioinformatics-distribution analysis (Figure III-6e). Meanwhile, in human, CD99 is most abundant in the brain (~49%; Figure III-6f). Therefore, it is no wonder that the effect of GM1-containing formulations in prolonging half-life in the bloodstream has been only observed in mouse models; whilst in human, GM1-containing formulations may be cleared faster from the blood and subsequently eliminated by the more potent macrophages in the brain[46, 125].

Furthermore, deliberating the high similarity of protein interactomes between mice and human species in our studied case (Figure III-6b–c, Figure S III-5—Figure S III-6 vs Figure S III-7—Figure S III-8, respectively), the high brain accumulation of non-spherical BCCNs is also very likely to occur in human. This can act as

important anticipation for further (clinical) study. Considering all reported results herein and concerning the translation of the non-spherical BCCNs as clinical drug carriers, many challenges and opportunities await. Admittedly, no erythrocyte blood types have been reported in mice[127] or lower animal species, requiring more cautions into clinical translation. Also, the toxicity issue of organism' cell component-containing drug carriers, which is currently the authority's main concern[128], should be minimized by more comprehensive experimental studies. Accordingly, to date there is still no FDA-approved carrier product based on cell components[128], not to mention the fact that the most advanced in terms of the clinical study are exosomes[123], owning an average diameter of ~100 nm and BBB-crossing properties, including for erythrocytic one[129, 130]. Because the BBB-crossing properties are substantially aided and amplified by the unoriginal protein presence in formulations, consequently some of the suspected proteins from the formulations should be analyzed to demonstrate the formulation's nature and the degree of purity[131].

To sum up, from the abovementioned explanation, it is very clear that the fate (amount and duration) of particles in the organ, including the brain, is linked to the physiological characteristics of particles, which are readily and uniquely fingerprinted by biomolecular corona in the circulation system. Under physiological conditions, particles will show a certain influx (absorption) and efflux (excretion) into/from organs. To date, the research is generally focused on the influx aspect, which may be linked to the typically low success rate of drug delivery to the brain. The proposed quadruple principles (Figure III-6d) refine this simplified view and appear to support our current in vivo results showing a significantly higher accumulation of BCCNs in the brain. This can also serve as a basis for anticipating and explaining other in vivo-in vitro results[130].

4.4.2. Binding Affinity

To better understand the interactions between various core particle surfaces and various proteins (especially the components of NErys), various-complementing binding affinity methods were performed using both computational and experimental laboratory methods (Figure III-7a). In the beginning, to predict to what extent the disturbance of cell membrane functionality occurs from the proteins suspected to interact with the core particle surface, we continue to utilize the similarity of protein interactomes between mice and human species (Figure III-6b, Figure S III-5—Figure S III-6 vs Figure S III-7—Figure S III-8, respectively). Expectedly, the direct interactions between the core particle surface and the lower impact proteins are desirable to minimize the negative impact on the entire functionality of erythrocyte membranes. Accordingly, the total red blood cell membrane functionality on the artificial particles can be conserved. On the other

hand, given the most abundant concentration of Band 3 (the colloquial protein name; standardly[41, 42] abbreviated to SLC4A1; Table S III-4), its location in the membrane, and its very high surface hydrophobicity (3D-structure-based final protein surface hydrophobicity index, Φ_f 0.608; Table S III-4; see Methods, specifically “Correlation to Experimental Hydrophobic Interaction Chromatography (HIC) and Interfacial Activity Parameters” for further details), Band 3 appears to be the most probable protein interacting with the core particle surface. From the protein interactome analysis, it is revealed that besides CD47, Band 3 also shows lower interconnectedness with other proteins. Therefore, Band 3 appears to fulfill the expectation to less affect the total cell membrane functionality, but still can be strongly attached to the core particles.

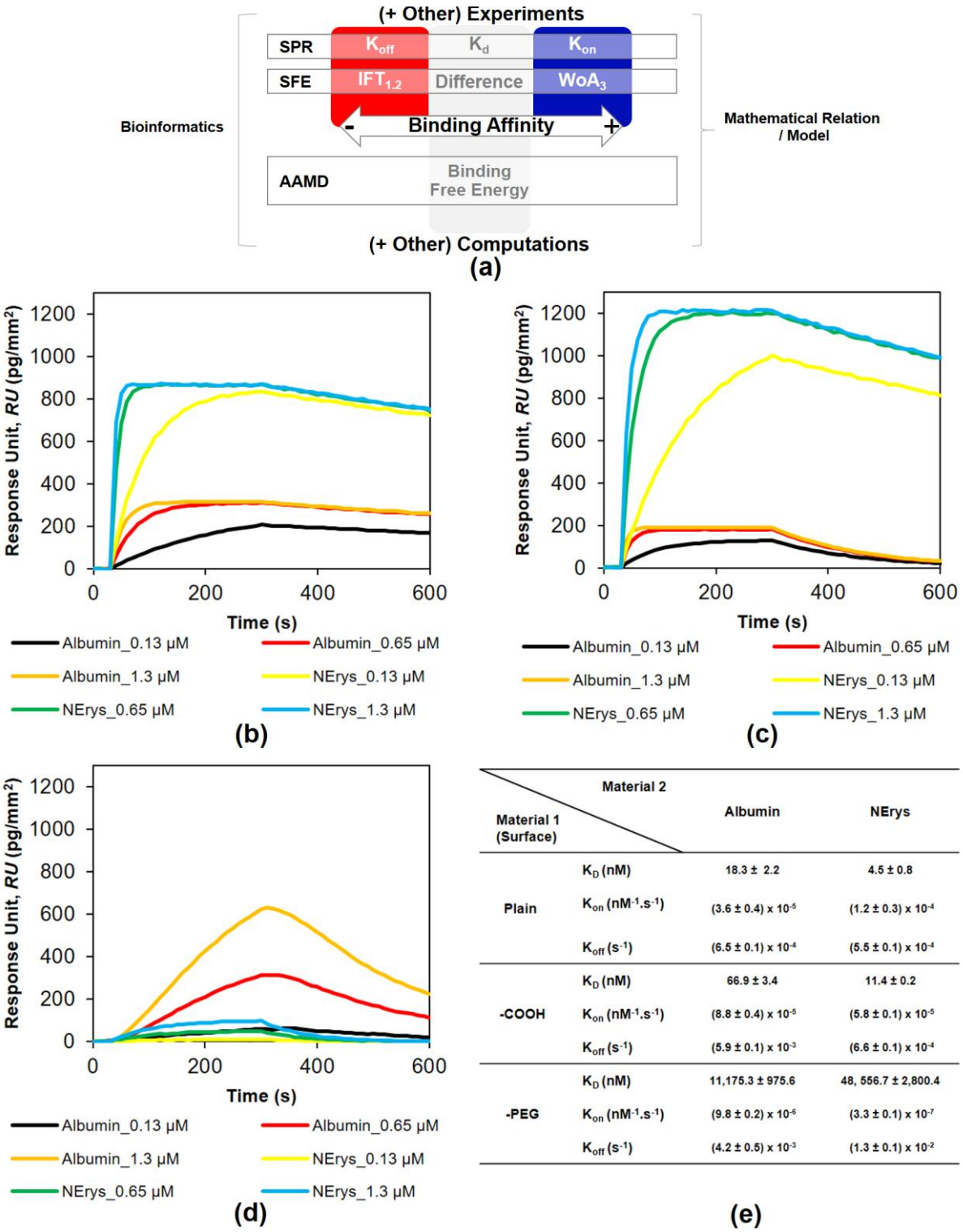

Material 1 (Surface) \ Material 2		Albumin	NErys
Plain	K_D (nM)	18.3 ± 2.2	4.5 ± 0.8
	K_{on} ($nM^{-1}.s^{-1}$)	(3.6 ± 0.4) x 10^{-5}	(1.2 ± 0.3) x 10^{-4}
	K_{off} (s^{-1})	(6.5 ± 0.1) x 10^{-4}	(5.5 ± 0.1) x 10^{-4}
-COOH	K_D (nM)	66.9 ± 3.4	11.4 ± 0.2
	K_{on} ($nM^{-1}.s^{-1}$)	(8.8 ± 0.4) x 10^{-5}	(5.8 ± 0.1) x 10^{-5}
	K_{off} (s^{-1})	(5.9 ± 0.1) x 10^{-3}	(6.6 ± 0.1) x 10^{-4}
-PEG	K_D (nM)	11,175.3 ± 975.6	48, 556.7 ± 2,800.4
	K_{on} ($nM^{-1}.s^{-1}$)	(9.8 ± 0.2) x 10^{-6}	(3.3 ± 0.1) x 10^{-7}
	K_{off} (s^{-1})	(4.2 ± 0.5) x 10^{-3}	(1.3 ± 0.1) x 10^{-2}

(e)

Figure III-7. (a) Overview of three orthogonal methods for determination of binding affinity between (potential) core materials and blood plasma components: surface plasmon resonance (SPR), surface free energy (SFE), and all-atom molecular dynamics (AAMD), initiated/accompanied by bioinformatics analyses (see the details in Methods: Computational Laboratory Methods (Auxiliary Analyses)), thereby resulting mathematical relations/models and permitting reasonable conversion between the parameters(Figure S III-17). The first two binding affinity determination methods were conducted experimentally, while the latter thereof was performed computationally. Measurements of protein-material binding affinity using SPR. Comparative interactions (shown as association and dissociation curves) between protein-containing samples (NErys & albumin) and different sensor chip's surface functionalizations: (b) plain, (c) carboxylated (-COOH), and (d) PEGylated (-PEG). These functionalizations mimic any unmodified, carboxylated, and PEGylated particles used in this and the previous chapter, including but not limited to polystyrene ones. (e) Summary of samples' binding affinities to the corresponding surfaces.

Afterward, the experimental binding affinity using Surface Plasmon Resonance (SPR) was performed. To take full advantage thereof and to enable direct comparison to another experimental study (i.e. Surface Free Energy, *SFE*), the study was undertaken with the assumption to minimize additional interference of radius of curvature ($R_c(t)$) and undesired effect of additional adsorbents (i.e. nanoparticles). Given our preliminary data[16] and the well-known high hydrophobicity of its gold chip surface, three different functionalizations (plain, carboxylated, and PEGylated) of SPR sensor chips (thereby diverse surface hydrophobicity) were used to define the wider range of the binding affinity. Subsequently, these sensors were incubated with proteinaceous samples (NErys and albumin) with standardized protein concentration over a range of concentrations to analyze the corresponding association and dissociation signals (Figure III-7b-e). The resultant binding constant values (listed in Figure III-7e) are ranked as follows (strongest-to-lowest binding affinity corresponding to the lowest-to-highest K_D value): K_D (NErys) < K_D (BSA) in all three surfaces, with an also similar trend for both proteinaceous samples, i.e. K_D (@plain) < K_D (@carboxylated) < K_D (@PEGylated). These calculated K_D values agree well with the relative adsorption capacity trend observed in Figure III-7b-d. More interestingly, it turned out that the results from SPR measurement have a strong correlation with the results from SFE measurements (correlation coefficient, r = -0.97 with the classification of correlation coefficient strength based on the convention[132]; Figure III-8-a-left and Table S III-7), suggesting that the higher throughput SFE measurement could be applied for more samples (e.g. proteins, polymers, small molecules, metals, etc.). Importantly, through SFE measurement, one can obtain more information about various interfacial activity parameters, from surface hydrophobicity to the calculation of (Difference of WoA_3-$IFT_{1.2}$) binding affinity. Briefly, the (difference of WoA_3-$IFT_{1.2}$), a secondary interfacial activity parameter, is derived from the determination of the primary interfacial activity parameters of samples (i.e. directly from SFE, surface polarity, and [solid-liquid, specifically material-water] interfacial tension as in Table S III-8; see our previous work[16] for further details about the interfacial activity parameters' derivation, calculation, and applications). Moreover, considering also the possibility to couple the current data to the available interfacial activity database[16] for wider discussion and applications, SFE measurement seems to be a very feasible option for comparing and understanding a large dataset.

With this premise, we reasonably proceeded to utilize a set of interfacial activity parameters as a basis for further studies. The studies cover initially all-atom molecular dynamics (AAMD) and subsequently development of mathematical relations/models, linking between proteins' experimental interfacial activity parameters and their apparently-versatile computational descriptor (i.e. $\Phi_{f,}$).

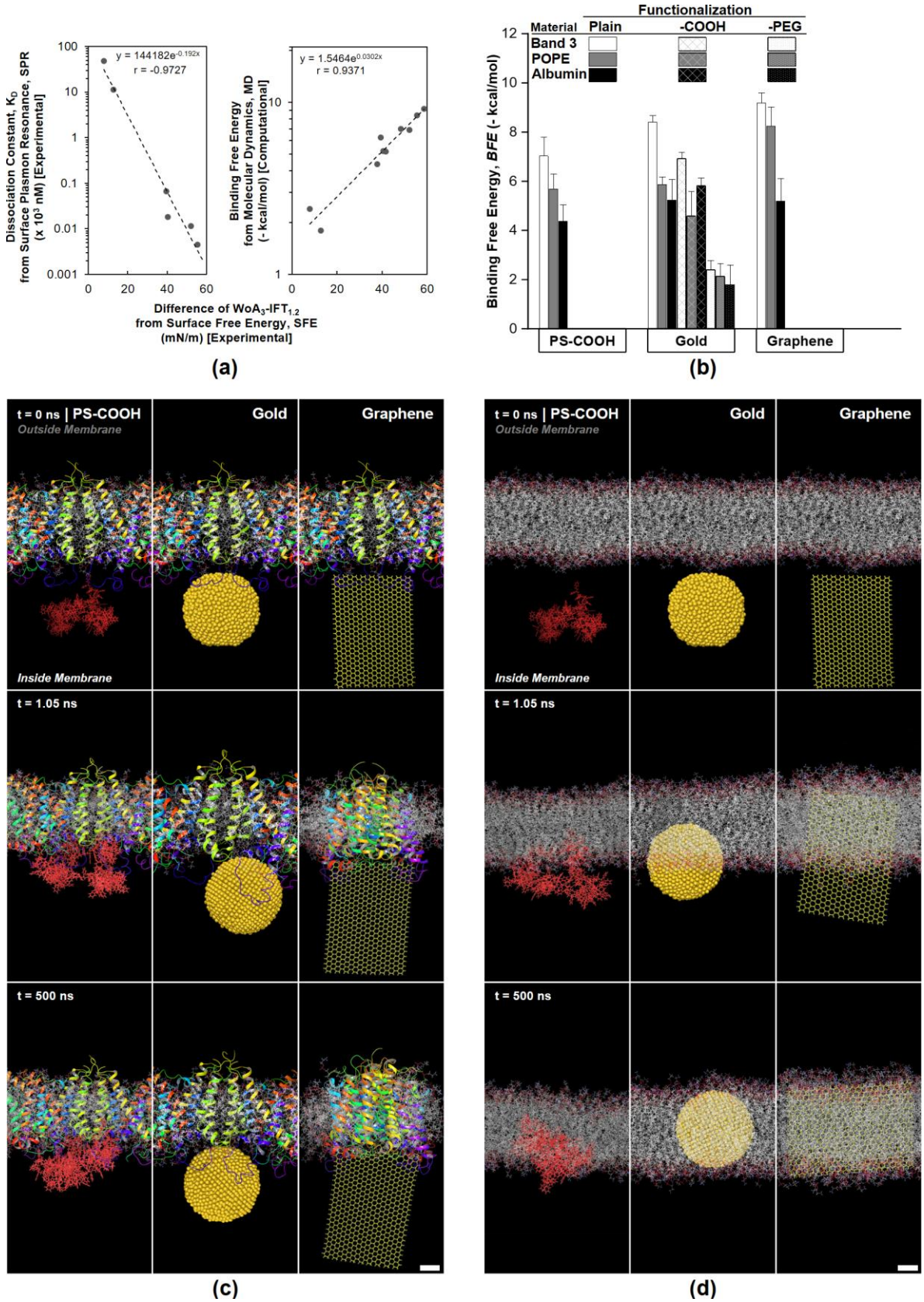

Figure III-8. (a) Binding free energy profiles. PS-COOH representing the main core particles of BCCNs, gold particles representing the experimentally used surface plasmon resonance sensor chip, and graphene representing one of the most hydrophobic materials as discussed in our previous report[16]). (b) Correlation between the difference of WoA_3-$IFT_{1.2}$ (calculated as Haryadi et al.[16]) from experimental SFE measurement and (left panel) simulation binding free energy, BFE as well as (right panel) experimental dissociation constant from SPR measurement. Representative simulated trajectories of various materials with the experimentally-related radius of curvature and different physiological components: either membrane components (panel (c) with and (d) without the most abundant protein at membrane of RBC, i.e. Band 3). Scale bars = 1 nm. The all-atom models of full-length PS-COOH (17 kDa), PEG (5 kDa),

spherical gold nanoparticle (AuNP; ø 4 nm), and graphene (width x length 4 x 5.5 nm) are colored by red, cyan, gold, and yellow respectively. Meanwhile, all proteins and membranes (of POPE; palmitoyl-oleoyl-phosphatidylethanolamine) are colored according to the standard amino acid sequence-colored ribbon and standard element color convention, consecutively. For clarity, the free water and salts (e.g. Na^+ and Cl^-) molecules as the solvent components are made invisible.

The AAMD is a confirmative study concerning the good correlation between the binding affinity results from two previous experiments. It can also serve as an extension of those studies, with additional inclusions of a) effect of radius of curvature and b) more hydrophobic materials. Noteworthily, the AAMD results revealed a comparably strong correlation to the SPR results (r = 0.94) (Figure III-8a right & Table S III-7), suggesting that all the three parameters describing binding affinity are reliable and complementary. Also, AAMD could verify the proposal of Band 3, accounting for the main interaction with the core particles, as suggested by the bioinformatics analyses and described at the beginning of this section. From our converged simulations, Band 3 showed the strongest interaction compared to other blood (cell) components to different materials, as exemplified in Figure III-8-a-b and portrayed in Figure III-8c-d. However, the weaker binding affinities were seen in general from the AAMD study compared to the abovementioned experiments. This is expected, since in AAMD, we have the radius of curvature effect from the main adsorbents (e.g. polystyrene, gold, and graphene; notice the scale bars in Figure III-8c-d & Figure III-9a-c). Intriguingly, this acts as a very useful reminder that confinement effects do exist and affect directly interfacial activity parameters[16], thereby indirectly reducing the binding affinities. Further explanation, discussion, and interpretation of this issue are comprehensively presented in the next sections.

Meanwhile, recognizing the abovementioned findings and widely-known facts that higher proteins' surface hydrophobicity tends to exhibit higher retention time in hydrophobic interaction chromatography (HIC)[62] as well as non-specific bindings (NSB) to any objects[133], we decided to pursue this matter more quantitatively. Taking the experimental results of HIC as a starting point, we found out that Φ_f is a dominant descriptor for describing many interfacial activity parameters from the commonly used proteins in the experiments (see Methods for further details). It has a very strong, non-linear correlation with interfacial activity parameters, indicated by |r| > 0.96 for all four models, i.e. surface free energy (*SFE*), surface polarity (*Xp*), material-water interfacial tension ($IFT_{[1.3]}$), and equilibrium surface pressure (*EqSP*) (Figure S III-9a-d, respectively). Accordingly, we can formulate quantitatively such well-known facts by first reliably estimating their corresponding interfacial activity parameter values. Furthermore, we can also provide the quantitative rationalization of their (non-specific) binding affinity to other materials (proteins, particle surface, etc.) as well as the further interpretation using the cases from the current and other studies as well as interfacial activity

database[16]. The discussion and application thereof are presented in the next sections.

To summarize this section, based on our results, SFE measurements appear to exhibit reliable and comparable approximation of binding affinity between materials (cell membranes-particle surface or protein-surface) with the more intricate experiments, such as SPR and AAMD. Its potential and applications in assessing the binding affinity of many samples (especially proteins) are even enhanced, considering the possibility to extrapolate the interfacial activity parameters from Φ_f.

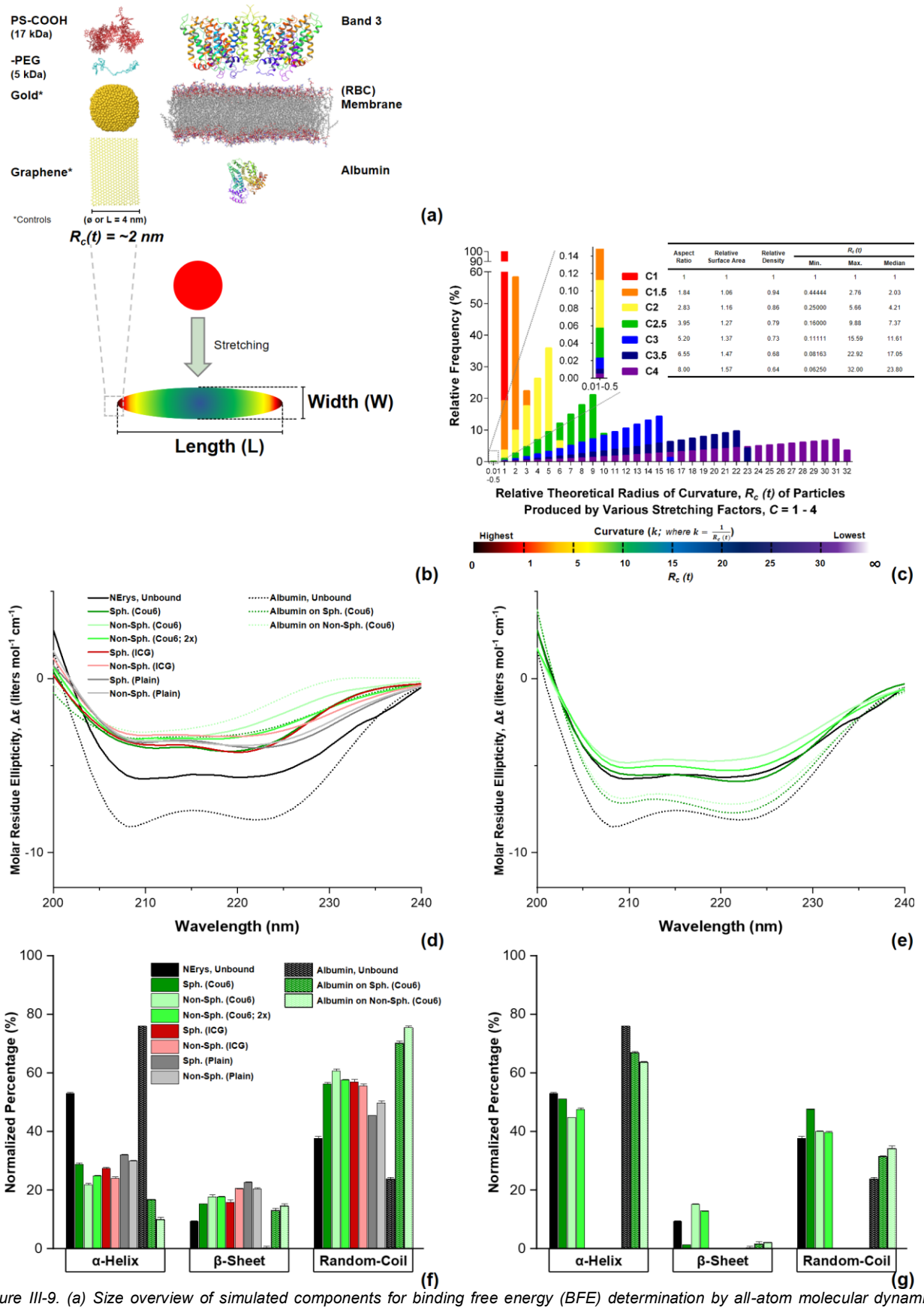

Figure III-9. (a) Size overview of simulated components for binding free energy (BFE) determination by all-atom molecular dynamics (AAMD) in Figure III-8. (b) Visualization of the radius of curvature from spherical and prolate nanoparticles. (c) The radius of curvature is one of the altered critical physical factors on non-spherical (prolate ellipsoid) particles, affected by the uniaxial stretching process (Adopted from our previous report[16], copyright 2019, with permission from Advanced Healthcare Materials). This feature is simulated and portrayed in Figure III-8. Circular dichroism (CD) spectra of protein adsorbed on different shapes of particles with different functionalizations: (d) plain and carboxylated as well as (e) PEGylated. The color legend in panel (d) represents the same proteins and particle shapes until panel

(g). The assigned secondary structure content of each corresponding spectra is demonstrated in (f) and (g), respectively. For BCCN samples, NErys were adsorbed to the CNPs instead of albumin, which was used as a reference and also used in the SPR study (Figure III-7b-e).

4.4.3. Structural-Interfacial Stability

From Circular Dichroism (CD) analyses (Figure III-9d-f), NErys, which were used as coating on BCCNs, clearly appear to be more robust (i.e. elicit less conformational changes, hence higher structural stability) compared to the albumin (serving as reference and representation of the most abundant proteins in blood plasma[134, 135]), irrespective of the type of core particles. The relativity of these conformational changes was controlled by the unbounded protein-containing samples (i.e. cell membranes/NErys and albumin). The confirmative results are also demonstrated by the FTIR analyses (Figure S III-10). Thus, several possible explanations thereof could rationally be proposed: (a) high chemical- and conformational-stability of the most abundant proteins in erythrocyte membranes (e.g. Band 3[136]-actins-spectrins) accounting for more than 60% w/w[137], (b) crowding effect of proteins at interfaces[103, 133], resulting in less probability for proteins to unfold, and (c) reasonable presences of natural chaperones. The latter are represented by spectrins and small heat shock proteins (sHsps families, e.g. Hsp27 [aka HSPB1] in humans & Hsp25 [aka Hspb1] in mice) that can spontaneously refold other severely unfolded proteins in erythrocyte membranes[116, 138].

A decrease of alpha-helices at NErys, which were adsorbed on all CNPs, was observed[103]. However, evidently the decrease of alpha-helices to about 20s% could not be necessarily ascribed to the negative effects, such as the unfolding of proteins that are notoriously and also importantly linked with the increase of flexible and tightly packed beta-sheets, therefore inducing protein aggregation. To some extent, the negative effects of beta-sheet formation might also be counterbalanced by the formation of rigid (unordered/) random-coils (also either called extended structure or coiled-coil[139]). The random-coils (Figure S III-5c & d), which exist relatively high (~50% or more) and natively in motor or cytoskeletal proteins like spectrins and actins[139], even pronouncedly reformed.

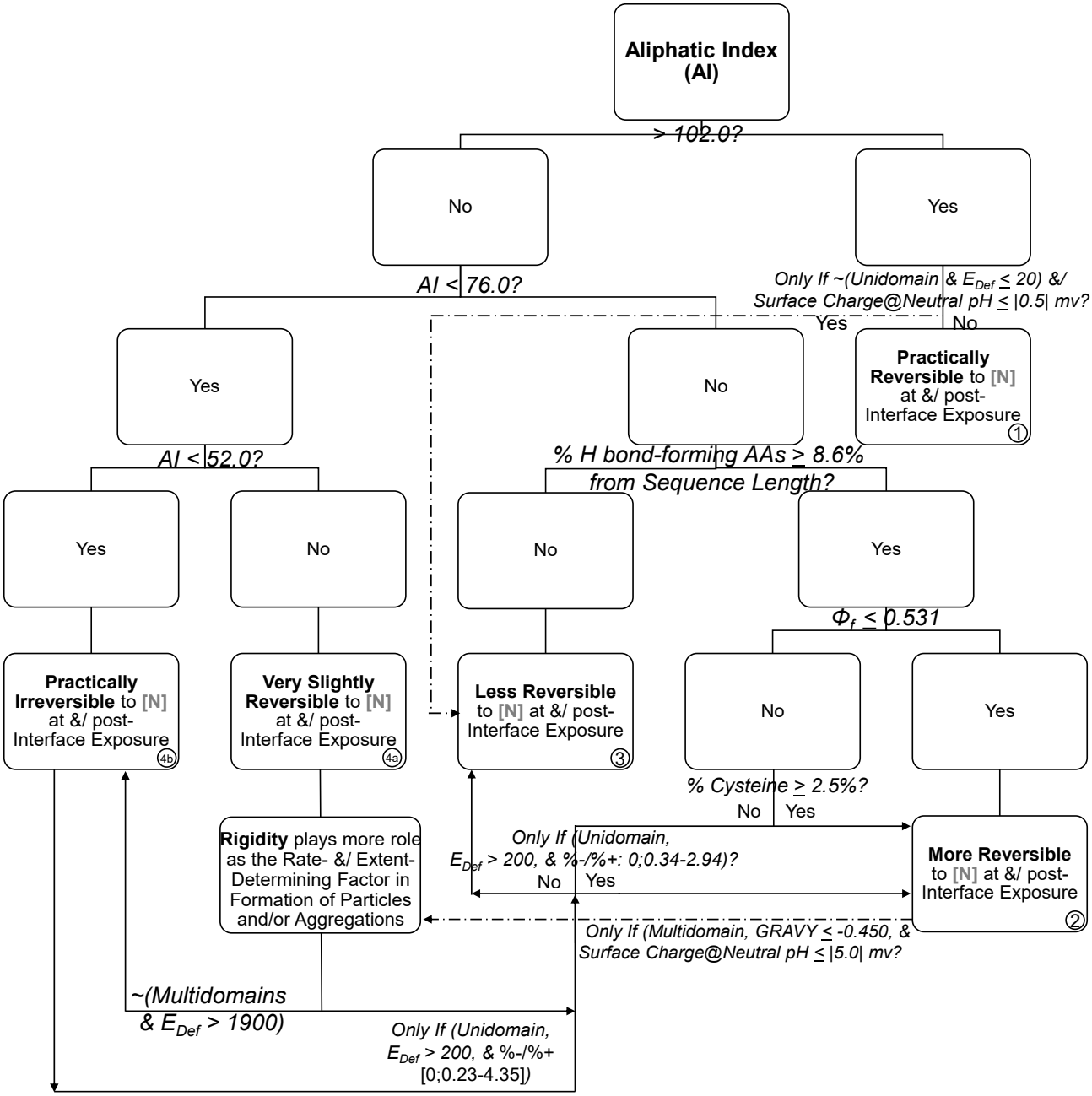

Examples for each class

Class 1 : Band 3 (/SLC4A1), CD47, Pulmonary surfactant-associated protein B & C, Beta-Lactoglobulin, Surfactin(-C), Preproinsulin, Cell shape-determining protein MreB from *Methanopyrus kandleri*, etc.

Class 2 : Actins, Spectrins, Intact Hemoglobin, Albumin, Erythropoietin, Deoxyribonuclease-1 (/INN: Dornase Alfa), Ribonuclease A, Angiopep-2, Insulin, Growth Hormone (/Somatotropin/INN: Somatropin), Hyaluronidase(PH-20), etc.

Class 3 : ApoA-I, ApoE, Myoglobin, Lysozyme, Filgrastim (Recombinant Granulocyte-Colony Stimulating Factor [G-CSF]), Interleukin-2, Invasin from *Yersinia pseudotuberculosis* (497 amino acid length fragment of the C-terminal region [InvA497]), etc.

Class 4a: Intact Immunoglobulins (including all intact monoclonal antibodies), Intact Fibrinogen, ApoJ (/clusterin), Transferrin, most Coagulation Factors (i.e. VIII), Fc-Fusion Proteins, Dibotermin Alfa, Liraglutide, etc.

Class 4b: Clinically Fatal Amyloidogenic Immunoglobulin Light Chain, Major Prion Protein, TNFRSF1A (Tumor Necrosis Factor-Binding Protein 1 aka Soluble Form of Tumor Necrosis Factor Receptor Superfamily Member 1A), etc.

Figure III-10. Proposal of a new Physiological-Therapeutic Biologics Classification System (PTBCS), classifying proteins/peptides according to their interfacial stabilities.

All in all, this unique protein refolding route due to CNP presence in (non-spherical) BCCNs may rationally be proposed and accounted for the beneficial cell membrane-coating technology. Most of these proteins are represented by the classes, called Class 1 (the best of a total 5) in the proposed Physiological-Therapeutic Biologics Classification System (PTBCS), i.e. SLC4A1 & CD47, and Class 2 (Table S III-3 & Figure III-10). For common protein examples of the latter, alpha-lactalbumin was also reported can be detached from relatively hydrophobic polystyrene surfaces and can still be practically refolded to its native form[140]. Although the proposed PTBCS cut-off values might be dialectical and the subject of science progression, to date they are a strong foundation to explain a vast heterogenic group of many proteins, both physiologic (aka natural, e.g. ~560,000s curator-reviewed protein entries in December 2021[41-43]) or therapeutic ones (~6,000 entries in December 2021[48]). In our case, we selected PTBCS cut-offs by following the currently available experimental results, both ours and others[141, 142, 143], so that they are pragmatic and also already proven to be statistically comparable to other prominent experimental, but low-throughput refoldability classification across organisms and protein types in physiologically relevant condition (Figure S III-13).

CD47 is a dysopsonic hydrophilic glycoprotein on the surface (externally), but hydrophobic globally, indicated by Φ_f 0.352 & GRAVY [Grand Average of Hydropathy] 0.541, respectively (Figure S III-11a; see their relative obtainable comparisons with other relevant [blood] proteins in Figure S III-11 and Figure S III-12). Therefore, it is also logical to elicit higher experimental melting temperature and thereby conformational stability (Figure S III-14). A striking contrast thereof is shown by clusterin, another dysopsonic hydrophilic protein, which is abundant on PEGylated particles (~35 kDa in SDS-PAGE analysis, as in Figure III-4a lane 10-11 and reported elsewhere, due to cleavage thereof[144]). Recently, clusterin (Apolipoprotein J; Φ_f 0.248) is known to highly interact with hydrophilic functionalizations, including PEG, although PEG-involving formulations exhibit low total protein adsorption[144]. Thus, this study essentially adds new insight to the current paradigm and accompanying phenomena about dysopsonin (also called “marker-of-self” or “do not eat me” signal) and PEG, which has also lately shifted remarkably. In brief, the parameters used in the PTBCS determination of CD47 and Clusterin are illustrated in Figure S III-15. Our future work will also discuss further PTBCS and its further applications for therapeutic proteins.

Experimental aging of erythrocytes triggers a conformational change in CD47 that alters the molecule from an inhibitory signal into an activating one by means of its preconjugation to Mac-1 Receptor(ITGAM–ITGB2) of macrophages before the normal recognition process by Sirpa[120]. Therefore, it is really rational to classify CD47 as a very stable molecule (including interfacially) during its lifetime, which is representatively depicted

from the RBCs half-life of 120 days. Intriguingly, our proposed novel PTBCS algorithm can distinguish it and categorize CD47 to Class 1, e.g. with SLC4A1 and other interfacially renowned stable proteins at physiological conditions (pH around 7 & 310 mOsm): beta-lactoglobulin[141], surfactin-C[145], Pulmonary surfactant-associated protein B & C, etc. (Figure III-10; Table S III-9). Furthermore, the nature/origin of proteins, such as red blood cell (membrane), blood plasma, and opsonins, can be well determined using this classification. The proteins' interfacial stability is descending from red blood cell membrane to opsonin, having none of Class 1 and much higher (i.e. 65%) Class 4a or worse compared to the two others(Figure S III-16). To represent Class 4a or worse, transferrin (Class 4a; Figure III-10), a long-researched molecule for (e.g. brain or tumor) targeting, is selected. It turns out recently to be interfacially unstable and hardly to refold, leading to its aggregation and/or easy loss of targeting capabilities, as proven experimentally and computationally, albeit their weak adsorption to any interface[124]. This behavior is in stark contrast to the Angiopep-2 (Class 2; Table S III-9), which is the most clinically-advanced protein used for targeting on drug carriers and approved by FDA in 2016[118]. Further discussion of the PTBCS algorithm is projected for our near-future independent work.

Principally, material-water interfacial tensions (IFTs; Table S III-8) represent material hydrophobicities. These serve as one of the predominant determinants of material (structural-interfacial) stability during and post-its adsorption to other materials, especially if the involved materials are relatively soft (Young's modulus < 1 GPa)[16], such as in typical cases of proteins. Therefore, understanding the hydrophobic matching concept (; analogous to the general rule "like dissolves like" or miscibility) in engineering (bio)materials and/or drug carriers is highly suggested and can be implemented starting from the interfacial activity database. So far, its availability is still limited to the synthetic ones[16], thus there is a need to develop for natural ones, i.e proteins. Herein (and as introduced in the section "Binding Affinity"), we address such issues and rationally provide tools using a hybrid of computational (3D structure of proteins) and mathematical modeling (Figure S III-9).

Generally speaking, the more hydrophobic and less solid adsorbents (e.g. [particle] surfaces) are notoriously more damaging for proteins, particularly if the proteins with lower intrinsic stability (i.e. refoldability, classified in poorer PTBCS classes, such as Class 3 or worse) are adsorbed onto it. For instance from our current study, Class 3 can be exemplified by Apolipoprotein A-I and Apolipoprotein E (Table S III-3), which are not part of the NErys, thus classified as the soft corona. According to the interfacial tension value (expressed using the versatile Owens and Wendt approach[34]), the air-water interface can be classified as one of the

harshest interfaces with about 72.8 mN/m at room temperature. Therefore, this interface can reasonably be a destructive place for any matters, ranging from (generally soft) proteins[146] to (commonly stiffer non-spherical nano) particles[16]. To compare and illustrate how detrimental and certain proteins can tackle the interfacial tension of 72.8 mN/m, the increased material-water interfacial tensions of the following materials studied herein (gold < polystyrene < graphene; Table S III-8) can be exemplified: 36.21 < 42.03 < 93.29 mN/m, respectively. These details address the abovementioned illustrations:

1) Non-spherical gold nanoparticles, which are propitious for photothermal therapeutics and drug delivery[147], are prone to be spherical ones. Interestingly, although gold-water interfacial tension is as "low" as 36.21 mN/m, however it can currently be considered a major external inducer for reshaping (into spheres) of non-spherical gold nanoparticles[148], having the sharp tips with radii of curvature ≤ 20 nm. This fact becomes more attractive, considering how rigid gold is, characterized by high mechanical properties value: bulk Young's modulus ~65 GPa and melting temperature 1,064°C[16].

2) Besides our in vivo study using polystyrene as core nanoparticles, RBC membrane is experimentally proven to also aid graphene[149], an unwrapped SWCNT (single-walled carbon nanotubes), and graphene oxide[150] during in vivo study. Employing the PTBCS concept discussed in the previous paragraph, this concept rationalizes the reason why RBC membrane coatings (i.e. NErys) herein and are also reported elsewhere[9, 151] to bestow adequate protection and cell-like functionality to even very hydrophobic surfaces in real organisms, protecting the core particles having material-water interfacial tension up to even 93.29 mN/m. Furthermore, in our current study, NErys are also proven to confer longer non-spherical shape stability. The rationalization in terms of particle shape stability is discussed deeper in the next section.

Ideally for better overall stability in long-term storage, protein-containing formulations should be stored on the surface (i.e. particles) (a) having a reasonably high binding affinity to such proteins[152, 153], (b) also possessing as low as possible $IFT_{1.2}$ (if possible, much lower than water surface tension), (c) at saturated surface-concentration or higher, (d) in the minimum presence of water, and (e) in the presence of excipients permitting preferential exclusion mechanism (e.g. trehalose, sucrose, glycerol). In this way, it has been also proven experimentally (but unfortunately to date, to our best knowledge, still without an adequate explanation in terms of interfacial activity parameters), that even freeze-dried protein with lower interfacial stability (e.g. Class 4a, such as immunoglobulin G[IgG][154], *Staphylococcus aureus*' Protein A[spa][155]; in Table S III-9) can have years-long product shelf lives in the room temperature storage on the gold nanoparticle, suggesting that the abovementioned strategies successfully mitigate the air-water interfacial tension (also called water surface tension) 72.8 mN/m. Accordingly, the long-term stability of more

degradable and drug-containing BCCNs (e.g. that can be achieved by lyophilization) will be our next further study.

All in all, the tolerable conformational changes of proteins from cell membranes during adsorption to the core particles appear to escort in yielding proper protection from notorious blood plasma protein adsorption. In turn, this study enlightens the biological complexity of cell membrane-coating technology, offering a promising alternative to synthetic coating.

4.4.4. Rationale of Particle Shape Stability

Adsorbed proteins do impact particle properties (i.e. shape / geometry [because of "size" or radius of curvature] and surface chemistry [especially hydrophobicity]), or vice versa. A better understanding of all these aspects is crucial to engineering fully functional BCCNs.

4.4.4.1. Influence of Adsorbates: Benchmarking to Others and Classification of RBC Membrane Proteins as Non-Washable

In principle, widely-useful surface active proteins have very high Φ_f and intrinsic stability (as classified in PTBCS Class 2 or better), thereby possessing higher affinity to the (very) hydrophobic material interface (e.g. air-water), decreasing that material-water interfacial tension, and withstanding it at the interface. As a general benchmark, beta-lactoglobulin (Φ_f 0.500 & Class 1; Table S III-9) can exemplify these premises and explain why it is known as the best proteinaceous surface stabilizer, prevalently used for air-water interfaces (foaming) in diverse industries[141]. With such characteristics, beta-lactoglobulin spontaneously sacrifices itself by receiving high protein-water interfacial tension, in exchange for decreasing another material-water interfacial tension (i.e. air-water one, also called water surface tension) or in other words, increasing equilibrium surface pressure). This very high Φ_f (i.e. cut-off ≥ 0.500), which strongly corresponds to both primary and secondary interfacial activity parameters (as described in the previous section "Binding Affinity"), appears to be absolutely required to persist longer in a hydrophobic material interface (such as in our tested and discussed nanoparticles), considering the radius-of-curvature-dependent interfacial activity parameters[16, 39, 156]. Noteworthily, sharp tips of non-spherical nanoparticles can have radii of curvature ≤ 20 nm, thus decreasing significantly the binding affinities and leading to its detachment propensity from the adsorbed surface. Accordingly, the rate of biomolecular corona detachment will also depend on the radius of curvature (; $R_c(t)$, i.e. size and geometry) of particles as well as on the location of certain proteins on RBC membranes. These phenomena are parts of the common confinement effects that have been discussed

more technically in chapter II[16].

The results here clearly reveal the superior ability of non-spherical BCCNs to decrease MPS clearance and increase accumulation in the brain. Expectedly, (inside surfaces of) RBC membranes were physically (/ non-covalently) adsorbed on the surface of core nanoparticles (CNPs). During circulation time, particles are unlikely desorbed, as confirmed by SPR, SFE measurements, and via all-atom molecular dynamics (AAMD) results. Our results also justify the finding of (weaker) non-covalent adsorption between similar polymeric nanoparticles (i.e. PS-COOH) and outer surface of RBC[11, 157, 158] (recently called RBC-hitchhiking). Anticipatedly, the interaction strength yields different "protection" of RBC components to nanoparticles, thus subsequent dissimilar biodistribution profile and circulation time.

From our converged simulations (Figure III-8c-d), it is clear that the Band 3 (a transmembrane [TM]) protein may vindicate the location of nanoparticle attachment. For the BCCN system, the stronger interaction of Band 3-nanoparticle (compared to phospholipid-nanoparticle) causes nanoparticles to stay on the inside surface of RBC membranes. The experimental works, displaying and proving that spherical BCCNs entirely get inside to the red blood cell membrane, were already performed by Dehaini et al. (2017)[159]. While for the RBC-hitchhiking case, considering the relatively more hydrophilic (including due to rich glycosylations of) proteins on the outer surface of RBC membranes, hydrophobic nanoparticles preferentially and evidently attach to RBC membranes via partial embedment thereof to the central dimple of RBC membranes[157] (specifically to hydrophobic phospholipid tail and/or sphingomyelin-enriched domain[160]). Interestingly, this particle positioning preference on RBC membranes appears to agree with the hydrophobic matching concept, with the relatively more hydrophobic sphingomyelin(-enriched domain; higher logP and logD; Table S III-13) is reportedly located on the lower curvature (center) area of RBC membranes. On the contrary, the relatively less hydrophobic (free) cholesterol (-enriched domain; lower logP and logD) exists on the higher curvature (edge) area[160]. Taken together, given the less amount of cholesterol in the processed RBC membranes (i.e. NErys; the similar current finding as our previous report[103]), both edges of BCCNs (owning higher curvature area) may rationally be even more hydrophilic, leading to the lower material-water interfacial tension and consequently better non-spherical shape stability (for nanoparticles with materials enabling higher density of NErys on the BCCN surface, i.e. relatively hydrophobic PS-COOH).

At physiological temperature (37°C), physiological phospholipids (including POPE, which is the most abundant phospholipid variant in RBC and is used in the computational study) exist in the fluid phase

because this temperature exceeds the phase transition temperature thereof (i.e. ~26°C[161]). Hence, likewise in a previous report[162], the presence of cholesterol at membranes at 37°C is reasonable to also decrease the membrane fluidity, by means of generally: (a) decrease area per lipid, diffusivity of both lipid at membranes and water through membranes, as well as (b) increase membrane liquefaction/phase transition temperature and thickness (data not shown).

As our[103] and other[153, 163, 164] previous reports indicate, coating of core particles using strongly-bound natural polymeric sources (cell membrane and/or protein) can considerably maintain non-sphericity and colloidal stability of particles, even at lower pH (i.e. up to 4) representing the lowest intracellular pH in the lysosomes. The effectivity thereof is comparable to the strongly-bound synthetic ones, e.g. PVA[16] and PVP[81], to the hydrophobic particles. Please recall that reshaping into spheres preferentially occurred when weakly bound conventional/synthetic (i.e. CTAB, PEG, phosphatidylcholine) or no stabilizer is applied for coating of hydrophobic materials[16, 165].

Interestingly, in the presence of additional lysosomal proteases (i.e. cathepsins) at pH ~5, we found that the cell membrane-coating (or may also be called “hard corona” in the other fields[166]) still can maintain the shape stability of non-spherical BCCNs. However, it is lower by about an order of magnitude compared to the condition at pH 7.4 (data not shown). Additionally, this can reinforce the current knowledge that the biomolecular corona is well-preserved during particle cellular uptake, but it may be (slowly; from ca. 8 to 24 h) degraded in the endosomes—lysosomes[163, 167], depending on its binding affinity onto the core particles. The stronger the binding affinity between them is, the higher the protection of the biomolecular corona is. This is analogous to the mechanism of immunoglobulin G (IgG) or albumin half-life prolongation, facilitated by their high binding affinity to neonatal Fc receptor (FcRn; also standardly abbreviated FCGRT[41, 42] or called IgG receptor FcRn large subunit p51, or Brambell receptor) in cells to escape from endosomal—endo-lysosomal compartments[168].

According to the comprehensive study comparison[16], interfacial tensions (IFTs; which are calculated based on the Owens-Wendt approach[34] and to its later secondary interfacial activity parameters[16]) appear to act as one of the reliable foundations to rank materials' hydrophobicity and binding affinity. They explain well the stabilizers' "non-washability" from materials/particles. Here, the IFT and secondary interfacial activity parameters (Table S III-8 & Table S III-10, respectively) demonstrate the accurate agreements to our and other experimental results[169] and calculable rationales thereof. This approach vindicates and quantifies the

concept that the spatially correct anchored entities in the membrane may increase the right-side-out membrane orientation when the entity-membrane interaction elicits adequately strong binding free energy[170]. Table S III-10 clearly displays that for relatively hydrophobic entities, such as poly(d,l-lactic-co-glycolic acid) [PLGA; IFT 6.08 mN/m], it can facilitate the higher right-side-out membrane orientation through simple physical adsorption compared to the relatively more hydrophilic ones (e.g. human hyaluronidase PH-20 and water). Based on IFT values (Table S III-8), the hydrophobicity of these material increases: hyaluronidase PH-20 < fibrinogen < plasma < fibrin < serum < collagen (0.28 < 2.51 < 11.89 < 18.34 < 20.66 < 44.40 mN/m), respectively. In fact, to overcome the poor surface activity of superficially hydrophilic human hyaluronidase PH-20 (Φ_f 0.295, which is equivalent to the estimated X_p and SFE of ~0.7557 and ~71.42 mN/m, respectively; Figure S III-9), experiments of Zhou et al.[170] demonstrates troubleshoot thereof by producing the stronger interaction of this protein via an additional covalent bond (chemical adsorption) with a long-enough linker/spacer length. This step is indispensable for the higher enzymatic activity of human hyaluronidase PH-20. This also strongly suggests that higher correctness of membrane orientation can be reached in various ways, both optimizing the strength and spatial configuration of the adsorbents.

In other cases, thanks to the cell membrane-coating technology, the hydrophobic Gold (Au)[13] and the hydrophilic derivative of highly hydrophobic graphene, i.e. graphene oxide[151] nanoparticles have also been proven to result in a prolonged circulation time. From our own data, it is very clear that the really strong binding affinity of the cell membrane (i.e. NErys; Table S III-10) to the core particles was escorted by significant modulation of cell membrane protein components. Nonetheless, cell membranes still display considerable positive effects in protecting shape stability, colloidal, and biological stability of (“correctly” and ”sufficiently”) coated particles. It can be implied that the perturbed secondary structures do not necessarily affect the functionality of protein cell membranes, reasonably due to a larger proportion of relatively high protein intrinsic stability (i.e. refoldable) proteins as classified in PTBCS class 2 or better.

Non-spherical (rod) prions (as pathological major prion proteins, or also called and designated Scrapie Prion Proteins[171] and PrP^{Sc}[172], respectively; with their dimensions ~150 x ~15 x ~15 nm) do not produce immune or inflammatory responses[173], although the surface hydrophobicity on PrP^{Sc} increases (compared to the native PrP) because of loss of glycosylation(s) at particular site(s)[41, 42, 174]. Based on those facts, the new insights of PrP^{Sc} longevity in the body are proposed and correlate well to the recent findings[16, 175, 176], including our results here and in Chapter II[16]. The presence of a certain internal structure (crystallinity), relatively low final protein surface hydrophobicity index (Φ_f), and Young’s Modulus can be considered as the

positive factors influencing the stable PrP^{Sc}'s non-sphericity and/or circulation time, respectively. For the two former, besides the well-known crystallinity of PrP^{Sc}[175], our bioinformatic analysis reveals that even PrP^{Sc} loses a deglycosylation site, it still has a final protein surface hydrophobicity index (Φf) as low as 0.449, corresponding to the surface free energy (SFE) 55 mN/m and material-water interfacial tension ~6 mN/m, experimentally proven borderline values still permitting much longer non-sphericity for any materials[16]. This Φ_f value is also even getting closer to the cumulative Φ_f of blood plasma 0.448 (Table S III-14). For the latter factor, low Young's modulus of PrP^{Sc} (0.1 - 1.4 GPa[177]; which is interpreted as quite soft/elastic/flexible) also aligns with the current insight, i.e. the lower the Young's Modulus of materials is, the lower the endocytosis and phagocytosis thereof are, the longer the blood circulation thereof is[176].

In general and according to our bioinformatic analyses to the most recent, seminal reports (Figure S III-18), the development of blood plasma proteins' surface hydrophobicity over time in human (and other organisms') body depends on the core entities' (e.g. material's and/or particle's) hydrophobicity. For example, below a certain cut-off value (i.e. Φ_f 0.410), the more hydrophilic the particle materials are, the more hydrophilic adsorbed blood plasma corona is; also, the more hydrophilic their protein corona is until intermediate time, and later (if observation time is proper,) they tend to gradually rise again. By comparison, the contrary occurs above the cut-off value. These new interesting bioinformatic findings appear to correlate well with the current facts. Lectin pathway-guided complement activation epitomizes the former, while the classic pathway represents the latter. In this case, very hydrophilic exogenous objects (e.g. bacteria or highly/densely PEGylated particles, resulting in "brush" configuration, such as used until in vitro study herein; Figure S III-18 & Figure S III-19) initially attract many hydrophilic and abundant proteins, such as Immunoglobulin A (IgA) and importantly: fibrinogen. At the intermediate time, due to the conversion of (relatively more hydrophilic) fibrinogen to (relatively more hydrophobic) fibrin (clot), the surface hydrophobicity of protein corona rises. Consequently, these fibrin-coated objects can transiently protect the objects from phagocytosis and isolate them from other defenses of the host, including tissue deposition[44, 49, 95, 178-180].

These simulation results are very reasonable and relevant because short-range forces (non-polar: hydrophobic/van der Waals interactions) are dominating characteristics of surface hydrophobicity at high protein concentration matrices[181, 182], such as in organisms' blood circulation (i.e. human ~70 mg/mL). Besides the current study, the dominance of short-range forces is also reflected experimentally in the result of Wan et al. 2015[183]. They first adsorbed blood plasma proteins to bare spherical silica nanoparticles (initial & consequent Ø ~70 & 120 nm, respectively) to form "hard corona" in situ and later deglycosylated it.

Surprisingly, deglycosylation could not remove protein from particles. Instead, it could only cut a part of glycan chains, thus letting proteins expose the new inner glycan chain, which is subsequently and vigorously recognized by macrophages. This can be interpreted that a) the surface hydrophobicity is one of the main factors affecting protein adsorption to the material surface, irrespective of protein glycosylation state and b) once strong enough binding affinity (due to hydrophobic part of proteins) reaches a surface, it is practically non-washable, thereby eliciting binding-memory effect (as also reported elsewhere[184]). In our current work, this interpretation can be translated into that Φ_f and Φ_i play a role in the short term (minutes-to-hour) and long term interaction (hours upwards), respectively. Our previous work[16] provides an algorithm about material non-washability (Figure S III-22; therein: stabilizer equal), which interestingly can also be extended and applied for biomolecular corona cases. As proof thereof, the exemplary dataset is displayed in Table S III-12a. Evidently, our calculated binding affinity value (difference of WoA_3-$IFT_{1.2}$) appears to explain and distinguish the phenomena & stability difference between all tested particles, Furthermore, our proposed algorithm, calculation, and conversions are also proven for the more organic cases, such as dextran and polystyrene (Table S III-12b). For instance, dextran, a relatively hydrophilic polymer (Table S III-8), tends to also adsorb relatively more hydrophilic opsonins, i.e. C3 instead of IgGs(‘ fragments) (Figure S III-11a & Figure S III-19).

4.4.4.2. Influence of Adsorbents: Core Particles

As mentioned in the first section ”Non-spherical Shape Stability” and in Chapter II[16], complex manufacturing aspects, including mechanical properties (i.e. Young’s modulus and Tg) affect substantially the shape stability of non-spherical particles. Admittedly, the experimentally developed non-spherical nanoparticles here represent mostly the case of small molecule drugs incorporated into macromolecule drug carriers. This may cause differences in in vivo results. For example, using a similar dimension as our non-spherical particles and with mice as in vivo subjects, Wibroe et al.[158] reported that the biodistribution difference between differently shaped non-coated particles (loaded by radioactive H^3-oleic acid; MW 282.5 Da; relatively smaller than the MW of used dyes here; but important to note, hitchhiked to intact, healthy erythrocytes) lasted relatively shorter in mice circulation system than reported in our studies. We argue that in such non-spherical systems, a few aspects have to be considered in the circulation system: 1) they might exert a fast reshaping to spheres in abundant blood plasma proteins (i.e. opsonins), thereby being more rapidly recognized by the MPS cells. 2) Additionally and importantly, the reshaping phenomenon of non-spherical particles into spheres occurs in high shear conditions within the blood circulation, causing faster

dynamic exchanges of loosely bound protecting biomolecules[148].

Additionally, using the same approaches[16], we also found a proportional correlation between the interfacial activity parameters of loaded substances in particles and their release patterns, both in our current study and in literature elsewhere (Table S III-8 & Table S III-11).

4.4.5. Overall Rationale and Outlook

Non-spherical BCCNs provide a new, bioinspired way to deliver nanoparticles in the close vicinity of vascular endothelium in the brain. The beneficial effects thereof are expected to be higher in tissues with extensive microvascular networks, as is the case of the brain and lungs (Figure III-6a), allowing close contact between particles and the endothelium. This close contact likely plays a role in dislodging the weakly attached biomolecular corona from nanoparticle surfaces in the circulation system (extracellularly), besides the strongly-attached one occurring progressively inside cellular lysosome (intracellularly).

At a fundamental level, the use of non-spherical (prolate) BCCNs offers a new hybrid approach for drug delivery. Synthetic systems, such as nanoparticles, provide the advantages of control over particle composition and manufacturability. They, however, suffer from the limitations caused by immune system clearance. On the other hand, a RBC membrane naturally prevents MPS clearance for about 120 days and allows particulate structures continuously to reach all tissues. An approach based on the use of natural RBC membranes to encapsulate synthetic non-spherical nanoparticles (projecting to carry drugs; herein already simulated by clinically relevant substances) and to subsequently deliver them to tissues, offers an optimal blend of natural and synthetic systems. Cell membrane-coating also provides an ideal combination of enhanced circulation and targeting. Current ways of improving circulation are based on the use of PEGs or poloxamers, which suffer from limited circulation times and accelerated blood clearance (ABC) after multiple administrations[7, 95]. The ability of non-spherical BCCNs to exhibit longer circulation and unique tissue distribution after repetitive administrations need further investigations, albeit no immune response upon multiple administration of spherical counterparts has been reported [185]. Also, to achieve the full potential of non-spherical BCCNs delivery, additional questions have to be answered. These comprise of understanding the differently loaded substances' effect on the fate of non-spherical BCCNs in (more) organs, limits of substance loading on the system, and behavior of the system post multiple administrations. It is also important to note that for more universal applications to human patients, the system requires the use of

either patient's own (autologous) cells or other pre-treated cells which can safely be transfused into patients.

Non-spherical (prolate) BCCNs provide new ways to address two major issues that nanoparticles regularly face; the superior evasion of MPS organs, liver, and spleen, and targeted delivery to difficult-to-reach sites in the body, such as the brain and lungs. As proven in an in vivo study, these effects are better than those achievable by conventional spherical BCCNs, which have been attractive to scientists since the last decade as a novel approach[9]. While studies herein were conducted with less biodegradable polystyrene particles for proof of concept and testing the limits of protein adsorption behavior, non-spherical BCCNs can be extended to more biodegradable materials, such as certain aliphatic polyesters owning glass transition temperature and hydrophobicity as close as or even higher than polystyrene.

Compared to the prolate counterparts, there was only a minor increase in shape stability after the oblate ellipsoid core nanoparticles were coated by the RBC cell membrane (characterized by typical shifting time). This strongly suggests that more abundant smaller radii of curvature on oblate ellipsoid core nanoparticles may weaken the RBC cell membrane binding affinity/adsorption to core nanoparticles (as also generally estimated in Figure S III-17), leading to poorer protection from high core particle material-water interfacial tension and subsequent pressure.

In a relatively static in vitro environment, the protein corona readily adsorbs onto particles and reaches equilibrium. In vivo, a molecularly richer protein corona is formed in flowing conditions within the blood circulation and by the dynamic exchange of proteins, it evolves over time[166]. Interestingly, the evolution thereof heavily depends on the particles' surface chemistry (mainly hydrophobicity) and uniquely determines the subsequent immune system responses as well as the fate of particles in organisms[16, 180, 186].

Our finding agrees with the fact about the curvature-dependent binding affinity between any material, especially protein-related interactions[187, 188]. Importantly, the results herein are also in agreement with the evidence that hydrophobic interaction (represented usually as interfacial tension) is virtually the main factor determining binding affinity[187, 189]. As emphasized in Chapter II[16], the radius of curvature-dependent shape is also an important feature determining the particles' fate, starting from protein adsorption in the circulation system until the behavior inside cells. Frankly, oblate ellipsoid nanoparticles, which are produced by biaxial stretching, possess a much higher proportion (about 40x) of the radius of curvature less than 1 compared to the prolate counterpart with the same volume ([Figure S III-20, Figure S III-21 & Supplemental Calculation]

vs Figure III-9c). Therefore, it is not surprising that such particles exhibit lower non-spherical shape stability regardless of any coating (including with cell membrane; Figure S III-20 & Figure S III-21). Also because of this reason, the oblate nanoparticles showed poorer in vivo performances compared to prolate ones, including and importantly half-life[186]. This strongly suggests that the functionality of cell membrane-coating is also limited by its case-by-case binding affinity to the core particles. Also, this implies that a relatively stronger interaction is absolutely required, in case longer protection of (non-spherical) particles from a molecularly rich biomolecular (especially protein) corona within the blood circulation is expected. Otherwise, given also highly flowing conditions within the blood circulation leading to the faster dynamic exchanges of biomolecule and evolution of biomolecular corona over time[166], a weaker interaction (e.g. between poly(d,l-lactic-co-glycolic acid) [PLGA]-NErys; Table S III-8 & Table S III-10) reasonably demonstrates a higher gain of more strongly attached (hydrophobic) proteins, including usually relatively hydrophobic exogenous toxins (e.g. melittin [Φ_f 0.518; Table S III-9], alpha-hemolysin [Φ_f 0.464; Table S III-9], etc.; see their relative obtainable comparisons with blood proteins in Figure S III-11 and Figure S III-12). Our new quantitative, mechanistic understanding of protein corona attachment can also explain the development of biomimetic nanosponges, preferably employing (relatively hydrophilic and porous) PLGA and erythrocyte membranes as the core nanoparticles and cell membrane-coating, besides the common reason of the core particle materials' biodegradability[190].

To enlighten the abovementioned issues, the new quantitative confinement effects (Figure S III-17a-d) are proposed. This estimates excellently the following reported facts:

(1) the adsorbed blood plasma proteins demonstrate an exponentially reduced affinity to the lower nanoparticles' radius (of curvature), as described herein or as used elsewhere[191] (e.g. to gold particles with the radius of curvature of 50 nm to 2.5 nm). This occurs due to much higher pressure from air-water interfacial tension working on any objects at interfaces of smaller nanoparticles' radius of curvature, enabling the higher possibility to a) mobilize nanoparticle materials at surfaces and b) detach any adsorbates (i.e. protein and other membrane components) out of the nanoparticle surfaces, and

(2) the therapeutic proteins, which are adsorbed to particles with increasing radius of curvature (from ~50 nm to 1 nm), exhibit a positively exponential affinity to their corresponding receptors[17]. This is reasonable because of more exposure to cryptic epitopes of the adsorbed proteins through unfolding[192].

5. Conclusions

Non-spherical bioinspired red blood cell membrane-coated nanoparticles (BCCNs) reduced significantly the uptakes by cells and organs of mononuclear phagocyte system (MPS), as compared to their non-coated or spherical counterpart. Consequently, the non-spherical BCCNs displayed a remarkably higher concentration in blood over a 72 h period and interestingly permitted temporary accumulation in the brain for 48 h, while decreasing their uptake by liver and spleen. The non-spherical BCCNs and their rationale reported here can be utilized to design more advanced carrier systems, which not only target specific tissues, but also minimize association with clearance organs. The in vivo and auxiliary studies in this report have complemented each other well. The very strong and practically irreversible interactions of (superficially) hydrophobic proteins from the intracellular part of cell membranes to the core particle materials serve as a good anchor, while also improving the right-side-out membrane orientation and integrity. Furthermore, this interaction also proves that the better maintenance of non-spherical shape stability can only be attained by the adequate amount of stabilizers because of the strong affinity between particles and stabilizers. Taken together, we have successfully combined multiple aspects (shape and cell membrane-coating) to develop a single formulation. With further research focused to treat clinically relevant diseases, methods for incorporating drugs into particles into more biodegradable polymers with similar or more supportive physicochemical properties (e.g. hydrophobicity and Young's modulus) and/or crystalline delivery systems require to be investigated.

6. Acknowledgements

DAAD (Deutscher Akademischer Austauschdienst) is greatly thanked for BMH's scholarship. Dr. Aditi Mehta, Natascha Hartl, and Prof. Dr. Olivia Merkel (Ludwig-Maximilians-Universität München, Germany) are highly thanked for the kind gift of human monocytes cell line THP-1, the introduction to work with cell lines, and the use of flow cytometry in the uptake study. Kavisha Ulapane and Isaac Alejandro Nevarez-Saenz (group of Prof. Dr. Teruna J. Siahaan, Department of Pharmaceutical Chemistry, The University of Kansas, USA) are kindly thanked for the surface plasmon resonance (SPR)'s introduction and discussion. Dr. Björn-Hendrik Peters (group of Prof. Dr. Christian Schöneich, Department of Pharmaceutical Chemistry, The University of Kansas, USA) is acknowledged for the access and technical help of the probe sonicator. We thank Christian Minke (Department of Chemistry, Ludwig-Maximilians-Universität München, Germany) for SEM-EDX assistance. Dr. med. Georg Wittmann (Abteilung für Transfusionsmedizin, Zelltherapeutika und Hämostaseologie, Klinikum der Universität München, München, Germany) is thanked for the access of human packed red blood cells and plasma. Gratitude is expressed to Dr. Wei Zhang (group of Prof. Dr. Ernst Wagner, Department of Pharmaceutical Biotechnology, Ludwig-Maximilians-Universität München, Germany)

for providing negative staining material for TEM analysis. Dr. Markus Döblinger (group of Prof. Dr. Thomas Bein, Department of Chemistry, Ludwig-Maximilians-Universität München, Germany) is kindly acknowledged for assistance in TEM investigations. All computational works, which were performed using Schrödinger Software (Release 2017-4), were processed in the Linux Cluster of Leibniz-Rechenzentrum (LRZ) Supercomputing Centre of Bavarian Academy of Sciences and Humanities. We are thankful to Raisa M. R. Yogiaman for the creation of the illustrations. Part of Graphical Abstract contains an image template which is freely provided by Servier Medical Art (http://smart.servier.com). Over the course of our research (with an initial part was already disseminated in October 2016[193]), there was an unintentional, but similar work direction to this work emerged later in December 2016[194]. Therefore, for faster, progressive, fair, and rigorous science advancement in this research area, the reader could combine knowledge from and is also kindly asked to acknowledge both.

7. References

[1] E. Blanco, H. Shen, M. Ferrari, *Nat Biotech* **2015**, *33*, 941; S. Azarmi, W. H. Roa, R. Löbenberg, *Adv. Drug Delivery Rev.* **2008**, *60*, 863; A. H. Faraji, P. Wipf, *Biorg. Med. Chem.* **2009**, *17*, 2950; Q. Wang, H. Cheng, H. Peng, H. Zhou, P. Y. Li, R. Langer, *Adv. Drug Delivery Rev.* **2015**, *91*, 125.

[2] D. Peer, J. M. Karp, S. Hong, O. C. Farokhzad, R. Margalit, R. Langer, *Nat. Nanotechnol.* **2007**, *2*, 751; L. Brannon-Peppas, J. O. Blanchette, *Adv. Drug Delivery Rev.* **2012**, *64*, 206; S. Dhar, F. X. Gu, R. Langer, O. C. Farokhzad, S. J. Lippard, *Proc. Natl. Acad. Sci. U. S. A.* **2008**, *105*, 17356; M. E. Davis, Z. Chen, D. M. Shin, *Nature Reviews Drug Discovery* **2008**, *7*, 771; N. Bertrand, J. Wu, X. Xu, N. Kamaly, O. C. Farokhzad, *Adv. Drug Delivery Rev.* **2014**, *66*, 2; O. C. Farokhzad, R. Langer, *ACS Nano* **2009**, *3*, 16.

[3] J. Hrkach, D. Von Hoff, M. M. Ali, E. Andrianova, J. Auer, T. Campbell, D. De Witt, M. Figa, M. Figueiredo, A. Horhota, S. Low, K. McDonnell, E. Peeke, B. Retnarajan, A. Sabnis, E. Schnipper, J. J. Song, Y. H. Song, J. Summa, D. Tompsett, G. Troiano, T. Van Geen Hoven, J. Wright, P. LoRusso, P. W. Kantoff, N. H. Bander, C. Sweeney, O. C. Farokhzad, R. Langer, S. Zale, *Sci. Transl. Med.* **2012**, *4*, 128ra39; J. Kattan, J.-P. Droz, P. Couvreur, J.-P. Marino, A. Boutan-Laroze, P. Rougier, P. Brault, H. Vranckx, J.-M. Grognet, X. Morge, *Investigational new drugs* **1992**, *10*, 191; M. Green, G. Manikhas, S. Orlov, B. Afanasyev, A. Makhson, P. Bhar, M. Hawkins, *Annals of Oncology* **2006**, *17*, 1263; R.-D. Hofheinz, S. U. Gnad-Vogt, U. Beyer, A. Hochhaus, *Anti-cancer drugs* **2005**, *16*, 691.

[4] T. M. Allen, P. R. Cullis, *Science* **2004**, *303*, 1818; E. Ruoslahti, *Adv. Mater.* **2012**, *24*, 3747; B. Wang, L. Hu, T. J. Siahaan, *Drug Delivery: Principles and Applications*, Wiley, **2016**.

[5] J.-W. Yoo, E. Chambers, S. Mitragotri, *Current pharmaceutical design* **2010**, *16*, 2298; K. Riehemann, S. W. Schneider, T. A. Luger, B. Godin, M. Ferrari, H. Fuchs, *Angew. Chem. Int. Ed.* **2009**, *48*, 872; W. R. Sanhai, J. H. Sakamoto, R. Canady, M. Ferrari, *Nat. Nanotechnol.* **2008**, *3*, 242; F. Alexis, E. Pridgen, L. K. Molnar, O. C. Farokhzad, *Mol. Pharmaceutics* **2008**, *5*, 505.

[6] J. L. Perry, K. G. Reuter, M. P. Kai, K. P. Herlihy, S. W. Jones, J. C. Luft, M. Napier, J. E. Bear, J. M. DeSimone, *Nano Lett.* **2012**, *12*, 5304; D. Bazile, C. Prud'homme, M.-T. Bassoullet, M. Marlard, G. Spenlehauer, M. Veillard, *J. Pharm. Sci.* **1995**, *84*, 493.

[7] T. Ishihara, M. Takeda, H. Sakamoto, A. Kimoto, C. Kobayashi, N. Takasaki, K. Yuki, K.-i. Tanaka, M. Takenaga, R. Igarashi, T. Maeda, N. Yamakawa, Y. Okamoto, M. Otsuka, T. Ishida, H. Kiwada, Y. Mizushima, T. Mizushima, *Pharm. Res.* **2009**, *26*, 2270; T. Ishida, K. Masuda, T. Ichikawa, M. Ichihara, K. Irimura, H. Kiwada, *Int. J. Pharm.* **2003**, *255*, 167; T. Ishida, R. Maeda, M. Ichihara, K. Irimura, H. Kiwada, *J. Controlled Release* **2003**, *88*, 35.

[8] P. L. Rodriguez, T. Harada, D. A. Christian, D. A. Pantano, R. K. Tsai, D. E. Discher, *Science* **2013**, *339*, 971.

[9] C.-M. J. Hu, L. Zhang, S. Aryal, C. Cheung, R. H. Fang, L. Zhang, *Proc. Natl. Acad. Sci. U. S. A.* **2011**, *108*, 10980.

[10] C.-M. J. Hu, R. H. Fang, B. T. Luk, K. N. H. Chen, C. Carpenter, W. Gao, K. Zhang, L. Zhang, *Nanoscale* **2013**, *5*, 2664.

[11] E. Chambers, S. Mitragotri, *J. Controlled Release* **2004**, *100*, 111.

[12] E. Chambers, S. Mitragotri, *Exp Biol Med (Maywood)* **2007**, *232*, 958; V. R. Muzykantov, *Expert opinion on drug delivery* **2010**, *7*, 403; V. Muzykantov, D. Sakharov, M. Smirnov, S. Domogatsky, G. Samokhin, *FEBS Lett.* **1985**, *182*, 62.

[13] W. Gao, C. M. Hu, R. H. Fang, B. T. Luk, J. Su, L. Zhang, *Adv. Mater.* **2013**, *25*, 3549.

[14] Q. Jiang, Z. Luo, Y. Men, P. Yang, H. Peng, R. Guo, Y. Tian, Z. Pang, W. Yang, *Biomaterials* **2017**.

[15] J. A. Champion, S. Mitragotri, *Proc. Natl. Acad. Sci. U. S. A.* **2006**, *103*, 4930; J. A. Champion, S. Mitragotri, *Pharm. Res.* **2009**, *26*, 244; R. Mathaes, G. Winter, A. Besheer, J. Engert, *Int. J. Pharm.* **2014**, *465*, 159.

[16] B. M. Haryadi, D. Hafner, I. Amin, R. Schubel, R. Jordan, G. Winter, J. Engert, *Adv. Healthcare Mater.* **2019**, *8*, 1900352.

[17] W. Jiang, B. Y. S. Kim, J. T. Rutka, W. C. W. Chan, *Nat. Nanotechnol.* **2008**, *3*, 145.

[18] D. T. Wiley, P. Webster, A. Gale, M. E. Davis, *Proc. Natl. Acad. Sci. U. S. A.* **2013**, *110*, 8662.

[19] Graz University of Technology, Institute of Analytical Chemistry, Applied Sensor Group, Fluorophores.org (http://www.fluorophores.tugraz.at/), **2019**; AAT Bioquest Inc., AAT Bioquest®Spectrum Viewer (https://www.aatbio.com/spectrum/), **2019**.

[20] K. Leung, *Hoechst 33258-polyethylene glycol-IR-786*, National Institutes of Health (NIH), Bethesda, MD, USA **2013**.

[21] Bangs Laboratories; Inc., (Ed: Bangs Laboratories; Inc. (A Division of Polysciences)), Ask "The Particle Doctor®", Fishers, IN, USA **2011**.

[22] EDQM, Guide to the Preparation, Use and Quality Assurance of Blood Components, European Directorate for the Quality of Medicines & HealthCare, Strasbourg, France **2015**.

[23] EDQM, *European Pharmacopoeia, 9th Edition, Including Subscription to Supplement 9.6-9.8*, Council of Europe, European Pharmacopoeia Commission, European Directorate for the Quality of Medicines & Healthcare, Strasbourg, France **2019**.

[24] J. T. Dodge, C. Mitchell, D. J. Hanahan, *Arch. Biochem. Biophys.* **1963**, *100*, 119.

[25] D. L. Kasper, J. L. Jameson, S. L. Hauser, J. Loscalzo, A. S. Fauci, D. L. Longo, *Harrison's Principles of Internal Medicine 19/E (Vol.1 & Vol.2)*, McGraw-Hill Education, New York, NY, USA **2015**.

[26] Thermo Fisher Scientific, in *Instructions: Micro BCA Protein Assay Kit (Catalog Number 23235) & Pierce™ BCA Protein Assay Kit (Catalog Number 23225),* thermofisher.com, Thermo Fisher Scientific, Rockford, IL, USA **2018**.

[27] J. C. M. Stewart, *Anal. Biochem.* **1980**, *104*, 10.

[28] Sigma-Aldrich, in *www.sigmaaldrich.com*, Product Information: Cholesterol Quantitation Kit (Catalog Number MAK043), Merck KGaA, Darmstadt, Germany **2018**.

[29] J.-G. Piao, L. Wang, F. Gao, Y.-Z. You, Y. Xiong, L. Yang, *ACS Nano* **2014**, *8*, 10414.

[30] P. J. Sinko, *Martin's Physical Pharmacy and Pharmaceutical Sciences*, Lippincott Williams & Wilkins, Philadelphia, PA, USA **2016**.

[31] S. I. Jeon, J. H. Lee, J. D. Andrade, P. G. De Gennes, *J. Colloid Interface Sci.* **1991**, *142*, 149; M. Vittaz, D. Bazile, G. Spenlehauer, T. Verrecchia, M. Veillard, F. Puisieux, D. Labarre, *Biomaterials* **1996**, *17*, 1575.

[32] V. Oberle, U. Bakowsky, I. S. Zuhorn, D. Hoekstra, *Biophys. J.* **2000**, *79*, 1447.

[33] C. J. Van Oss, R. J. Good, M. K. Chaudhury, *J. Chromatogr. A* **1987**, *391*, 53.

[34] D. K. Owens, R. C. Wendt, *J. Appl. Polym. Sci.* **1969**, *13*, 1741.

[35] R. H. Muller, S. S. Davis, L. Illum, E. Mak, in *Targeting of Drugs With Synthetic Systems*, (Eds: G. Gregoriadis, J. Senior, G. Poste), Springer US, Boston, MA **1986**, 239.

[36] A. Savitzky, M. J. E. Golay, *Anal. Chem.* **1964**, *36*, 1627.

[37] N. J. Greenfield, *Nature protocols* **2006**, *1*, 2876.

[38] C. Louis-Jeune, M. A. Andrade-Navarro, C. Perez-Iratxeta, *Proteins: Structure, Function, and Bioinformatics* **2012**, *80*, 374.

[39] P. Roach, D. Farrar, C. C. Perry, *J. Am. Chem. Soc.* **2006**, *128*, 3939.

[40] T. Mosmann, *Journal of Immunological Methods* **1983**, *65*, 55.

[41] R. Apweiler, A. Bairoch, C. H. Wu, W. C. Barker, B. Boeckmann, S. Ferro, E. Gasteiger, H. Huang, R. Lopez, M. Magrane, M. J. Martin, D. A. Natale, C. O'Donovan, N. Redaschi, L. S. L. Yeh, *Nucleic Acids Res.* **2004**, *32*, D115.

[42] The-UniProt-Consortium, *Nucleic Acids Res.* **2018**, *47*, D506.

[43] The-UniProt-Consortium, *Nucleic Acids Res.* **2020**, *49*, D480.

[44] M. Hadjidemetriou, Z. Al-Ahmady, M. Mazza, R. F. Collins, K. Dawson, K. Kostarelos, *ACS Nano* **2015**, *9*, 8142; M. Hadjidemetriou, Z. Al-Ahmady, K. Kostarelos, *Nanoscale* **2016**, *8*, 6948.

[45] S. S. Raesch, S. Tenzer, W. Storck, A. Rurainski, D. Selzer, C. A. Ruge, J. Perez-Gil, U. F. Schaefer, C.-M. Lehr, *ACS Nano* **2015**, *9*, 11872.

[46] M. L. Immordino, F. Dosio, L. Cattel, *Int. J. Nanomed.* **2006**, *1*, 297.

[47] D. S. Wishart, C. Knox, A. C. Guo, S. Shrivastava, M. Hassanali, P. Stothard, Z. Chang, J. Woolsey, *Nucleic Acids Res.* **2006**, *34*, D668; D. S. Wishart, Y. D. Feunang, A. C. Guo, E. J. Lo, A. Marcu, J. R. Grant, T. Sajed, D. Johnson, C. Li, Z. Sayeeda, N. Assempour, I. Iynkkaran, Y. Liu, A. Maciejewski, N. Gale, A. Wilson, L. Chin, R. Cummings, D. Le, A. Pon, C. Knox, M. Wilson, *Nucleic Acids Res.* **2017**, *46*, D1074.

[48] T. Peryea, N. Southall, M. Miller, D. Katzel, N. Anderson, J. Neyra, S. Stemann, Đ.-T. Nguyễn, D. Amugoda, A. Newatia, R. Ghazzaoui, E. Johanson, H. Diederik, L. Callahan, F. Switzer, *Nucleic Acids Res.* **2020**, *49*, D1179.

[49] U.S. Food & Drug Administration, *Vol. FDA Approved Drug Products, accessdata.fda.gov/scripts/cder/daf/*, FDA/Center for Drug Evaluation and Research, Silver Spring **2022**, Package Insert.

[50] J. Kyte, R. F. Doolittle, *J. Mol. Biol.* **1982**, *157*, 105.

[51] L. P. Kozlowski, *Biol. Direct* **2016**, *11*, 55.

[52] B. Bjellqvist, G. J. Hughes, C. Pasquali, N. Paquet, F. Ravier, J.-C. Sanchez, S. Frutiger, D. Hochstrasser, *ELECTROPHORESIS* **1993**, *14*, 1023; B. Bjellqvist, B. Basse, E. Olsen, J. E. Celis, *ELECTROPHORESIS* **1994**, *15*, 529.

[53] A. Ikai, *The Journal of Biochemistry* **1980**, *88*, 1895.

[54] S. P. Tiwari, E. Fuglebakk, S. M. Hollup, L. Skjærven, T. Cragnolini, S. H. Grindhaug, K. M. Tekle, N. Reuter, *BMC Bioinformatics* **2014**, *15*, 427; S. M. Hollup, G. Salensminde, N. Reuter, *BMC Bioinformatics* **2005**, *6*, 52; K. Hinsen, *Proteins: Structure, Function, and Bioinformatics* **1998**, *33*, 417.

[55] D. Szklarczyk, J. H. Morris, H. Cook, M. Kuhn, S. Wyder, M. Simonovic, A. Santos, N. T. Doncheva, A. Roth, P. Bork, L. J. Jensen, C. von Mering, *Nucleic Acids Res.* **2016**, *45*, D362; D. Szklarczyk, A. L. Gable, D. Lyon, A. Junge, S. Wyder, J. Huerta-Cepas, M. Simonovic, N. T. Doncheva, J. H. Morris, P. Bork, L. J. Jensen, Christian v. Mering, *Nucleic Acids Res.* **2018**, *47*, D607.

[56] P. Shannon, A. Markiel, O. Ozier, N. S. Baliga, J. T. Wang, D. Ramage, N. Amin, B. Schwikowski, T. Ideker, *Genome Res* **2003**, *13*, 2498.

[57] C.-H. Chin, S.-H. Chen, H.-H. Wu, C.-W. Ho, M.-T. Ko, C.-Y. Lin, *BMC Systems Biology* **2014**, *8*, S11.

[58] A. J. D. Magenau, J. A. Richards, M. A. Pasquinelli, D. A. Savin, R. T. Mathers, *Macromolecules* **2015**, *48*, 7230.

[59] R. Mannhold, G. I. Poda, C. Ostermann, I. V. Tetko, *J. Pharm. Sci.* **2009**, *98*, 861.

[60] S. Kim, P. A. Thiessen, E. E. Bolton, J. Chen, G. Fu, A. Gindulyte, L. Han, J. He, S. He, B. A. Shoemaker, J. Wang, B. Yu, J. Zhang, S. H. Bryant, *Nucleic Acids Res.* **2015**, *44*, D1202.

[61] Schrödinger, *Schrödinger Release 2017-4: Desmond Molecular Dynamics System, D. E. Shaw Research, Maestro-Desmond Interoperability Tools* **2017**, *New York, NY, USA*.

[62] M. E. Lienqueo, A. Mahn, J. A. Asenjo, *J. Chromatogr. A* **2002**, *978*, 71.

[63] L. Cavallo, J. Kleinjung, F. Fraternali, *Nucleic Acids Res.* **2003**, *31*, 3364.

[64] A. Nayeem, D. Sitkoff, S. Krystek, *Protein Science : A Publication of the Protein Society* **2006**, *15*, 808; M. A. Dolan, J. W. Noah, D. Hurt, in *Homology Modeling: Methods and Protocols*, (Eds: A. J. W. Orry, R. Abagyan), Humana Press, Totowa, NJ **2012**, 399.

[65] R. Cowan, R. G. Whittaker, *Peptide research* **1990**, *3*, 75.

[66] A. Goyon, V. D'Atri, O. Colas, S. Fekete, A. Beck, D. Guillarme, *J. Chromatogr. B* **2017**, *1065-1066*, 35.

[67] M. Kreuß, T. Strixner, U. Kulozik, *Food Hydrocolloids* **2009**, *23*, 1818; H. G. Botros, P. Poncet, J. Rabillon, T. Fontaine, J.-M. Laval, B. David, *Eur. J. Biochem.* **2001**, *268*, 3126; W. Bernhard, H. P. Haagsman, T. Tschernig, C. F. Poets, A. D. Postle, M. E. v. Eijk, H. v. d. Hardt, *Am. J. Respir. Cell Mol. Biol.* **1997**, *17*, 41; M. L. de Vocht, K. Scholtmeijer, E. W. van der Vegte, O. M. H. de Vries, N. Sonveaux, H. A. B. Wösten, J.-M. Ruysschaert, G. Hadziioannou, J. G. H. Wessels, G. T. Robillard, *Biophys. J.* **1998**, *74*, 2059.

[68] R. Liu, W. Jiang, C. D. Walkey, W. C. W. Chan, Y. Cohen, *Nanoscale* **2015**, *7*, 9664.

[69] J. Koehler Leman, M. B. Ulmschneider, J. J. Gray, *Proteins: Structure, Function, and Bioinformatics* **2015**, *83*, 1.

[70] A. Maciejewski, M. Pasenkiewicz-Gierula, O. Cramariuc, I. Vattulainen, T. Rog, *J. Phys. Chem. B* **2014**, *118*, 4571.

[71] M. Xue, L. Cheng, I. Faustino, W. Guo, S. J. Marrink, *Biophys. J.* **2018**, *115*, 494.

[72] D. E. Discher, V. Ortiz, G. Srinivas, M. L. Klein, Y. Kim, D. Christian, S. Cai, P. Photos, F. Ahmed, *Prog. Polym. Sci.* **2007**, *32*, 838; F. Pierce, M. Tsige, O. Borodin, D. Perahia, G. S. Grest, *J. Chem. Phys.* **2008**, *128*, 214903.

[73] E. Harder, W. Damm, J. Maple, C. Wu, M. Reboul, J. Y. Xiang, L. Wang, D. Lupyan, M. K. Dahlgren, J. L. Knight, J. W. Kaus, D. S. Cerutti, G. Krilov, W. L. Jorgensen, R. Abel, R. A. Friesner, *Journal of Chemical Theory and Computation* **2016**, *12*, 281.

[74] H. J. C. Berendsen, J. P. M. Postma, W. F. van Gunsteren, J. Hermans, in *Intermolecular Forces: Proceedings of the Fourteenth Jerusalem Symposium on Quantum Chemistry and Biochemistry Held in Jerusalem, Israel, April 13–16, 1981*, (Ed: B. Pullman), Springer Netherlands, Dordrecht **1981**, 331.

[75] K. J. Bowers, D. E. Chow, H. Xu, R. O. Dror, M. P. Eastwood, B. A. Gregersen, J. L. Klepeis, I. Kolossvary, M. A. Moraes, F. D. Sacerdoti, J. K. Salmon, Y. Shan, D. E. Shaw, "*Scalable Algorithms for Molecular Dynamics Simulations on Commodity Clusters*", presented at *SC '06: Proceedings of the 2006 ACM/IEEE Conference on Supercomputing*, 11-17 Nov. 2006, **2006**.

[76] U. Essmann, L. Perera, M. L. Berkowitz, T. Darden, H. Lee, L. G. Pedersen, *J. Chem. Phys.* **1995**, *103*, 8577.

[77] G. J. Martyna, M. L. Klein, M. Tuckerman, *J. Chem. Phys.* **1992**, *97*, 2635.

[78] G. J. Martyna, M. E. Tuckerman, D. J. Tobias, M. L. Klein, *Mol. Phys.* **1996**, *87*, 1117.

[79] M.-C. Giocondi, D. Yamamoto, E. Lesniewska, P.-E. Milhiet, T. Ando, C. Le Grimellec, *Biochimica et Biophysica Acta (BBA) - Biomembranes* **2010**, *1798*, 703.

[80] N. Barapatre, P. Symvoulidis, W. Möller, F. Prade, N. C. Deliolanis, S. Hertel, G. Winter, A. Ö. Yildirim, T. Stoeger, O. Eickelberg, V. Ntziachristos, O. Schmid, *J. Pharm. Biomed. Anal.* **2015**, *102*, 129.

[81] Y. Wang, K. C. L. Black, H. Luehmann, W. Li, Y. Zhang, X. Cai, D. Wan, S.-Y. Liu, M. Li, P. Kim, Z.-Y. Li, L. V. Wang, Y. Liu, Y. Xia, *ACS Nano* **2013**, *7*, 2068.

[82] G. Hong, A. L. Antaris, H. Dai, *Nature Biomedical Engineering* **2017**, *1*, 0010.

[83] R. H. Müller, D. Rühl, M. Lück, B.-R. Paulke, *Pharm. Res.* **1997**, *14*, 18.

[84] C. Mayr, W. Brütting, *Chem. Mater.* **2015**, *27*, 2759; M. A. El-Shahawy, *Polym. Test.* **1999**, *18*, 389.

[85] W. Small, M. F. Metzger, T. S. Wilson, D. J. Maitland, *IEEE Journal of Selected Topics in Quantum Electronics* **2005**, *11*, 892.

[86] S. L. Anderson, E. A. Grulke, P. T. DeLassus, P. B. Smith, C. W. Kocher, B. G. Landes, *Macromolecules* **1995**, *28*, 2944.

[87] C. Bouissou, J. J. Rouse, R. Price, C. F. van der Walle, *Pharm. Res.* **2006**, *23*, 1295; J. Elversson, A. Millqvist-Fureby, *Int. J. Pharm.* **2006**, *323*, 52.

[88] B. Wang, L. Zhang, S. C. Bae, S. Granick, *Proc. Natl. Acad. Sci. U. S. A.* **2008**, *105*, 18171.

[89] N. Uyanik, B. M. Baysal, *J. Appl. Polym. Sci.* **1990**, *41*, 1981; L.-B. Feng, S.-X. Zhou, B. You, L.-M. Wu, *J. Appl. Polym. Sci.* **2007**, *103*, 1458; Y. K. Luu, K. Kim, B. S. Hsiao, B. Chu, M. Hadjiargyrou, *J. Controlled Release* **2003**, *89*, 341.

[90] J. E. Hogan, in *Pharmaceutical Coating Technology*, (Ed: G. Cole, Hogan J., Aulton, M.), Taylor & Francis, London **2002**, 6; V. Chan, K.-K. Liu, C. Le Visage, B.-F. Ju, K. W. Leong, *Biomaterials* **2004**, *25*, 4327.

[91] M. A. Dobrovolskaia, D. R. Germolec, J. L. Weaver, *Nat. Nanotechnol.* **2009**, *4*, 411; M. Coureuil, H. Lécuyer, S. Bourdoulous, X. Nassif, *Nature Reviews Microbiology* **2017**, *15*, 149.

[92] S. B. Hedges, *Nature Reviews Genetics* **2002**, *3*, 838.

[93] G. A. Kimbrell, *Nanotech. L. & Bus.* **2006**, *3*, 329.

[94] W. M. S. Russell, R. L. Burch, C. W. Hume, *The principles of humane experimental technique*, *Vol. 238*, Methuen London, **1959**.

[95] American Society of Health-System Pharmacists, *AHFS Drug Information*, American Society of Health-System Pharmacists, Bethesda, MD, USA **2011**.

[96] B. Kaundal, A. K. Srivastava, M. N. Sardoiwala, S. Karmakar, S. R. Choudhury, *Nanoscale Advances* **2019**, *1*, 2188; S. L. Raut, B. Kirthivasan, M. M. Bommana, E. Squillante, M. Sadoqi, *Nanotechnology* **2010**, *21*, 395102.

[97] J. S. Brenner, D. C. Pan, J. W. Myerson, O. A. Marcos-Contreras, C. H. Villa, P. Patel, H. Hekierski, S. Chatterjee, J.-Q. Tao, H. Parhiz, K. Bhamidipati, T. G. Uhler, E. D. Hood, R. Y. Kiseleva, V. S. Shuvaev, T. Shuvaeva, M. Khoshnejad, I. Johnston, J. V. Gregory, J. Lahann, T. Wang, E. Cantu, W. M. Armstead, S. Mitragotri, V. Muzykantov, *Nat. Commun.* **2018**, *9*, 2684.

[98] S. M. Moghimi, A. C. Hunter, J. C. Murray, *Pharmacol. Rev.* **2001**, *53*, 283.

[99] Sigma-Aldrich, in *www.sigmaaldrich.com*, Merck KGaA, Darmstadt **2018**.

[100] L. Shargel, A. B. C. Yu, *Applied Biopharmaceutics & Pharmacokinetics, Seventh Edition*, McGraw-Hill Education, **2015**.

[101] S. X. Vasquez, F. Gao, F. Su, V. Grijalva, J. Pope, B. Martin, J. Stinstra, M. Masner, N. Shah, D. M. Weinstein, *PloS one* **2011**, *6*, e19099.

[102] A. Banerjee, J. Qi, R. Gogoi, J. Wong, S. Mitragotri, *J. Controlled Release* **2016**, *238*, 176; K. C. L. Black, Y. Wang, H. P. Luehmann, X. Cai, W. Xing, B. Pang, Y. Zhao, C. S. Cutler, L. V. Wang, Y. Liu, Y. Xia, *ACS Nano* **2014**, *8*, 4385.

[103] B. M. Haryadi, D. Hafner, I. Amin, R. Schubel, L. Isert, R. Jordan, O. Merkel, G. Winter, J. Engert, *In Preparation* **2022**.

[104] B. M. Haryadi, G. Winter, J. Engert, "*Overcoming Non-Spherical Shape Instability of Nanoparticles Intended for Drug Delivery Using a Bioinspired Approach*", presented at *11th World Meeting on Pharmaceutics, Biopharmaceutics and Pharmaceutical Technology (PBP) (https://www.dphg.de/fileadmin/downloads/DPhG2016_ConferenceBook_final.pdf)*, Granada, Spain, March, **2018**; D. Kozak, W. Anderson, R. Vogel, M. Trau, *Nano Today* **2011**, *6*, 531.

[105] L. T. Dunn, *Journal of Neurology, Neurosurgery, and Psychiatry* **2002**, *73*, i23.

[106] G. Kovacs, A. Berghold, S. Scheidl, H. Olschewski, *European Respiratory Journal* **2009**, *34*, 888.

[107] M. Moazen, A. Alazmani, K. Rafferty, Z.-J. Liu, J. Gustafson, M. L. Cunningham, M. J. Fagan, S. W. Herring, *Journal of Biomechanics* **2016**, *49*, 123.

[108] J. Gomez-Arroyo, S. J. Saleem, S. Mizuno, A. A. Syed, H. J. Bogaard, A. Abbate, L. Taraseviciene-Stewart, Y. Sung, D. Kraskauskas, D. Farkas, D. H. Conrad, M. R. Nicolls, N. F. Voelkel, *American Journal of Physiology-Lung Cellular and Molecular Physiology* **2012**, *302*, L977.

[109] E. Casals, T. Pfaller, A. Duschl, G. J. Oostingh, V. F. Puntes, *Small* **2011**, *7*, 3479.

[110] A. L. Barrán-Berdón, D. Pozzi, G. Caracciolo, A. L. Capriotti, G. Caruso, C. Cavaliere, A. Riccioli, S. Palchetti, A. Laganà, *Langmuir* **2013**, *29*, 6485.

[111] C. Wu, C. Orozco, J. Boyer, M. Leglise, J. Goodale, S. Batalov, C. L. Hodge, J. Haase, J. Janes, J. W. Huss, A. I. Su, *Genome Biology* **2009**, *10*, R130.

[112] M. Uhlén, L. Fagerberg, B. M. Hallström, C. Lindskog, P. Oksvold, A. Mardinoglu, Å. Sivertsson, C. Kampf, E. Sjöstedt, A. Asplund, I. Olsson, K. Edlund, E. Lundberg, S. Navani, C. A.-K. Szigyarto, J. Odeberg, D. Djureinovic, J. O. Takanen, S. Hober, T. Alm, P.-H. Edqvist, H. Berling, H. Tegel, J. Mulder, J. Rockberg, P. Nilsson, J. M. Schwenk, M. Hamsten, K. von Feilitzen, M. Forsberg, L. Persson, F. Johansson, M. Zwahlen, G. von Heijne, J. Nielsen, F. Pontén, *Science* **2015**, *347*.

[113] L. Rajendran, M. Honsho, T. R. Zahn, P. Keller, K. D. Geiger, P. Verkade, K. Simons, *Proc. Natl. Acad. Sci. U. S. A.* **2006**, *103*, 11172.

[114] J. Kreuter, T. Hekmatara, S. Dreis, T. Vogel, S. Gelperina, K. Langer, *J. Controlled Release* **2007**, *118*, 54; J. Kreuter, *Adv. Drug Delivery Rev.* **2014**, *71*, 2.

[115] L. Rao, Q.-F. Meng, L.-L. Bu, B. Cai, Q. Huang, Z.-J. Sun, W.-F. Zhang, A. Li, S.-S. Guo, W. Liu, T.-H. Wang, X.-Z. Zhao, *ACS Appl. Mater. Interfaces* **2017**, *9*, 2159.

[116] A. H. Bryk, J. R. Wiśniewski, *J. Proteome Res.* **2017**, *16*, 2752.

[117] H. Saito, S. Lund-Katz, M. C. Phillips, *Prog. Lipid Res.* **2004**, *43*, 350.

[118] C. C. O'Sullivan, M. Lindenberg, C. Bryla, N. Patronas, C. J. Peer, L. Amiri-Kordestani, N. Davarpanah, E. M. Gonzalez, M. Burotto, P. Choyke, S. M. Steinberg, D. J. Liewehr, W. D. Figg, T. Fojo, S. Balasubramaniam, S. E. Bates, *Breast Cancer Research and Treatment* **2016**, *160*, 51.

[119] D. K. Male, J. Brostoff, D. Roth, I. Roitt, *Immunology: With STUDENT CONSULT Online Access*, Elsevier/Saunders, **2013**.

[120] N. P. Podolnikova, M. Hlavackova, Y. Wu, V. P. Yakubenko, J. Faust, A. Balabiyev, X. Wang, T. P. Ugarova, *J. Biol. Chem.* **2019**, *294*, 7833.

[121] B. Engelhardt, P. Vajkoczy, R. O. Weller, *Nature Immunology* **2017**, *18*, 123.

[122] L. Costantino, D. Boraschi, *Drug Discovery Today* **2012**, *17*, 367.

[123] U.S. National Library of Medicine, *Vol. ClinicalTrials.gov, clinicaltrials.gov*, U.S. National Institutes of Health, Bethesda, MDA, USA **2019**.

[124] A. Salvati, A. S. Pitek, M. P. Monopoli, K. Prapainop, F. B. Bombelli, D. R. Hristov, P. M. Kelly, C. Aberg, E. Mahon, K. A. Dawson, *Nat. Nanotechnol.* **2013**, *8*, 137; L. Gentiluomo, H. L. Svilenov, D. Augustijn, I. El Bialy, M. L. Greco, A. Kulakova, S. Indrakumar, S. Mahapatra, M. M. Morales, C. Pohl, A. Roche, A. Tosstorff, R. Curtis, J. P. Derrick, A. Noergaard, T. A. Khan, G. H. J. Peters, A. Pluen, Å. Rinnan, W. W. Streicher, C. F. van der Walle, S. Uddin, G. Winter, D. Roessner, P. Harris, W. Friess, *Mol. Pharmaceutics* **2020**, *17*, 426; B. M. Haryadi, J. Engert, G. Winter, *In Preparation* **2022**.

[125] S. S. Yoon, K. I. Jung, Y.-L. Choi, E. Y. Choi, I.-S. Lee, S. H. Park, T. J. Kim, *FEBS Lett.* **2003**, *540*, 217.

[126] A. Chonn, S. C. Semple, P. R. Cullis, *J. Biol. Chem.* **1992**, *267*, 18759.

[127] J. G. Fox, S. Barthold, M. Davisson, C. E. Newcomer, F. W. Quimby, A. Smith, *The Mouse in Biomedical Research: Normative Biology, Husbandry, and Models*, Elsevier Science, Amsterdam, Netherlands **2006**.

[128] U.S. Centers for Disease Control Prevention, *Stem Cell and Exosome Products: Warning about Unapproved Therapies, U.S. Department of Health and Human Services, CDC, Healthcare-associated*

Infections (HAI), Outbreak and Patient Notifications, Atlanta, GA, USA **2019**, https://www.cdc.gov/hai/outbreaks/stem.

[129] L. Alvarez-Erviti, Y. Seow, H. Yin, C. Betts, S. Lakhal, M. J. A. Wood, *Nat. Biotechnol.* **2011**, *29*, 341; R. Kalluri, V. S. LeBleu, *Science* **2020**, *367*, eaau6977.

[130] S. Saeedi, S. Israel, C. Nagy, G. Turecki, *Translational Psychiatry* **2019**, *9*, 122.

[131] C. Théry, K. W. Witwer, E. Aikawa, M. J. Alcaraz, J. D. Anderson, R. Andriantsitohaina, A. Antoniou, T. Arab, F. Archer, G. K. Atkin-Smith, D. C. Ayre, J.-M. Bach, D. Bachurski, H. Baharvand, L. Balaj, S. Baldacchino, N. N. Bauer, A. A. Baxter, M. Bebawy, C. Beckham, A. Bedina Zavec, A. Benmoussa, A. C. Berardi, P. Bergese, E. Bielska, C. Blenkiron, S. Bobis-Wozowicz, E. Boilard, W. Boireau, A. Bongiovanni, F. E. Borràs, S. Bosch, C. M. Boulanger, X. Breakefield, A. M. Breglio, M. Á. Brennan, D. R. Brigstock, A. Brisson, M. L. D. Broekman, J. F. Bromberg, P. Bryl-Górecka, S. Buch, A. H. Buck, D. Burger, S. Busatto, D. Buschmann, B. Bussolati, E. I. Buzás, J. B. Byrd, G. Camussi, D. R. F. Carter, S. Caruso, L. W. Chamley, Y.-T. Chang, C. Chen, S. Chen, L. Cheng, A. R. Chin, A. Clayton, S. P. Clerici, A. Cocks, E. Cocucci, R. J. Coffey, A. Cordeiro-da-Silva, Y. Couch, F. A. W. Coumans, B. Coyle, R. Crescitelli, M. F. Criado, C. D'Souza-Schorey, S. Das, A. Datta Chaudhuri, P. de Candia, E. F. De Santana, O. De Wever, H. A. del Portillo, T. Demaret, S. Deville, A. Devitt, B. Dhondt, D. Di Vizio, L. C. Dieterich, V. Dolo, A. P. Dominguez Rubio, M. Dominici, M. R. Dourado, T. A. P. Driedonks, F. V. Duarte, H. M. Duncan, R. M. Eichenberger, K. Ekström, S. El Andaloussi, C. Elie-Caille, U. Erdbrügger, J. M. Falcón-Pérez, F. Fatima, J. E. Fish, M. Flores-Bellver, A. Försönits, A. Frelet-Barrand, F. Fricke, G. Fuhrmann, S. Gabrielsson, A. Gámez-Valero, C. Gardiner, K. Gärtner, R. Gaudin, Y. S. Gho, B. Giebel, C. Gilbert, M. Gimona, I. Giusti, D. C. I. Goberdhan, A. Görgens, S. M. Gorski, D. W. Greening, J. C. Gross, A. Gualerzi, G. N. Gupta, D. Gustafson, A. Handberg, R. A. Haraszti, P. Harrison, H. Hegyesi, A. Hendrix, A. F. Hill, F. H. Hochberg, K. F. Hoffmann, B. Holder, H. Holthofer, B. Hosseinkhani, G. Hu, Y. Huang, V. Huber, S. Hunt, A. G.-E. Ibrahim, T. Ikezu, J. M. Inal, M. Isin, A. Ivanova, H. K. Jackson, S. Jacobsen, S. M. Jay, M. Jayachandran, G. Jenster, L. Jiang, S. M. Johnson, J. C. Jones, A. Jong, T. Jovanovic-Talisman, S. Jung, R. Kalluri, S.-i. Kano, S. Kaur, Y. Kawamura, E. T. Keller, D. Khamari, E. Khomyakova, A. Khvorova, P. Kierulf, K. P. Kim, T. Kislinger, M. Klingeborn, D. J. Klinke, M. Kornek, M. M. Kosanović, Á. F. Kovács, E.-M. Krämer-Albers, S. Krasemann, M. Krause, I. V. Kurochkin, G. D. Kusuma, S. Kuypers, S. Laitinen, S. M. Langevin, L. R. Languino, J. Lannigan, C. Lässer, L. C. Laurent, G. Lavieu, E. Lázaro-Ibáñez, S. Le Lay, M.-S. Lee, Y. X. F. Lee, D. S. Lemos, M. Lenassi, A. Leszczynska, I. T. S. Li, K. Liao, S. F. Libregts, E. Ligeti, R. Lim, S. K. Lim, A. Linē, K. Linnemannstöns, A. Llorente, C. A. Lombard, M. J. Lorenowicz, Á. M.

Lörincz, J. Lötvall, J. Lovett, M. C. Lowry, X. Loyer, Q. Lu, B. Lukomska, T. R. Lunavat, S. L. N. Maas, H. Malhi, A. Marcilla, J. Mariani, J. Mariscal, E. S. Martens-Uzunova, L. Martin-Jaular, M. C. Martinez, V. R. Martins, M. Mathieu, S. Mathivanan, M. Maugeri, L. K. McGinnis, M. J. McVey, D. G. Meckes, K. L. Meehan, I. Mertens, V. R. Minciacchi, A. Möller, M. Møller Jørgensen, A. Morales-Kastresana, J. Morhayim, F. Mullier, M. Muraca, L. Musante, V. Mussack, D. C. Muth, K. H. Myburgh, T. Najrana, M. Nawaz, I. Nazarenko, P. Nejsum, C. Neri, T. Neri, R. Nieuwland, L. Nimrichter, J. P. Nolan, E. N. M. Nolte-'t Hoen, N. Noren Hooten, L. O'Driscoll, T. O'Grady, A. O'Loghlen, T. Ochiya, M. Olivier, A. Ortiz, L. A. Ortiz, X. Osteikoetxea, O. Østergaard, M. Ostrowski, J. Park, D. M. Pegtel, H. Peinado, F. Perut, M. W. Pfaffl, D. G. Phinney, B. C. H. Pieters, R. C. Pink, D. S. Pisetsky, E. Pogge von Strandmann, I. Polakovicova, I. K. H. Poon, B. H. Powell, I. Prada, L. Pulliam, P. Quesenberry, A. Radeghieri, R. L. Raffai, S. Raimondo, J. Rak, M. I. Ramirez, G. Raposo, M. S. Rayyan, N. Regev-Rudzki, F. L. Ricklefs, P. D. Robbins, D. D. Roberts, S. C. Rodrigues, E. Rohde, S. Rome, K. M. A. Rouschop, A. Rughetti, A. E. Russell, P. Saá, S. Sahoo, E. Salas-Huenuleo, C. Sánchez, J. A. Saugstad, M. J. Saul, R. M. Schiffelers, R. Schneider, T. H. Schøyen, A. Scott, E. Shahaj, S. Sharma, O. Shatnyeva, F. Shekari, G. V. Shelke, A. K. Shetty, K. Shiba, P. R. M. Siljander, A. M. Silva, A. Skowronek, O. L. Snyder, R. P. Soares, B. W. Sódar, C. Soekmadji, J. Sotillo, P. D. Stahl, W. Stoorvogel, S. L. Stott, E. F. Strasser, S. Swift, H. Tahara, M. Tewari, K. Timms, S. Tiwari, R. Tixeira, M. Tkach, W. S. Toh, R. Tomasini, A. C. Torrecilhas, J. P. Tosar, V. Toxavidis, L. Urbanelli, P. Vader, B. W. M. van Balkom, S. G. van der Grein, J. Van Deun, M. J. C. van Herwijnen, K. Van Keuren-Jensen, G. van Niel, M. E. van Royen, A. J. van Wijnen, M. H. Vasconcelos, I. J. Vechetti, T. D. Veit, L. J. Vella, É. Velot, F. J. Verweij, B. Vestad, J. L. Viñas, T. Visnovitz, K. V. Vukman, J. Wahlgren, D. C. Watson, M. H. M. Wauben, A. Weaver, J. P. Webber, V. Weber, A. M. Wehman, D. J. Weiss, J. A. Welsh, S. Wendt, A. M. Wheelock, Z. Wiener, L. Witte, J. Wolfram, A. Xagorari, P. Xander, J. Xu, X. Yan, M. Yáñez-Mó, H. Yin, Y. Yuana, V. Zappulli, J. Zarubova, V. Žėkas, J.-y. Zhang, Z. Zhao, L. Zheng, A. R. Zheutlin, A. M. Zickler, P. Zimmermann, A. M. Zivkovic, D. Zocco, E. K. Zuba-Surma, *Journal of Extracellular Vesicles* **2018**, *7*, 1535750.

[132] U. Kuckartz, S. Rädiker, T. Ebert, J. Schehl, in *Statistik: Eine verständliche Einführung*, VS Verlag, Wiesbaden **2013**, 207; J. Frost, E-book. https://statisticsbyjim.com, **2019**; B. Ratner, *Statistical and Machine-Learning Data Mining: Techniques for Better Predictive Modeling and Analysis of Big Data, Third Edition*, CRC Press, Boca Raton, FL, USA **2017**.

[133] G. Gunkel, W. T. S. Huck, *J. Am. Chem. Soc.* **2013**, *135*, 7047.

[134] V. Nanjappa, J. K. Thomas, A. Marimuthu, B. Muthusamy, A. Radhakrishnan, R. Sharma, A. Ahmad Khan, L. Balakrishnan, N. A. Sahasrabuddhe, S. Kumar, B. N. Jhaveri, K. V. Sheth, R. Kumar Khatana, P. G. Shaw, S. M. Srikanth, P. P. Mathur, S. Shankar, D. Nagaraja, R. Christopher, S. Mathivanan, R. Raju, R. Sirdeshmukh, A. Chatterjee, R. J. Simpson, H. C. Harsha, A. Pandey, T. S. K. Prasad, *Nucleic Acids Res.* **2014**, *42*, D959.

[135] J. M. Schwenk, G. S. Omenn, Z. Sun, D. S. Campbell, M. S. Baker, C. M. Overall, R. Aebersold, R. L. Moritz, E. W. Deutsch, *J. Proteome Res.* **2017**, *16*, 4299.

[136] J. M. Salhany, R. L. Sloan, K. A. Cordes, *J. Biol. Chem.* **1990**, *265*, 17688.

[137] F. Despa, D. P. Orgill, J. Neuwalder, R. C. Lee, *Burns* **2005**, *31*, 568.

[138] A. Basu, A. Chakrabarti, *Journal of Proteomics* **2015**, *128*, 469; T. Rogalla, M. Ehrnsperger, X. Preville, A. Kotlyarov, G. Lutsch, C. Ducasse, C. Paul, M. Wieske, A.-P. Arrigo, J. Buchner, M. Gaestel, *J. Biol. Chem.* **1999**, *274*, 18947.

[139] J. Howard, *Mechanics of Motor Proteins and the Cytoskeleton*, Sinauer Associates, Inc., Sunderland, MA, USA **2001**.

[140] M. F. M. Engel, A. J. W. G. Visser, C. P. M. van Mierlo, *Langmuir* **2003**, *19*, 2929.

[141] Z. Du, M. P. Bilbao-Montoya, B. P. Binks, E. Dickinson, R. Ettelaie, B. S. Murray, *Langmuir* **2003**, *19*, 3106.

[142] S. Rudiuk, L. Cohen-Tannoudji, S. Huille, C. Tribet, *Soft Matter* **2012**, *8*, 2651; D. Shiomi, M. Sakai, H. Niki, *The EMBO Journal* **2008**, *27*, 3081; D. Krieg, H. Svilenov, J. H. Gitter, G. Winter, *European Journal of Pharmaceutical Sciences* **2020**, *141*, 105073; S. Cavagnero, Z. H. Zhou, M. W. W. Adams, S. I. Chan, *Biochemistry* **1995**, *34*, 9865; K. Takai, K. Nakamura, T. Toki, U. Tsunogai, M. Miyazaki, J. Miyazaki, H. Hirayama, S. Nakagawa, T. Nunoura, K. Horikoshi, *Proc. Natl. Acad. Sci. U. S. A.* **2008**, *105*, 10949.

[143] M. J. Kerner, D. J. Naylor, Y. Ishihama, T. Maier, H.-C. Chang, A. P. Stines, C. Georgopoulos, D. Frishman, M. Hayer-Hartl, M. Mann, F. U. Hartl, *Cell* **2005**, *122*, 209; K. Fujiwara, Y. Ishihama, K. Nakahigashi, T. Soga, H. Taguchi, *The EMBO Journal* **2010**, *29*, 1552.

[144] S. Schöttler, G. Becker, S. Winzen, T. Steinbach, K. Mohr, K. Landfester, V. Mailänder, F. R. Wurm, *Nat. Nanotechnol.* **2016**, *11*, 372.

[145] M. Morikawa, H. Daido, T. Takao, S. Murata, Y. Shimonishi, T. Imanaka, *J. Bacteriol.* **1993**, *175*, 6459.

[146] E. Koepf, S. Eisele, R. Schroeder, G. Brezesinski, W. Friess, *Int. J. Pharm.* **2018**, *537*, 202.

[147] A. M. Alkilany, L. B. Thompson, S. P. Boulos, P. N. Sisco, C. J. Murphy, *Adv. Drug Delivery Rev.* **2012**, *64*, 190; C. Burda, X. Chen, R. Narayanan, M. A. El-Sayed, *Chem. Rev*. **2005**, *105*, 1025.

[148] R. García-Álvarez, M. Hadjidemetriou, A. Sánchez-Iglesias, L. M. Liz-Marzán, K. Kostarelos, *Nanoscale* **2018**, *10*, 1256.

[149] Y. Tu, M. Lv, P. Xiu, T. Huynh, M. Zhang, M. Castelli, Z. Liu, Q. Huang, C. Fan, H. Fang, R. Zhou, *Nat. Nanotechnol.* **2013**, *8*, 594.

[150] C. Ge, J. Du, L. Zhao, L. Wang, Y. Liu, D. Li, Y. Yang, R. Zhou, Y. Zhao, Z. Chai, C. Chen, *Proc. Natl. Acad. Sci. U. S. A.* **2011**, *108*, 16968; Y. Chong, C. Ge, Z. Yang, J. A. Garate, Z. Gu, J. K. Weber, J. Liu, R. Zhou, *ACS Nano* **2015**, *9*, 5713.

[151] J. Li, X. Huang, R. Huang, J. Jiang, Y. Wang, J. Zhang, H. Jiang, X. Xiang, W. Chen, X. Nie, R. Gui, *Carbon* **2019**, *146*, 660.

[152] S. Mauri, M. Volk, S. Byard, H. Berchtold, H. Arnolds, *Langmuir* **2015**, *31*, 8892.

[153] M. Tebbe, C. Kuttner, M. Männel, A. Fery, M. Chanana, *ACS Appl. Mater. Interfaces* **2015**, *7*, 5984.

[154] K. May, M. E. Prior, Google Patents (US5275785), **1994**.

[155] H. K. Chan, Google Patents (US7531362), **2009**.

[156] A. A. Vertegel, R. W. Siegel, J. S. Dordick, *Langmuir* **2004**, *20*, 6800.

[157] A. C. Anselmo, V. Gupta, B. J. Zern, D. Pan, M. Zakrewsky, V. Muzykantov, S. Mitragotri, *ACS Nano* **2013**, *7*, 11129.

[158] P. P. Wibroe, A. C. Anselmo, P. H. Nilsson, A. Sarode, V. Gupta, R. Urbanics, J. Szebeni, A. C. Hunter, S. Mitragotri, T. E. Mollnes, S. M. Moghimi, *Nat. Nanotechnol.* **2017**, *12*, 589.

[159] D. Dehaini, X. Wei, R. H. Fang, S. Masson, P. Angsantikul, B. T. Luk, Y. Zhang, M. Ying, Y. Jiang, A. V. Kroll, W. Gao, L. Zhang, *Adv. Mater.* **2017**, 1606209.

[160] C. Leonard, L. Conrard, M. Guthmann, H. Pollet, M. Carquin, C. Vermylen, P. Gailly, P. Van Der Smissen, M. P. Mingeot-Leclercq, D. Tyteca, *Sci. Rep.* **2017**, *7*, 4264.

[161] S. J. Slater, M. B. Kelly, F. J. Taddeo, C. Ho, E. Rubin, C. D. Stubbs, *J. Biol. Chem.* **1994**, *269*, 4866.

[162] G. Shahane, W. Ding, M. Palaiokostas, M. Orsi, *J. Mol. Model.* **2019**, *25*, 76.

[163] F. Wang, L. Yu, M. P. Monopoli, P. Sandin, E. Mahon, A. Salvati, K. A. Dawson, *Nanomedicine (N. Y., NY, U. S.)* **2013**, *9*, 1159.

[164] V. S. Marangoni, J. Cancino Bernardi, I. B. Reis, W. J. Fávaro, V. Zucolotto, *ACS Applied Bio Materials* **2019**, *2*, 728.

[165] C. Rosman, S. Pierrat, A. Henkel, M. Tarantola, D. Schneider, E. Sunnick, A. Janshoff, C. Sönnichsen, *Small* **2012**, *8*, 3683; Y. Horiguchi, K. Honda, Y. Kato, N. Nakashima, Y. Niidome, *Langmuir* **2008**, *24*, 12026.

[166] M. Hadjidemetriou, K. Kostarelos, *Nat. Nanotechnol.* **2017**, *12*, 288.

[167] J. Zhuang, H. Gong, J. Zhou, Q. Zhang, W. Gao, R. H. Fang, L. Zhang, *Science Advances* **2020**, *6*, eaaz6108.

[168] D. C. Roopenian, S. Akilesh, *Nature Reviews Immunology* **2007**, *7*, 715.

[169] Z. Fan, H. Zhou, P. Y. Li, J. E. Speer, H. Cheng, *Journal of Materials Chemistry B* **2014**, *2*, 8231.

[170] H. Zhou, Z. Fan, P. K. Lemons, H. Cheng, *Theranostics* **2016**, *6*, 1012.

[171] S. B. Prusiner, M. P. McKinley, K. A. Bowman, D. C. Bolton, P. E. Bendheim, D. F. Groth, G. G. Glenner, *Cell* **1983**, *35*, 349.

[172] K.-M. Pan, M. Baldwin, J. Nguyen, M. Gasset, A. Serban, D. Groth, I. Mehlhorn, Z. Huang, R. J. Fletterick, F. E. Cohen, S. B. Prusiner, *Proc. Natl. Acad. Sci. U. S. A.* **1993**, *90*, 10962.

[173] K. J. Ryan, N. Ahmad, J. A. Alspaugh, W. L. Drew, M. Lagunoff, P. Pottinger, L. B. Reller, M. E. Reller, C. R. Sterling, S. Weissman, *Sherris Medical Microbiology*, McGraw-Hill Education Lange®, New York, NY, USA **2018**.

[174] S. Capellari, S. I. Zaidi, A. C. Long, E. E. Kwon, R. B. Petersen, *Journal of Alzheimer's Disease* **2000**, *2*, 27.

[175] H. Inouye, D. A. Kirschner, in *Adv. Protein Chem.*, *Vol. 73*, Academic Press, **2006**, 181.

[176] A. C. Anselmo, M. Zhang, S. Kumar, D. R. Vogus, S. Menegatti, M. E. Helgeson, S. Mitragotri, *ACS Nano* **2015**, *9*, 3169.

[177] G. Lamour, C. K. Yip, H. Li, J. Gsponer, *ACS Nano* **2014**, *8*, 3851.

[178] C. J. van Oss, *J. Protein Chem.* **1990**, *9*, 487.

[179] G. J. Tortora, B. R. Funke, C. L. Case, *Microbiology: An Introduction*, Pearson, **2018**.

[180] I. Hamad, O. Al-Hanbali, A. C. Hunter, K. J. Rutt, T. L. Andresen, S. M. Moghimi, *ACS Nano* **2010**, *4*, 6629.

[181] J. N. Israelachvili, *Intermolecular and Surface Forces*, Academic Press, San Diego, CA, USA **2011**.

[182] M. Domnowski, J. Jaehrling, W. Frieß, *Pharm. Res.* **2020**, *37*, 29.

[183] S. Wan, P. M. Kelly, E. Mahon, H. Stöckmann, P. M. Rudd, F. Caruso, K. A. Dawson, Y. Yan, M. P. Monopoli, *ACS Nano* **2015**, *9*, 2157.

[184] O. Vilanova, J. J. Mittag, P. M. Kelly, S. Milani, K. A. Dawson, J. O. Rädler, G. Franzese, *ACS Nano* **2016**, *10*, 10842.

[185] L. Rao, L.-L. Bu, J.-H. Xu, B. Cai, G.-T. Yu, X. Yu, Z. He, Q. Huang, A. Li, S.-S. Guo, W.-F. Zhang, W. Liu, Z.-J. Sun, H. Wang, T.-H. Wang, X.-Z. Zhao, *Small* **2015**, *11*, 6225.

[186] E. Ben-Akiva, R. A. Meyer, H. Yu, J. T. Smith, D. M. Pardoll, J. J. Green, *Science Advances* **2020**, *6*, eaay9035.

[187] Y. Cao, L. Li, *Bioinformatics* **2014**, *30*, 1674.

[188] S. Goy-López, J. Juárez, M. Alatorre-Meda, E. Casals, V. F. Puntes, P. Taboada, V. Mosquera, *Langmuir* **2012**, *28*, 9113.

[189] Y. Li, L. Han, Z. Liu, R. Wang, *Journal of Chemical Information and Modeling* **2014**, *54*, 1717; S. Dominguez-Medina, J. Blankenburg, J. Olson, C. F. Landes, S. Link, *ACS Sustainable Chemistry & Engineering* **2013**, *1*, 833.

[190] C.-M. J. Hu, R. H. Fang, J. Copp, B. T. Luk, L. Zhang, *Nat. Nanotechnol.* **2013**, *8*, 336.

[191] S. H. D. P. Lacerda, J. J. Park, C. Meuse, D. Pristinski, M. L. Becker, A. Karim, J. F. Douglas, *ACS Nano* **2010**, *4*, 365.

[192] G. M. Mortimer, N. J. Butcher, A. W. Musumeci, Z. J. Deng, D. J. Martin, R. F. Minchin, *ACS Nano* **2014**, *8*, 3357.

[193] B. M. Haryadi, G. Winter, J. Engert, "*Engineering of Bioinspired Nanoparticles for Drug Delivery*", presented at *DPhG Annual Meeting (https://www.dphg.de/fileadmin/downloads/DPhG2016_ConferenceBook_final.pdf)*, Munich, Germany, October, **2016**.

[194] R. Meyer, E. Ben-Akiva, K. Cheung, J. Green, "*Biomimetic Anisotropic Polymeric Particles with Naturally Derived Cell Membranes for Enhanced Drug Delivery*", presented at *TISSUE ENGINEERING PART A, December 11-14*, **2016**.

8. Supporting Information

8.1. Supplemental Tables & Figures

8.1.1. Supplemental Tables

Table S III-1. Basic Characteristics of Spherical and Non-Spherical Nanoparticles Utilized in This Study, Including Pre- and Post-Incubation for 24 h in DMEM (for J774A.1 macrophages) and RPMI 1640 medium (for THP-1 monocytes)

Parameter &/ Treatment	[Coating &] Particle Type								
	[Bare] Core Nanoparticle (CNP)			[PEG] PEGylated Nanoparticle (CNP-PEG)			[NErys] Bioinspired Cell Membrane-Coated Nanoparticle (BCCN)		
	Spherical[#]	Non-Spherical (2X)^	Non-Spherical (3x)^[#]	Spherical	Non-Spherical (2X)^	Non-Spherical (3x)^	Spherical[#]	Non-Spherical (2X)^	Non-Spherical (3x)^[#]
Typical Shifting Time (Days)	N/A[*]	69 ± 11	65 ± 10	N/A*	95 ± 17	93 ± 17	N/A*	116 ± 22	110 ± 21
Hydrodynamic Size, S_h (nm)									
• **Pre-Incubation**	181.3 ± 2.6	474.3 ± 12.8	513.5 ± 16.2	187.0 ± 3.1	491.2 ± 23.2	525.9 ± 17.2	198.1 ± 8.7	490.1 ± 25.1	533.4 ± 31.6
• **Post-DMEM**	257.1 ± 12.3	541.4 ± 23.4	592.3 ± 18.3	194.2 ± 5.8	505.3 ± 36.1	535.7 ± 13.7	195.3 ± 10.1	483.2 ± 16.7	531.2 ± 25.1
• **Post-RPMI**	267.4 ± 9.1	523.8 ± 18.9	603.1 ± 21.5	196.5 ± 4.4	501.0 ± 21.7	536.2 ± 23.1	197.7 ± 16.3	494.8 ± 17.4	519.3 ± 31.3
Polydispersity Index, *PDI*									
• **Pre-Incubation**	0.065 ± 0.034	0.267 ± 0.045	0.245 ± 0.061	0.033 ± 0.037	0.281 ± 0.035	0.275 ± 0.043	0.175 ± 0.038	0.351 ± 0.052	0.343 ± 0.031
• **Post-DMEM**	0.254 ± 0.041	0.371 ± 0.021	0.379 ± 0.041	0.102 ± 0.021	0.323 ± 0.026	0.345 ± 0.023	0.173 ± 0.026	0.332 ± 0.034	0.328 ± 0.026
• **Post-RPMI**	0.276 ± 0.029	0.388 ± 0.032	0.382 ± 0.017	0.096 ± 0.011	0.339 ± 0.035	0.319 ± 0.031	0.153 ± 0.018	0.337 ± 0.026	0.349 ± 0.034
Zeta Potential (mV)									
• **Pre-Incubation**	-29.7 ± 2.3	-22.3 ± 3.1	-20.9 ± 2.2	-10.3 ± 3.2	-9.5 ± 3.7	-9.7 ± 2.8	-10.0 ± 1.4	-11.1 ± 4.9	-9.9 ± 3.8
• **Post-DMEM**	-12.0 ± 4.8	-13.3 ± 2.7	-10.1 ± 2.3	-10.7 ± 5.4	-10.3 ± 3. 3	-10.4 ± 4.6	-11.2 ± 2.7	-9.3 ± 6.5	-10.8 ± 6.5
• **Post-RPMI**	-13.9 ± 3.4	-12.6 ± 2.3	-9.8 ± 3.1	-9.9 ± 2.9	-9.7 ± 5.3	-11.8 ± 3.7	-10.7 ± 3.6	-10.2 ± 3.4	-10.3 ± 4.3
Adsorbed Protein (mg/m^2)									
• **Plasma**	3.77 ± 0.12	3.94 ± 0.07	4.03 ± 0.10	0.71 ± 0.10	0.66 ± 0.09	0.74 ± 0.07	6.23 ± 0.18[§]	6.34 ± 0.09[§]	6.54 ± 0.17[§]
• **NErys (Derived Erythrocyte Membranes)**	N/A*	N/A*	N/A*	N/A*	N/A*	N/A*	6.36 ± 0.08	6.28 ± 0.13	6.44 ± 0.11
Other Adsorbed Constituents									
Plasma									
• **Phospholipid (mg/m^2)**	0.09 ± 0.00	0.09 ± 0.01	0.08 ± 0.00	0.02 ± 0.00	0.01 ± 0.00	0.02 ± 0.00	3.71 ± 0.18[§]	4.21 ± 0.35[§]	4.20 ± 0.11[§]
• **Cholesterol (mg/m^2)**	0.10 ± 0.01	0.11 ± 0.00	0.11 ± 0.00	0.02 ± 0.00	0.02 ± 0.00	0.02 ± 0.00	1.06 ± 0.09[§]	1.06 ± 0.13 [§]	1.06 ± 0.08[§]
• **Cholesterol-Phospholipid Ratio (molar/molar)**	0.70 ± 0.03	0.71 ± 0.03	0.73 ± 0.04	0.71 ± 0.02	0.72 ± 0.01	0.72 ± 0.04	0.36 ± 0.03[§]	0.33 ± 0.04[§]	0.33 ± 0.01[§]
• **Protein-Total Lipid Ratio (w/w)**	19.96 ± 0.44	20.06 ± 0.39	20.66 ± 0.50	20.07 ± 0.63	20.23 ± 0.32	20.10 ± 0.47	1.30 ± 0.04[§]	1.20 ± 0.05[§]	1.24 ± 0.03[§]
• **Protein Binding Ability[+] (g protein/mol total lipid)**	9930 ± 38	9839 ± 52	10043 ± 85	9842 ± 47	9891 ± 24	9850 ± 59	808 ± 27[§]	757 ± 39[§]	783 ± 24[§]
NErys (Derived Erythrocyte Membranes)									
• **Phospholipid (mg/m^2)**	N/A*	N/A*	N/A*	N/A*	N/A*	N/A*	4.14 ± 0.22	3.73 ± 0.31	3.98 ± 0.13
• **Cholesterol (mg/m^2)**	N/A*	N/A*	N/A*	N/A*	N/A*	N/A*	1.07 ± 0.12	1.06 ± 0.14	1.06 ± 0.10
• **Cholesterol-Phospholipid Ratio (molar/molar)**	N/A*	N/A*	N/A*	N/A*	N/A*	N/A*	0.33 ± 0.02	0.36 ± 0.05	0.34 ± 0.04
• **Protein-Total Lipid Ratio (w/w)**	N/A*	N/A*	N/A*	N/A*	N/A*	N/A*	1.22 ± 0.04	1.31 ± 0.05	1.28 ± 0.03
• **Protein Binding Ability[+] (g protein/mol total lipid)**	N/A*	N/A*	N/A*	N/A*	N/A*	N/A*	768 ± 23	813 ± 42	799 ± 30
PEG Surface Density (PEG/nm^2)	N/A*	N/A*	N/A*	1. 67 ± 0.22	1.68 ± 0.17	1.65 ± 0.18	N/A*	N/A*	N/A*
Cell Viability (%)									
• **Macrophages**	83.3 ± 5.4	84.2 ± 7.2	87.5 ± 4.6	95.0 ± 10.1	94.9 ± 7.8	92.5 ± 9.0	95.7 ± 3.1	96.3 ± 3.1	96.3 ± 6.8
• **Monocytes**	85.1 ± 8.7	85.7 ± 3.3	84.6 ± 8.9	93.3 ± 5.6	93.4 ± 4.0	93.3 ± 5.3	101.2 ± 5.7	97.6 ± 2.4	98.1 ± 11.2
Endotoxin Content (EU/mg)	0.566 ± 0.125	0. 481 ± 0.334	0.529 ± 0.137	0.672 ± 0.099	0.554 ± 0.251	0.647 ± 0.181	0.687 ± 0.263	0.594 ± 0.215	0.619 ± 0.315

Data is expressed as mean ± standard deviation (n=3).

^…X denotes the used stretching factor for non-spherical particles. The particle-related factors, which are affected by the film-stretching method, have been described in detail in the previous report[16].

[#]Selected for in vivo study.

*N/A: Not Applicable.

[+]Defined as and comparable to elsewhere[126, 195].

[§]Not significant ($p > 0.05$) compared to the corresponding freshly prepared BCCN counterparts, rationally due to practically no significant additional adsorption of related-constituent.

Table S III-2. (a) Physicochemical Properties of Indocyanine Green (ICG) and Coumarin-6[196]. (b) Pharmacokinetics' Parameter of ICG.

(a)

Properties	ICG	Coumarin-6
Molecular Weight, *MW* (g/mol)	775.0	350.4
LogP	6.05 at pKa 2.70	4.79
LogD at pH 7.4 (representing circulation system)	4.91	4.79

(b)

Pharmacokinetics' Parameter	Description
Volume of Distribution, *Vd* (L)	70 - 90[197]
Protein Binding	High (up to ~98% to various proteins)[198]

Table S III-3. List of Proteins, Involved in the Proposed Brain-Targeting & -Clearance Mechanism, and Their Computational Biophysicochemical Properties from the Current Work.

No.	Recommended Protein/Peptide Name	Recommended Abbreviation After UniProt[41, 42] (Apweiler et al. 2004; The UniProt Consortium, 2018)	UniProt Entry; Homology Modeling Status[Y= Yes, S= Semi, N=No]; PDB ID (_Chain, if applicable)	Colloquial / Alternative Protein Name (/Abbreviation, if applicable)	Type (Physiologic [P]; Pathologic [Pa] or Therapeutic [T]?)	Full-Length of Mature Protein[2] (Amino Acids; AAs)	Number of Glycosylation Sites[1]	Molecular Weight from Amino Acid Analysis (kDa) (Apweiler et al. 2004; The UniProt Consortium, 2018)	Isoelectric Point, *IEP* (Bjellqvist et al. 1993)	Cumulative Surface Charge (Bjellqvist et al. 1993) or Zeta Potential at pH 7.4	Grand Average of Hydropathy, *GRAVY*[4]	Initial Surface Hydrophobicity, Φ_i	(Final) Surface Hydrophobicity, Φ_f	%-/%+	Deformation Energy, E_{def} as Global Rigidity (Monomer; Mode 7; Default)	Multi-domains / Multi-subunits ?	Aliphatic Index, *AI*[3]	%Cysteine	% H bond-forming AAs[3]	PTBCS Class
1	Leukocyte surface antigen CD47	CD47	Q08722 Y- (7myz_c)	CD47	P	305	6	33.468	7.00	-0.51	0.541	0.632	0.352	0.67	21.73	No	118.85	1.64	14.10	Class 1
2	Phospholipid-transporting ATPase ABCA7	ABCA7	Q8IZY2 Y-(5ayj)	ATP-binding cassette sub-family A member 7	P	2146	0	234.350	6.86	-5.51	0.055	0.486	0.486	0.70	3.80	No	99.13	1.68	11.46	Class 2
3	Phospholipid-transporting ATPase ABCA1	ABCA1	O95477 S-(5yjy)	ATP-binding cassette sub-family A member 1	P	2261	2	254.302	6.43	-12.24	-0.074	0.453	0.446	0.74	1.65	No	93.27	1.72	13.27	Class 2
4	ATP-binding cassette sub-family G member 1	ABCG1	P45844 S-1h2h_h	ATP-binding cassette transporter 8 (ABC B8)	P	678	0	75.592	8.05	2.53	0.163	0.589	0.589	0.67	1.14	Yes	96.34	2.51	13.42	Class 2
5	Flotillin-1	FLOT1	O75955 Y-(5h7c)	N/A	P	427	0	47.355	7.21	-0.33	-0.338	0.481	0.481	0.62	0.02	Yes	89.18	0.94	9.84	Class 2
6	Flotillin-2	FLOT2	Q14254 Y-(1win)	Epidermal surface antigen; ESA (ESA1)	P	427	0	46.933	5.19	-12.51	-0.153	0.518	0.518	0.83	0.04	Yes	101.01	1.64	8.67	Class 2
7	Tyrosine-protein phosphatase non-receptor type substrate 1	SIRPA	P78324 Y-(2wng)	SHPS substrate 1; Macrophage fusion receptor (SHPS1; MFR)	P	474	3	52.105	6.54	-3.19	-0.518	0.517	0.493	0.84	0.43	Yes	75.86	1.48	16.88	Class 4a
8	Apolipoprotein A-I	APOA1	P02647 N-3lk2s	(Apo-A1; Apo-AI)	P	243	0	28.079	5.27	-9.29	-0.840	0.538	0.538	0.93	0.05	No	82.72	0.00	10.29	Class 3
9	Apolipoprotein E	APOE	P02649 N-2l7b	(Apo-E)	P	299	6	34.237	5.52	-5.38	-0.727	0.498	0.220	0.88	1410.86	Yes	83.91	0.33	8.36	Class 3
10	Prolow-density lipoprotein receptor-related protein 1	LRP1	Q07954 Y-(1tsh_a)	Apolipoprotein E receptor; Alpha-2-macroglobulin receptor (APOER; A2MR)	P	4525	52	502.665	5.16	-182.16	-0.522	0.537	0.432	0.88	6.76	Yes	63.48	7.31	12.51	Class 4a
11	Scavenger receptor class B member 1	SCARB1	Q8WTV0 Y-4f7b	SR-BI; SRB1; CLA-1 (CLA1)	P	552	2	60.878	8.56	5.62	0.125	0.613	0.604	0.51	35.69	No	87.25	2.54	13.04	Class 2
12	Sodium-dependent dopamine transporter	SLC6A3	Q01959 Y-4m48_a	DAT transporter (DAT1)	P	620	0	68.495	6.48	-3.40	0.499	0.641	0.641	0.72	14.52	Yes	105.32	2.10	13.06	Class 1
13	Integrin alpha-M	ITGAM	P11215 Y-3i6s	1 of 2 Component of Mac-1 (Macrophage-1 antigen) receptor / CR3 (Complement Receptor 3) / CD11b	P	1136	3	125.471	6.75	-3.34	-0.212	0.491	0.470	0.70	8.71	No	84.48	1.94	15.05	Class 2
14	Integrin beta-2	ITGB2	P05107 Y-3i6s	1 of 2 Component of Mac-1 (Macrophage-1 antigen) receptor / CR3 (Complement Receptor 3) / CD18	P	747	6	82.564	6.54	-4.42	-0.377	0.496	0.468	0.72	0.15	No	72.68	7.50	11.24	Class 4a

*Unless otherwise specified, the recommended abbreviations of the mouse proteins are the same as the human ones according to UniProt[41, 42].

Table S III-4. List of 20 Most Abundant Proteins in Erythrocyte (Membrane)[116] and Their Computational Biophysicochemical Properties from the Current Work.

No.	Recommended Protein/Peptide Name	Recommended Abbreviation After UniProt[Apweiler et al., 2004. The UniProt Consortium, 2018]	UniProt Entry, Homology Modeling Status (Y= Yes, S=Semi, N= No), (Main) PDB ID (_Chain, if applicable)	Colloquial / Alternative Protein Name (/Abbreviation, if applicable)	Type (Physiologic [P] Pathologic [Pa] or Therapeutic [T]?)	Full-Length of Mature Protein[2] (Amino Acids; AAs)	Number of Glycosylation Sites[1]	Molecular Weight from Amino Acid Analysis (kDa)[Apweiler et al., 2004. The UniProt Consortium, 2018]	Isoelectric Point, *IEP*[Bellevist, 1993]	Cumulative Surface Charge[Bellevist, 1993] or Zeta Potential at pH 7.4	Grand Average of Hydropathy, *GRAVY*[4]	Initial Surface Hydrophobicity, Φ_I	(Final) Surface Hydrophobicity, Φ_F	%-/%+	Deformation Energy, E_{Def} as Global Rigidity (Monomer; Mode 7; Default)	Multi-domains / Multi-subunits ?	Aliphatic Index, *AI*[3]	%Cysteine	% H bond-forming AAs[3]	PTBCS Class
1	Band 3 anion transport protein	SLC4A1	P02730 Y-3oqp	Band 3	P	911	1	101.792	5.08	-31.95	0.213	0.618	0.608	1.15	56.32	No	109.03	0.55	11.09	Class 1
2	Actin, cytoplasmic 1	ACTB	P60709 N-6anu	Actin	P	375	0	41.737	5.29	-12.31	-0.200	0.528	0.528	1.12	296.13	No	81.95	1.60	13.60	Class 2
3	Erythrocyte band 7 integral membrane protein	STOM	P27105 Y-(21k)	Band 7	P	288	0	31.731	7.87	0.61	0.043	0.562	0.562	0.81	1.56	Yes	102.36	1.04	13.89	Class 1
4	Spectrin beta chain, erythrocytic	SPTB	P11277 Y-(3ddt)	Spectrin	P	2136	0	246.337	5.15	-105.54	-0.672	0.516	0.516	1.04	0.26	Yes	85.41	0.70	9.60	Class 2
5	Spectrin alpha chain, erythrocytic 1	SPTA1	P02549 Y-(5j4o)	Spectrin	P	2419	0	280.014	4.95	-151.65	-0.762	0.500	0.500	1.26	0.07	Yes	83.75	0.87	9.22	Class 2
6	Glyceraldehyde-3-phosphate dehydrogenase	GAPDH	P04406 N-6yne	GAPDH	P	334	0	35.922	8.58	2.79	-0.114	0.459	0.459	0.61	910.65	Yes	84.94	0.90	12.57	Class 2
7	Ankyrin-1	ANK1	P16157 Y-(3udt)	Ankyrin	P	1881	0	206.265	5.65	-58.41	-0.378	0.493	0.493	0.87	0.17	No	88.41	1.12	13.18	Class 2
8	Protein 4.2	EPB42	P16452 Y-(1f13)	Band 4.2	P	690	0	76.878	8.40	4.61	-0.232	0.517	0.517	0.68	252.09	Yes	91.03	2.17	12.75	Class 2
9	Protein 4.1	EPB41	P11171 Y-(1gg3)	Band 4.1	P	864	0	97.017	5.41	-29.00	-0.770	0.513	0.513	1.06	0.07	No	73.83	1.16	15.51	Class 4a
10	Tropomyosin alpha-3 chain	TPM3	P06753 S-(6dtn)	Tropomyosin	P	284	0	32.819	4.68	-28.43	-1.051	0.536	0.536	1.42	0.07	Yes	83.70	0.35	6.69	Class 3
11	Beta-adducin	ADD2	P35612 Y-(3ocr)	Beta-adducin	P	726	0	80.854	5.67	-15.17	-0.663	0.521	0.521	0.91	3.91	Yes	68.50	1.10	16.53	Class 4a
12	55 kDa erythrocyte membrane protein	MPP1	Q00013 Y-(3nej)	p55	P	465	0	52.165	6.98	-1.14	-0.515	0.489	0.489	0.75	238.88	No	78.84	0.86	13.98	Class 2
13	Tropomodulin-1	TMOD1	P28289 Y-(4pkl)	Tropomodulin	P	359	0	40.569	5.03	-13.43	-0.604	0.524	0.524	0.86	109.08	No	90.19	0.56	10.58	Class 2
14	Solute carrier family 2, facilitated glucose transporter member 1	SLC2A1	P11166 S-(1suk)	Glut 1	P	492	1	54.084	8.93	5.55	0.534	0.631	0.620	0.58	42.92	No	108.94	1.22	12.40	Class 1
15	Dematin	DMTN	Q08495 Y-(1qzp)	Band 4.9	P	405	0	45.514	8.95	4.79	-0.894	0.520	0.520	0.55	0.04	Yes	64.54	0.49	17.78	Class 4a
16	CD59 glycoprotein	CD59	P13987 N-2i8b	CD59	P	77	4	8.961	5.18	-2.67	-0.578	0.481	0.017	1.23	4836.91	No	57.01	12.99	10.39	Class 2
17	Alpha-adducin	ADD1	P35611 Y-(3ocr)	Alpha-adducin	P	737	0	80.955	5.60	-16.16	-0.632	0.543	0.543	0.90	6.07	Yes	71.07	0.95	13.70	Class 4a
18	Blood group Rh(D) polypeptide	RHD	Q02161 Y-(3hd6)	Rh polypeptide	P	416	0	45.079	8.71	3.75	0.748	0.670	0.670	0.44	225.77	No	121.63	1.20	13.22	Class 1
19	Glycophorin-A	GYPA	P02724 Y-(1afo)	Glycophorin A	P	131	17	14.253	5.27	-6.27	-0.363	0.539	0.265	1.23	791.10	No	82.52	0.00	25.95	Class 2
20	Aquaporin-1	AQP1	P29972 S-(6poj)	Aquaporin-1	P	268	1	28.395	7.12	-0.38	0.490	0.598	0.584	0.65	1.58	Yes	115.75	1.49	14.18	Class 3

*Unless otherwise specified, the recommended abbreviations of the mouse proteins are the same as the human ones according to UniProt[41, 42].

Table S III-5. List of 20 Most Abundant Proteins in Blood Plasma[134, 135] and Their Computational Biophysicochemical Properties from the Current Work.

No.	Recommended Protein/Peptide Name	Recommended Abbreviation After UniProt (Apweiler et al., 2004; The UniProt Consortium, 2018)	UniProt Entry, Homology Modeling Status (Y= Yes, S=Semi, N= No), (Main) PDB ID (_Chain, if applicable)	Colloquial / Alternative Protein Name (/Abbreviation, if applicable)	Type (Physiologic [P] / Pathologic [Pa] or Therapeutic [T]?)	Full-Length of Mature Protein[2] (Amino Acids; AAs)	Number of Glycosylation Sites[1]	Molecular Weight from Amino Acid Analysis (kDa) (Apweiler et al., 2004; The UniProt Consortium, 2018)	Isoelectric Point, *IEP* (Bellevist, 1993)	Cumulative Surface Charge (Bellevist, 1993) or Zeta Potential at pH 7.4	Grand Average of Hydropathy, *GRAVY*[4]	Initial Surface Hydrophobicity, Φ_I	(Final) Surface Hydrophobicity, Φ_F	%-/%+	Deformation Energy, E_{Def} as Global Rigidity (Monomer; Mode 7; Default)	Multi-domains / Multi-subunits ?	Aliphatic Index, *AI*[3]	%Cysteine	% H bond-forming AAs[3]	PTBCS Class
1	Albumin	ALB	P02768 S-1ao6_a	Albumin	P	585	0	66.472	5.67	-15.82	-0.395	0.454	0.454	1.12	159.84	No	76.92	5.98	8.89	Class 2
2	Fibrinogen alpha chain	FGA	P02671 S-3ghg_g	Fibrinogen	P	831	4	91.359	5.79	-15.12	-0.885	0.490	0.457	0.80	0.94	No	51.37	1.44	19.37	Class 4b
3	Serotransferrin	TF	P02787 S-3qyt	Transferrin	P	679	4	75.195	6.70	-3.82	-0.411	0.468	0.435	0.92	84.53	No	70.27	5.60	10.46	Class 4a
4	Apolipoprotein A-I	APOA1	P02647 N-3k2s	Apolipoprotein A1; Apolipoprotein AI (Apo-A1; ApoA-1; Apo-AI; ApoA-I; ApoA1; ApoAI)	P	243	0	28.079	5.27	-9.29	-0.840	0.538	0.538	0.93	0.05	No	82.72	0.00	10.29	Class 3
5	Alpha-2-macroglobulin	A2M	P01023 S-4aoq	Alpha-2-macroglobulin	P	1451	8	160.810	5.98	-22.85	-0.214	0.530	0.384	0.98	40.74	Yes	85.06	1.72	15.30	Class 2
6	Alpha-1-antitrypsin	SERPINA1	P01009 Y-1oph_a	(AAT)	P	394	3	44.325	5.37	-15.04	-0.302	0.494	0.468	1.38	8.23	No	87.11	0.25	12.94	Class 2
7	Fibrinogen beta chain	FGB	P02675 S-3ghg_h	Fibrinogen	P	447	1	50.763	7.95	1.46	-0.849	0.484	0.473	0.53	0.35	No	58.88	2.46	11.63	Class 4a
8	Complement C3	C3	P01024 S-2a73	Complement C3	P	1641	3	184.951	6.00	-18.33	-0.340	0.476	0.456	0.86	32.32	No	86.85	1.65	12.74	Class 2
9	Haptoglobin	HP	P00738 Y-4fao_c	Haptoglobin	P	388	4	43.349	6.13	-6.36	-0.527	0.503	0.464	1.09	4.59	Yes	76.08	3.09	10.05	Class 2
10	Hemopexin	HPX	P02790 Y-1qjs	Hemopexin	P	439	7	49.295	6.45	-5.10	-0.537	0.497	0.157	0.79	400.76	No	63.10	2.73	12.07	Class 2
11	Apolipoprotein B-100	APOB	P04114 Y-1ls.h	Apolipoprotein B100	P	4536	19	512.858	6.57	-23.70	-0.306	0.556	0.448	0.80	0.06	No	91.73	0.53	15.26	Class 2
12	Alpha-1-acid glycoprotein 1	ORM1	P02763 Y-3iio0	Orosomucoid-1; AGP 1;	P	183	5	21.560	5.00	-8.47	-0.764	0.501	0.167	1.12	143.22	No	70.33	2.19	12.02	Class 4a
13	Fibrinogen gamma chain	FGG	P02679 S-3ghg_i	Fibrinogen	P	427	2	48.493	5.24	-15.38	-0.682	0.511	0.502	1.10	0.04	No	64.00	2.34	12.88	Class 4a
14	Alpha-1-acid glycoprotein 2	ORM2	P19652 Y-3apu	Orosomucoid-2; AGP 2; OMD 2 (AGP2)	P	183	5	21.651	5.12	-7.49	-0.816	0.496	0.163	1.10	143.22	No	62.35	2.73	12.57	Class 4a
15	Alpha-2-HS-glycoprotein	AHSG	P02765 Y-6hpv	Fetuin-A (FETUA)	P	309	8	32.960	4.73	-17.50	-0.218	0.586	0.385	1.37	183.63	Yes	81.42	3.88	10.68	Class 2
16	Vitamin D-binding protein	GC	P02774 S-1kw2	N/A	P	458	0	51.197	5.16	-15.96	-0.405	0.481	0.481	1.05	115.55	No	73.69	6.11	16.16	Class 4a
17	Alpha-1-antichymotrypsin	SERPINA3	P01011 S-(1yxa)	ACT; Serpin A3 (AACT)	P	400	6	45.266	5.32	-12.18	-0.163	0.506	0.251	1.05	1185.82	No	94.38	0.25	14.75	Class 2
18	Cellular retinoic acid-binding protein 1	CRABP1	P04003 Y-2qsx	Proline-rich protein (PRP)	P	549	3	61.671	6.24	-6.86	-0.532	0.542	0.518	0.54	0.02	No	61.38	6.56	15.85	Class 4a
19	Antithrombin-III	SERPINC1	P01008 S-2ant	ATIII; Serpin C1 (AT3)	P	432	4	49.039	5.95	-4.47	-0.359	0.492	0.454	1.05	501.65	No	81.94	1.39	12.73	Class 2
20	Apolipoprotein A-II	APOA2	P02652 Y-2ouf	Apolipoprotein A2; Apolipoprotein A-II (Apo-A2; ApoA-2; Apo-AII; ApoA-II; ApoA2; ApoAII)	P	77	0	8.708	5.05	-2.49	-0.503	0.569	0.569	1.14	56.62	Yes	74.68	1.30	15.58	Class 4a

*Unless otherwise specified, the recommended abbreviations of the mouse proteins are the same as the human ones according to UniProt[41, 42].

Table S III-6. [Part 1 of 3] Non-Exhaustive List of Opsonins[199] and Their Computational Biophysicochemical Properties from the Current Work.

No.	Recommended Protein/Peptide Name	Recommended Abbreviation After UniProt[Apweiler et al., 2004; The UniProt Consortium, 2018]	UniProt Entry, Homology Modeling Status (Y=Yes; S=Semi; N=No); (Main) PDB ID (_Chain, if applicable)	Source	Type (Physiologic [P] Pathologic [Pa] or Therapeutic [T]?)	Full-Length of Mature Protein[2] (Amino Acids; AAs)	Number of Glycosylation Sites[1]	Molecular Weight from Amino Acid Analysis (kDa) [Apweiler et al., 2004; The UniProt Consortium, 2018]	Isoelectric Point, IEP [Bellevue, 1993]	Cumulative Surface Charge [Bellevue, 1993] or Zeta Potential at pH 7.4	Grand Average of Hydropathy, GRAVY[4]	Initial Surface Hydrophobicity, Φ_I	(Final) Surface Hydrophobicity, Φ_F	%-/%+	Deformation Energy, $E_{D,e}$ as Global Rigidity (Monomer, Mode 7; Default)	Multi-domains / Multi-subunits ?	Aliphatic Index, AI[3]	%Cysteine	% H bond-forming AAs[3]	PTBCS Class
1	Immunoglobulin heavy constant gamma 1	IGHG1	P01857 S-1hzh_h	Homo sapiens (Human)	P	330	1	36.106	8.46	3.59	-0.428	0.481	0.469	0.59	0.32	No	71.33	2.73	19.70	Class 4a
2	Immunoglobulin heavy constant gamma 2	IGHG2	P01859 Y-1hzh_h	Homo sapiens (Human)	P	326	1	35.901	7.64	0.52	-0.419	0.526	0.513	0.71	0.18	No	66.20	3.37	19.94	Class 4a
3	Immunoglobulin heavy constant gamma 3	IGHG3	P01860 Y-1hzh_h	Homo sapiens (Human)	P	377	2	41.287	8.23	3.35	-0.511	0.525	0.515	0.72	3.23	No	61.67	4.77	19.63	Class 4a
4	Immunoglobulin heavy constant gamma 4	IGHG4	P01861 Y-1hzh_h	Homo sapiens (Human)	P	327	1	35.941	7.15	-0.47	-0.423	0.529	0.517	0.75	0.22	No	68.99	2.75	20.49	Class 4a
5	Immunoglobulin heavy constant mu	IGHM	P01871 Y-6hyg	Homo sapiens (Human)	P	453	5	49.440	6.35	-3.45	-0.319	0.560	0.302	0.75	71.72	No	71.39	2.65	20.75	Class 4a
6	Immunoglobulin heavy constant alpha 1	IGHA1	P01876 Y-3ohn_I	Homo sapiens (Human)	P	353	7	37.655	6.08	-4.54	-0.206	0.562	0.195	1.02	0.01	No	72.07	4.25	22.10	Class 4a
7	Immunoglobulin heavy constant alpha 2	IGHA2	P01877 Y-1i70_b	Homo sapiens (Human)	P	340	5	36.591	5.85	-6.48	-0.268	0.560	0.290	1.18	10.55	No	72.26	4.12	20.00	Class 4a
8	Immunoglobulin heavy constant delta	IGHD	P01880 Y-1zvo_c	Homo sapiens (Human)	P	384	10	42.353	8.37	2.69	-0.566	0.529	0.492	0.63	0.04	No	67.32	2.08	19.01	Class 4a
9	Immunoglobulin heavy constant epsilon	IGHE	P01854 Y-6hyg_a	Homo sapiens (Human)	P	428	6	47.019	8.39	3.61	-0.375	0.525	0.272	0.65	63.89	No	67.41	3.04	23.36	Class 4a
10	Immunoglobulin kappa constant	IGKC	P01834 S-1hzh_I	Homo sapiens (Human)	P	107	0	11.766	6.11	-1.46	-0.537	0.465	0.465	0.91	1203.93	Yes	66.45	2.80	22.43	Class 4a
11	Immunoglobulin lambda constant 1	IGLC1	P0CG04 N-2fb4	Homo sapiens (Human)	P	106	0	11.348	7.89	0.53	-0.520	0.464	0.454	0.67	834.97	Yes	59.81	2.83	23.58	Class 4a
12	Immunoglobulin lambda constant 2	IGLC2	P0DOY2 N-1iil	Homo sapiens (Human)	P	106	0	11.294	6.91	-0.46	-0.444	0.480	0.480	0.70	853.41	No	60.75	2.83	25.47	Class 2
13	Immunoglobulin lambda constant 3	IGLC3	P0DOY3 N-1eqk_I	Homo sapiens (Human)	P	106	0	11.266	6.91	-0.47	-0.439	0.482	0.482	0.86	355.43	No	60.75	2.83	25.47	Class 2
14	Immunoglobulin lambda constant 6	IGLC6	P0CF74 Y-6qn7_I	Homo sapiens (Human)	P	106	0	11.277	6.91	-0.46	-0.467	0.497	0.497	0.84	1368.77	No	60.75	2.83	23.58	Class 2
15	Immunoglobulin lambda constant 7	IGLC7	A0M8Q6 Y-1nc4_a	Homo sapiens (Human)	P	106	0	11.254	8.50	1.54	-0.458	0.490	0.490	0.59	1418.08	No	62.55	2.83	22.64	Class 2
16	Complement C1q subcomponent subunit A	C1QA	P02745 Y-2jg8_a	Homo sapiens (Human)	P	223	4	23.688	9.34	6.50	-0.547	0.514	0.276	0.56	1072.19	No	63.32	1.79	10.76	Class 2

Table S III-6. [Part 2 of 3] Continued

No.	Recommended Protein/Peptide Name	Recommended Abbreviation After UniProt[(Apweiler et al., 2004; The-UniProt-Consortium, 2018)]	UniProt Entry, Homology Modeling Status[Y=Yes, S=Semi, N=No]-(Main) PDB ID (_Chain, if applicable)	Source	Type (Physiologic [P]- Patologic [Pa] or Therapeutic [T]?)	Full-Length of Mature Protein‡ (Amino Acids; AAs)	Number of Glycosylation Sites[1]	Molecular Weight from Amino Acid Analysis (kDa) [Apweiler et al., 2004; The-UniProt-Consortium, 2018]	Isoelectric Point, *IEP* [Bjellqvist, 1993]	Cumulative Surface Charge [Bjellqvist, 1993] or Zeta Potential at pH 7.4	Grand Average of Hydropathy, *GRAVY*[4]	Initial Surface Hydrophobicity, Φ_i	(Final) Surface Hydrophobicity, Φ_f	%-/%+	Deformation Energy, E_{DefG} as Global Rigidity (Monomer; Mode 7; Default)	Multi-domains / Multi-subunits ?	Aliphatic Index, *AI*[3]	%Cysteine	% H bond-forming AAs[3]	PTBCS Class
17	Complement C1q subcomponent subunit B	C1QB	P02746 Y-2jg8_b	N/A	P	226	0	23.742	8.85	3.53	-0.468	0.556	0.556	0.67	616.66	No	60.00	1.77	10.62	Class 2
18	Complement C1q subcomponent subunit C	C1QC	P02747 Y-2jg8_c	(C1QG)	P	217	1	22.813	8.33	1.60	-0.336	0.564	0.549	0.59	1136.96	No	65.48	1.84	10.14	Class 2
19	Complement component 1 Q subcomponent-binding protein, mitochondrial	C1QBP	Q07021 Y-1p32	Hyaluronan-binding protein 1; ASF/SF2-associated protein p32 (HABP1; SF2AP32)	P	209	0	23.783	4.32	-28.29	-0.690	0.521	0.521	2.43	80.11	Yes	75.98	0.48	13.88	Class 4a
20	Complement C1r subcomponent	C1R	P00736 Y-(1zjk)	Complement component 1 subcomponent r	P	688	4	78.213	5.76	-14.53	-0.559	0.527	0.493	0.83	169.47	Yes	66.44	3.78	10.90	Class 4a
21	Complement C1s subcomponent	C1S	P09871 Y-(4igd)	C1 esterase	P	673	2	74.887	4.85	-31.77	-0.425	0.554	0.546	1.32	247.52	Yes	67.01	3.86	11.14	Class 4a
22	Complement C2	C2	P06681 Y-(2ok5)	C3/C5 convertase	P	732	8	81.085	7.56	0.62	-0.349	0.516	0.356	0.65	238.88	No	77.10	3.14	13.66	Class 2
23	Complement C3	C3	P01024 S-2a73	(CPAMD1)	P	1641	3	184.951	6.00	-18.33	-0.340	0.476	0.456	0.86	32.32	No	86.85	1.65	12.74	Class 2
24	Complement C4-A	C4A	P0C0L4 Y-4fxg_a	(CPAMD2)	P	1714	5	188.914	6.15	-17.90	-0.241	0.542	0.342	0.86	19.76	Yes	87.09	1.63	13.42	Class 2
25	Complement C4-B	C4B	P0C0L5 Y-4fxg_b	(CPAMD3)	P	1714	3	188.880	6.28	-14.84	-0.242	0.537	0.517	0.71	14.72	Yes	86.98	1.58	13.54	Class 2
26	C4b-binding protein alpha chain	C4BPA	P04003 Y-2gsx	Proline-rich protein (PRP)	P	549	3	61.671	6.24	-6.86	-0.532	0.542	0.518	0.54	0.02	No	61.38	6.56	15.85	Class 4a
27	C4b-binding protein beta chain	C4BPB	P20851 Y-2q7z	N/A	P	235	3	26.351	4.97	-12.60	-0.413	0.550	0.519	1.54	2.65	No	71.74	5.96	11.49	Class 4a
28	Complement C5	C5	P01031 Y-3cu7	Hemolytic complement (Hc)	P	1654	3	185.775	5.96	-21.29	-0.188	0.545	0.525	0.95	299.57	No	90.60	1.75	14.69	Class 2
29	Complement component C6	C6	P13671 S-4a5w	N/A	P	913	10	102.412	6.17	-10.44	-0.622	0.501	0.471	0.88	0.17	No	60.65	7.01	14.79	Class 4a
30	Complement component C7	C7	P10643 Y-6h04_d	N/A	P	821	7	91.115	6.10	-10.29	-0.535	0.535	0.497	1.08	0.09	No	59.81	6.82	14.86	Class 4a
31	Complement component C8 alpha chain	C8A	P07357 Y-3qjy_a	Complement component 8 subunit alpha	P	554	5	61.711	5.74	-8.91	-0.566	0.515	0.280	0.92	137.08	No	62.53	5.23	13.54	Class 4a
32	Complement component C8 beta chain	C8B	P07358 Y-3qjy_b	Complement component 8 subunit beta	P	537	5	61.043	7.89	2.25	-0.574	0.506	0.271	0.69	149.53	No	64.95	5.21	13.22	Class 4a
33	Complement component C8 gamma chain	C8G	P07360 Y-2qos_c	Complement component 8 subunit gamma	P	182	0	20.385	8.52	1.65	-0.212	0.499	0.499	0.62	1030.24	No	83.63	1.65	10.44	Class 2

Table S III-6. [Part 3 of 3] Continued

No.	Recommended Protein/Peptide Name	Recommended Abbreviation After UniProt (Apweiler et al., 2004; The-UniProt-Consortium, 2018)	UniProt Entry, Homology Modeling Status(Y=Yes,S=Semi,N=No)-(Main) PDB ID (_Chain, if applicable)	Source	Type (Physiologic [P]- Patologic [Pa] or Therapeutic [T]?)	Full-Length of Mature Protein[2] (Amino Acids; AAs)	Number of Glycosylation Sites[1]	Molecular Weight from Amino Acid Analysis (kDa) (Apweiler et al., 2004; The-UniProt-Consortium, 2018)	Isoelectric Point, *IEP* (Bjellqvist, 1993)	Cumulative Surface Charge (Bjellqvist, 1993) or Zeta Potential at pH 7.4	Grand Average of Hydropathy, *GRAVY*[4]	Initial Surface Hydrophobicity, Φ_I	(Final) Surface Hydrophobicity, Φ_f	%-/%+	Deformation Energy, E_{DefG} as Global Rigidity (Monomer; Mode 7; Default)	Multi-domains / Multi-subunits ?	Aliphatic Index, *AI*[3]	%Cysteine	% H bond-forming AAs[3]	PTBCS Class
34	Complement component C9	C9	P02748 Y-5fmw	Homo sapiens (Human)	P	538	4	60.979	5.42	-13.78	-0.534	0.538	0.503	0.90	0.01	No	69.22	4.46	14.13	Class 4a
35	Collagen alpha-1(I) chain	COL1A1	P02452 Y-3hr2_a	Homo sapiens (Human)	P	1057	3	94.796	9.29	7.63	-0.881	0.568	0.546	0.63	11.85	No	27.45	0.00	5.39	Class 4b
36	Collagen alpha-2(I) chain	COL1A2	P08123 Y-3hr2_b	Homo sapiens (Human)	P	1040	1	93.609	9.88	16.97	-0.678	0.576	0.566	0.62	1.22	No	41.04	0.00	4.90	Class 4b
37	Mannose-binding protein C	MBL2	P11226 Y-1hup	Homo sapiens (Human)	P	228	0	24.021	5.40	-3.60	-0.590	0.500	0.500	0.81	33.46	Yes	62.50	3.07	12.28	Class 4a
38	Pulmonary surfactant-associated protein A1	SFTPA1	Q8IWL2 Y-1r14	Homo sapiens (Human)	P	228	1	24.170	4.89	-10.48	-0.662	0.554	0.539	1.22	53.50	Yes	56.05	3.07	9.65	Class 4a
39	Pulmonary surfactant-associated protein A2	SFTPA2	Q8IWL1 Y-1r14	Homo sapiens (Human)	P	228	1	24.138	5.07	-8.46	-0.689	0.517	0.502	1.08	293.59	Yes	55.61	2.63	10.09	Class 4a
40	Pulmonary surfactant-associated protein D	SFTPD	P35247 Y-(4kzv)	Homo sapiens (Human)	P	355	1	35.499	6.94	-0.55	-0.625	0.561	0.548	0.56	8.23	Yes	51.46	1.69	9.58	Class 4b
41	Ficolin-1	FCN1	O00602 Y-1ei3_c	Homo sapiens (Human)	P	297	0	32.018	6.11	-3.47	-0.564	0.544	0.544	0.90	0.33	No	59.16	2.69	10.10	Class 4a
42	Ficolin-2	FCN2	Q15485 Y-2j3u	Homo sapiens (Human)	P	288	1	31.413	6.65	-1.46	-0.616	0.556	0.542	0.88	5.22	No	57.92	2.78	10.76	Class 4a
43	Ficolin-3	FCN3	O75636 S-1la5	Homo sapiens (Human)	P	276	1	30.354	6.22	-4.29	-0.593	0.519	0.505	0.85	0.03	No	60.11	2.90	10.87	Class 4a
44	C-reactive protein	CRP	P02741 N-1b09	Homo sapiens (Human)	P	206	0	23.047	5.28	-4.45	-0.140	0.521	0.521	0.86	3519.39	Yes	80.83	0.97	16.50	Class 2
45	Serum amyloid P-component	APCS	P02743 N-1s sc	Homo sapiens (Human)	P	204	1	23.259	6.12	-2.38	-0.185	0.520	0.505	0.77	5213.93	Yes	92.60	0.98	12.25	Class 2
46	Pentraxin-related protein PTX3	PTX3	P26022 Y-4pbo	Homo sapiens (Human)	P	364	0	40.121	4.90	-19.36	-0.273	0.557	0.557	1.19	781.07	Yes	85.00	2.47	11.26	Class 3
47	Lactadherin	MFGE8	Q08431 Y-2biq	Homo sapiens (Human)	P	364	5	40.773	8.22	2.69	-0.346	0.539	0.277	0.78	190.98	Yes	79.29	3.30	12.64	Class 2
48	Fibronectin, Intact	FN1 (Intact)	P02751 Y-(1fnf)	Homo sapiens (Human)	P	4892	16	538.499	5.25	-140.22	-0.525	0.500	0.423	0.96	0.05	Yes	67.50	2.53	18.97	Class 4a
49	IgM, Intact (Immunoglobulin M)	N/A	N/A	Homo sapiens (Human)	P	7514	50	808.806	8.75	94.20	-0.330	0.480	0.415	0.62	0.19	Yes	69.93	2.04	22.62	Class 4a

Table S III-7. List of Secondary Interfacial Activity Parameters as in Figure III-8

#	(Surface/Particle) Material **1**	Material **2**					
		NErys (Inside)			Albumin (BSA)		
		WoA_3 (mN/m)	$IFT_{1.2}$ (mN/m)	Difference of WoA_3-$IFT_{1.2}$ (mN/m)	WoA_3 (mN/m)	$IFT_{1.2}$ (mN/m)	Difference of WoA_3-$IFT_{1.2}$ (mN/m)
1	Gold (Plain)	57.31	1.78	**55.54**	45.73	5.26	**40.47**
2	Gold (COOH)	53.33	1.16	**52.17**	42.93	3.45	**39.49**
3	Gold (PEGylated)	17.95	9.95	**7.99**	16.28	3.52	**12.76**
4	Graphene	49.21	0.87	**48.34**	39.97	2.01	**37.96**
5	Graphene Oxide	39.55	0.54	**39.01**	31.48	0.51	**30.97**
6	NErys (Outside)	N/A[#]	N/A[#]	**N/A[#]**	-0.58	15.45	**-16.03**
7	PS-COOH	61.78	3.13	**58.66**	49.22	7.59	**41.63**
8	Coumarin-6	65.28	4.40	**60.89**	51.79	9.79	**42.00**
9	ICG	54.15	1.06	**53.09**	43.23	3.88	**39.34**

Table S III-8. Primary Interfacial Activity Parameters of Various Materials Used in This Research and References

Material	Water Contact Angle, *WCA* (°)	Surface Free Energy, *SFE* (mN/m)	Surface Polarity, $Xp^{‡}$	Material-Water Interfacial Tension, *IFT* (mN/m)
(a) Synthetic				
PS-COOH	87.6[16, 200]	45.08	0.0207	42.03
ICG	91.9	44.45	0.0078	46.80
Coumarin-6	80.3	44.59	0.0679	32.34
PLGA 50/50-COOH	48.0[16]	54.79	0.4299	6.08
PLGA 50/50-COOR	59.1	50.63	0.2800	13.27
Sucrose Stearate	46.8[201]	51.86	0.6409	2.02
Sucrose Palmitate	18.5[201]	69.16	0.7286	0.12
Paracetamol	39.3[201]	61.88	0.4297	5.56
PEG	21.5[16]	71.39	0.4808	3.66
PVA	53.0[16]	50.05	0.4449	6.23
Gold (Plain)	83.2	44.78	0.0452	36.21
Gold (COOH)	77.6	47.19	0.0738	31.61
Gold (PEGylated)	25.8	70.56	0.4415	5.02
Graphene	127.0[16, 202]	49.47[§]	0.1082	93.29[§]
Graphene Oxide	67.4[202]	45.19[§]	0.2246	17.1[§]
Ag (Silver)	82.4[203]	32.06[§]	0.0692	32.06[§]
Fe_3O_4 (Iron(III) Oxide; Magnetite)	73.7[204]	30.74[§]	0.5651	10.25[§]
CoO (Cobalt(II) Oxide)	59.0[205]	44.19[§]	0.4704	6.70[§]
CeO_2 (Cerium(IV) Oxide; Ceria)	6.3[206]	72.93[§]	0.6171	0.57[§]
Dextran	23.0[16, 207]	69.00[§]	0.5405	2.00[§]
(b) Natural				
NErys (Inside)	77.3	38.90	0.1576	22.88
NErys (Outside)	18.9	68.96	0.7245	0.10
MErys (Inside)	73.6	41.46	0.1779	20.95
MErys (Outside)	21.5	67.84	0.7028	0.09
RBCs	15.0[208]	70.35[§]	0.7065	0.02[§]
Water	(Practically) 0[34]	72.80	0.7006	~0
FBS (Fetal Bovine Serum)	74.3	40.35	0.1839	20.66
Human Blood Plasma	61.7	46.46	0.3159	11.89
HSA[33]	63.5	48.27[§]	0.2418	15.78[§]
BSA	56.7	54.74	0.2515	14.77
Fibrinogen[178]	31.8	64.39[§]	0.5246	2.51[§]
Fibrin[178]	68.7	44.75[§]	0.2086	18.34[§]

[§]Recalculated values of interfacial activity parameters using Owens and Wendt approach[34] from corresponding reference(s).

[‡]Defined as = $\frac{\mathrm{SFE_{polar}}}{\mathrm{SFE}}$.

Additional abbreviations: HSA: Human Serum Albumin; BSA: Bovine Serum Albumin

Table S III-9. [Part 1 of 4] List of Proteins, Used as Instances for Each Class of Physiological-Therapeutic Biologics Classification System (PTBCS) in Figure III-10, and Their Computational Biophysicochemical Properties.

No.	Recommended Protein/Peptide Name	Recommended Abbreviation After UniProt (Bowler et al. 2004; The UniProt Consortium, 2018)	UniProt Entry, Homology Modeling Status (Y=Yes; N=No); (Main) PDB ID (_Chain, if applicable)	Source	Type (Physiologic [P]; Pathologic [Pa] or Therapeutic [T]?)	Full-Length of Mature Protein[2] (Amino Acids; AAs)	Number of Glycosylation Sites[1]	Molecular Weight from Amino Acid Analysis (kDa) (Bowler et al. 2004; The UniProt Consortium, 2018)	Isoelectric Point, *IEP* (Patterson, 1993)	Cumulative Surface Charge (Bertolini et al. 1993) or Zeta Potential at pH 7.4	Grand Average of Hydropathy, *GRAVY*[4]	Initial Surface Hydrophobicity, Φ_I	(Final) Surface Hydrophobicity, Φ_F	%-/%+	Deformation Energy, *Edef* as Global Rigidity (Monomer; Mode 7; Default)	Multi-domains / Multi-subunits ?	Aliphatic Index, *AI*[3]	%Cysteine	% H bond-forming AAs[3]	PTBCS Class
1	Pulmonary surfactant-associated protein B	SFTPB	P15781 Y-3bpp	Bos taurus (Bovine)	P&T	79	2	8.706	9.03	4.41	1.092	0.640	0.616	0.13	5158.76	Yes	147.85	8.86	7.59	Class 1
2	Pulmonary surfactant-associated protein C	SFTPC	P15783 Y-1spf	Bos taurus (Bovine)	P&T	34	0	3.568	8.96	1.51	2.582	0.832	0.832	0.00	120.93	No	231.47	5.88	0.00	Class 1
3	Beta-lactoglobulin	LGB	P02754 S-1cj5	Bos taurus (Bovine)	P	162	0	18.281	4.83	-8.52	-0.162	0.500	0.500	1.22	2002.82	No	102.41	3.09	9.26	Class 1
4	Surfactin-C	N/A	N/A N-2npv	Bacillus subtilis	P	7	0	0.814	3.67	-2.44	1.771	0.856	0.856	0.00	14085.72	No	264.29	0.00	0.00	Class 1
5	Preproinsulin	INS	P01308 Y-2kqp	Homo sapiens (Human)	P	110	0	11.981	5.22	-3.52	0.193	0.585	0.585	0.92	85.85	No	102.91	5.45	7.27	Class 1
6	Cell shape-determining protein MreB	mreB	Q8TYX3 Y-1jcf	Methanopyrus kandleri	P	393	0	42.760	4.50	-37.37	-0.241	0.547	0.547	1.73	119.00	No	103.18	0.00	8.65	Class 1
7	Cell shape-determining protein MreB	mreB	Q9WZ57 N-1jcf	Thermotoga maritima (strain ATCC 43589 / MSB8 / DSM 3109 / JCM 10099)	P	336	0	35.787	5.35	-4.46	0.193	0.536	0.536	0.85	681.25	No	115.42	0.00	12.20	Class 1
8	Cell shape-determining protein MreB	mreB	Q9Z756 Y-1jcf	Chlamydia pneumoniae (Chlamydophila pneumoniae)	P	366	0	39.539	8.89	4.66	0.117	0.541	0.541	0.51	575.28	No	108.99	1.37	9.29	Class 1
9	Cell shape-determining protein MreB	mreB	A0M0H3C7 V-4 S-4czf	Caulobacter vibrioides (strain NA1000 / CB15N) (Caulobacter crescentus)	P	347	0	36.685	6.29	-3.27	0.090	0.541	0.541	0.69	608.52	No	103.69	1.15	9.22	Class 1
10	Cell shape-determining protein MreB	mreB	A0A071KW P5 Y-1jcf	Pseudomonas aeruginosa	P	345	0	36.976	5.31	-7.43	0.037	0.545	0.545	0.81	581.30	No	101.45	1.16	11.88	Class 2
11	Cell shape-determining protein MreB	mreB	P0A9X4 Y-1jcf	Escherichia coli (strain K12)	P	347	0	36.952	5.17	-10.33	0.057	0.549	0.549	0.84	588.02	No	98.33	0.86	10.37	Class 2
12	Cell shape-determining protein MreB	mreB	O31465 Y-1jcf	Bacillus subtilis (strain 168)	P	337	0	35.917	5.09	-8.45	0.048	0.540	0.540	0.82	672.97	No	100.15	0.59	11.87	Class 2
13	Cell shape-determining protein MreB	mreB	H8L459 Y-1jcf	Vibrio cholerae serotype O1 (strain ATCC 39315 / El Tor Inaba N16961)	P	347	0	36.901	5.02	-12.37	0.032	0.550	0.550	0.70	400.00	No	100.29	1.15	10.66	Class 2
14	Hemoglobin, Intact	N/A	N/A N-2dn2	Homo sapiens (Human)	P&T	574	0	61.933	8.13	2.70	0.017	0.469	0.469	0.75	820.85	Yes	92.79	1.05	11.15	Class 2
15	Erythropoietin (INN: Epoetin Alfa)	EPO	P01588 S-1buy	Homo sapiens (Human)	P	166	4	18.396	8.74	2.52	-0.188	0.492	0.222	0.54	643.14	No	96.45	2.41	12.65	Class 2
16	Deoxyribonuclease-1 (INN: Dornase alfa)	DNASE1	P24855 N-4aws	Homo sapiens (Human)	P&T	260	1	29.254	4.58	-15.39	-0.083	0.544	0.530	1.53	2241.15	No	88.88	1.54	11.92	Class 2

Table S III-9. [Part 2 of 4] Continued

No.	Recommended Protein/Peptide Name	Recommended Abbreviation After UniProt[Apweiler et al., 2004; The-UniProt-Consortium, 2018]	UniProt Entry, Homology Modeling Status[Y=Yes, S=Semi, N=No]-(Main) PDB ID (_Chain, if applicable)	Source	Type (Physiologic [P]- Patologic [Pa] or Therapeutic [T]?)	Full-Length of Mature Protein[1] (Amino Acids; AAs)	Number of Glycosylation Sites[1]	Molecular Weight from Amino Acid Analysis (kDa) [Apweiler et al., 2004; The-UniProt-Consortium, 2018]	Isoelectric Point, *IEP* [Bjellqvist 1993]	Cumulative Surface Charge [Bjellqvist, 1993] or Zeta Potential at pH 7.4	Grand Average of Hydropathy, *GRAVY*[4]	Initial Surface Hydrophobicity, Φ_i	(Final) Surface Hydrophobicity, Φ_f	%-/%+	Deformation Energy, $E_{Def/G}$ as Global Rigidity (Monomer; Mode 7; Default)	Multi-domains / Multi-subunits ?	Aliphatic Index, *AI*[3]	%Cysteine	% H bond-forming AAs[3]	PTBCS Class
17	Ribonuclease pancreatic	RNASE1	P61823 N-1afu	Bos taurus (Bovine)	P	124	0	13.690	8.64	3.48	-0.663	0.417	0.417	0.42	1151.57	No	46.45	6.45	20.16	Class 2
18	Angiopep-2 (Trevatide)	N/A (Angiopep-2 or Trevatide)	N/A Y-3l33_e	Peptide Synthesis	T	19	0	2.302	9.52	1.55	-1.495	0.456	0.456	0.41	1404.60	No	0.00	0.00	15.79	Class 2
19	Insulin	INS	P01308 N-1aiy	Homo sapiens (Human)	P&T	51	0	5.796	5.40	-2.52	0.218	0.536	0.536	0.92	2170.12	Yes	85.88	11.76	11.76	Class 2
20	Somatotropin (Growth Hormone; INN: Somatropin)	GH1	P01241 S-1a22	Homo sapiens (Human)	P&T	191	0	22.129	5.27	-5.45	-0.411	0.512	0.512	1.08	163.45	No	83.72	2.09	14.66	Class 2
21	Hyaluronidase PH-20	N/A (SPAM1 Analog)	N/A (P38567 Analog) Y-2pe4	Homo sapiens (Human)	P	447	6	51.106	5.73	-5.65	-0.219	0.543	0.295	0.86	509.20	No	86.78	2.68	11.41	Class 2
22	Neutrophil defensin 3	DEFA3	P59666 N-1dfn	Homo sapiens (Human)	P	30	0	3.492	8.33	1.40	0.123	0.633	0.633	0.67	2791.31	No	62.00	20.00	3.33	Class 2
23	Semaglutide	GCG, i.e. GLP1(7-37), Derivative	P01275 S-7k0_P	Genetic Engineering	T	31	0	3.384	5.53	-1.41	-0.255	0.523	0.523	0.86	448.50	No	69.35	0.00	16.13	Class 2
24	Myoglobin	MB	P68082 N-1ymb	Equus caballus (Horse)	P	153	0	16.951	7.36	-0.07	-0.396	0.430	0.430	0.86	1734.63	No	89.35	0.00	7.84	Class 3
25	Lysozyme C	LYZ	P00698 N-3wun	Gallus gallus (Chicken)	P	129	0	14.313	9.32	7.38	-0.472	0.456	0.456	0.30	2454.07	No	65.12	6.20	13.18	Class 3
26	Granulocyte colony-stimulating factor	CSF3	P09919 S-1gnc	Homo sapiens (Human)	P	177	1	18.987	5.43	-5.39	0.195	0.608	0.591	1.31	23.89	No	105.37	2.82	12.43	Class 1
27	Filgrastim (Recombinant human of Granulocyte colony-stimulating factor, i.e. identic, but non-glycosylated one due to its production in E. coli)	N/A (CSF3 Analog)	N/A N-1gnc	Genetic Engineering	T	175	0	18.803	5.66	-4.39	0.209	0.611	0.611	1.25	16.10	No	104.91	2.86	12.00	Class 3
28	Interleukin-2	IL2	P60568 S-1irl	Homo sapiens (Human)	P	133	1	15.418	7.01	-0.43	-0.171	0.527	0.508	0.75	658.97	No	103.38	2.26	15.79	Class 3
29	Aldesleukin (Proleukin®)	N/A (IL2 Analog)	N/A S-1irl	Genetic Engineering	T	132	0	15.331	7.02	-0.40	-0.211	0.522	0.522	0.65	713.39	No	103.41	1.52	16.67	Class 3
30	Invasin, 497 amino acid	N/A (YPTB1668	N/A (P11922	Yersinia pseudotubercul	P	497	0	52.388	4.47	-19.43	-0.064	0.536	0.536	1.18	0.09	No	79.05	0.40	22.54	Class 3
31	IgA, Intact (Blood, mainly monomeric; Immunoglobulin A)	N/A	N/A	Homo sapiens (Human)	P	1378	10	148.377	7.58	1.10	-0.305	0.508	0.413	0.74	86.36	Yes	68.62	3.19	21.77	Class 4a
32	IgG2, Intact (Immunoglobulin G)	N/A	N/A	Mus musculus (Mouse)	P	1316	2	145.230	7.31	-0.52	-0.402	0.488	0.480	0.77	0.26	Yes	69.54	2.58	21.43	Class 4a

Table S III-9. [Part 3 of 4] Continued

No.	Recommended Protein/Peptide Name	Recommended Abbreviation After UniProt[Apweiler et al., 2004; The-UniProt-Consortium, 2018]	UniProt Entry, Homology Modeling Status[Y=Yes, S=Semi, N=No]- (Main) PDB ID (_Chain, if applicable)	Source	Type (Physiologic [P]; Pathologic [Pa] or Therapeutic [T]?)	Full-Length of Mature Protein† (Amino Acids; AAs)	Number of Glycosylation Sites‡	Molecular Weight from Amino Acid Analysis (kDa) [Apweiler et al., 2004; The-UniProt-Consortium, 2018]	Isoelectric Point, *IEP* [Bjellqvist, 1993]	Cumulative Surface Charge [Bjellqvist, 1993] or Zeta Potential at pH 7.4	Grand Average of Hydropathy, *GRAVY*[4]	Initial Surface Hydrophobicity, Φ_I	(Final) Surface Hydrophobicity, Φ_I	%-/%+	Deformation Energy, E_{DefG} as Global Rigidity (Monomer: Mode 7; Default)	Multi-domains / Multi-subunits ?	Aliphatic Index, *AI*[3]	%Cysteine	% H bond-forming AAs[3]	PTBCS Class
33	IgG1, Intact (Immunoglobulin G)	N/A	N/A N- 1hzh	Homo sapiens (Human)	P	1344	2	148.134	8.80	21.60	-0.470	0.466	0.459	0.56	22.78	Yes	66.50	2.38	19.79	Class 4a
34	Trastuzumab	N/A	N/A Y- 1hzh	Genetic Engineering	T	1328	2	145.337	8.45	11.44	-0.414	0.478	0.471	0.69	1.04	Yes	68.78	2.41	20.48	Class 4a
35	Adalimumab	N/A	N/A Y- 1hzh	Genetic Engineering	T	1330	2	145.425	8.36	9.45	-0.397	0.474	0.466	0.65	0.73	Yes	71.32	2.41	20.45	Class 4a
36	Bevacizumab	N/A	N/A Y- 1hzh	Genetic Engineering	T	1334	2	146.478	8.09	5.50	-0.412	0.483	0.475	0.69	24.16	Yes	67.29	2.40	21.14	Class 4a
37	Rituximab	N/A	N/A Y- 1hzh	Genetic Engineering	T	1328	2	144.544	8.66	17.41	-0.417	0.482	0.475	0.56	5.91	Yes	66.30	2.41	21.54	Class 4a
38	Nivolumab	N/A	N/A Y- 1hzh	Genetic Engineering	T	1308	2	143.579	7.92	3.27	-0.420	0.477	0.470	0.65	1.00	Yes	69.37	2.45	20.64	Class 4a
39	Pembrolizumab	N/A	N/A S- 5dk3	Genetic Engineering	T	1330	2	146.246	7.63	1.31	-0.418	0.490	0.482	0.69	21.12	Yes	67.04	2.41	20.90	Class 4a
40	Ipilimumab	N/A	N/A Y- 1hzh	Genetic Engineering	T	1326	2	145.313	8.54	13.38	-0.406	0.490	0.483	0.67	0.38	Yes	69.32	2.41	20.36	Class 4a
41	Blinatumomab	N/A	N/A Y- 1hzh	Genetic Engineering	T	504	0	54.095	7.22	-0.41	-0.544	0.514	0.514	0.51	312.04	Yes	54.40	1.79	22.22	Class 4a
42	Fibrinogen, Intact	N/A	N/A N- 3ghg_G,H,I N_J,K,L,O,R, S,T	Homo sapiens (Human)	P	1963	14	224.601	6.16	-17.89	-0.752	0.477	0.444	0.71	0.15	Yes	65.61	2.75	12.18	Class 4a
43	Clusterin	CLU	P10909 Y- (1hq_a)	Homo sapiens (Human)	P	427	6	50.063	5.89	-9.25	-0.761	0.496	0.248	0.79	5.64	Yes	68.22	2.34	13.58	Class 4a
44	Coagulation factor VIII	F8	P00451 Y- (6m2)	Homo sapiens (Human)	P&T	2332	22	264.726	6.96	-5.64	-0.533	0.500	0.486	0.78	254.91	Yes	74.95	0.99	15.91	Class 4a
45	Etanercept	N/A	N/A Y- 3alu_S	Genetic Engineering	T	934	32	102.458	7.20	-1.19	-0.529	0.524	0.479	0.53	15.69	Yes	56.72	6.21	19.06	Class 4a
46	Bone morphogenetic protein 2 (INN: Dibotermin Alfa)	N/A (BMP2 Analog)	P12643 S- 3bmp	Homo sapiens (Human)	T	262	2	29.756	8.93	9.81	-0.556	0.467	0.456	0.53	229.60	Yes	71.37	5.34	9.16	Class 4a
47	Liraglutide	GCG, i.e. GLP1(7-37), Derivative	P01275 N- 4qod	Genetic Engineering	T	31	0	3.384	5.53	-1.41	-0.255	0.500	0.500	1.17	65.57	No	69.35	0.00	16.13	Class 4a
48	Light Chain of IgG, Wild Type	N/A (~IGLV2-14 Fragment)	P01704 S- (6em1)	Homo sapiens (Human)	P	99	0	10.391	5.58	-1.48	-0.398	0.521	0.521	1.15	1661.95	Yes	59.09	2.02	29.29	Class 4a
49	Light Chain of IgG, Amyloidogenic Type	N/A	N/A S- (6em2)	Homo sapiens (Human)	Pa	99	0	10.495	4.65	-3.48	-0.325	0.531	0.531	1.75	1978.11	Yes	63.03	2.02	27.27	Class 4b
50	Major prion protein	PRNP	P04156 Y- 1qlz	Homo sapiens (Human)	P	208	2	22.747	9.39	6.83	-1.097	0.464	0.452	0.30	4.18	No	29.52	0.96	10.58	Class 4b
51	Tumor necrosis factor-binding protein 1 (Soluble form of Tumor necrosis factor receptor superfamily member 1A)	TNFRSF1A	P19438 S- 1ri	Homo sapiens (Human)	P	161	0	18.181	7.07	-0.80	-0.591	0.446	0.446	0.85	28.40	No	50.19	14.91	15.53	Class 4b

Table S III-9. [Part 4 of 4] Continued

No.	Recommended Protein/Peptide Name	Recommended Abbreviation After UniProt[Apweiler et al., 2004; The-UniProt-Consortium, 2018]	UniProt Entry, Homology Modeling Status[Y=Yes,S= Semi, N=No]-(Main) PDB ID (_Chain, if applicable)	Source	Type (Physiologic [P]-Patologic [Pa] or Therapeutic [T]?)	Full-Length of Mature Protein[‡] (Amino Acids; AAs)	Number of Glycosylation Sites[1]	Molecular Weight from Amino Acid Analysis (kDa)[Apweiler et al., 2004; The-UniProt-Consortium, 2018]	Isoelectric Point, *IEP*[Bjellqvist, 1993]	Cumulative Surface Charge[Bjellqvist, 1993] or Zeta Potential at pH 7.4	Grand Average of Hydropathy, *GRAVY*[4]	Initial Surface Hydrophobicity, Φ_i	(Final) Surface Hydrophobicity, Φ_f	%-/%+	Deformation Energy, E_{DefG} as Global Rigidity (Monomer; Mode 7; Default)	Multi-domains / Multi-subunits ?	Aliphatic Index, *AI*[3]	%Cysteine	% H bond-forming AAs[3]	PTBCS Class
52	Alpha-lactalbumin	LALBA	P00709 N-1a4v	Homo sapiens (Human)	P	123	2	14.078	4.70	-7.59	-0.255	0.608	0.592	1.12	2241.95	No	91.22	6.50	12.20	Class 2
53	Immunoglobulin G-binding protein A	spa	P02976 Y-4yay	Staphylococcus aureus (strain NCTC 8325 / PS 47)	P	449	0	49.643	5.18	-13.36	-1.401	0.496	0.496	0.97	0.03	No	54.90	0.00	5.79	Class 4a
54	Alpha-hemolysin	hly	P09616 N-7ahl	Staphylococcus aureus	P	293	0	33.248	7.91	0.62	-0.795	0.464	0.464	0.74	1.27	No	63.52	0.00	16.72	Class 4a
55	Melittin	MELT	P01501 N-2mlt	Apis mellifera (Honeybee)	P	26	0	2.847	12.02	4.55	0.273	0.518	0.518	0.00	702.83	No	135.00	0.00	11.54	Class 1
56	Collagen alpha-(I), Intact [Collagen Type I]	N/A (Col1a1-Col1a2 2:1 mol[ar] ratio)	N/A (P02454 & P02466) S-3hr2	Rattus Norvegicus (Rat)	P	3152	7	283.258	9.56	33.93	-0.833	0.546	0.528	0.65	0.01	Yes	31.05	0.00	6.06	Class 4b
57	Glycinin A1a subunit (Glycinin acidic 1a subunit of Glycinin 11S Gf1)	N/A (GY1 Derivative)	P04776 S-1fxz	Glycine max (Soybean) (Glycine hispida)	P	287	0	32.647	5.19	-10.43	-1.140	0.471	0.471	1.07	444.57	No	56.06	2.09	9.41	Class 2
58	Albumin	ALB	P02769 N-4f5s	Bos taurus (Bovine)	P	583	0	66.433	5.60	-17.79	-0.475	0.461	0.461	1.13	201.84	No	76.14	6.00	10.46	Class 2
59	Chymotrypsin A (Alpha-Chymotrypsin)	N/A (CTRA)	P00766 S-1cgi_e	Bos taurus (Bovine)	P	241	0	25.208	8.33	2.35	0.091	0.511	0.511	0.41	2870.11	No	83.73	4.15	20.33	Class 2
60	Alpha-amylase A type-1/2	amyl	P0C1B3 S-3vx1	Aspergillus oryzae (strain ATCC 42149 / RIB 40) (Yellow koji mold)	P	478	1	52.489	4.48	-24.51	-0.280	0.521	0.510	1.72	944.51	No	75.10	1.88	15.90	Class 2
61	Chymotrypsinogen A (Alpha-Chymotrypsinogen)	N/A (CTRA)	P00766 N-1cgi_e	Bos taurus (Bovine)	P	245	0	25.666	8.52	3.35	0.051	0.496	0.496	0.38	3535.10	No	82.37	4.08	20.82	Class 2
62	Thaumatin I	N/A (THM1)	P02883 N-1thv	Thaumatococcus daniellii (Katemfe) (Phrynium daniellii)	P	207	0	22.205	8.32	3.13	-0.301	0.486	0.486	0.50	1599.40	No	53.77	7.73	16.43	Class 2
63	Ovotransferrin	N/A (TRFE)	P02789 N-1aiv	Gallus gallus (Chicken)	P	686	1	75.828	6.69	-2.87	-0.436	0.463	0.452	0.77	95.95	No	71.22	4.37	12.39	Class 4a
64	Cytochrome c	CYCS	P00004 N-1hrc	Equus caballus (Horse)	P	104	0	11.702	9.59	8.57	-0.902	0.403	0.403	0.49	4750.76	No	59.13	1.92	9.62	Class 2
65	Ovalbumin	SERPINB14	P01012 S-1ova_d	Gallus gallus (Chicken)	P	385	1	42.750	5.19	-12.37	-0.006	0.490	0.478	1.16	1085.89	No	90.18	1.56	13.77	Class 2

Table S III-10. Relationship between Materials' and NErys' (Primary and Secondary) Interfacial Activity Parameters and the Affinity between Them as well as Correctness of Membrane Orientation

#	Material **1** (Mostly Nanoparticle)	Material **2**						dDiff (mN/m)[#]	%Correct Membrane Orientation
		NErys (Outside)			NErys (Inside)				
		WoA_3 (mN/m)	$IFT_{1.2}$ (mN/m)	Difference of WoA_3-$IFT_{1.2}$ (mN/m)	WoA_3 (mN/m)	$IFT_{1.2}$ (mN/m)	Difference of WoA_3-$IFT_{1.2}$ (mN/m)		
1	PLGA 50/50-COOH	0.04	5.69	-5.66	22.69	5.81	16.88	22.54	84%[169]
2	Hyaluronidase PH-20	0.28	0.11	0.17	-2.95	26.12	-29.07	-29.14	N/A[×‡]
3	Water	0.00	0.10	-0.10	0.00	22.88	-22.89	-22.79	70%[169]
4	Gold	-0.33	36.64	-36.97	57.31	1.78	55.54	92.51	N/A[×]
5	Graphene Oxide	-0.20	17.51	-17.72	39.55	0.54	39.01	56.73	N/A[×]
6	Graphene	-0.52	27.83	-28.36	49.21	0.87	48.34	76.70	N/A[×]
7	PS-COOH	-0.33	42.46	-42.79	61.78	3.13	58.66	56.80	N/A[×]
8	SiO_2 (as TEOS)[209]	-0.99	3.96	-4.05	18.50	8.15	10.35	3.37	N/A[×]

[§]Recalculated values of interfacial activity parameters using Owens and Wendt approach[34] from corresponding reference(s).

[#]Difference of outside and inside energy, *dDiff* = $Difference_{inside}$ - $Difference_{outside}$. The more positive the dDiff, the stronger the tendency to provide the higher percentage of correct (right-side-out) cell membrane orientation.

*Computed from the mathematical models mentioned in Figure S III-9 by using Φ_f = 0.295 for Hyaluronidase PH-20 (with its sequence was taken from UniProt Q12794, subsequently selected for 447 amino acid N-terminal domain, representing soluble fragment thereof as the commercially available recombinant product[210] and used in the corresponding references[170],) calculated using POPS[63] and ^the equations derived by Owens and Wendt[34].

×N/A: Not Available.

‡However, merely physical adsorption of Hyaluronidase PH-20 to the outside NErys elicited practically no enzymatic activity[170], apparently due to the relatively low binding affinity between Hyaluronidase PH-20 and the NErys, thereby easily washing-off Hyaluronidase PH-20 during sample purification. Our data and calculation above vindicate their experimental result.

Table S III-11. Correlation of Material Matrix's' Secondary Interfacial Activity Parameters and Release Profile of Incorporated (Fluorescence/Drug) Substance

#	Material 1	Material 2	WoA_3 (mN/m)	$IFT_{1.2}$ (mN/m)	Difference of WoA_3-$IFT_{1.2}$ (mN/m)	Release Profile (% at Certain Time Point(s); h)	Interpretation to Material Non-Washability Algorithm[16](Figure S III-22)	Comparative Case(s)
1	PS-COOH	ICG	88.69	0.14	88.55	0.03; 3 h 0.02; 24 h 0.04; 48 h 0.05; 72 h	Practically Non-Washable	-
2	PS-COOH	Coumarin-6	73.73	0.64	73.09	0.05; 3 h 0.08; 24 h 0.09; 48 h 0.12; 72 h	Practically Non-Washable	-
3	PLGA-COOR	Coumarin-6	41.34	4.27	37.07	0.55; 24 h 0.59; 48 h	Practically Non-Washable	Desai et al. 1997[211]
4	PVA	Coumarin-6	28.31	10.26	18.06	0.55; 24 h 0.59; 48 h	Practically Non-Washable	Desai et al. 1997[211]
5	BSA	Coumarin-6	43.23	3.88	39.34	0.55; 24 h 0.59; 48 h	Practically Non-Washable	Desai et al. 1997[211]
6	Sucrose Stearate	Paracetamol	8.22	8.58	-0.36	21; 3 h	Practically Washable	Szuts et al. 2010[201]
7	Sucrose Palmitate	Paracetamol	-0.69	6.36	-7.05	78; 3 h	Practically Washable	Szuts et al. 2010[201]

[§]Recalculated values of interfacial activity parameters using Owens and Wendt approach[34] from corresponding reference(s).

Table S III-12. Correlation of Materials' Interfacial Activity Parameters with (a) Biomolecular Corona Kinetic Formation and (b) Biological Relations/Effects in High Protein Physiological(-Mimicking) Condition

(a)

Material 1 (Nanoparticle)	Material 2 FBS			Interpretation to Material Non-Washability Algorithm[16] (Figure S III-22)	FBS Corona Kinetic Formation (Days)[109]	Material 2 NErys (Inside)			Interpretation to Material Non-Washability Algorithm[16] (Figure S III-22)
	WoA_3 (mN/m)	$IFT_{1.2}$ (mN/m)	Difference of WoA_3-$IFT_{1.2}$ (mN/m)			WoA_3 (mN/m)	$IFT_{1.2}$ (mN/m)	Difference of WoA_3-$IFT_{1.2}$ (mN/m)	
CeO_2 (Cerium(IV) Oxide; Ceria)	5.14	16.08	-10.94	Practically Washable	>> 2 (the slowest & least stable)	5.34	18.10	-12.76	Practically Washable
CoO (Cobalt(II) Oxide)	23.17	4.18	18.99	Practically Washable	> 2	24.45	5.13	19.32	Practically Washable
Fe_3O_4 (Iron(III) Oxide; Magnetite)	24.11	6.42	17.68	Practically Washable	> 2	25.61	7.14	18.47	Practically Washable
Ag (Silver)	51.43	1.29	50.14	Practically Non-Washable	< 2	54.08	0.86	53.22	Practically Non-Washable
Au (Gold)	54.53	2.33	52.20	Practically Non-Washable	< 2 (the fastest & most stable)	57.31	1.78	55.54	Practically Non-Washable
Graphene Oxide[151]	37.62	0.25	37.38	Practically Non-Washable	N/A*	39.55	0.54	39.01	Practically Non-Washable

#All particles have a similar radius of curvature ~5 nm[109] (except graphene oxide with [lateral size of 500 - 5,000 nm & thickness of 0.8 - 1.2 nm[151]]), thus the (radius of)curvature-dependent affinity issue is already minimized.

*N/A: Not Applicable.

(b)

Material 1 (Nanoparticle)	Material 2 Blood Plasma			Interpretation to Material Non-Washability Algorithm[16] (Figure S III-22)	Observed (& Estimated) Biological Relations/Effects	Mean of Radius of Curvature, $R_c(t)$
	WoA_3 (mN/m)	$IFT_{1.2}$ (mN/m)	Difference of WoA_3-$IFT_{1.2}$ (mN/m)			
Dextran (as coating of SPIO [Superparamagnetic Iron Oxide: Fe_3O_4—γ-Fe_2O_3])	10.88	10.19	0.69	Practically Washable	• Still too much biomolecular "soft corona" during in vitro study → appreciable adsorption/insertion of relatively hydrophilic complement C3 (compared to other opsonins, e.g. IgG; Figure S III-11a) to the corona via covalent bond (→ ↑ phagocytosis/cellular uptake)[212] • Biomolecular corona loss during in vivo study(→ unprotected from relatively hydrophilic opsonins [e.g. complement C3] due to the following dextran as the outermost layer → ↑ phagocytosis/cellular uptake)[212]	~70 nm
Polystyrene	57.51	4.92	52.59	Practically Non-Washable	Sufficient "hard corona" during in vitro study (→ the highest protection from any opsonins) → the lowest phagocytosis/cellular uptake compared to lipoproteins[213]	~50 nm

Table S III-13. Hydrophobicity Comparison between (Free) Cholesterol and (Palmitoyl or C16) Sphingomyelin (Abbreviated "PSM") in the RBC membranes

Properties	(Free) Cholesterol	PSM*
LogP[196]	7.11	12.30 at pKa 7.65
LogD[196]: pH 7.4 (representing circulation system)	7.11	9.00

*Moreover, sphingomyelin variants of RBC membranes reportedly[214] tend to even have longer acyl chain length, e.g. the longest and the second most abundant C24 (saturated lignoceroyl- and unsaturated nervonoylsphingomyelin), leading to higher logP and logD.

Table S III-14. Comparison between Physicochemical Properties of Blood Plasma Proteins and Certain Functional Proteins

Parameter	All Human Proteins	Human Blood Plasma (All; based on the Most Current Database)	Human Blood Plasma (Limited to Only Known Experimental Concentrations)	Human Blood Plasma (Limited to the Available &/ Reasonably 3D-Structure Modeled Protein)	Invasin (Fragment; Extracellular Region)
PDB ID	N/A[#]	N/A[#]	N/A[#]	N/A[#]	1CWV
UniProt ID (Further Details)	N/A[#]; 20,386 items (2018 Reviewed Database)[42]	N/A[#]; 3,669 items (2018 Reviewed Database & Schwenk et al. 2017[135])	N/A[#]; 1,237 items (2018 Database, Nanjappa et al. 2014[134] & Schwenk et al. 2017[135])	N/A[#]; 133 items **(-)**	P11922 (N/A)
Cumulative GRAVY or Amino Acid Sequence Hydrophobicity (Unitless), computed as Kyte & Doolittle 1982[50]	N/A[#]; only available as Geometric Mean: -0.345	N/A[#]; only available as Geometric Mean: -0.360	-0.347	-0.377	-0.064 (as PDB, Hamburger et al. 1999[215] & used by Castoldi et al. 2018[291])
Cumulative Surface Hydrophobicity, Φ_f (Unitless), calculated from modified Lienqueo et al.'s method[62]	N/A[#]; only available as Geometric Mean: 0.439	N/A[#]; only available as Geometric Mean: 0.462	0.448	0.443	0.536
Cumulative Surface Charge (mV) •at pH 8.0 (~mitochondria[216]) •at pH 5.5 (~endosome[217]; intracellular) •at pH 7.4 (~circulation system / tissue plasma / extracellular / interstitial)	 N/A[#] N/A[#] N/A[#]	 N/A[#] N/A[#] N/A[#]	 -27.17 +3.64 -17.10	 -35.93 +4.82 -22.61	 -21.10 -14.40 -19.20
Isoelectric Point computed as[51]	N/A[#]; only available as Geometric Mean: 6.805	N/A[#]; only available as Geometric Mean: 6.308	N/A[#]; only available as Geometric Mean: 6.247	N/A[#]; only available as Geometric Mean: 6.278	4.379

[#]N/A: Not Applicable.

*Interpretation:

- **GRAVY** (Grand Average of the Hydropathy): the more positive the value (range: -4.5 to +4.5), the more hydrophobic the protein/condition. GRAVY considers the protein hydrophobicity based merely on amino acid sequence (/primary structure).
- **Φ_f**: the higher the value (range: 0 to 1), the more hydrophobic the protein surface in the practically physiological-related pH (7.0) using experimental Hydrophobic Interaction Chromatography (HIC). Φ_f considers the 3D-structure of protein and glycosylation (i.e. experimental carbohydrate content [or so-called glycosylation content]).
- **Surface Charge**: is analogous with experimental zeta potential measurement result at corresponding pHs. There are positive, negative, and zero values.

Table S III-15. Basic Parameters of Erythrocytes and Their Freshly Produced Derivatives as well as Blood Plasma

Samples	Counts		Hemoglobin Concentration[c]	Protein Concentration	Phospholipid Concentration	Cholesterol Concentration	Cholesterol - Phospholipid Ratio	Protein-Total Lipid[d] Ratio	Protein Binding Ability[e]
	Flow Cytometry	TRPS							
	($x10^6$ objects/µL)	($x10^{11}$ objects/mL)	(mg/mL)	(mg/mL)	(mg/mL)	(mg/mL)	(molar/molar)	(w/w)	(g protein/mol total lipid)
RBCs[a]	4.93 ± 0.48	5.14 ± 0.36[b]	143.9 ± 2.6	3.5226 ± 0.13	2.0453 ± 0.1813	0.6881 ± 0.0532	0.65 ± 0.03	1.29 ± 0.08	781 ± 36
MErys	23.16 ± 0.58	22.14 ± 0.79[b]	Not Detected	N/A[#2)]	N/A[#2)]	N/A[#2)]	N/A[#2)]	N/A[#2)]	N/A[#2)]
NErys	N/A[#1)]	0.31 ± 0.08	Not Detected	3.3854 ± 0.0817	2.0386 ± 0.0923	0.5897 ± 0.0313	0.56 ± 0.04	1.29 ± 0.06	798 ± 44
Blood Plasma	N/A[#1)]	Not Determined	Not Detected	67.0278 ± 0.5612	1.2893 ± 0.2374	1.8821 ± 0.1263	2.83 ± 0.04	21.14 ± 0.08	10,176 ± 397

Data is expressed as mean ± standard deviation (n=3).

[a]always standardized as 40% hematocrit (HCT).

[b]For direct comparison to flow cytometry results, these values are already converted to the unit of "$x10^6$ objects/µL".

[c]Using Drabkin's reagent[218] (limit of detection 0.3 mg/mL).

[d]Total lipid concentration = phospholipid concentration + cholesterol concentration.

[e]Defined as and comparable to[126, 195].

[#...)]N/A: Not Applicable due to 1) size < limit detection or 2) the similar analytes, method, and value as NErys.

Table S III-16. Details of C values, which are used herein and developed based on UniProt Database(July 2018[41-43])

Glycosylation Sites/Protein \ MW (kDa)	≤35	35-≤75	75-≤135	135k-≤243	> 243
1	120	120	120	120	120
2	600	600	600	600	600
3	500	500	500	500	500
4	120	600	600	660	660
5	140	140	140	140	140
6-to-7	200	200	1600	200	3000
8-to-9	500	500	500	500	500
10-to-11	4000	4000	4000	1200	1200
12-to-13	2500	2500	2500	6600	2500
14-to-15	6600	6600	6600	6600	6600
16-20	2500	2500	2500	10000	3500
21-50	27000	27000	27000	27000	40000
51-200	40000	40000	40000	27000	27000
>200	570000	570000	570000	570000	570000

Table S III-17. [Part 1 of 2] List of Proteins, Compared to Kerner et al.-Fujiwara et al.'s[143] Refoldability Classification System in Figure S III-13b as well as Their Average Abundance in each Escherichia coli[219] and Computational Biophysicochemical Properties.

No.	Recommended Protein/Peptide Name	Recommended Abbreviation After UniProt[Mölleken et al., 2004; The-UniProt-Consortium, 2018]	UniProt Entry, Homology Modeling Status[Yes-Yes_S=Semi, No-No]; (Main) PDB ID (_Chain, if applicable)	Protein Weight, Average/Cell (fg)	Type (Physiologic [P]; Pathologic [Pa] or Therapeutic [TP])	Full-Length of Mature Protein[2] (Amino Acids; AAs)	Number of Glycosylation Sites	Molecular Weight from Amino Acid Analysis (kDa)[Mölleken et al., 2004; The-UniProt-Consortium, 2018]	Isoelectric Point; IEP[Bellmont, 1993]	Cumulative Surface Charge[Bellmont, 1993] or Zeta Potential at pH 7.4	Grand Average of Hydropathy, GRAVY[4]	Initial Surface Hydrophobicity, Φ_I	(Final) Surface Hydrophobicity, Φ_F	%-/%+	Deformation Energy, Eces as Global Rigidity (Monomer; Mode 7; Default)	Multi-domains / Multi-subunits ?	Aliphatic Index, AI[3]	%Cysteine	% H bond-forming AAs[3]	PTBCS Class
1	Pyruvate dehydrogenase E1 component	aceE	P0AFG8 Y-118a	11.05772565	P	886	0	99.537	5.46	-25.87	-0.440	0.489	0.489	1.09	71.68	Yes	80.72	0.68	9.59	Class 2
2	Dihydrolipoyllysine-residue acetyltransferase component of pyruvate dehydrogenase complex	aceF	P06959 Y-7b9k	6.802311328	P	629	0	65.965	5.09	-18.34	0.001	0.511	0.511	0.96	1.55	No	94.98	0.16	8.90	Class 2
3	Acetate kinase	ackA	P0A6A3 Y-xxxx	2.559599761	P	400	0	43.290	5.85	-10.09	-0.047	0.510	0.510	1.07	325.31	Yes	96.40	1.50	11.50	Class 2
4	Glutamate-pyruvate aminotransferase AlaA	alaA	P0A959 N-4cvq	0.171346107	P	405	0	45.517	5.85	-7.26	-0.163	0.510	0.510	0.80	55.49	Yes	97.06	1.23	8.64	Class 2
5	Chaperone protein DnaJ	dnaJ	P08622 Y-1kpl	0.388195503	P	375	0	40.969	8.02	1.63	-0.641	0.461	0.461	0.61	4.16	Yes	63.97	2.67	8.00	Class 4a
6	Chaperone protein DnaK	dnaK	P0A6Y8 S-4b9q	5.116479153	P	637	0	68.984	4.83	-30.24	-0.412	0.457	0.457	1.05	5.41	No	88.71	0.16	10.83	Class 2
7	Enolase	eno	P0A6P9 N-5dng_H	4.110673378	P	431	0	45.524	5.33	-11.28	-0.162	0.461	0.461	0.78	1416.80	Yes	89.33	0.23	9.98	Class 2
8	Elongation factor G	fusA	P0A6M8 N-3jbe_H	10.84068023	P	703	0	77.450	5.24	-24.04	-0.289	0.477	0.477	0.98	35.74	No	85.87	0.43	9.53	Class 2
9	Glutamate decarboxylase alpha	gadA	P69908 Y-1wey	0.111111111	P	466	0	52.685	5.22	-14.41	-0.278	0.535	0.535	1.04	9.15	Yes	80.64	2.15	7.94	Class 3
10	Glyceraldehyde-3-phosphate dehydrogenase A	gapA	P0A9B2 N-6ubm	6.245508621	P	330	0	35.401	6.67	-1.36	-0.139	0.475	0.475	0.73	917.24	Yes	87.76	0.91	12.73	Class 2
11	Translation initiation factor IF-2	infB	P0A705 Y-6o9k	2.231787884	P	890	0	97.350	5.80	-14.03	-0.533	0.441	0.441	0.74	1.30	No	83.55	0.34	9.66	Class 2
12	2-dehydro-3-deoxyphosphooctonate aldolase	kdsA	P0A715 N-1g7v	0.330543328	P	284	0	30.833	6.35	-2.36	-0.028	0.499	0.499	0.88	151.97	Yes	91.30	1.41	7.75	Class 3

Table S III-17 [Part 2 of 2] Continued

No.	Recommended Protein/Peptide Name	Recommended Abbreviation After UniProt[Apweiler et al., 2004; The-UniProt-Consortium,2018]	UniProt Entry, Homology Modeling Status[Y=Yes, S=Semi, N=No]-(Main) PDB ID (_Chain, if applicable)	Protein Weight, Average/Cell (fg)	Type (Physiologic [P]-Patologic [Pa] or Therapeutic [T]?)	Full-Length of Mature Protein‡ (Amino Acids; AAs)	Number of Glycosylation Sites	Molecular Weight from Amino Acid Analysis (kDa) [Apweiler et al., 2004; The-UniProt-Consortium, 2018]	Isoelectric Point, *IEP* [Bjellqvist, 1993]	Cumulative Surface Charge[Bjellqvist, 1993] or Zeta Potential at pH 7.4	Grand Average of Hydropathy, *GRAVY*[4]	Initial Surface Hydrophobicity, Φ_I	(Final) Surface Hydrophobicity, Φ_f	%-/%+	Deformation Energy, E_{DefG} as Global Rigidity (Monomer; Mode 7; Default)	Multi-domains / Multi-subunits ?	Aliphatic Index, *AI*[3]	%Cysteine	% H bond-forming AAs[3]	PTBCS Class
13	Dihydrolipoyl dehydrogenase	lpdA	P0A9P0 Y-4jdr	3.776849446	P	473	0	50.557	5.79	-10.15	-0.015	0.477	0.477	0.78	172.67	Yes	98.35	1.06	8.46	Class 3
14	Cell shape-determining protein MreB	mreB	P0A9X4 Y-xxxx	0.693616137	P	347	0	36.952	5.17	-10.33	0.057	0.517	0.517	0.91	470.89	No	98.33	0.86	10.37	Class 2
15	Outer membrane protein A	ompA	P0A910 Y-3nb3_A	12.82533471	P	325	0	35.172	5.60	-5.37	-0.444	0.545	0.545	0.90	319.46	Yes	74.43	0.62	11.38	Class 4a
16	Outer membrane porin C	ompC	P06996 Y-2j1n	10.96238388	P	346	0	38.308	4.48	-15.49	-0.660	0.540	0.540	1.77	421.32	Yes	60.61	0.00	11.56	Class 4a
17	DNA-directed RNA	rpoA	P0A7Z4 Y-5ezk_A	2.887484769	P	329	0	36.512	4.97	-18.25	-0.228	0.491	0.491	1.08	0.43	Yes	106.93	1.22	10.94	Class 1
18	DNA-directed RNA	rpoB	P0A8V2 N-5uac_C	4.041051742	P	1342	0	150.632	5.14	-44.05	-0.394	0.494	0.494	1.06	15.91	No	90.76	0.52	9.99	Class 2
19	DNA-directed RNA polymerase subunit beta'	rpoC	P0A8T7 Y-6rh3_D	4.522517066	P	1407	0	155.160	6.69	-4.19	-0.240	0.491	0.491	0.73	17.48	No	95.10	1.07	10.52	Class 2
20	Threonine--tRNA ligase	thrS	P0A8M3 Y-1qf6	1.48663634	P	642	0	74.014	5.80	-17.00	-0.494	0.459	0.459	0.92	10.67	Yes	79.58	2.02	8.41	Class 3
21	Trigger factor	tig	P0A850 N-1w26	5.572955543	P	432	0	48.193	4.83	-23.40	-0.428	0.456	0.456	1.24	10.34	No	88.24	0.00	7.64	Class 3
22	Thiol peroxidase	tpx	P0A862 N-3hvs	1.405946781	P	167	0	17.704	4.75	-5.49	0.246	0.517	0.517	1.11	4188.77	Yes	102.81	1.80	13.17	Class 1
23	Elongation factor Ts	tsf	P0A6P1 N-1efu_A	4.805428293	P	282	0	30.292	5.22	-9.38	-0.125	0.472	0.472	1.03	11.10	Yes	92.06	0.71	7.45	Class 3
24	Uncharacterized tRNA/rRNA methyltransferase YfiF	yfiF	P0AGJ5 Y-xxxx	0.247767396	P	345	0	37.784	8.94	4.72	-0.682	0.425	0.425	0.58	0.32	No	67.57	1.16	11.01	Class 4a

8.1.2. Supplemental Figures

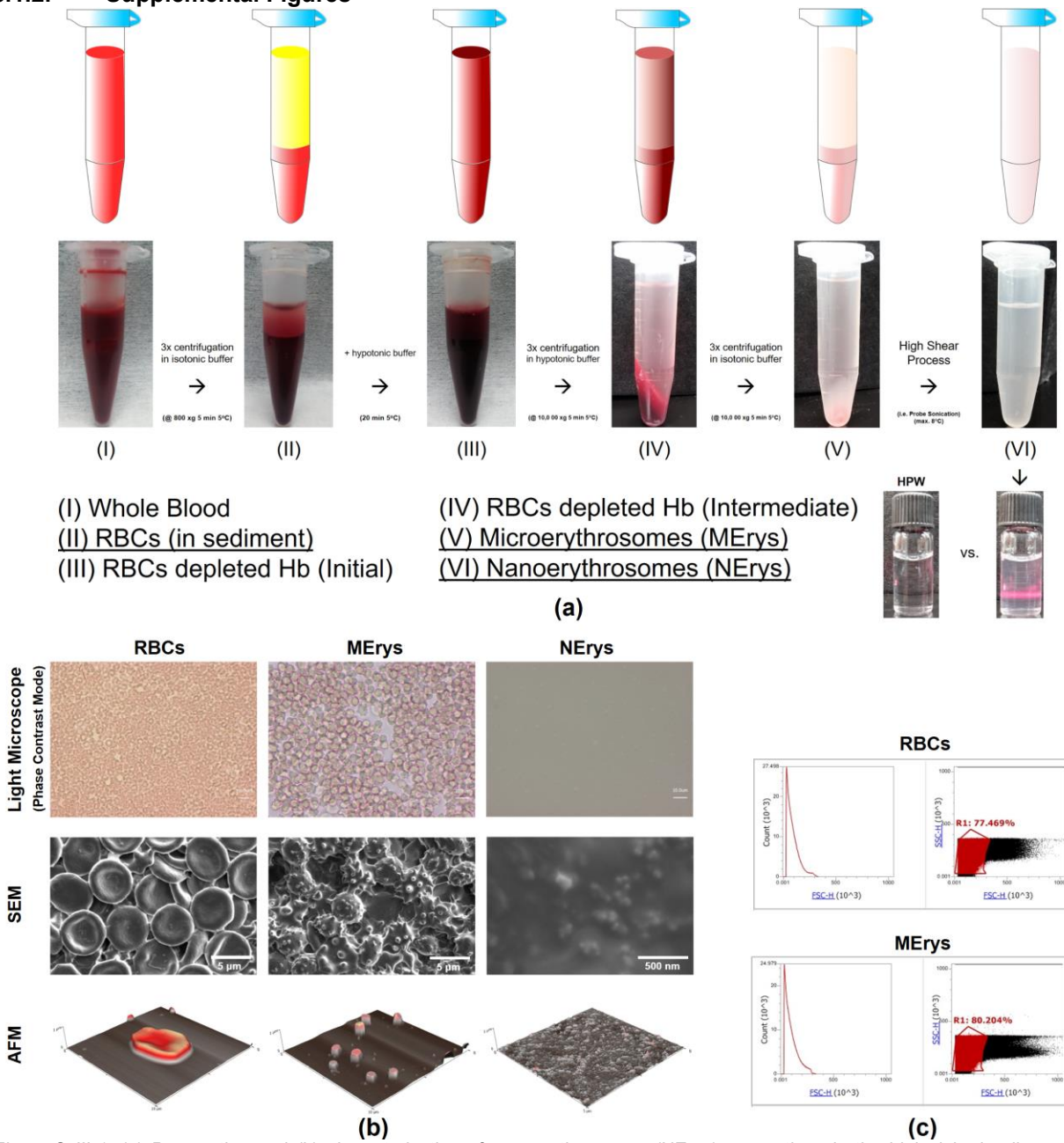

Figure S III-1. (a) Preparation and (b) characterization of nanoerythrosomes (NErys) as coatings in the bioinsipired cell membrane-coated nanoparticles (BCCN)s, which are derived from RBCs and microerythrosomes (MErys), respectively. (c) Flow cytometry histograms and density dot plots of RBCs and MErys.

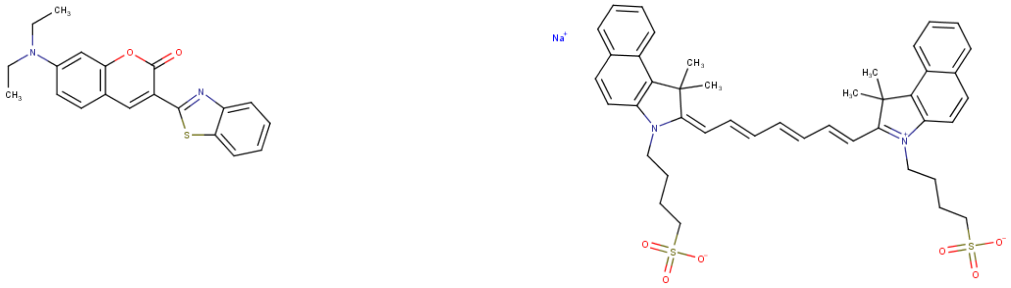

(a) (b)

Figure S III-2. Molecular structures of (a) Coumarin-6 (Cou6) and (b) Indocyanine Green (ICG).

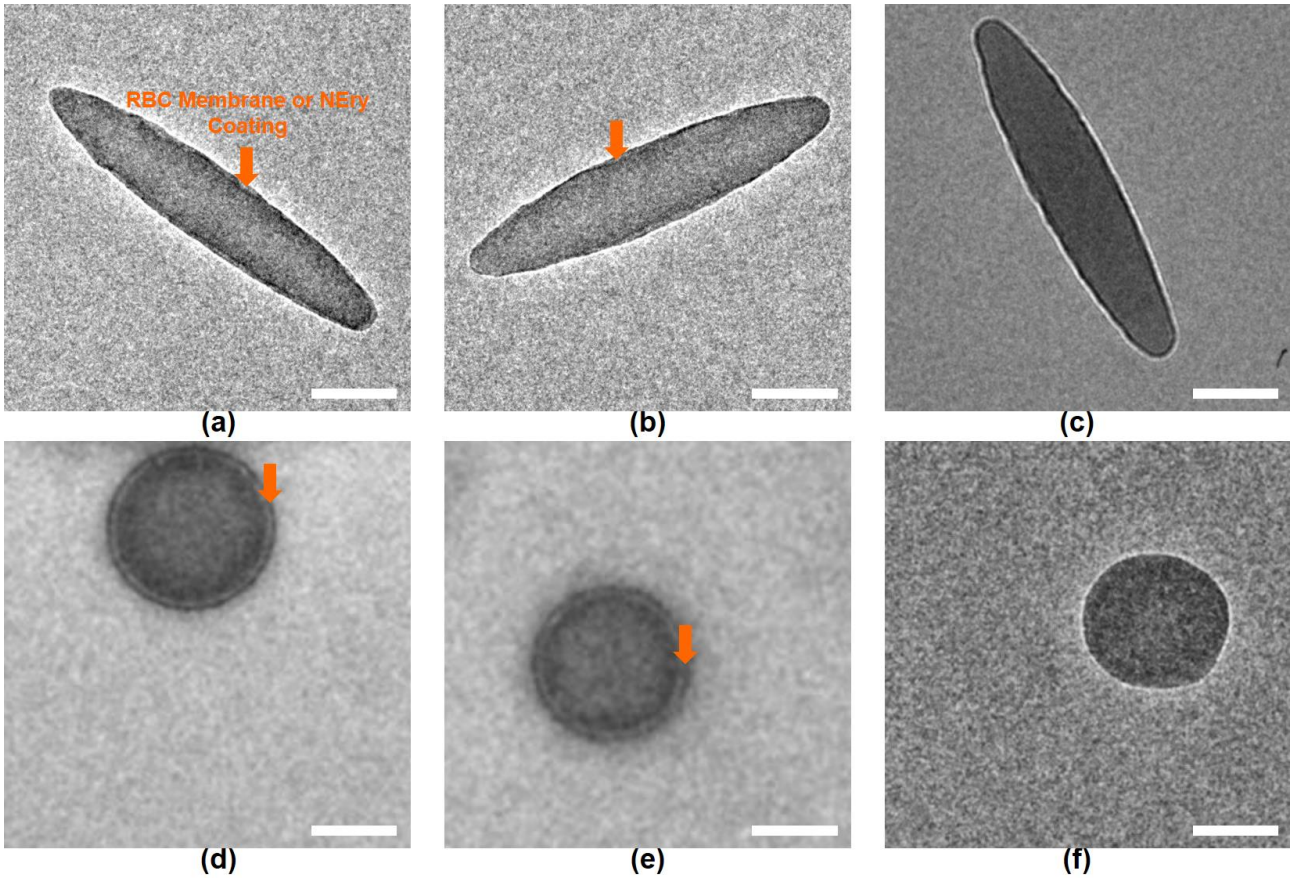

Figure S III-3. Transmission electron micrographs of spherical (a-c) and non-spherical (d-f; 3-fold stretching factor) nanoparticles with further details: (a), (b), (d), (e) are BCCNs, while (c) and (f) are CNPs. Nanoparticles in panels: (a) and (d) are loaded with coumarin-6, whilst the rest are unloaded. Scale bars = 100 nm.

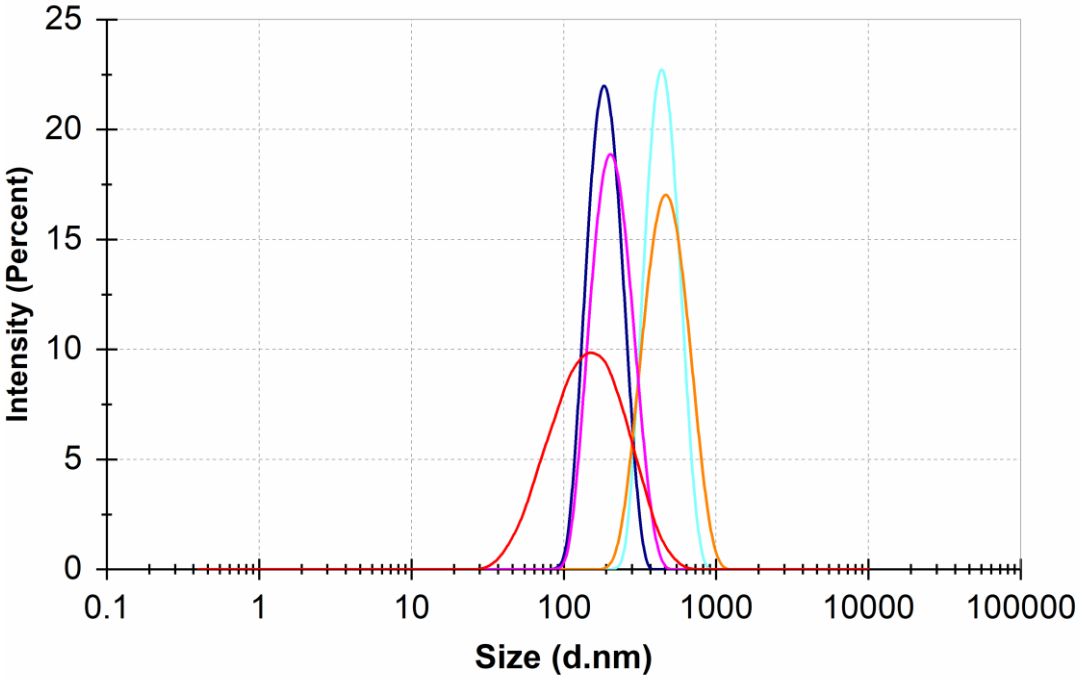

(a)

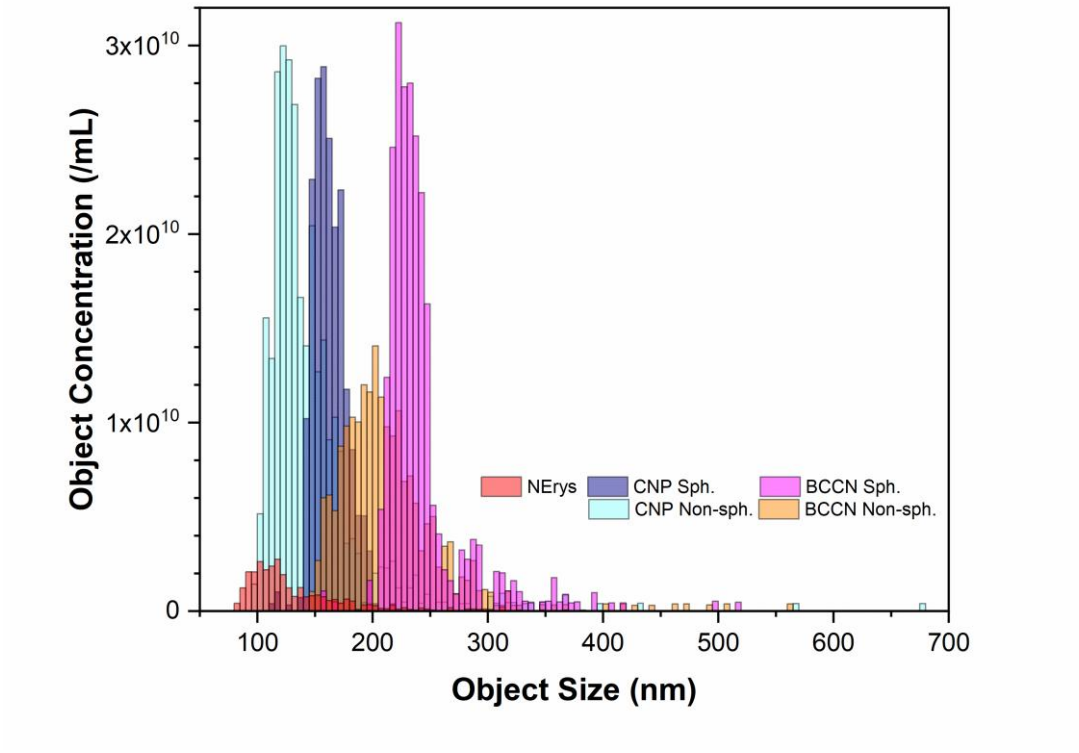

(b)

Figure S III-4. (a) Intensity size distribution of NErys (RBC cell membrane), various shapes of CNPs (core nanoparticles), and BCCNs (bioinspired cell membrane-coated nanoparticles, measured by DLS (Dynamic Light Scattering). (b) Size histogram of the same samples as in panel (a), measured by TRPS (Tunable Resistive Pulse Sensing). Thus, the same color legend applies to all panels. All results here are in good agreements with the results from microscopies (SEM, TEM, and AFM). For clarity, non-spherical nanoparticles (both CNPs and BCCNs) are exemplified by prolate ones (3-fold stretching factor) and PEGylated ones are not shown.

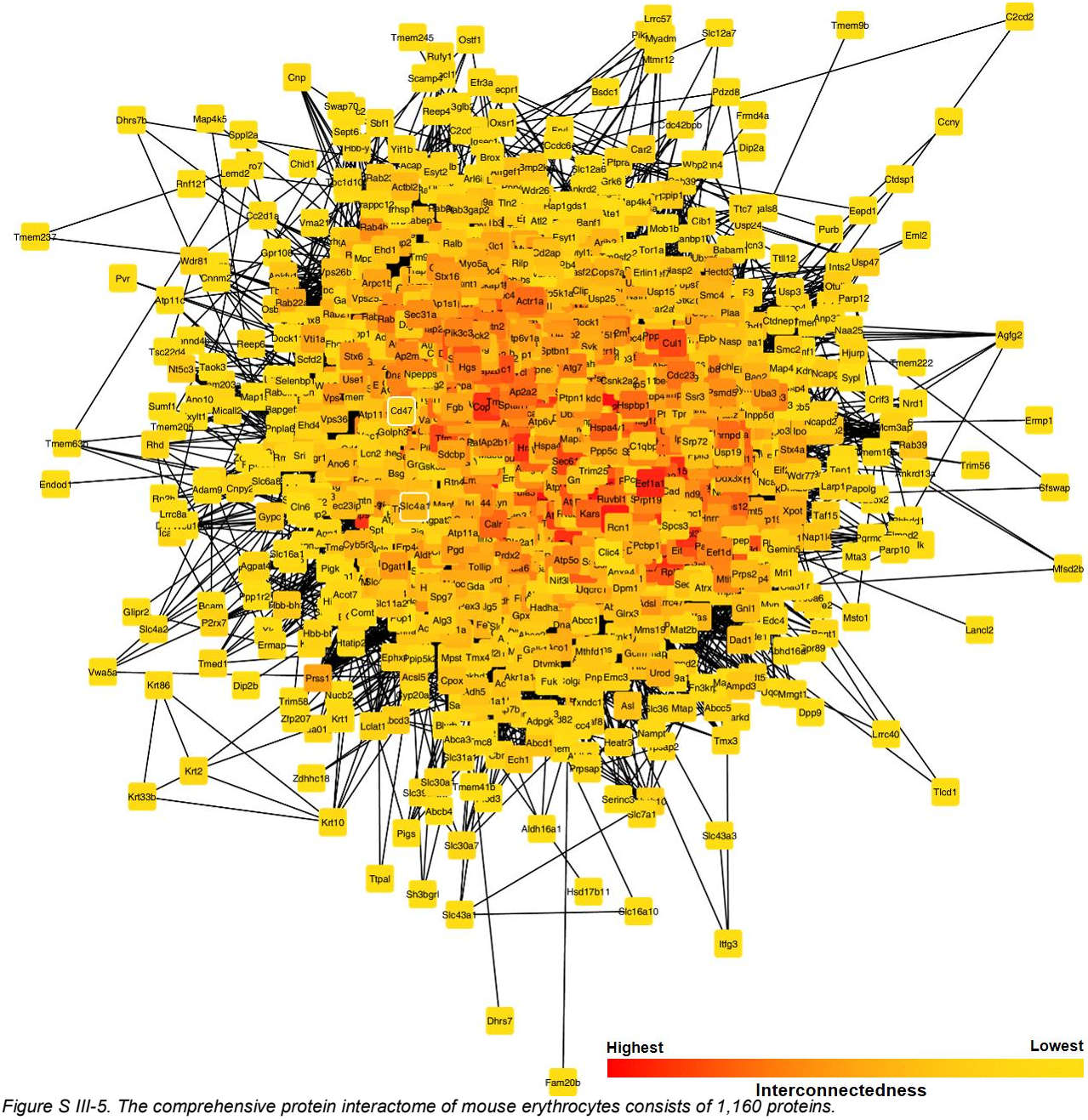

Figure S III-5. The comprehensive protein interactome of mouse erythrocytes consists of 1,160 proteins.

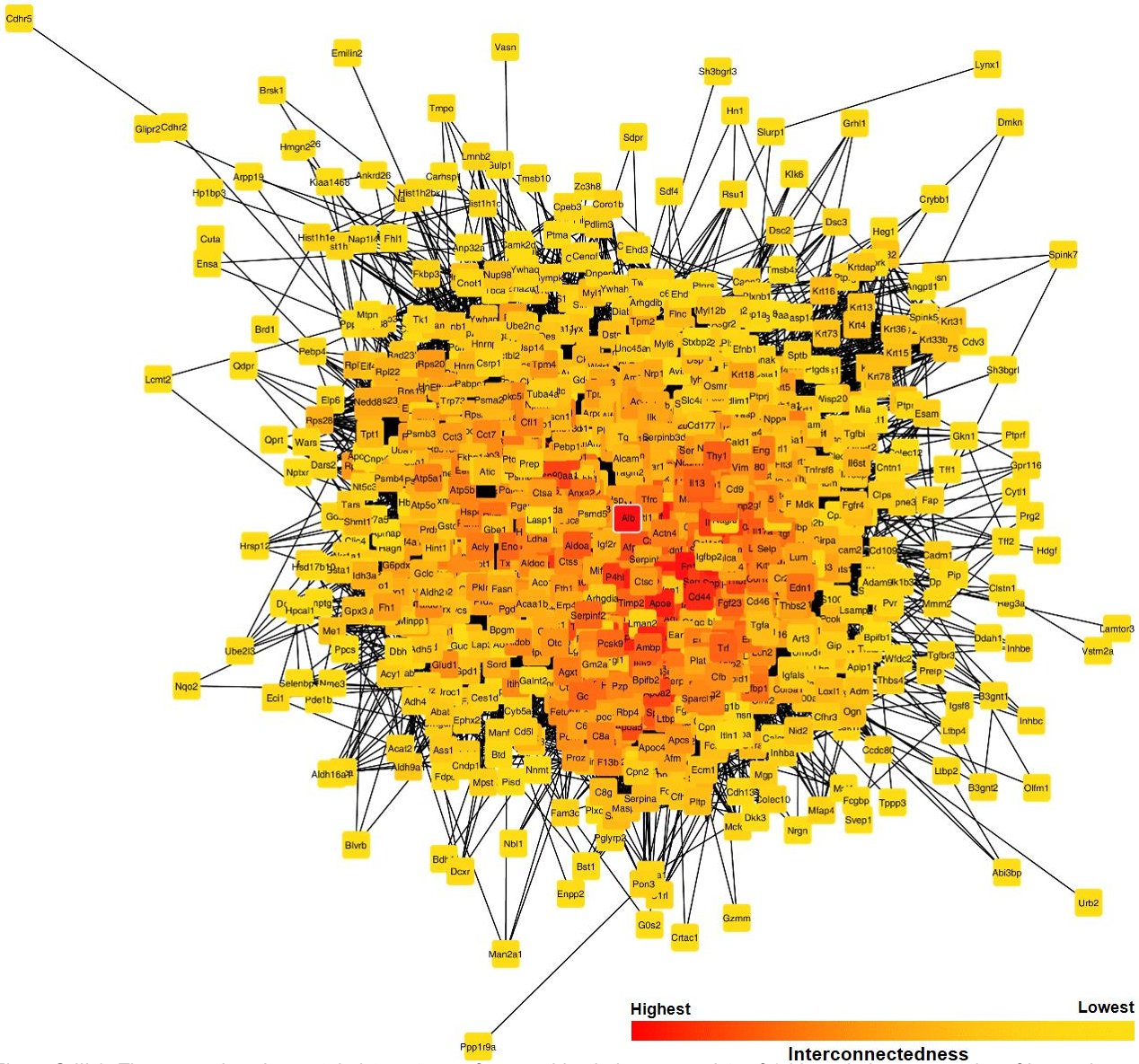

Figure S III-6. The comprehensive protein interactome of mouse blood plasma consists of 1,237 orthologous proteins of known human blood plasma protein concentrations as reported elsewhere[134, 135].

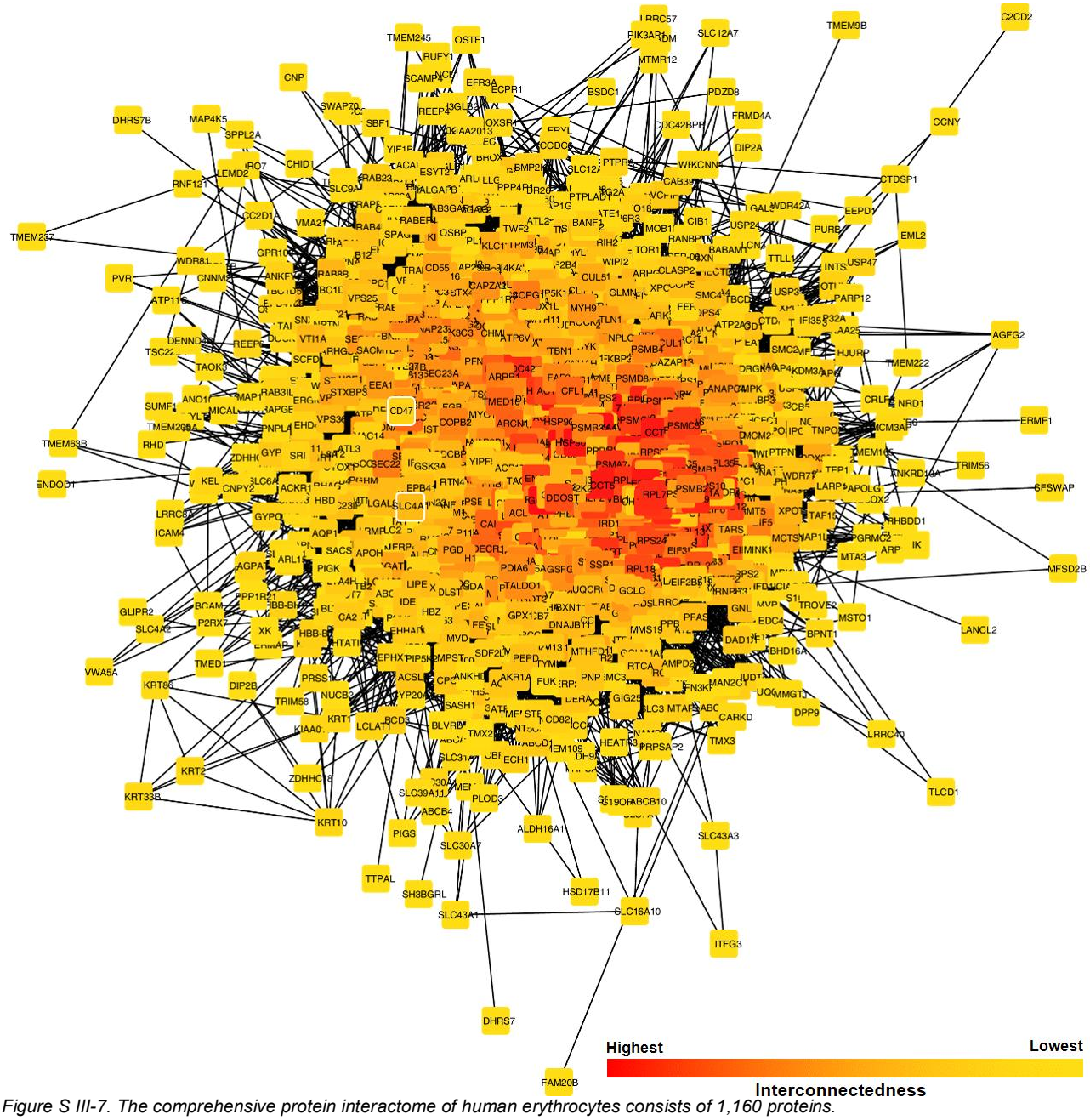

Figure S III-7. The comprehensive protein interactome of human erythrocytes consists of 1,160 proteins.

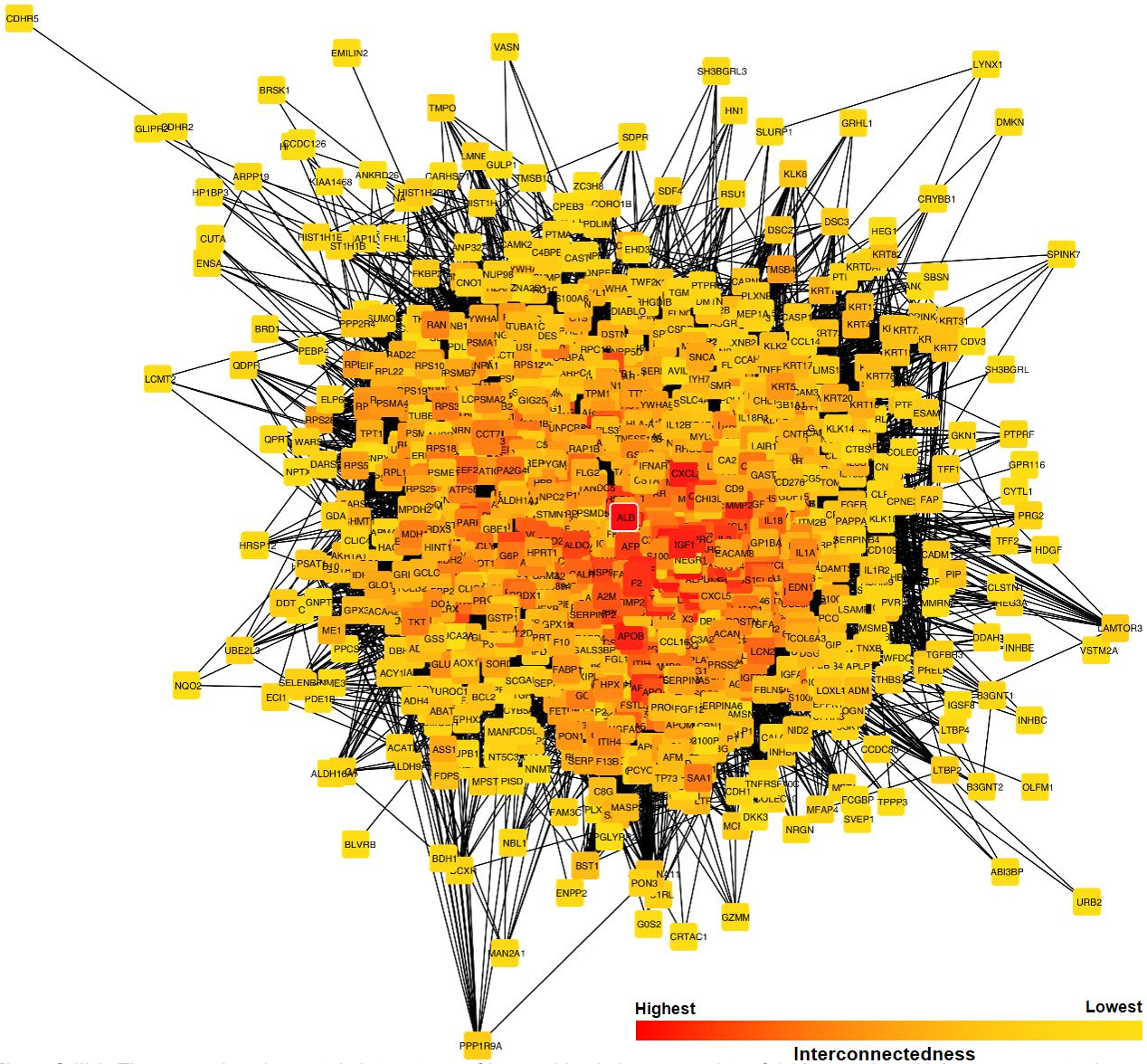

Figure S III-8. The comprehensive protein interactome of human blood plasma consists of 1,237 proteins with known concentrations as reported elsewhere[134, 135].

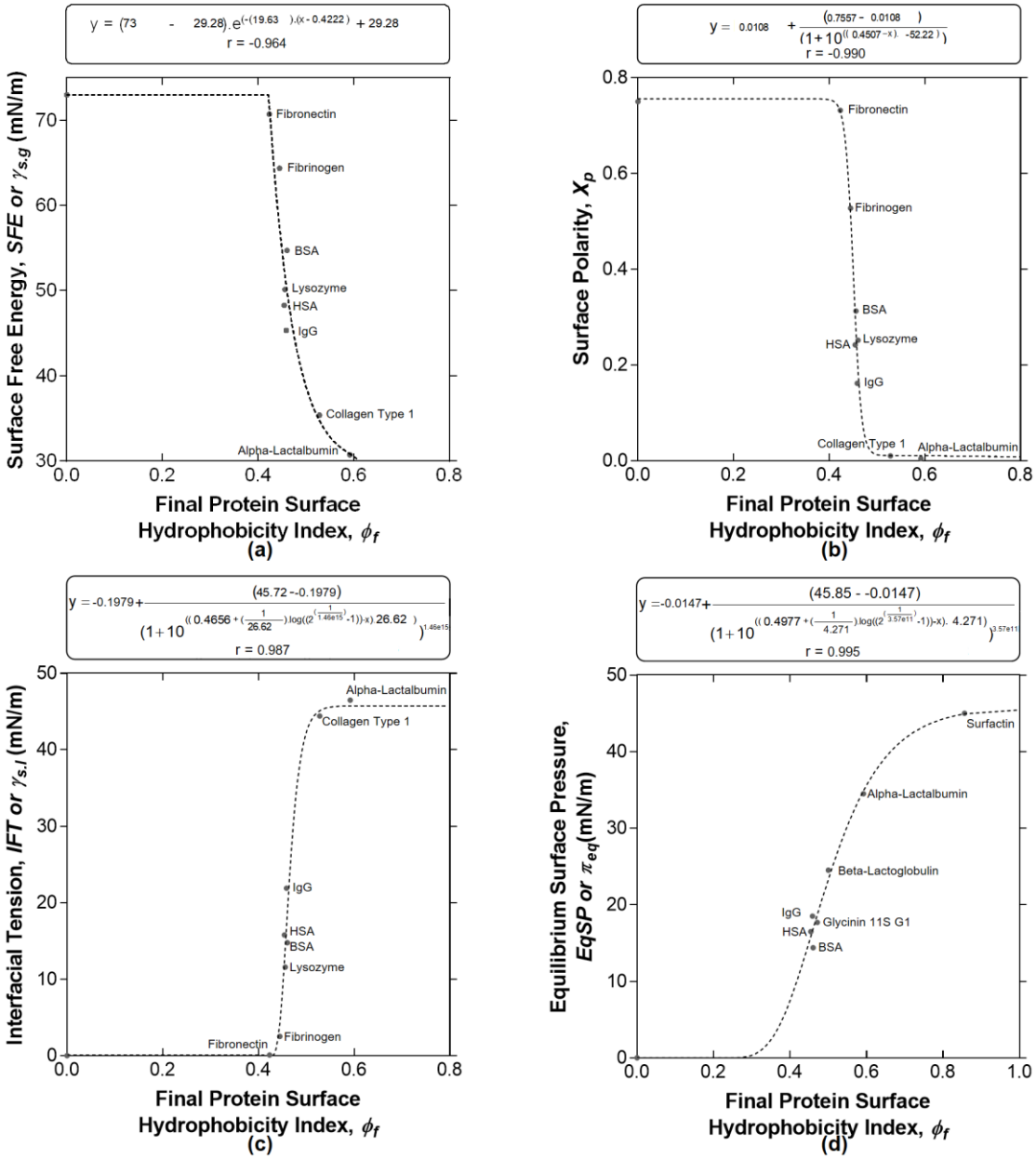

Protein Name	Main PDB ID	UniProt ID	Experimental Data Availability	
			SFE, Xp & IFT	EqSP
Surfactin	2NPV	N/A	No	Yes[145]
Collagen Type I	3HR2	P02454 & P02466	Yes[220]	No
Alpha-Lactalbumin	1A4V	P00709	Yes	Yes[221]
Beta-Lactoglobulin	1CJ5	P02754	No	Yes[222]
Glycinin 11S G1	1FXZ	P04776	No	Yes[222]
IgG	1HZH & 1IGT	P01857 & P01834	Yes[33]	Yes[223]
HSA	1AO6	P02768	Yes[33]	Yes
BSA	4F5S	P02769	Yes	Yes[222]
Lysozyme	3WUN	P00698	Yes[33]	No
Fibrinogen	3GHG	P02671, P02675, & P02679	Yes[178]	No
Fibronectin	1FNF	P02751	Yes[178]	No

(e)

Figure S III-9. Mathematical relations between the computational values of final protein surface hydrophobicity index (Φ_f) based on the Cowan-Whittaker hydrophobicity scale and the experimental values of common protein's (a) surface free energy—SFE or $\gamma_{s.g}$, (b) surface polarity—Xp, (c) (i.e. protein) material-water interfacial tension—$IFT_{1.3}$ or $\gamma_{s.l}$, and (d) equilibrium surface pressure—EqSP. (e) Details of proteins and correlated PDB IDs(-UniProt ID) thereof, which were used in calculations of protein surface hydrophobicity indices. Unless reference(s) specified for the available values of SFE-X_p-IFT and EqSP, experimental data is obtained from the recent study.

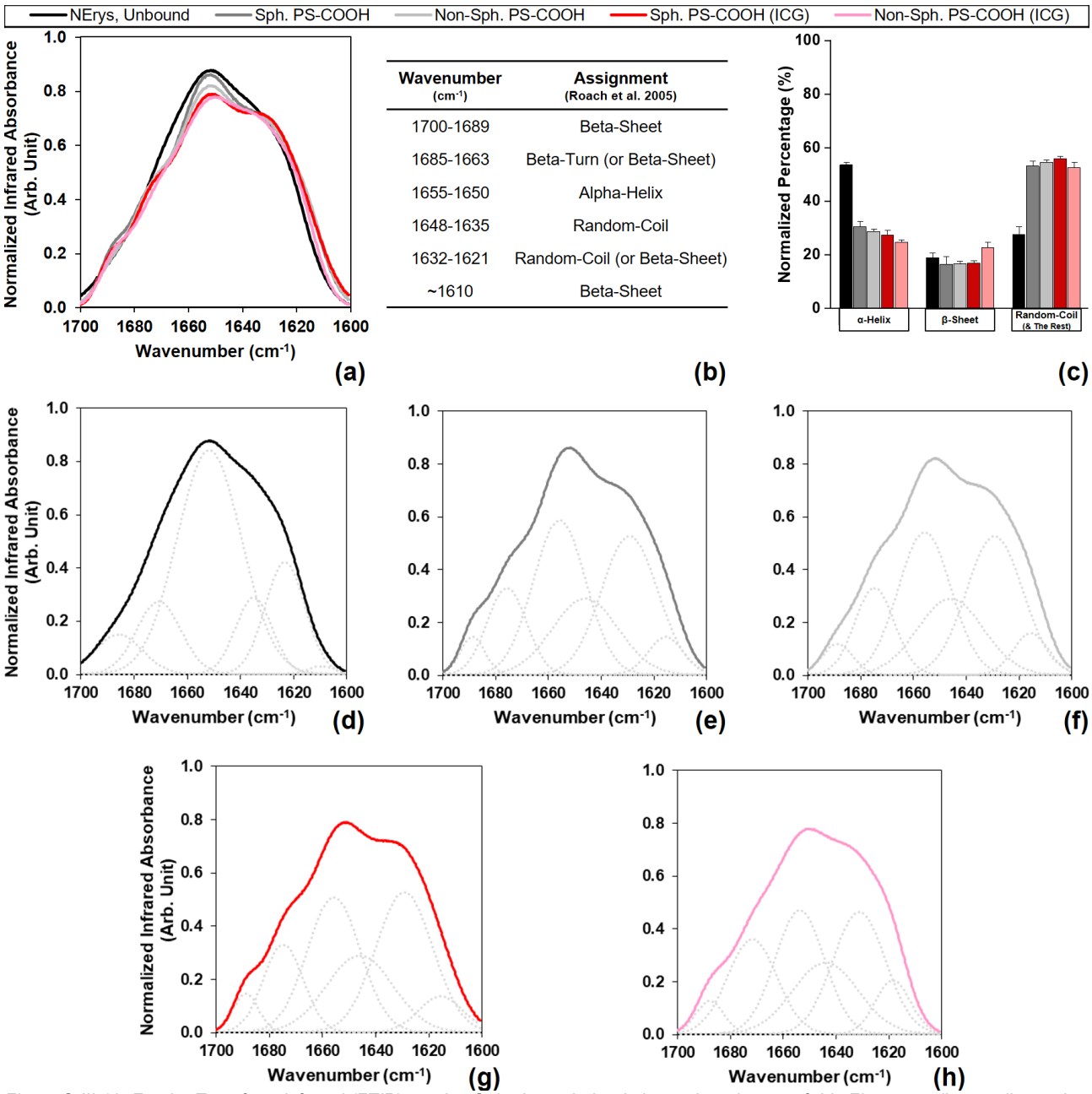

Figure S III-10. Fourier Transform Infrared (FTIR) results. Color legend, that is located on the top of this Figure, applies to all samples. (a) Comparative FTIR absorbance spectra of various samples, which are subjects of (b) the assignment of protein secondary structures. (c) Summarized protein secondary structures of the deconvoluted FTIR absorbance spectra from NErys containing samples in the different states: (d) unbound, adsorbed on fluorescently (e) unloaded spherical BCCNs, (f) unloaded non-spherical BCCNs, (g) ICG loaded spherical BCCNs, and (h) ICG loaded non-spherical BCCNs.

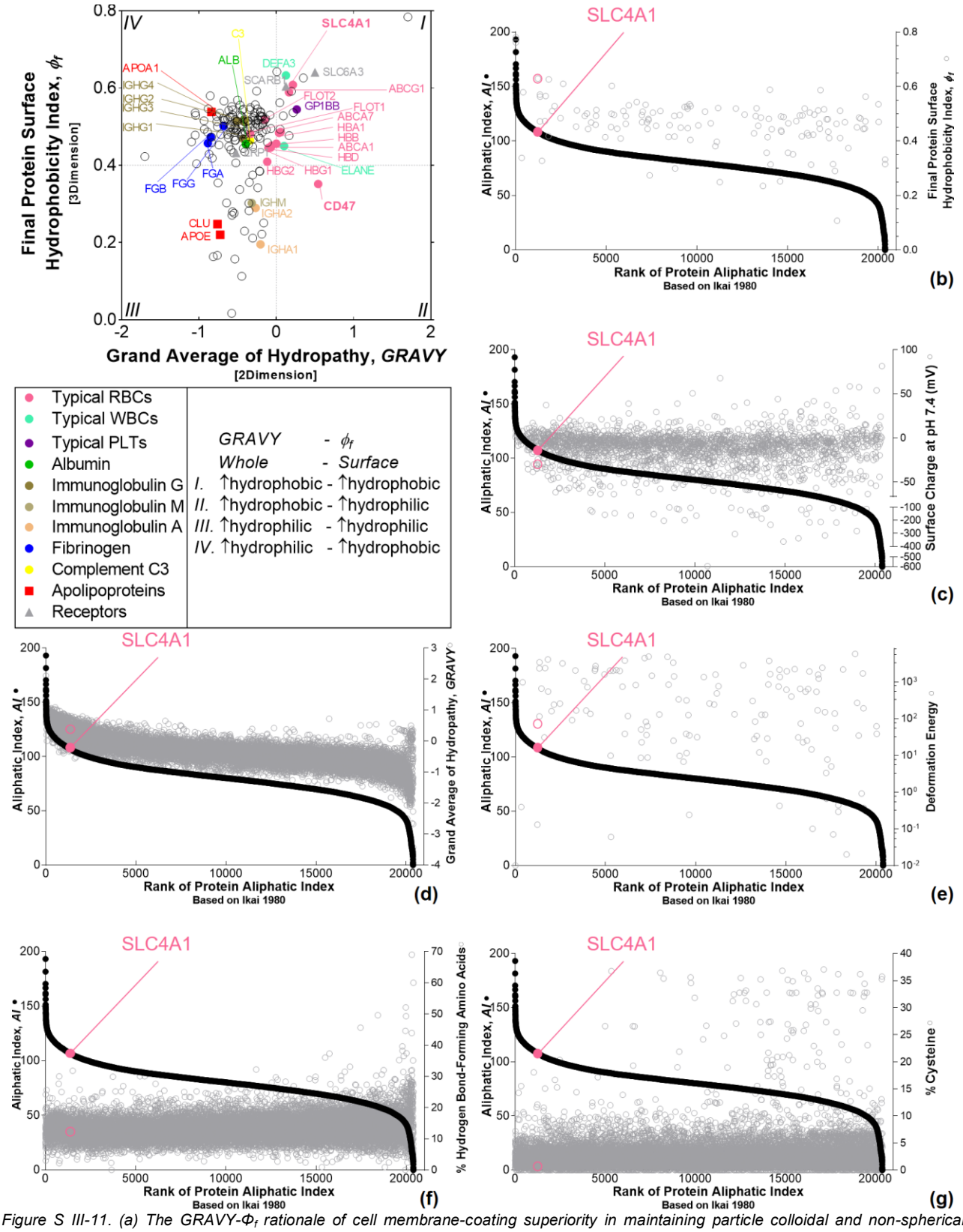

Figure S III-11. (a) The GRAVY-Φ_f rationale of cell membrane-coating superiority in maintaining particle colloidal and non-spherical shape stability. The former shows a statistically significant correlation with proteins' melting temperature, one of the most common biophysical parameters describing conformational stability (Figure S III-14); while the latter demonstrates a very strong correlation with interfacial stability and parameters (Figure S III-9). Rank and value of reviewed, canonical human proteins' aliphatic index based on Ikai 1980[53] versus other parameters (b) final protein surface hydrophobicity index, Φf, (c) surface charge at pH 7.4, (d) Grand Average of Hydropathy, GRAVY, (e) deformation energy, (f) %hydrogen bond-forming amino acids (%serine+%threonine [mol/mol]), and (g) %cysteine [mol/mol]. The relative position of SLC4A1 (Band 3) is indicated in each panel from (b)-(g).

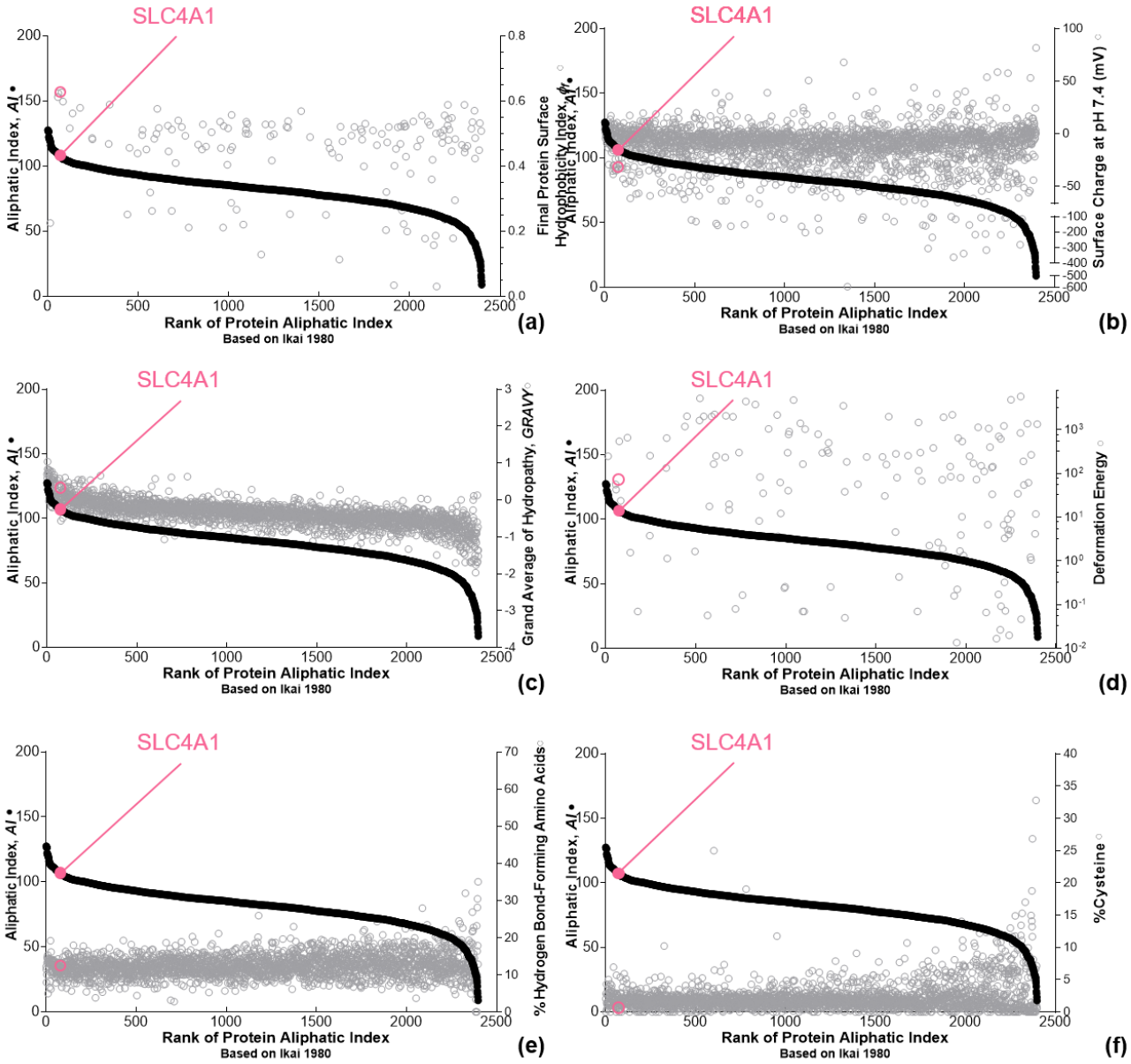

Figure S III-12. These panels are the focused on 2,397 proteins involving known protein concentrations[116, 134, 135]. All corresponding panels here (in order) are directly comparable/zoomed-in versions of panels (b)-(g) in Figure S III-11.

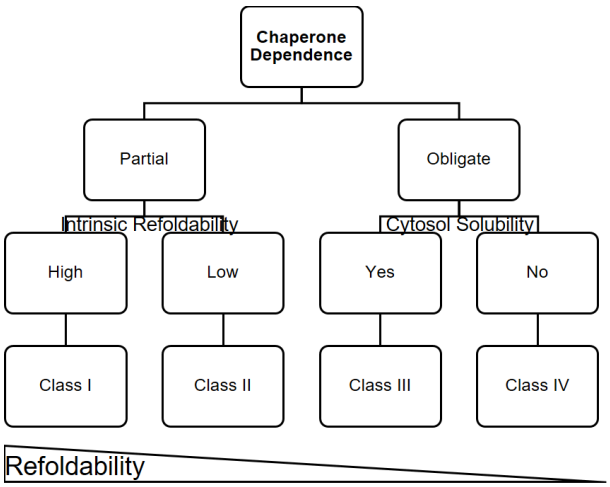

(a)

p< 0.05 by Chi-Square Test (i.e. 6 x 10^{-4})

PTBCS \ Kerner-Fujiwara	Class I	Class II	Class III	Class IV
Class 1	1	0	0	0
Class 2	8	5	0	0
Class 3	3	3	0	2
Class 4a	0	0	2	0
Class 4b	0	0	0	0

(b)

Figure S III-13. (a) Overview of experimental protein refoldability classification after Kerner-Fujiwara[143]. (b) Statistically comparable relationship between PTBCS and Kerner-Fujiwara classification. The list and further details of compared proteins (24 typical Escherichia coli proteins) are listed in Table S III-17.

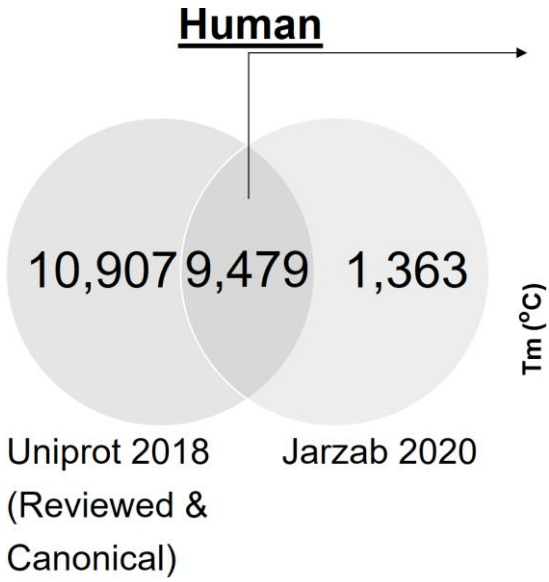

(a)

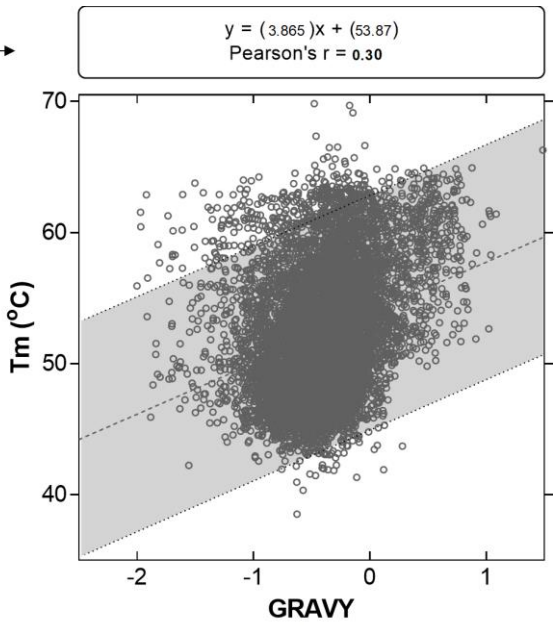

(b)

Figure S III-14. (a) Basis of bioinformatics analysis used in the following panel (b), involving 9,479 reviewed human proteins from elsewhere[42, 224]. (b) A statistically significant positive correlation between GRAVY and experimental proteins' melting temperature (Pearson's r = 0.30; p < 0.0001).

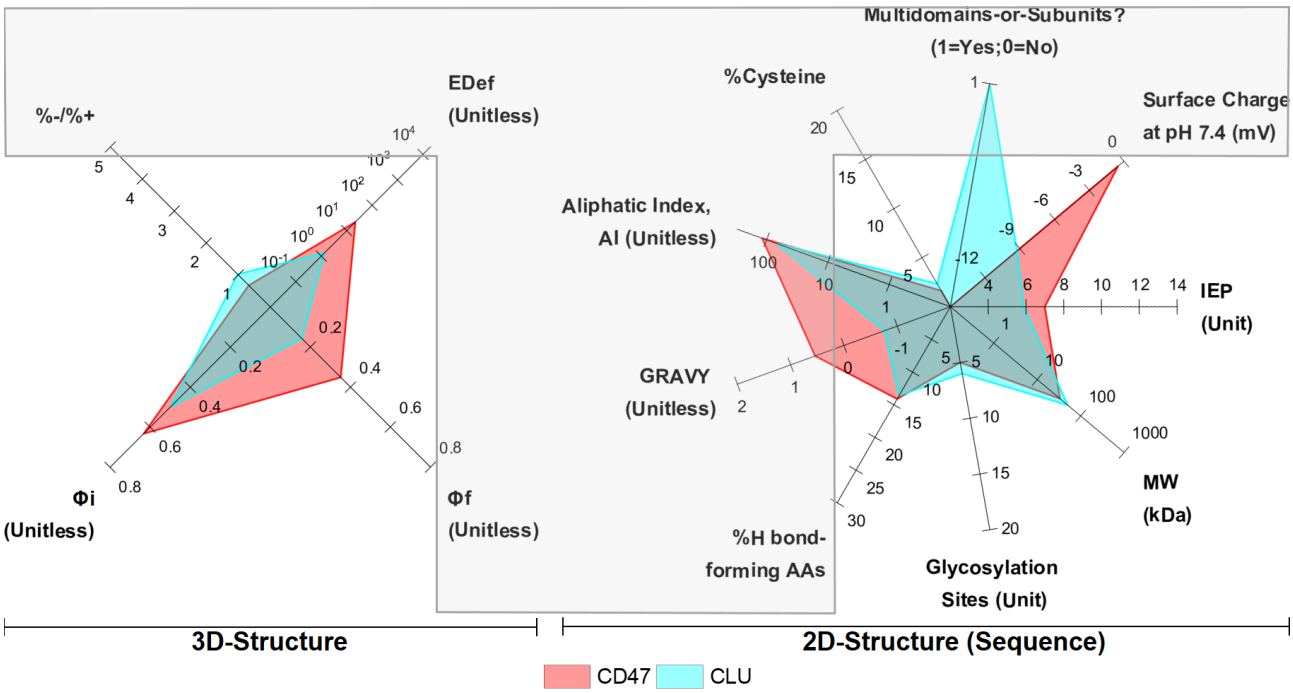

Figure S III-15. Illustration of detailed comparison between CD47 and Clusterin (CLU) involving all 13 parameters used in the PTBCS algorithm, both mature protein's 2D and 3D structures (4 and 9 parameters from left and right, respectively). These and other protein data, discussed in the text, are distributed separately according to the discussion topic in Table S III-3, Table S III-4, Table S III-5, Table S III-6, and Table S III-9. The 9 parameters (highlighted in gray) are explicitly shown in the PTBCS algorithm in Figure III-10.

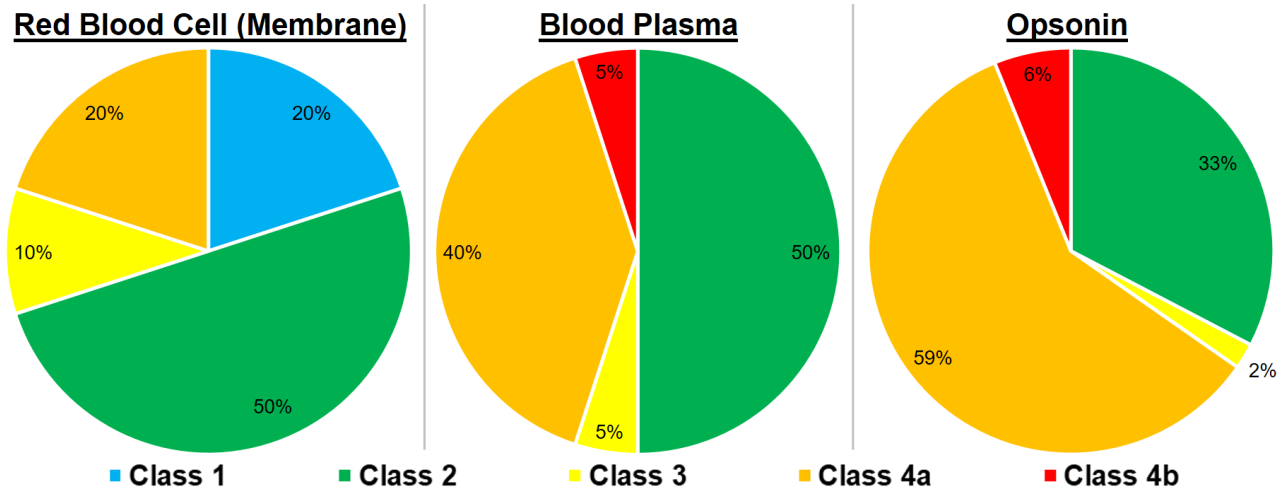

Figure S III-16. Application of Physiological-Therapeutic Biologics Classification System (PTBCS) to the exemplary proteins from three different natures: red blood cell membrane, blood plasma, and opsonin. The tabularized version and more complete data are available in Table S III-4, Table S III-5, and Table S III-6, respectively.

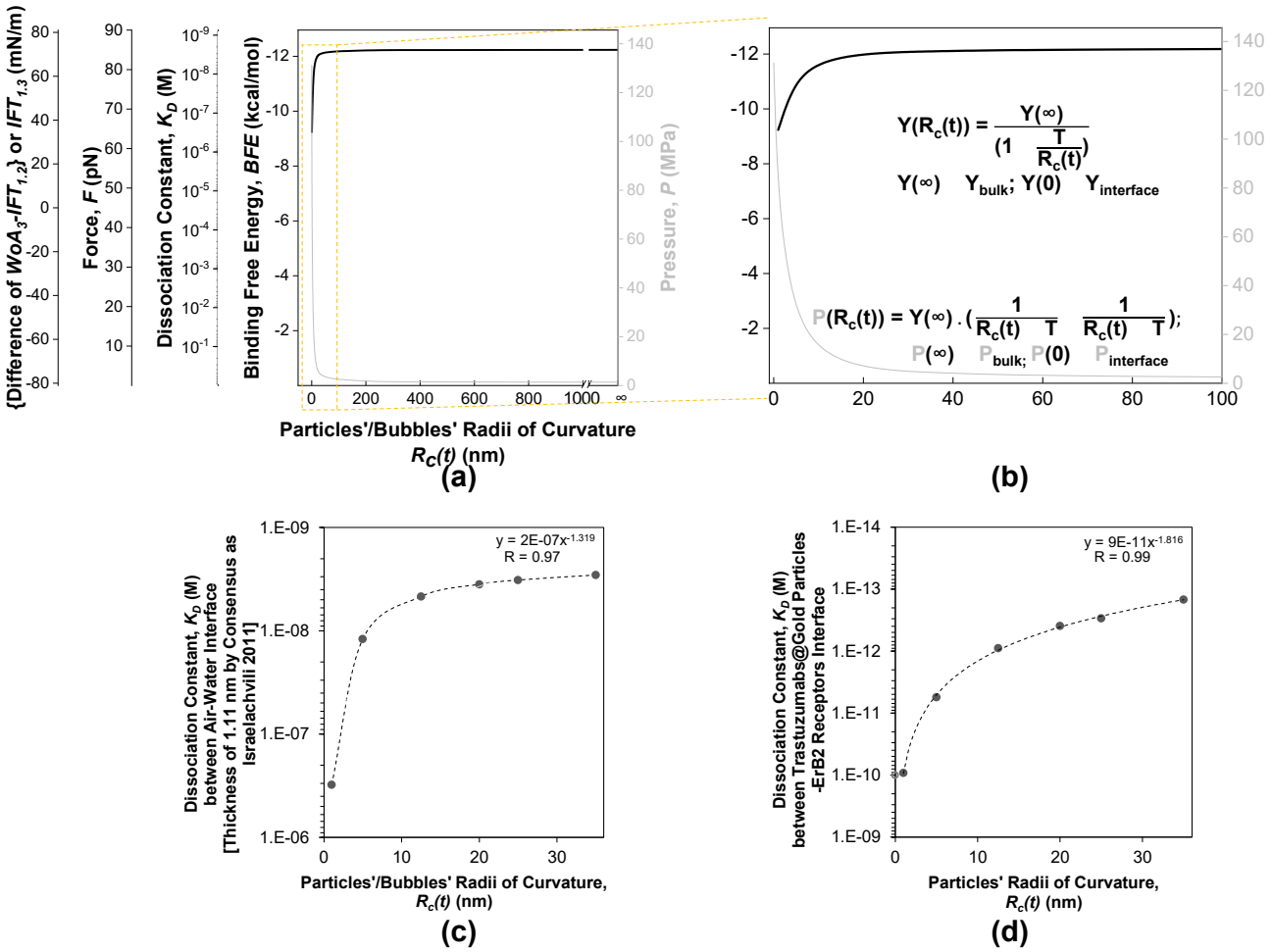

Figure S III-17. (a) Confinement effects alter considerably energy-related units at interfaces / interaction areas, i.e. binding affinities, as a function of the radius of curvature. This occurs over sizes / radii of curvature, specifically at lower radius radii, as zoomed-in panel (b) containing the adapted theoretical equations[181]; where T = interfacial thickness (in nm; which is experimentally justifiable, ranging from 0.3 - 30 nm), depending on what and how the orientation of the interacted molecules at interfaces. The binding affinities can be obtained from various methods, both experimental and computational laboratory methods, with the overview of the used ones herein in Figure III-7a. They are interconvertible, thereby enabling a direct comparison. For conversion calculation of (Difference of WoA_3-$IFT_{1.2}$)-or-$IFT_{1.3}$, Force and Pressure, the given graphs are exemplified using an air-water interface having surface tension (i.e. $IFT_{1.3}=\gamma_{g.l}$=) 72.8 mN/mm with the interfacial thickness of 1.11 nm (by consensus[181]). This interfacial thickness allows an excellent explanation for proteins' partial unfolding (or also called partial denaturation) behavior during and after their exposure to the air-water interface through a force of about 80.81 pN (corresponding to about 40% of the wholly unfolding force at 200 pN[225]), leading to the commonly-found aggregation of partially unfolded proteins. Interestingly, the theoretical equations appear to correlate strongly with the power function mathematical model visualized in panel (c), which also even better describe the experimental result[17] in panel (d). For further theoretical discussions and experimental proofs of confinement effects occurring importantly on any materials and interfaces, other literature is highly referred[16, 226].

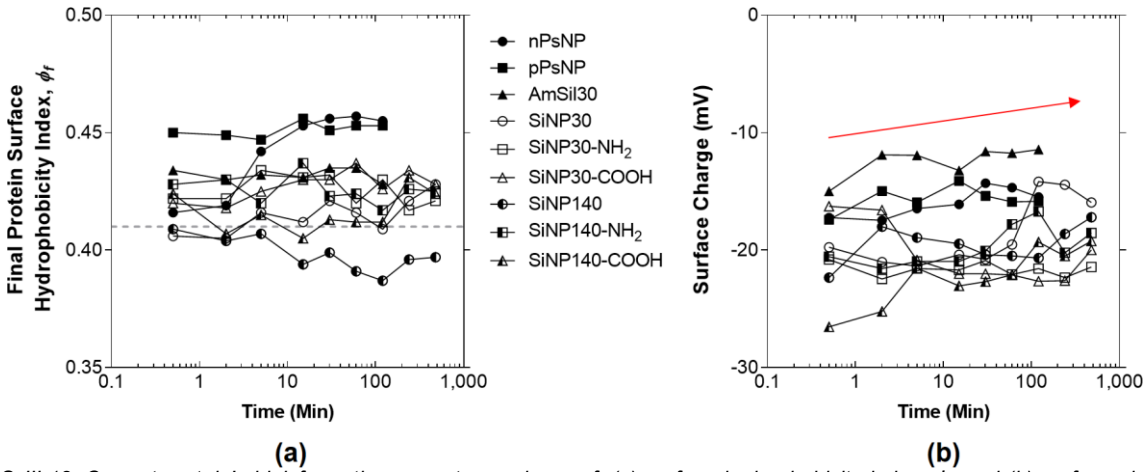

Figure S III-18. Current protein's bioinformatic parameter analyses of: (a) surface hydrophobicity index, Φ_f and (b) surface charge (or also called zeta potential) of nanoparticles used in reference[227]. Legend nomenclature: commercial silica nanoparticles (AmSil30), laboratory-synthesized silica nanoparticles (SiNP), and laboratory-synthesized polystyrene nanoparticles (Ø ≈120 nm); followed by size (Ø in nm) and functional group, if applicable. The legend in panel (a) applies until panel (b). The gray dashed line in panel (a) displays the cut-off value (Φ_f 0.410), while the red arrows in panel (b) show the trend.

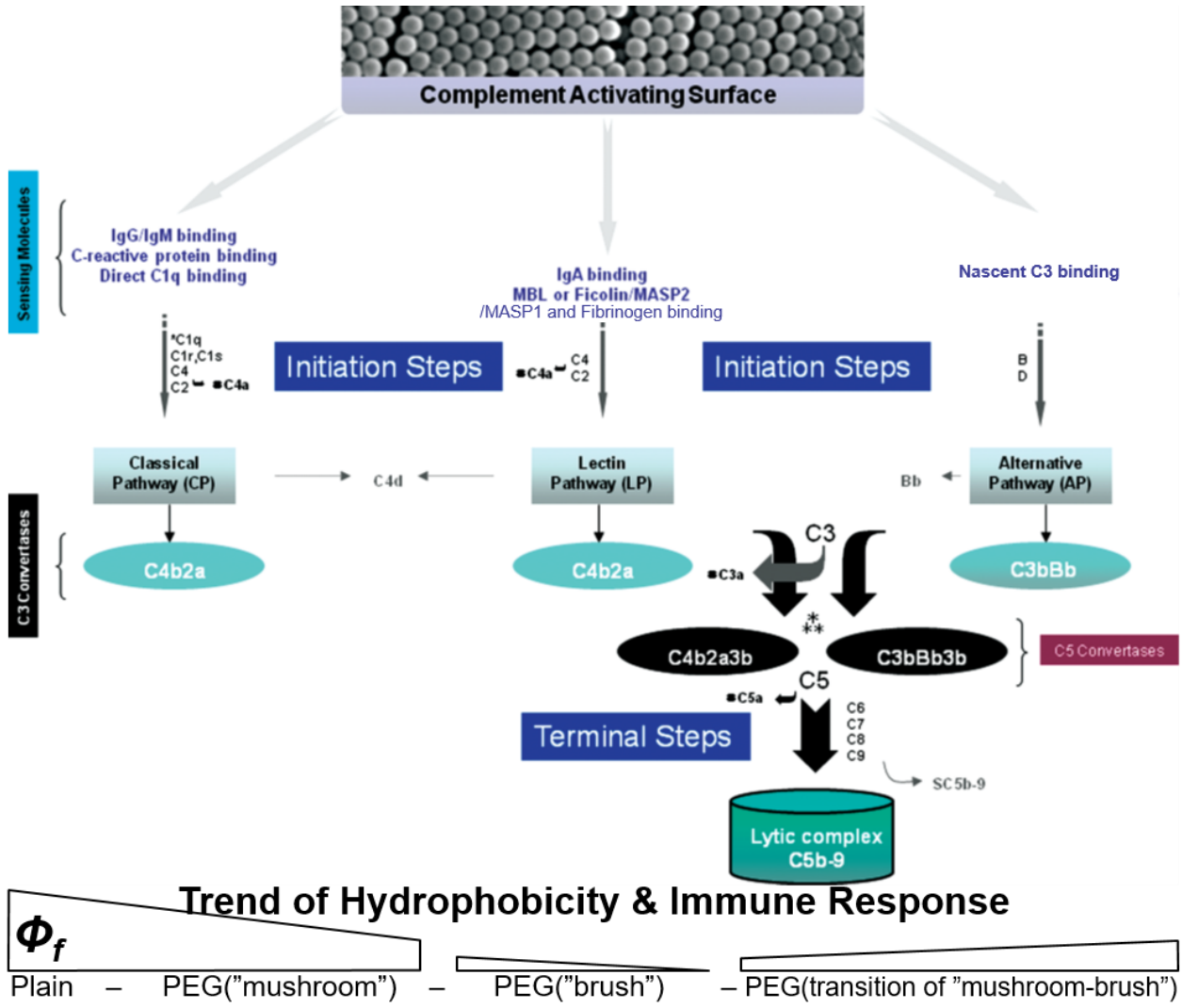

Figure S III-19. The correlation of complement activation pathways and their corresponding drug delivery system's biophysicochemical characteristics, including protein corona properties, consisted of the final protein surface hydrophobicity index, Φ_f. It reveals that these pathways use systematically different Φ_f of sensing molecules (or also called opsonins) proportionally according to the hydrophobicity of drug carriers (e.g. particles). For foremost instance, the descending order of Φ_f is C-reactive protein > IgG > C3 > Fibrinogen, Intact > IgA, Intact (0.521 > 0.459 > 0.456 > 0.444 > 0.413), which is in excellent agreements with both complement activation pathways (classical pathway > alternative pathway > lectin pathway) and (bulk-nanoparticle) material hydrophobicity. The latter is exemplified by particles with plain > ascendingly different densities of PEG functionalization, resulting in various polymer configurations ("mushroom" > transition of "mushroom-brush" > "brush", consecutively). Adapted from ref.[180], copyright 2010, with permission from ACS Nano.

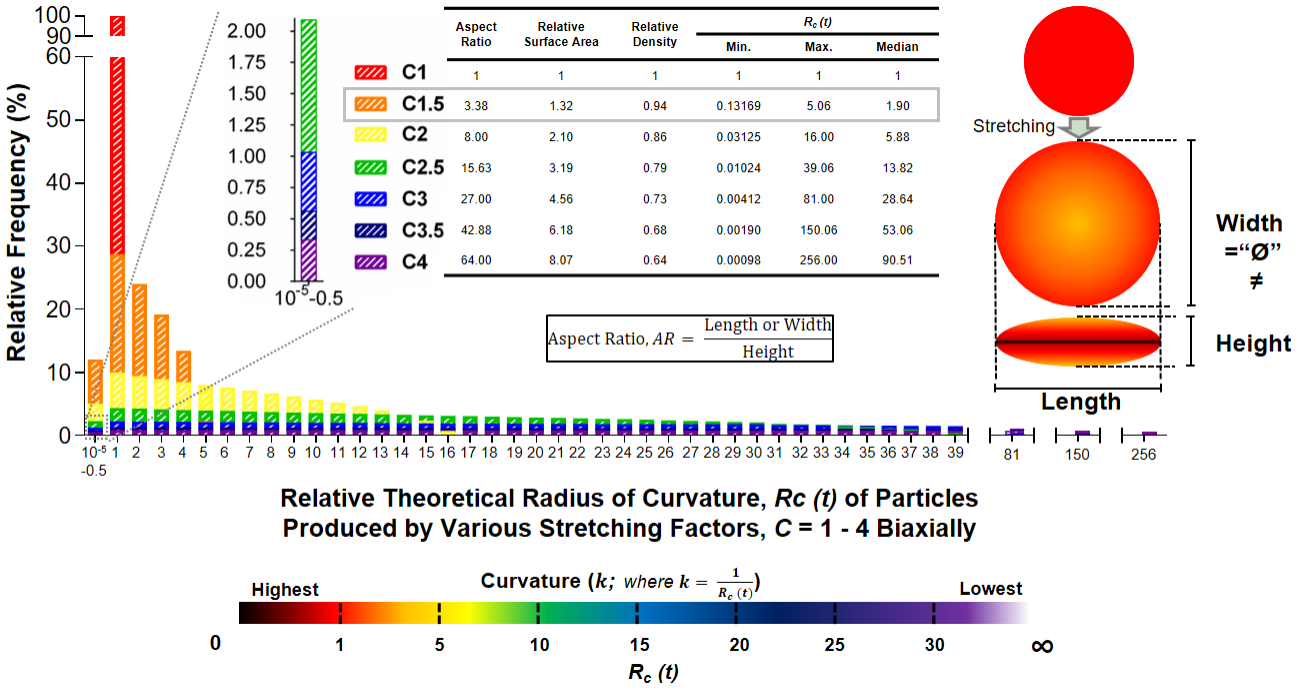

	Aspect Ratio	Relative Surface Area	Relative Density	$R_c(t)$ Min.	$R_c(t)$ Max.	$R_c(t)$ Median
C1	1	1	1	1	1	1
C1.5	3.38	1.32	0.94	0.13169	5.06	1.90
C2	8.00	2.10	0.86	0.03125	16.00	5.88
C2.5	15.63	3.19	0.79	0.01024	39.06	13.82
C3	27.00	4.56	0.73	0.00412	81.00	28.64
C3.5	42.88	6.18	0.68	0.00190	150.06	53.06
C4	64.00	8.07	0.64	0.00098	256.00	90.51

Figure S III-20. The cumulative distribution function of the radius of curvature and affected critical physical factors from oblate ellipsoid particles produced by the biaxial stretching process. The detailed calculation is displayed in Supplemental Calculation. The stretching factor of 1.5 biaxially is highlighted by a grey box, depicting the similar surface area and density as a prolate ellipsoid with a stretching factor of 3 (, used as the main core of multiply BCCNs; Figure III-9b-c). It is important to note that the theoretical aspect ratio definition of the oblate ellipsoid as displayed above is different from the prolate counterpart[16] (Inset Figure III-2c). Also, due to the limited experimental observation method, calculation of typical shifting time ($t_{1/2}$) for oblate ellipsoid was performed via a decrease of average gyration size/"diameter" (width ≈ height) of oblate particles (instead of aspect ratio as in the standard prolate ellipsoid).

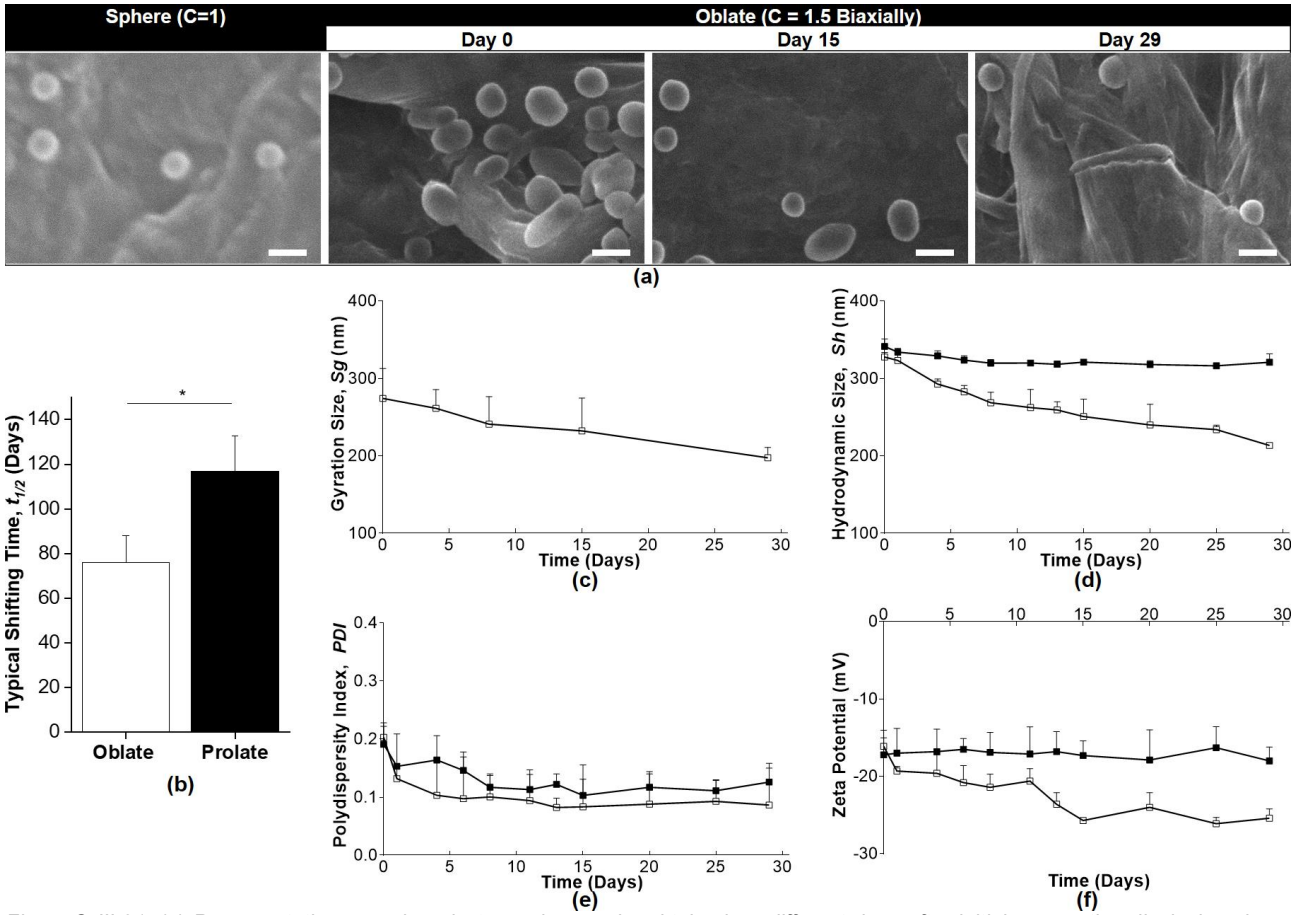

Figure S III-21. (a) Representative scanning electron micrographs obtained on different days after initial preparation displaying shape stability of oblate BCCNs in phosphate buffer saline (PBS) pH 7.4 310 mOsm for a maximum of 29 days at 37°C. Scale bars = 500 nm. Their other correlated data are displayed as (b) typical shifting time, plots of (c) gyration size/"diameter" which was determined from the aforementioned scanning electron micrographs, (d) hydrodynamic size, (e) polydispersity index/PDI, and (f) zeta potential over time.

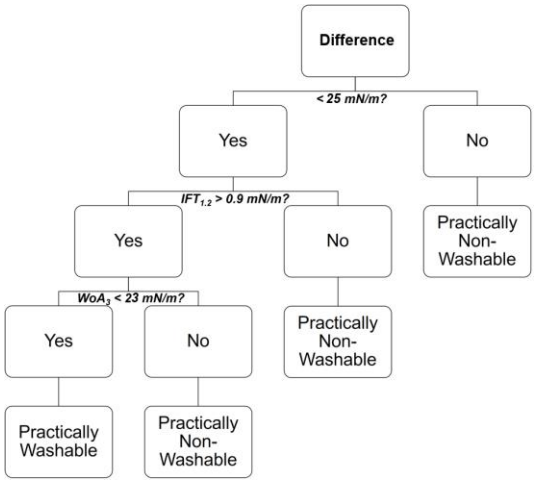

Figure S III-22. Proposed algorithms for material non-washability from another different material. Adopted from our previous report[16], copyright 2019, with permission from Advanced Healthcare Materials.

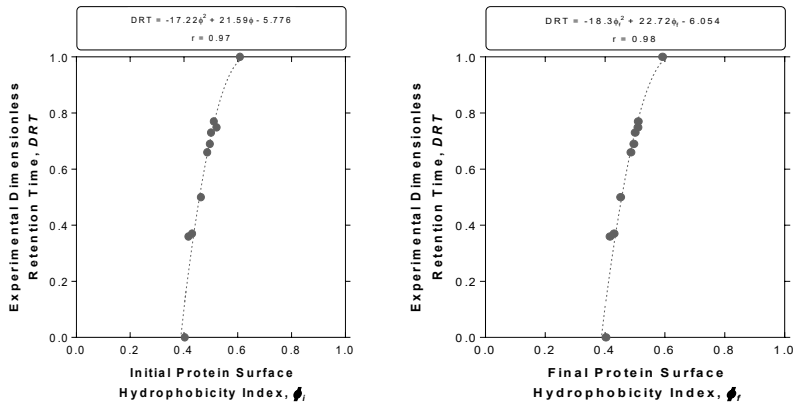

Colloquial Protein Name	Main PDB ID	UniProt ID
Alpha-Lactalbumin	1A4V	P00709
Alpha-Chymotrypsin	4CHA	P00766
Alpha-Amylase	3VX1	P0C1B3
Beta-Lactoglobulin	1CJ5	P02754
Chymotrypsinogen A	1CGI	P00766
Thaumatin	1THV	P02883
Ovotransferrin(=Conalbumin)	1AIV	P02789
Myoglobin	1YMB	P68082
RNAse A(=Ribonuclease pancreatic)	1AFU	P61823
Cytochrome C	1HRC	P00004

(a) **(b)** **(c)**

Figure S III-23. Relation between the values of computational protein surface hydrophobicity (Φ) based on the Cowan-Whittaker hydrophobicity scale and the experimental values of common protein's dimensionless retention time (DRT) using Hydrophobic Interaction Chromatography (HIC) with details as described in the Methods. (a) The currently validated method (using POPS[63] for amino acid residues' Solvent-Accessible Surface Area (SASA) calculation) to Lienqueo et al. dataset[62], which directly calculates 3D-structure, thus still does not consider comprehensive glycosylation density information. Very strong agreements (accuracy and repeatability) are obtained with a similar correlation coefficient (> 0.95), both for methods involving POPS (herein) and GRASP (Lienqueo et al.[62]). (b) The new proposed model, involving consideration of glycosylation from the UniProt database[41, 42], results in an even better correlation coefficient (0.98) between calculation and experimental data (see Methods for further details of glycosylation density calculation; see Figure S III-24 for further rationalization of glycosylation density). Please note that the correlations in both panel (a) & (b) are best described in a quadratic manner (as already proven by Lienqueo et al.[62]) between Φ_f and dimensionless retention time (DRT), which is already commonly used for many chromatographic methods in pharmaceutical and biomedical analysis area, including also Evaporative Light Scattering Detector (ELSD)[228], Gas Chromatography (GC)[229], etc. (c) Details of proteins and correlated PDB IDs(-UniProt IDs) thereof which were used in calculations representing diverse protein surface hydrophobicity, sorted in ascending order (from the lowest to the highest) of DRT from the bottom to the top of the table.

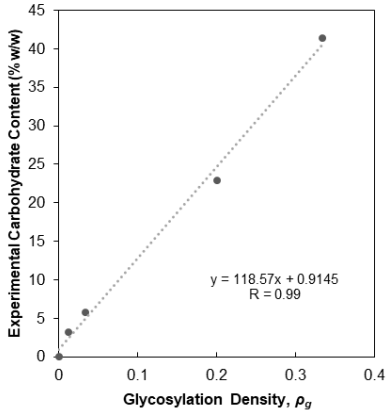

Colloquial Protein Name	Main PDB ID	UniProt ID
Orosomucoid-1	3KQ0	P02763
Fetuin-A	6HPV	P02765
Transferrin	3QYT	P02787
Ovalbumin	1OVA	P01012

(a) **(b)**

Figure S III-24. (a) A very strong correlation between glycosylation density, ρ_g and experimental carbohydrate content[230] (or so-called glycosylation content; correlation coefficient, r = 0.99). Combining this equation and ρ_g that can be obtained and calculated from bioinformatics analyses, for example, one can also reasonably compute the total molecular weight of CD47 ~49 kDa, using the molecular weight from amino acid analysis and the number of glycosylation sites in Table S III-3. This value is close to the experimental value herein ~49 kDa (Figure III-4a) & experimental range (45-55 kDa) elsewhere[231]. (b) Details of proteins and correlated PDB IDs(-UniProt IDs) thereof which were used in calculations accounting for a wide range of protein glycosylation density, sorted in ascending order (from the lowest to the highest) of experimental carbohydrate content from the bottom to the top of the table.

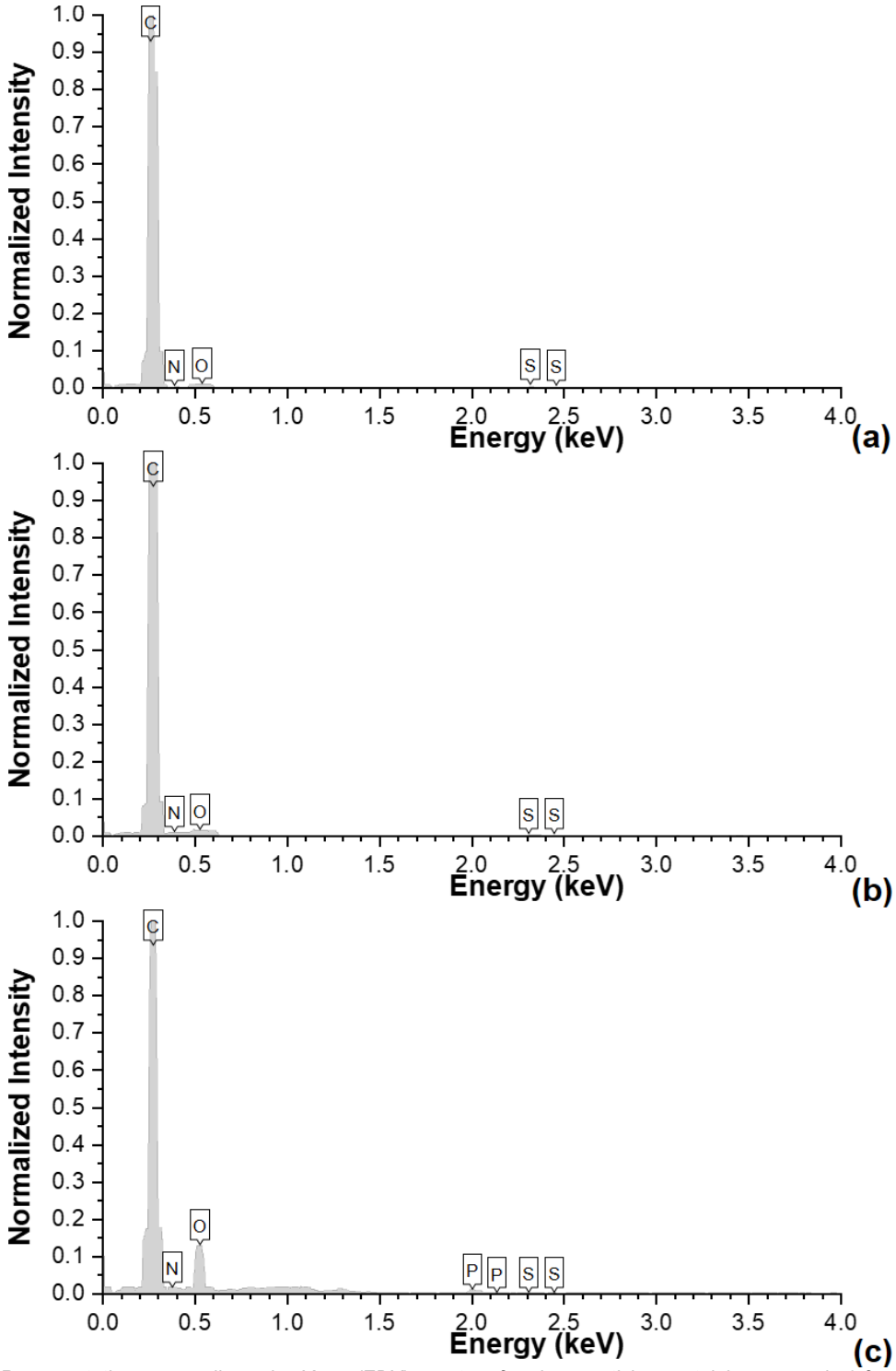

Figure S III-25. Representative energy dispersive X-ray (EDX) spectra of various particles containing coumarin-6 for in vitro study: (a) core nanoparticle (CNP), (b) PEGylated nanoparticle (CNP-PEG), and (c) bioinspired cell membrane-coated nanoparticle (BCCN). These serve as proofs of concept related to residual stabilizers. Please note that in the current study, nitrogen (N) and sulfur (S) elements could still be detected close to the limit of quantification of the instrument (with the closest one: CNP, followed by CNP-PEG and later BCCN) because of the presence of coumarin-6 (Figure S III-2). Otherwise, the S element could not be detected in CNP and CNP-PEG, while the N element could not be detected in CNP. This suggests that the CNPs, which were used to further manufacture other particles, contained minimal residual stabilizers.

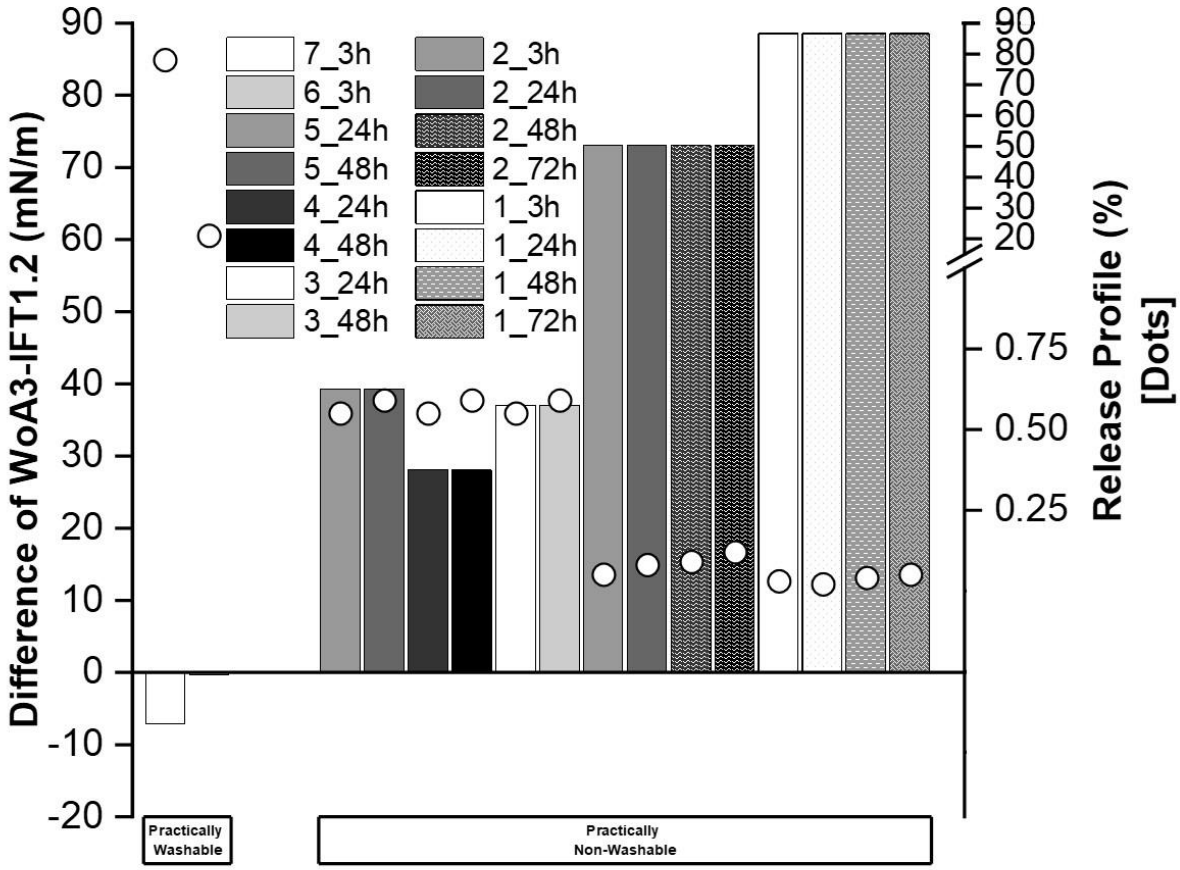

Figure S III-26. Correlation visualization of Table S III-11.

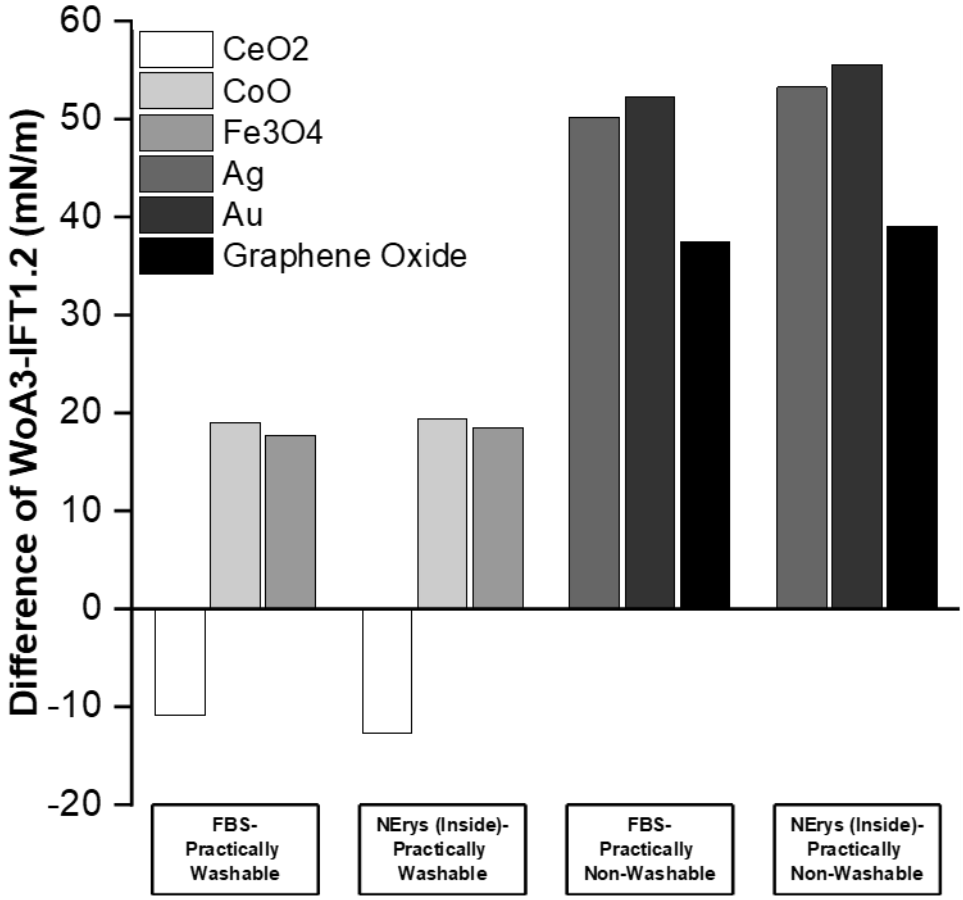

Figure S III-27. Correlation visualization of Table S III-12.

8.2. Supplemental Calculation
Distribution of Normalized Radius of Curvature on Non-Spherical (Oblate Ellipsoid) Particles Obtained by Stretching Biaxially Spherical Ones

Similar to the reported prolate ellipsoid[16], we can calculate the distribution of normalized radius of curvature in an oblate ellipsoid. In this case, instead of stretching uniaxially towards the x-axis, we can see the process of obtaining an oblate ellipsoid as biaxial stretching towards the y-axis and z-axis with the same stretching factor *C*. To preserve the volume of an oblate ellipsoid as our prolate ellipsoid, we need to reduce the radius along the x-axis by $\frac{1}{C^2}$ (which is later expressed as *C'*). Thus, following the notation in prolate ellipsoid[16], now we have the following mathematical definitions for oblate ellipsoid:

$$r_a = \frac{R}{C^2}, \quad r_b = R \cdot C \qquad \textit{Equation S III-5}$$

One may notice that we can simply substitute $\frac{1}{C^2}$ for C in the formula for a uniaxial prolate ellipsoid to obtain the formula for a biaxial oblate ellipsoid. This is indeed correct and we simply just need to adjust the normalization term to handle C < 1 and the reversed upper and lower limits. In the end, the normalization term for oblate ellipsoid is:

$$2\pi R \cdot \left(-\frac{3C'^2}{4} + \frac{3}{8C'} + \frac{\frac{3\pi}{2} - 3 \cdot \arcsin\left(C'^{3/2}\right)}{8C'^2\sqrt{C' - C'^4}} \right), \qquad C' = \frac{1}{C^2} \qquad \textit{Equation S III-6}$$

Consequently, the corresponding final distribution function $\bar{f}_C(\bar{R})$ for oblate ellipsoid is:

$$\bar{f}_C(\bar{R}) = \frac{\sqrt{\frac{1 - C'^{4/3} \cdot \bar{R}^{2/3}}{C' - C'^4}}}{-\frac{3C'^2}{4} + \frac{3}{8C'} + \frac{\frac{3\pi}{2} - 3 \cdot \arcsin\left(C'^{3/2}\right)}{8C'^2\sqrt{C' - C'^4}}}, \qquad C' = \frac{1}{C^2} \qquad \textit{Equation S III-7}$$

Meanwhile, its cumulative distribution function $\bar{F}_C(\bar{R})$ is (again, with $C' = \frac{1}{C^2}$):

$$\bar{F}_C(\bar{R}) = \frac{\sqrt{\frac{1 - C'^{4/3} \cdot \bar{R}^{2/3}}{C' - C'^4}} \left(\frac{3\bar{R}}{4} - \frac{3\bar{R}^{1/3}}{8C'^{4/3}} \right) + \frac{3 \cdot \arcsin\left(C'^{2/3} \cdot \bar{R}^{1/3}\right)}{8C'^2\sqrt{C' - C'^4}} - \frac{3C'^2}{4} + \frac{3}{8C'} - \frac{3 \cdot \arcsin\left(C'^{3/2}\right)}{8C'^2\sqrt{C' - C'^4}}}{-\frac{3C'^2}{4} + \frac{3}{8C'} + \frac{\frac{3\pi}{2} - 3 \cdot \arcsin\left(C'^{3/2}\right)}{8C'^2\sqrt{C' - C'^4}}} \qquad \textit{Equation S III-8}$$

Recall that the plain R is the original radius before stretching, while the $\bar{R}$ (with macron) is the radius of curvature after stretching.

8.3. Supplemental References

[195] M. Hadjidemetriou, S. McAdam, G. Garner, C. Thackeray, D. Knight, D. Smith, Z. Al-Ahmady, M. Mazza, J. Rogan, A. Clamp, K. Kostarelos, Adv. Mater. 2019, 31, 1803335.

[196] MarvinSketch, (Version 17.1.23.0), ChemAxon (http://www.chemaxon.com), Budapest 2017.

[197] D. K. F. Meijer, B. Weert, G. A. Vermeer, European Journal of Clinical Pharmacology 1988, 35, 295.

[198] G. R. Cherrick, S. W. Stein, C. M. Leevy, C. S. Davidson, J. Clin. Invest. 1960, 39, 592.

[199] D. E. Owens III, N. A. Peppas, Int. J. Pharm. 2006, 307, 93; M. L. Litvack, N. Palaniyar, Innate Immunity 2010, 16, 191.

[200] J. Bergendahl, D. Grasso, AIChE J. 1999, 45, 475.

[201] A. Szűts, M. Budai-Szűcs, I. Erős, N. Otomo, P. Szabó-Révész, Int. J. Pharm. 2010, 383, 132.

[202] S. Wang, Y. Zhang, N. Abidi, L. Cabrales, Langmuir 2009, 25, 11078.

[203] S. Joo, D. F. Baldwin, Nanotechnology 2009, 21, 055204.

[204] S. Kirchberg, Y. Abdin, G. Ziegmann, Powder Technol. 2011, 207, 311.

[205] M. Cichomski, K. Kośla, J. Grobelny, W. Kozłowski, P. J. Kowalczyk, A. Busiakiewicz, W. Szmaja, J. Balcerski, J. Alloys Compd. 2010, 507, 273.

[206] R. Lundy, C. Byrne, J. Bogan, K. Nolan, M. N. Collins, E. Dalton, R. Enright, ACS Appl. Mater. Interfaces 2017, 9, 13751.

[207] C. J. van Oss, R. J. Good, Journal of Macromolecular Science: Part A - Chemistry 1989, 26, 1183.

[208] C. J. van Oss, D. R. Absolom, A. W. Neumann, Ann. N.Y. Acad. Sci. 1983, 416, 332.

[209] J. Su, H. Sun, Q. Meng, P. Zhang, Q. Yin, Y. Li, Theranostics 2017, 7, 523.

[210] U.S. Food & Drug Administration, Vol. FDA Approved Drug Products: Hyaluronidase (Hylenex Recombinant®) Injection, FDA/Center for Drug Evaluation and Research, Silver Spring, MD, USA 2018, Package Insert; U.S. Food & Drug Administration, Vol. FDA Approved Drug Products: Rituximab-Hyaluronidase (Rituxan Hycela®; MabThera® EU [Subcutaneous]), FDA/Center for Drug Evaluation and Research, Silver Spring 2018, Package Insert.

[211] M. P. Desai, V. Labhasetwar, E. Walter, R. J. Levy, G. L. Amidon, Pharm. Res. 1997, 14, 1568.

[212] F. Chen, G. Wang, J. I. Griffin, B. Brenneman, N. K. Banda, V. M. Holers, D. S. Backos, L. Wu, S. M. Moghimi, D. Simberg, Nat. Nanotechnol. 2016, advance online publication.

[213] J. Müller, D. Prozeller, A. Ghazaryan, M. Kokkinopoulou, V. Mailänder, S. Morsbach, K. Landfester, Acta Biomaterialia 2018, 71, 420.

[214] K. Leidl, G. Liebisch, D. Richter, G. Schmitz, Biochimica et Biophysica Acta (BBA) - Molecular and Cell Biology of Lipids 2008, 1781, 655.

[215] Z. A. Hamburger, M. S. Brown, R. R. Isberg, P. J. Bjorkman, Science 1999, 286, 291.

[216] J. Llopis, J. M. McCaffery, A. Miyawaki, M. G. Farquhar, R. Y. Tsien, Proc. Natl. Acad. Sci. U. S. A. 1998, 95, 6803.

[217] H. Ando, A. Okamoto, M. Yokota, T. Asai, T. Dewa, N. Oku, J. Gene Med. 2013, 15, 375.

[218] D. L. Drabkin, J. H. Austin, J. Biol. Chem. 1935, 112, 51.

[219] G.-W. Li, D. Burkhardt, C. Gross, Jonathan S. Weissman, Cell 2014, 157, 624.

[220] A. Sionkowska, H. Kaczmarek, M. Wiśniewski, J. Kowalonek, J. Skopinska, Surf. Sci. 2004, 566-568, 608.

[221] P. Suttiprasit, V. Krisdhasima, J. McGuire, J. Colloid Interface Sci. 1992, 154, 316.

[222] S. Damodaran, L. Razumovsky, Surf. Sci. 2008, 602, 307.

[223] E. Koepf, R. Schroeder, G. Brezesinski, W. Friess, Eur. J. Pharm. Biopharm. 2017, 119, 396.

[224] A. Jarzab, N. Kurzawa, T. Hopf, M. Moerch, J. Zecha, N. Leijten, Y. Bian, E. Musiol, M. Maschberger, G. Stoehr, I. Becher, C. Daly, P. Samaras, J. Mergner, B. Spanier, A. Angelov, T. Werner, M. Bantscheff, M. Wilhelm, M. Klingenspor, S. Lemeer, W. Liebl, H. Hahne, M. M. Savitski, B. Kuster, Nature Methods 2020.

[225] R. B. Best, D. J. Brockwell, J. L. Toca-Herrera, A. W. Blake, D. A. Smith, S. E. Radford, J. Clarke, Anal. Chim. Acta 2003, 479, 87.

[226] R. D. Priestley, C. J. Ellison, L. J. Broadbelt, J. M. Torkelson, Science 2005, 309, 456; S. Napolitano, M. Wübbenhorst, Nat. Commun. 2011, 2, 260; M. Takagi, J. Phys. Soc. Jpn. 1954, 9, 359; W. M. Haynes, CRC Handbook of Chemistry and Physics, 97th Edition, CRC Press, 2016.

[227] S. Tenzer, D. Docter, J. Kuharev, A. Musyanovych, V. Fetz, R. Hecht, F. Schlenk, D. Fischer, K. Kiouptsi, C. Reinhardt, K. Landfester, H. Schild, M. Maskos, S. K. Knauer, R. H. Stauber, Nat. Nanotechnol. 2013, 8, 772.

[228] K. D. Dunn, J. Pharm. Biomed. Anal. 2001, 25, 539.

[229] D. Rood, J. Chromatogr. Sci. 1996, 34, 157; J. V. Hinshaw, LC GC Europe 2002, 24, 134.

[230] Thermo Fisher Scientific, in Instructions: Glycoprotein Carbohydrate Estimation Kit (Catalog Number 23260), thermofisher.com, Thermo Fisher Scientific, Rockford, IL, USA 2019.

[231] E. J. Brown, W. A. Frazier, Trends in Cell Biology 2001, 11, 130.

IV. SUMMARY AND OUTLOOK

Micro- and nanoparticles are systematically investigated as drug delivery systems (DDSs). Researchers have improved the performance of DDSs by optimizing their design parameters, such as size, surface charge, and attached target ligands. However, particle shape and mechanical properties were mostly practically neglected. As described in Chapter I, the aim of the current dissertation is to contribute in filling this particular void. Therefore, this dissertation has delved into a particle delivery system, combining non-spherical and natural mechanical properties of the Mother Nature instances, especially erythrocytes.

In the early phase of the project (Chapter II), a new, robust (silicone) oil-free method to fabricate non-spherical particles was successfully developed. This decreases considerably manufacturing time, undesired residual organic solvent, immunogenicity risk, and non-spherical shape instability of particles. Next, numerous analytical methods were utilized to characterize particle shape stability, especially at the submicron or nanoscale. At this size range, many unique advantages of DDS can be explored, such as the extension of the delivered drug half-life and uptake modulation into the target cells. However, it turns out that the non-spherical shape instability of particles at this size range is also much higher and challenging due to confinement effects. Therefore, it is an indispensable need to unravel and further understand the complexity of manufacturing aspects affecting shape stability, before proceeding with non-spherical particles towards in vitro and in vivo studies. Our report strongly suggests that shape change propensities of non-spherical particles to spherical particles might occur in favor of thermodynamics (triggered by material-water interfacial tension). The rate at which this alteration occurs is not only determined by the bulk material properties and storage temperature, but also importantly by the physicochemical properties of the resulting nanoparticles. The interfacial activity database, coupled with complete bulk-nanoparticle physicochemical properties, may be initial guidance to appraise the non-spherical particle shape stability in a dispersion medium. Besides, this rate of shape transformation can be tailored with the type and amount of (residual) stabilizers. Interestingly, the proposed interfacial activity-based algorithms can excellently be used to determine the suitability of a stabilizer for particle formation and “non-washability”. It appears that the (residual) stabilizers can be a great assistance for nanoparticles in maintaining their non-sphericity, if they are considered as a non-toxic, biodegradable, and biocompatible material. In chapter II extensive comparison and consideration of different manufacturing aspects toward (non-spherical) particle’s physicochemical properties and their potential and biological relations are presented. By that, a clear guideline for the design and manufacturing of non-spherical nanoparticles having adequate shape stability under physiological conditions is established.

In Chapter III, the established non-spherical nanoparticles were further tested in vitro and in vivo, followed by confirmatory studies in silico. This chapter describes the utilization of extracted red blood cell membrane (herein mainly abbreviated as NErys / Nanoerythrosomes) as a natural stabilizer for non-spherical nanoparticles, resulting in a novel system called “non-spherical bioinspired red blood cell membrane-coated nanoparticles” (non-spherical BCCNs). Non-spherical BCCNs reduced significantly the uptake by the cells and organs of the mononuclear phagocyte system (MPS) as compared to either only membrane-coated or only non-spherical systems. Accordingly, the non-spherical BCCNs displayed a remarkably higher concentration in blood over a 72 h period and interestingly permitted temporary accumulation in the brain for 48 h, while decreasing their uptake by the liver and spleen. The very strong and practically irreversible interactions of (superficially) hydrophobic proteins from the intracellular part of erythrocyte cell membranes to the core particle materials serve as the good anchors, while also improving the right-side-out membrane orientation and integrity. Furthermore, this interaction also proves that the better maintenance of non-spherical shape stability can only be attained by an adequate amount of stabilizers. This adequateness could be obtained because of the strong affinity between particles and stabilizers, i.e. RBC membrane (also called nanoerythrosomes [NErys]), compromising confinement effects. Interestingly, according to the in vitro and vivo results, the strong affinity appeared to not negatively impact the protein functionalities, specifically their function as a ”marker-of-self”. This finding suggests that the main proteins accounting for these functions (i.e. Band 3, the most abundant protein at the membrane of RBC, and CD47, respectively) are rather stable molecules, which are also representatively depicted from RBCs half-life of 120 days. Furthermore, the interfacially stable molecules at physiological condition can be differentiated by the computational biophysicochemical properties through my newly proposed Physiological-Therapeutic Biologics Classification System (PTBCS) algorithm concept. This concept offers a promising high throughput screening in the big data era, specifically in proteomics and interactomics, for the identification of low protein reversibility/refoldability at and/or post interface exposure, standardized to the air-water interface. Furthermore, the PTBCS can be complemented by interfacial activity parameters (calculated using Owens and Wendt approach) to predict the affinity of certain proteins to material surfaces enabling better control of biomolecular-excipient interactions, especially protein-protein interactions and protein-excipient interactions.

According to the conclusion of all chapters, (silicone) oil-free non-spherical particles were reproducibly manufactured and characterized. The dual influence of particle shape and red blood cell membrane-coating on the in vitro and in vivo levels was studied, followed by rationalization of these results by means of further in vitro and in silico analyses. A considerable character was demonstrated during all these analyses by the combination of non-spherical particles and cell membrane-coating. The dual combination between particle shape and cell membrane-coating has the potential to play an important design parameter in the future of drug delivery systems.

V. APPENDIX I

Publications in Journals Associated with This Dissertation:

B.M. Haryadi, G. Winter, Rationalization of Biological Drug Development and Delivery using an Integration of Experiments and Computations. (In Preparation)

B.M. Haryadi, G. Winter, J. Engert, Lyophilization as a Stabilization Approach for Non-spherical Bioinspired Cell Membrane-coated Nanoparticles. (In Preparation)

B.M. Haryadi, B.M. Kopec, L. Isert, N. Hartl, A. Mehta, D. Hafner, I. Amin, R. Schubel, A.O. Muis, R. Jordan, O.M. Merkel**,** T.J. Siahaan, G. Winter, J. Engert, Phagocytosis, Biodistribution, and Rationale of Multiply Bioinspired Nanoparticles: Non-Spherical Shape and Cell Membrane Coating. (In Preparation)

B.M. Haryadi, D. Hafner, I. Amin, R. Schubel, R. Jordan, L. Isert, O. Merkel, G. Winter, J. Engert, Improving Non-Spherical Shape Stability of Nanoparticles using a Bioinspired Approach. (In Preparation)

***B.M. Haryadi**, D. Hafner, I. Amin, R. Schubel, R. Jordan, G. Winter, J. Engert, 2019, Nonspherical Nanoparticle Shape Stability is Affected by Complex Manufacturing Aspects: Its Implications for Drug Delivery and Targeting. Advanced Healthcare Materials, 8, 1900352.

****Selected as 'Hot Topic: Drug Delivery' by Wiley-VCH (August-September 2019)***.

Publications in Conferences Associated with This Dissertation:

B.M. Haryadi, G. Winter, J. Engert, Rationalization of Drug Development and Delivery using an Integration of Simulations and Experiments, Roche Biotech Day, Penzberg-Germany, 2nd April 2019. (https://app.sli.do/event/uihydkv6/agenda)

B.M. Haryadi, G. Winter, J. Engert, Stabilization of Bioinspired Non-spherical Cell Membrane-coated Nanoparticles by Lyophilization, The Controlled Release Society (CRS) Annual Meeting & Exposition, New York-USA, 22nd-24th July 2018. (https://www.abstractsonline.com/pp8/#!/5717/presentation/13986)

B.M. Haryadi, G. Winter, J. Engert, Overcoming Non-Spherical Shape Instability of Nanoparticles Intended for Drug Delivery Using a Bioinspired Approach, 11th World Meeting on Pharmaceutics, Biopharmaceutics and Pharmaceutical Technology, Granada-Spain, 19th-22nd March 2018.

B.M. Haryadi, G. Winter, J. Engert, Systematic Studies on Shape Instability of Non-Spherical Nanoparticles, 11th World Meeting on Pharmaceutics, Biopharmaceutics and Pharmaceutical Technology, Granada-Spain, 19th-22nd March 2018.

B.M. Haryadi, G. Winter, J. Engert, Non-Spherical Nanoparticle Shape Stability is Affected by Manufacturing Aspects, 21st Annual Meeting of the Controlled Release Society (CRS) Germany Local Chapter, Marburg-Germany, 2nd-3rd March 2017.

B.M. Haryadi, G. Winter, J. Engert, Engineering of Bioinspired Nanoparticles for Drug Delivery, Annual Meeting of the German Pharmaceutical Society (Deutsche Pharmazeutische Gesellschaft / DPhG), Munich-Germany, 4th-7th October 2016. (https://www.dphg.de/fileadmin/downloads/DPhG2016_ConferenceBook_final.pdf)